

Dissertation zur Erlangung des Doktorgrades
der Fakultät für Chemie und Pharmazie
der Ludwig-Maximilians-Universität München

**Stabilizing Metastable Lead-Free Double
Perovskite by Morphological and Molecular Level
Dimensional Reduction**

Shizhe Wang

aus

Shaoxing, China

2024

Erklärung

Diese Dissertation wurde im Sinne von § 7 der Promotionsordnung vom 28. November 2011 von Herrn Prof. Dr. Thomas Bein betreut.

Eidesstattliche Versicherung

Diese Dissertation wurde eigenständig und ohne unerlaubte Hilfe bearbeitet.

München, den 28.06.2024

Shizhe Wang

Dissertation eingereicht am:	28.06.2024
Gutachter:	Prof. Dr. Thomas Bein
Zweitgutachter:	Prof. Dr. Achim Hartschuh
Mündliche Prüfung am:	19.09.2024

Acknowledgements

Foremost I would like to acknowledge and give my warmest thanks to my supervisor Prof. Dr. Thomas Bein for your guidance and advice throughout all the stages of my PhD study. I want to thank you for giving me the opportunity to study and work in your chair and for supporting me financially after the termination of my CSC stipend. In China, there is an ancient saying, "One day as a teacher, a lifetime as a father." In German, the word of supervisor is "Doktorvater", which conveys the same meaning. Your words and actions fully demonstrate that you are a perfect Doktorvater, and I will benefit from them throughout my life. You are a role model in my life. You made me understand the meaning of the word "charm". As another Chinese saying goes, "Peach and plum trees do not speak, yet a path is formed beneath them." The phrase metaphorically suggests that, like peach and plum trees that don't boast about their beauty or value, good teachers or mentors quietly and modestly contribute to the growth and success of their students. The path forming beneath them symbolizes the positive and fruitful development of those who are influenced by their guidance. At this moment, reflecting on my doctoral academic journey, all my progress and improvement are attributed to your earnest and patient guidance. I'm so grateful to be a part of AK Bein.

I would like to express my deepest gratitude to Prof. Dr. Achim Hartschuh for being my second supervisor. It's my great honour to collaborate with you. Thank you for your contributions to all our publications and for reviewing this thesis. Your meticulous approach to academia has deeply impressed me.

Many thanks go to my teammate and friend Rik Hooijer for our excellent collaboration. Your wisdom and persistence have elevated our project to a higher level. In addition to collaborating in the academic area, we have also developed a strong personal connection. I still remember you came to my office and talked to me on the first day when I joined our group. We had some tea and talked a lot about our own culture. It's such a good memory we share together that I believe our friendship will last forever. Also, I want to thank Hannah and you for bringing Mona to this beautiful world.

Acknowledgement

My special thanks go to Dr. Dan Han and Prof. Dr. Hubert Ebert for the excellent theoretical study for our projects. Dan was the only Chinese person in Building E before I arrived, giving me a sense of familiarity as a newcomer in a foreign land. We have started a good relationship in both academia and personal life since we met each other for the first time in the kitchen of the second floor. You take care of me in both academic and personal aspects, like an elder sister. I'm genuinely thrilled for you as you embark on a new chapter in your career as a professor at Jilin University in Changchun, China.

I would like to thank Dr. Markus Döblinger and Dr. Steffen Schmidt for the excellent investigations on electron microscopes. Without your help, my studies on the size and morphology of perovskite nanocrystals would not have been as fruitful. I want to thank Markus for all the inspiring discussion on the crystal structures of our new perovskite materials. I've learned a lot about crystallography from you, although I'm aware that these are just the tip of the iceberg of your knowledge. Steffen, conversations with you are always so intriguing. Your gentle personality and meticulous scholarly approach captivate me deeply.

I would like to thank Hannah Illner, Dr. Clément Maheu and Prof. Dr. Thomas Mayer for the great investigation on X-ray photoelectron spectroscopy and ultraviolet photoelectron spectroscopy. Hannah, I'm so grateful that you are willing to help me checking the oxidation state of Cu in my sample even you are really busy with your Praktikum duty. Your smile will always encourage me, even we don't achieve the expected results. Clément, you are the first French person I have ever known in my life and the first collaborator outside LMU during my PhD study. The first online meeting between us was so enjoyable that we not only discussed about our project but also talked a lot about your hometown, Paris. It's a pity that we still haven't had the chance to meet in person, but we believe we will find the time. I would like to thank Zehua Xu and Alexander Biewald for the excellent investigation on photoluminescence measurement. Zehua, the goal I scored with the assist from you on the pitch is the highlight of my "soccer career". I wish we can collaborate more in both academia and soccer. Alexander, thank you for always bringing your jokes to our office, even though sometimes I find them a bit challenging to understand.

Thank you, AK Bein, for the great working atmosphere during my whole PhD study. I have had a delightful time in the group. These wonderful memories will accompany me for a lifetime. I would like to thank Corinna Heidt for all the help, including my visa issue and contracts. Thank you for taking care of me in all the aspects during my stay in Germany. Thank you, Tina Reuther, for ensuring the

Acknowledgement

smooth operation of our laboratory. I want to thank Karin, Dana, Jenny, Laura S., Roman, Kathi, Meli and Negar for always being there when I need help.

My special thanks go to WhatsApp group “Guys from downstairs”. Thank you, Tianhao, Nacho, Marina, Klaudija and Apeksha, for not only supporting me in the lab but also brightening my after-work life with parties and birthday celebrations. The gift of Arsenal jersey you all gave me for my 30th birthday will be cherished dearly. Meeting here from different countries is fate, and this fate will evolve into a lifelong friendship.

My special thanks also go to the PV lab. I want to thank Nadja and Max for the introduction of perovskite lab. Thank you, Max, for helping me with my first hot-injection reaction and my first working solar cell. I’m so lucky to have you guiding me at the beginning of my PhD study. Thank you, Marci, Anderson, Rik, Andi, Flo and Ali for being such nice lab mates to work with. You always give me helpful advice on my projects. Thank you, Andi, for showing me the culture, customs and cuisine of Italy. You told me once that you wish you could talk to me in Italian. I’m still learning it. “Tutto Bene?” I regret not accepting your offer of an Italy national football team jersey to win my support for Italy in UEFA EURO 2020, the year your team won the championship. Thank you, Flo, for being the anti-perovskite comrade with me. It's also a cherished memory to go group hiking under your guidance. Thank you, Ali, for always sharing your tips on spin-coating technology with me. I want to thank Anderson for your kindness and assistance, guiding me through the laboratory and helping me integrate into the AK Bein family quickly. I want to thank Marci for all the guidance and help in the lab.

I want to express my gratitude to all the graduates I have worked with, Peter, Patrick, Erika, Julian, Dorothee, Sabrina, Jonathan, Niklas, Bernhard, Andre, Flo G., Michi, Daniel, Flo Z., Patricia, Sebastian, Derya, Stephan, Laura F. and Lisa. The joyful moments we spent together still shimmer in front of my eyes.

Many thanks to my Chinese community in Building E, Tinahao, Shuo, Bosong, as well as previous members Meizhu, Aijia, Yiling and Yilan. Thank you for the company during the lunch breaks, where we could talk about various things and have fun together. Special thanks to Tianhao for working together even late at night and on weekends, and for all the cherished moments we had together. After three years of company, you have become like family to me, someone with whom I can share anything.

Acknowledgement

Finally, my deepest gratitude goes to my parents, whom I haven't been able to meet in person for over 4 years. Initially, it was due to the pandemic, and later, it was because of academic commitments that I couldn't find the right time to be with you. This is the longest period of separation between us, and I hope to reunite with you soon. In my academic journey, you have provided me with complete freedom and unwavering support, enabling me to wholeheartedly pursue the life I desire. Without you, there is no me; without your guidance, I wouldn't have persevered to where I am today. Thank you!

最后，我要感谢我的父母。我们已经四年多没有见了，之前因为疫情的原因，后来又因为学业，无法找到合适的时间回到你们的身边。这是我们之间分别最长的一段时间，我也希望能早日回到你们身边。在学业上，你们给予我充分的自由和无限的支持，让我可以义无反顾地去追求自己想要的人生。没有你们，就没有我；没有你们的教导，就没有坚持走到现在的我。谢谢你们！

Table of Contents

Erklärung	II
Eidesstattliche Versicherung	II
Acknowledgements	III
Table of Contents	VII
List of Abbreviations	XIII
Abstract	1
1 Introduction	3
1.1 The Global Energy Crisis.....	3
1.2 The Development of Solar Cells (Three Generations).....	6
1.2.1 The First Generation.....	7
1.2.2 The Second Generation.....	8
1.2.3 The Third Generation.....	10
1.3 Perovskite Solar Cells.....	12
1.3.1 Crystal Structures of Metal Halide Perovskite Materials.....	13
1.3.2 Lead-Based Perovskite Materials.....	14
1.3.3 Device Categories.....	15
1.3.4 Working Principle of PSCs.....	16
1.3.5 The Commercialization of Perovskite Solar Cells: Large-Area Fabrication, Stability and Toxicity Issues	18

Table of Contents

1.4	Lead-Free Perovskite Materials.....	20
1.4.1	Single-Element-Substituted Lead-Free Halide Perovskites	20
1.4.2	Lead-Free Halide Double Perovskites	21
1.5	Lower-Dimensional Perovskite Materials.....	25
1.5.1	Perovskite Nanocrystals.....	25
1.5.2	Organic-Inorganic Hybrid Layered Perovskites.....	25
1.5.3	The Merits of Reduced Dimension for Metastable Double Perovskite Materials.....	31
1.6	Outline of the Thesis.....	33
1.7	References	35
2	Characterization Techniques.....	45
2.1	X-ray Diffraction (XRD).....	45
2.2	Grazing Incidence Wide Angle X-Ray Scattering (GIWAXS).....	47
2.3	Inductively Coupled Plasma-Optical Emission Spectroscopy (ICP-OES)	48
2.4	Electron Microscopy.....	48
2.4.1	Scanning Electron Microscopy (SEM).....	50
2.4.2	Energy Dispersive X-ray Spectroscopy (EDX).....	51
2.4.3	Transmission Electron Microscopy (TEM).....	51
2.5	Atomic Force Microscopy (AFM).....	52
2.6	Photoelectron Spectroscopy (PES).....	53
2.7	Nuclear Magnetic Resonance Spectroscopy (NMR)	54
2.8	Ultraviolet-Visible Spectroscopy (UV-Vis)	55
2.9	Photoluminescence Spectroscopy (PL)	56
2.10	Current-Voltage (<i>J-V</i>) Measurements.....	57
2.11	Quantum Efficiency (QE).....	59
2.12	References	61

3	Review Article: Perovskite Nanocrystals: Synthesis, Stability and Optoelectronic Applications	63
3.1	Abstract.....	65
3.2	Introduction.....	65
3.3	Synthesis of Perovskite Nanocrystals	68
3.3.1	Wet Synthesis Processes of PNCs.....	68
3.3.2	Dry Synthesis Processes of PNCs.....	82
3.3.3	Synthesis Methods of Lead-free PNCs	83
3.3.4	Anion-Exchange Reaction.....	87
3.4	Stability of Perovskite Nanocrystals.....	89
3.4.1	Crystal Structural Stability	89
3.4.2	Interface-Induced Instability	91
3.4.3	Environmental Stability	92
3.5	Encapsulation for improving the stability.....	97
3.5.1	Organics Protection.....	98
3.5.2	Inorganics Protection.....	100
3.6	Application	106
3.6.1	Solar Cells (SCs).....	106
3.6.2	Light-emitting Diodes (LEDs)	112
3.6.3	Photodetectors (PDs).....	118
3.7	Summary and Outlook.....	122
3.8	Conflict of Interest.....	124
3.9	Acknowledgements.....	124
3.10	References	125

4 Room-Temperature Synthesis of Lead-Free Copper(I)-Antimony(III)-Based Double Perovskite Nanocrystals.....	137
4.1 Abstract.....	138
4.2 Introduction.....	139
4.3 Experimental Methods	141
4.4 Results and Discussion.....	144
4.4.1 Theoretical Study of Cs ₂ CuSbCl ₆ HDP Structure	144
4.4.2 Synthesis of Cs ₂ CuSbCl ₆ DPNCs.....	145
4.4.3 Optical Properties of Cs ₂ CuSbCl ₆ DPNCs	149
4.4.4 Synthesis of Cs ₂ CuSbBr ₆ DPNCs by Anion-Exchange Reaction	150
4.4.5 Electronic structure of Cs ₂ CuSbCl ₆ and Cs ₂ CuSbBr ₆ DPNCs.....	151
4.4.6 Film Fabrication of Cs ₂ CuSbCl ₆ and Cs ₂ CuSbBr ₆ DPNCs	152
4.5 Conclusion	154
4.6 Associated Content.....	155
4.7 Author Information.....	155
4.8 Acknowledgements.....	156
4.9 References	156
4.10 List of Figure Legends.....	161
4.11 Supporting Information	168
4.11.1 Experimental Details	168
4.11.2 Supporting Figures.....	171
4.11.3 References.....	190
5 Overcoming Intrinsic Quantum Confinement and Ultrafast Self-Trapping in Ag-Bi-I and Cu-Bi-I Based 2D Double Perovskites through Electroactive Cations	191
5.1 Abstract.....	192

Table of Contents

5.2	Introduction.....	192
5.3	Results and Discussion.....	194
5.3.1	Structural Characterization	194
5.3.2	Electronic Structure and Band Alignment.....	196
5.3.3	Optical Properties	198
5.3.4	Photoconductivity and Photovoltaic Performance	205
5.4	Conclusion	211
5.5	Acknowledgment.....	212
5.6	References	212
5.7	Supporting Information	215
6	Conclusions and Outlook.....	257
7	Publications and Conference Contributions.....	261
7.1	Publications.....	261
7.2	Contribution to Conferences	261
7.2.1	Oral Presentations	261
7.2.2	Poster Presentations.....	262

Table of Contents

List of Abbreviations

ΔH	decomposition energies
0D	zero-dimensional
1D	one-dimensional
2D	two-dimensional
3D	three-dimensional
4AMP	4-(aminomethyl)piperidinium
4FPEA	4-fluorophenethylammonium
A	absorbance
AAO	anodized aluminum oxide
ACA ⁺	acetamidinium cations
ACI	alternating cations in the interlayer space
AE2T	5,5'-diylbis(aminoethyl)-[2,2'-bithiophene]
AFM	atomic force microscopy
AIRSS	ab Initio Random Structure Searching
AM1.5G	standard air mass 1.5 global
APS	Announced Pledges Scenario
APTES	(3-aminopropyl) triethoxysilane
AR6	Sixth Assessment Report

List of Abbreviations

a-Si	amorphous silicon
a-Si:H	hydrogenated amorphous silicon
AT&T	American Telephone and Telegraph
AX	A-site cation halide salt
BA ⁺	butylammonium
BDA ²⁺	1,4-butanediammonium
BHJ	bulk heterojunction
C ₆ H ₁₆ N ₂	1,4-cyclohexanediamine
CB	conduction band
CBC	Covalent Bond Classification
CBM	conduction band minimum
CCD	charge coupled device
CdS	cadmium sulphide
CdTe	cadmium telluride
CFI	Nikon Chrome-Free Infinity-Corrected
CIGS	copper indium gallium selenide
CLSM	confocal laser scanning microscope
CNC	cellulose nanocrystal
CO ₂	carbon dioxide
CO ₂ -eq	carbon dioxide equivalent
CQDs	colloidal quantum dots
Cr	chromium
c-Si	crystalline-silicon

List of Abbreviations

CsOAc	caesium acetate
CTL	charge transport layers
Cu	copper
CVD	chemical vapour deposition
DDAB	di-dodecyl dimethyl ammonium bromide
DFT	density functional theory
DJ	Dion-Jacobson
DMSO	dimethyl sulfoxide
DOS	density of states
DOSY	Diffusion Ordered NMR Spectroscopy
DPNCs	double perovskite nanocrystals
DSSCs	dye-sensitized solar cells
E_{acc}	acceleration energy
E_{b}	exciton binding energy
E_{BE}	electron binding energy
EDS	Energy-Dispersive X-ray Spectroscopy
EELS	Electron Energy Loss Spectroscopy
E_{Fn}	quasi-Fermi levels of electrons
E_{Fp}	quasi-Fermi levels of holes
$E_{\text{g}}/E_{\text{G}}$	band gap energy
E_{hull}	energy above the convex hull
EPFL	École Polytechnique Fédérale de Lausanne
EQE	external quantum efficiency

List of Abbreviations

ETL	electron transporting layer
F4TCNQ	2,3,5,6-tetrafluoro-7,7,8,8-tetracyanoquinodimethane
FA	formamidinium
FDA	Food and Drug Administration
Fe	iron
FET	field-effect transistor
<i>FF</i>	fill factor
F-PEA	4-fluorophenethylammonium
FTO	F-doped SnO ₂
FWHM	full width at half maximum
GA ⁺	guanidinium cation
GaAs	gallium arsenide
Ge	germanium
GHG	green-house gas
GIWAXS	Grazing incidence wide angle X-ray scattering
GRAS	Generally Recognized As Safe
Gt	gigatonne
<i>h</i>	Planck's constant
HDPs	halide double perovskites
HOMO	highest occupied molecular orbital
HRTEM	High-Resolution Transmission Electron Microscopy
HTL	hole transporting layer
<i>I</i>	measured intensity of transmitted light

List of Abbreviations

I_0	the intensity of incident light
ICMES-2022	the Fifth International Conference on Materials & Environmental Science
ICP-OES	Inductively coupled plasma optical emission spectroscopy
IEA	International Energy Agency
IPCC	Intergovernmental Panel on Climate Change
IQE	internal quantum efficiency
ITO	indium tin oxide
J_{int}	integrated photocurrent density
J_{max}	current density at maximum power point
J_{ref}	reference diode current density
J_{sa}	current density of a device at short circuit conditions
J_{sc}	short-circuit current density
J - V	current-voltage
k_B	Boltzmann constant
KE	the kinetic energy
KSF	$\text{K}_2\text{SiF}_6 \cdot \text{Mn}^{4+}$
LARP	ligand-assisted reprecipitation
LP	long-pass filter
LUMO	lowest unoccupied molecular orbital
MA	methylammonium
m_e	electron mass
MeOAc	methyl acetate
MHPs	metal halide perovskites

List of Abbreviations

Mo	molybdenum
MQWs	multiple quantum wells
MSHSs	magnesium silicate hollow spheres
NCus	nanocubes
NMR	Nuclear magnetic resonance
NOE	naphthalene-O-ethylammonium
NOE-Ag	(NOE) ₄ AgBiI ₈
NOE-Cu	(NOE) ₄ CuBiI ₈
NOP	naphthalene-O-propylammonium
NOP-Ag	(NOP) ₄ AgBiI ₈
NOP-Cu	(NOP) ₄ CuBiI ₈
NPLs	nanoplatelets
NREL	National Renewable Energy Laboratory
NRs	nanorods
NSs	nanosheets
NTSC	National Television System Committee
NWs	nanowires
OA	oleic acid
OAm	oleylamine
ODA-X	octadecylammonium halides
ODE	1-octadecene
OLAM-X	oleylammonium halides
OSCs	organic solar cells

List of Abbreviations

PBE	Perdew–Burke–Ernzerhof
PbX ₂	lead halide salts
PCE	power conversion efficiency
pc-LEDs	phosphor-converted light-emitting diodes
PDA ²⁺	1,3-propanediammonium
PDs	photodetectors
PEA ⁺	phenylethylammonium
PECVD	plasma-enhanced chemical vapor deposition
PeLEDs	perovskite-based light-emitting diodes
PES	photoelectron spectroscopy
P_{in}	power of incident light
PL	photoluminescence
PLQY	photoluminescence quantum yield
P_{max}	maximum power
PMMA	poly(methyl methacrylate)
PNCs	perovskite nanocrystals
POE	pyrene-O-ethylammonium
POE-Ag	(POE) ₄ AgBiI ₈
POE-Cu	(POE) ₄ CuBiI ₈
POP	pyrene-O-propylammonium
POP-Ag	(POP) ₄ AgBiI ₈
POP-Cu	(POP) ₄ CuBiI ₈
PPDA	para-phenylenediammonium

List of Abbreviations

PQDs	perovskite quantum dots
PSCs	perovskite solar cells
PV	photovoltaic
PVDF	polyvinylidene fluoride
PVK	poly(9-vinlycarbazole)
PVP	Polyvinyl pyrrolidone
PXRD	powder X-ray diffraction
q	elementary charge
QDs	quantum dots
QDSCs	quantum dot solar cells
QE	quantum efficiency
QLEDs	quantum dot light-emitting diodes
QW	quantum-well
QYs	quantum yields
R	reflectance
rcf	relative centrifugal force
RF	radiofrequency
RH	relative humidity
RP	Ruddlesden-Popper
rpm	revolutions per minute
RT	room temperature
SEM	Scanning Electron Microscopy
SLME	spectroscopic limited maximum efficiency

List of Abbreviations

Sn	tin
SOC	spin-orbit coupling
<i>spiro</i> -MeOTAD	2,2',7,7'-tetrakis(N,N-di-p-methoxyphenylamine)-9,9'-spirobifluorene
SPO	stabilized power output
SR	spectral responsivity
SR	supersaturated recrystallization
STEPS	Stated Policies Scenario
TAS	transient absorption spectroscopy
TBA-X	tetrabutylammonium halides
TCO	transparent conducting oxide
TCSPC	time-correlated single photon counting
TEM	Transmission Electron Microscopy
TEOS	tetraethyl orthosilicate
TGA	thermogravimetric analysis
THz	terahertz
TMOS	tetramethyl orthosilicate
TMPPA	bis(2,4,4-trimethylpentyl) phosphinic acid
TMSBr	bromotrimethylsilane
TMSI	iodotrimethylsilane
TMSX	trimethylsilyl halide
ToF-SIMS	time-of-flight secondary ion mass spectrometry
TRMC	time-resolved microwave conductivity
TRPL	time-resolved photoluminescence

List of Abbreviations

TWh	terawatt-hours
UPS	ultraviolet photoelectron spectroscopy
USD	United States dollar
UV-Vis	ultraviolet-visible
VASP	Vienna ab initio simulation package
VB	valence band
VBM	valence band maximum
V_{\max}	voltage at maximum power point
V_{oc}	open-circuit voltage
WDS	Wavelength-Dispersive X-ray Spectroscopy
WLED	white light-emitting devices
XPS	X-ray photoelectron spectroscopy
XRD	X-ray diffraction
λ	wavelength
$\mu\text{-Si}$	microcrystalline silicon
μGR	micrometer-sized graphene
ϕ	photon flux

Abstract

In the field of perovskite solar cells, explorations of new lead-free double perovskite materials are of great interest to address toxicity issues of lead-based perovskites. $\text{Cs}_2\text{AgBiBr}_6$ is the first and the most-studied double perovskite material as a promising candidate for photovoltaic applications, owing to its long carrier lifetime and outstanding stability. However, reported PCEs of $\text{Cs}_2\text{AgBiBr}_6$ solar cells remain mostly around 3% due to the large indirect band gap of this material and other factors. Therefore, the expansion of absorption to the longer wavelengths is being pursued for double perovskite solar cells. To address this issue, general strategies are either searching for alternative combinations of central metal atoms to replace Ag-Bi or developing its iodide analogue. Some candidates with theoretically promising optoelectronic properties consist of metastable octahedra, which can not be synthesized as bulk crystals but can be stabilized by morphological or molecular level dimensional reduction.

In this thesis, we first reviewed the strategy of morphological level dimensional reduction. We summarized the latest advances of the synthesis methods for both lead-based and lead-free perovskite nanocrystals (PNCs). Stability is one of the critical issues for the possible commercialization of PNCs. We reviewed the crystal structural stability, interface-induced stability and environmental stability, such as oxygen, moisture, light and thermal stability. Moreover, strategies for encapsulation to protect PNCs were discussed. Importantly, various applications of the PNCs in optoelectronics, like solar cells, light-emitting diodes and photodetectors, were briefly presented. Finally, the challenges remaining for improving the stability of PNCs and an outlook towards possible directions in developing PNC-based devices with high performance and great operation durability were addressed.

In the second part of the thesis, we describe the synthesis of $\text{Cs}_2\text{CuSbCl}_6$ double perovskite nanocrystals (DPNCs) at ambient conditions by a facile and fast method, namely, a modified ligand-assisted reprecipitation (LARP) method. We chose methanol as solvent for precursor salts as it is less toxic and easily removed in contrast to widely-used dimethylformamide. Our computational

structure search shows that the $\text{Cs}_2\text{CuSbCl}_6$ structure containing alternating $[\text{CuCl}_6]^{5-}$ and $[\text{SbCl}_6]^{3-}$ octahedral units is a metastable phase that is 30 meV/atom higher in energy compared to the ground state structure with $[\text{CuCl}_3]^{2-}$ and $[\text{SbCl}_6]^{3-}$ polyhedra. However, this metastable $\text{Cs}_2\text{CuSbCl}_6$ double perovskite structure can be stabilized through the solution-based nanocrystal synthesis. Using an anion-exchange method, $\text{Cs}_2\text{CuSbBr}_6$ DPNCs are obtained for the first time, featuring a narrow band gap of 0.9 eV. Finally, taking advantage of the solution processability of DPNCs, smooth and dense $\text{Cs}_2\text{CuSbCl}_6$ and $\text{Cs}_2\text{CuSbBr}_6$ DPNC films are successfully fabricated. Hence, we establish that these metastable $\text{Cs}_2\text{CuSbCl}_6$ and $\text{Cs}_2\text{CuSbBr}_6$ double perovskite structures can be successfully stabilized by morphological level dimensional reduction.

Besides searching for other metal combinations to enhance the optical absorption ability, replacing Br^- with I^- can significantly reduce the band gap of $\text{Cs}_2\text{AgBiBr}_6$ double perovskites. Unfortunately, $\text{Cs}_2\text{AgBiI}_6$ is unstable due to the lower formation energy of competing $\text{Cs}_3\text{Bi}_2\text{I}_9$ but can also be stabilized by *morphological level* dimensional reduction. In this context, we prove that the metastable iodide analogue can also be stabilized by *molecular level* dimensional reduction, which implies introducing large hydrophobic organic cations into double perovskite structures and “cutting” the 3-dimensional structures normal to a certain axis to form 2-dimensional perovskites. Here, we report that both Ag-Bi-I and Cu-Bi-I systems are thermodynamically stable within the structures of (aromatic-*O*-linker- NH_3) $_4\text{AgBiI}_8$ and (aromatic-*O*-linker- NH_3) $_4\text{CuBiI}_8$, respectively, where the aromatic moiety is naphthalene or pyrene and the linker is ethyl or propyl. The intrinsic electronic challenges of double perovskites are investigated and the electronic anisotropy of two-dimensional perovskites is alleviated. With more extended conjugated systems, (pyrene-*O*-ethyl- NH_3) $_4\text{AgBiI}_8$ was isolated from a total of eight new 2D double perovskites, exhibiting an electronic band structure forming a type IIb multiple quantum well system with favorable intraorganic layer arrangement for out-of-plane conductivity, leading to a photocurrent response ratio of almost three orders of magnitude under AM1.5G illumination. Finally, (pyrene-*O*-ethyl- NH_3) $_4\text{AgBiI}_8$ was also integrated to construct the first pure $n = 1$ Ruddlesden-Popper 2D double perovskite solar cell featuring 2D layers parallel to the electrode substrate.

1 Introduction

1.1 The Global Energy Crisis

The sustainable human development with the interrelated economic, social and environmental aims is highly dependent on the energy available. Although energy technologies based on fossil fuels (like coal, crude oil and natural gas) are well-developed and reliable for daily needs including transportation, heating and electricity generation, the unsustainable and non-renewable properties of these conventional energy sources have forced the energy research community to search for alternative green energy sources. Additionally, the use of fossil fuels, usually combustion, results in the emission of green-house gases (GHG) such as carbon dioxide (CO₂), which contributes to the global climate change. According to the Sixth Assessment Report (AR6) from Intergovernmental Panel on Climate Change (IPCC), global GHG emissions continued to rise and reached 59 ± 6.6 GtCO₂-eq in 2019, which were around 12% and 54% higher than the amounts in 2010 and 1990, respectively (Figure 1.1). The report emphasized that net emissions must be zero for the sake of stopping global warming.^[1] The Working Group III from IPCC, which focuses on climate change mitigation, estimated that the reduction of global GHG release by at least half the 2019 level by 2030 can be achieved by various mitigation options costing USD 100 tCO₂-eq⁻¹ or less. The wind and solar energy show great potential as alternative energy sources to reduce GHG emission but with cost less than USD 20 tCO₂-eq⁻¹. (Figure 1.2).^[1] This report indicates that the efficient utilization of solar energy is one of the most important and cost-efficient solutions for climate change mitigation.

As a clean, inexpensive and essentially inexhaustible energy source, solar energy can be utilized via converting it into heat, electricity or solar fuels,^[2] among which the conversion of solar energy into electricity via photovoltaic (PV) devices is the most direct and efficient way in many respects.^[3] In 2000, World Energy Council, UN Department of Economic and Social Affairs and the United Nations Development Programme published an assessment that the potential usable annual solar energy was estimated to be in the range between 1,575 and 49,837 exajoules [4.4×10^5 to 1.3×10^7 terawatt-hours

(TWh)] globally, taking into account factors like annual clear sky irradiance, annual average sky clearance and available land area.^[4] According to the report from International Energy Agency (IEA), global total electricity final consumption was 22,848 TWh in 2019^[5] and global electricity demand was estimated to rise by 5900 TWh in the Stated Policies Scenario (STEPS) and over 7000 TWh in the Announced Pledges Scenario (APS) by 2030^[6]. Clearly, the utilization of solar energy to efficiently convert sunlight into electricity can effectively meet the increasing energy demands of our global community.

Global net anthropogenic emissions have continued to rise across all major groups of greenhouse gases.

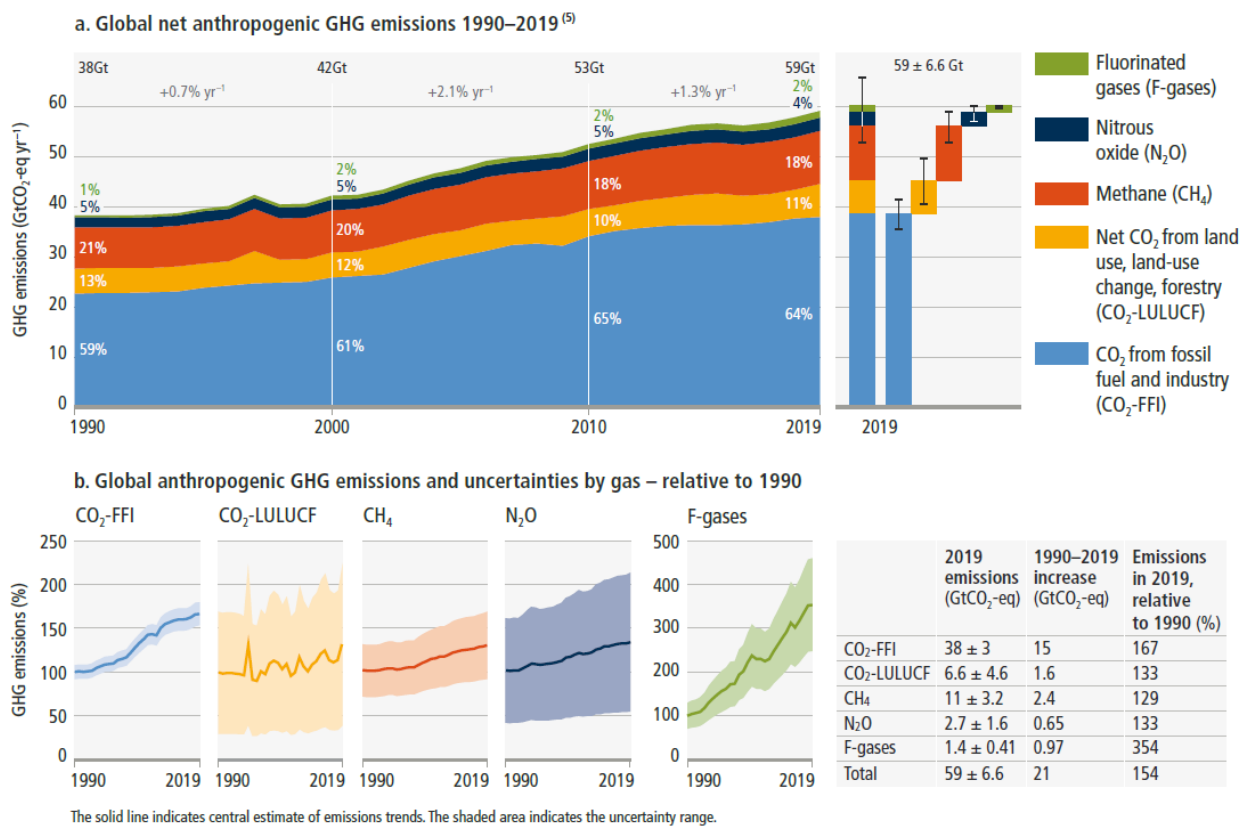


*Figure 1.1: Global net anthropogenic green-house gas (GHG) emissions (GtCO₂-eq yr⁻¹) 1990–2019. Global net anthropogenic GHG emissions include CO₂ from fossil fuel combustion and industrial processes (CO₂-FFI); net CO₂ from land use, land-use change and forestry (CO₂-LULUCF); methane (CH₄); nitrous oxide (N₂O); and fluorinated gases (HFCs, PFCs, SF₆, NF₃). **Panel a** shows aggregate annual global net anthropogenic GHG emissions by groups of gases from 1990 to 2019 reported in GtCO₂-eq converted. At the right side of **Panel a**, GHG emissions in 2019 are broken down into individual components with the associated uncertainties (90% confidence interval) indicated by the error bars: CO₂-FFI ±8%; CO₂-LULUCF ±70%; CH₄ ±30%; N₂O ±60%; F-gases ±30%; GHG ±11%. **Panel b** shows*

global anthropogenic CO₂-FFI, net CO₂-LULUCF, CH₄, N₂O and F-gas emissions individually for the period 1990-2019, normalized relative to 100 in 1990. Shaded areas indicate the uncertainty range. Uncertainty ranges as shown here are specific for individual groups of greenhouse gases and cannot be compared. The table shows the central estimate for: absolute emissions in 2019; the absolute change in emissions between 1990 and 2019; and emissions in 2019 expressed as a percentage of 1990 emissions.^[1]

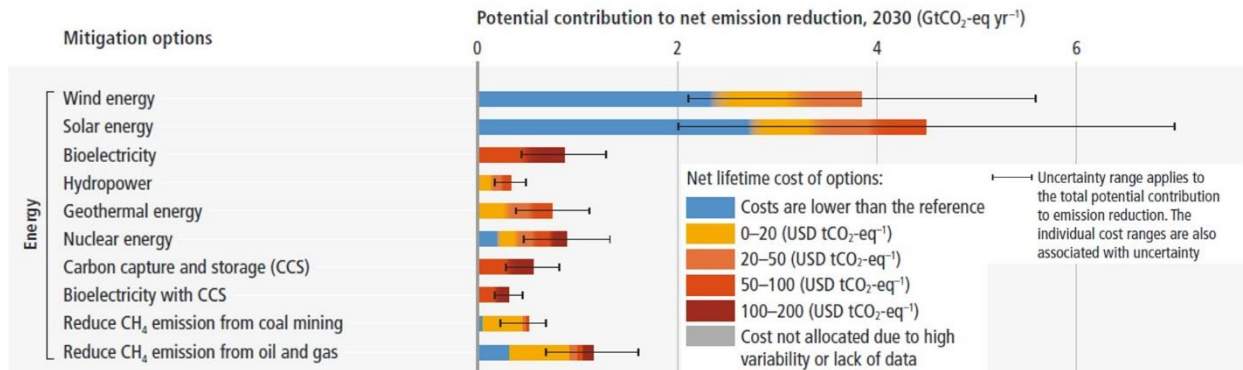


Figure 1.2: Overview of mitigation options for energy and their estimated ranges of costs and potentials in 2030. Costs shown are net lifetime costs of avoided greenhouse gas emissions. Costs are calculated relative to a reference technology. The assessments per sector were carried out using a common methodology, including definition of potentials, target year, reference scenarios, and cost definitions. The mitigation potential (shown in the horizontal axis) is the quantity of net GHG emission reductions that can be achieved by a given mitigation option relative to a specified emission baseline. Net GHG emission reductions are the sum of reduced emissions and/or enhanced sinks. The mitigation potentials are assessed independently for each option and are not necessarily additive. The length of the solid bars represents the mitigation potential of an option. The error bars display the full ranges of the estimates for the total mitigation potentials. Sources of uncertainty for the cost estimates include assumptions on the rate of technological advancement, regional differences, and economies of scale, among others. Those uncertainties are not displayed in the figure. Potentials are broken down into cost categories, indicated by different colors. Only discounted lifetime monetary costs are considered. Where a gradual color transition is shown, the breakdown of the potential into cost categories is not well known or depends heavily on factors such as geographical location, resource availability, and regional circumstances, and the colors indicate the range of estimates. Costs were taken directly from the underlying studies (mostly in the period 2015–2020) or recent datasets. No correction for inflation was applied, given the wide cost ranges used. The cost of the reference technologies was also taken from the underlying studies and recent datasets. Cost reductions through technological learning are taken into account.^[1]

1.2 The Development of Solar Cells (Three Generations)

In 1839, Edmond Becquerel first noticed the photovoltaic effect, which is the generation of electric current and voltage in materials when they are excited by light.^[7] In 1883, the first working solar cell based on selenium was designed by Charles Fritts, but the performance was poor with only about 1% power conversion efficiency (PCE).^[8] In 1941, Russell Shoemaker Ohl patented the first silicon p-n junction solar cell at American Telephone and Telegraph (AT&T)'s Bell Laboratories, which triggered the development of solar cells for practical use as an alternative option for power generation.^[9] The National Renewable Energy Laboratory (NREL) has run a compilation of the highest certified PCEs of research cells for different PV materials and technologies since 1976 (Figure 1.3), including multi-junction cells, gallium arsenide single-junction cells, crystalline silicon cells, thin film technologies and emerging photovoltaic technologies. The current world records for different PV materials and technologies are listed at the right edge with the technology symbols and efficiencies.^[10] After decades of advancement, photovoltaics have emerged as a primary technology contributing significantly to the ongoing shift from conventional fossil fuels to sustainable renewable energy sources. There are three primary generations of solar cells, and this section will delve into each classification in some more detail.

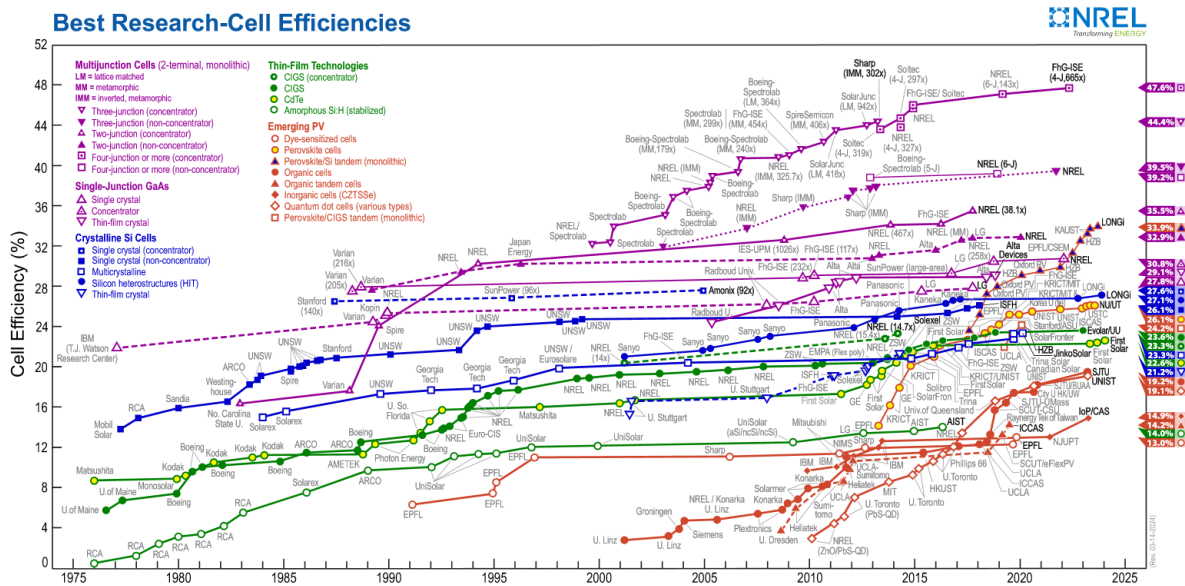


Figure 1.3: Record PCEs of research cells for different PV materials and technologies since 1976 compiled by the National Renewable Energy Laboratory (NREL).^[10]

1.2.1 The First Generation

The first generation of solar cells includes materials based on monocrystalline and polycrystalline silicon (Figure 1.4a), as well as III-V single-junction gallium arsenide, GaAs. In April 1954, Bell Lab announced the first practical silicon solar cell, which was created by a team of scientists Daryl Chapin, Calvin Fuller and Gerald Pearson. The first silicon solar cell had about 6% PCE and could power a radio transmitter or a small toy Ferris wheel, which was a great improvement compared to any previous PV devices.^[11] After decades of development, crystalline-silicon (c-Si) based PV technologies have achieved PCE exceeding 27%^[10], along with a proven longevity of > 25 years. The c-Si based solar cells have been dominating the PV market due to their excellent stability, high performance and long service time, constituting more than 80% of the global installed capacity.^[12] Nonetheless, a hundreds-micron thick c-Si absorber layer is required to effectively capture sunlight because of the indirect band gap of c-Si, resulting in elevated materials costs and limited application to specific scenarios such as wearable solar technology (Figure 1.4b). Moreover, silicon-based solar cells require high-purity silicon (ranging from 99.99% to 99.9999999%) as an absorber. The laborious production procedures and substantial material losses in manufacturing indicate a production process that is both time- and energy-intensive, resulting in an extended energy payback time. This payback time represents the duration required for a PV system to generate the equivalent amount of energy expended in its production.

The PCEs of single-junction GaAs (III-V) solar cells have reached 27.8% and 29.1% in the forms of a single crystal and a thin film, respectively.^[10] Owing to GaAs's optimal band gap value (1.4 eV) and a comparatively higher absorption coefficient (direct band gap), films with reduced thickness (ranging from 2 to 5 microns) are adequate for the complete absorption of incident sunlight.^[13] This characteristic allows for their construction on curved surfaces, yielding lightweight and flexible devices. PV devices based on GaAs exhibit excellent stability and high performance; however, their production costs are elevated, limiting their application to specialized fields such as aerospace (Figure 1.4c).^[14]

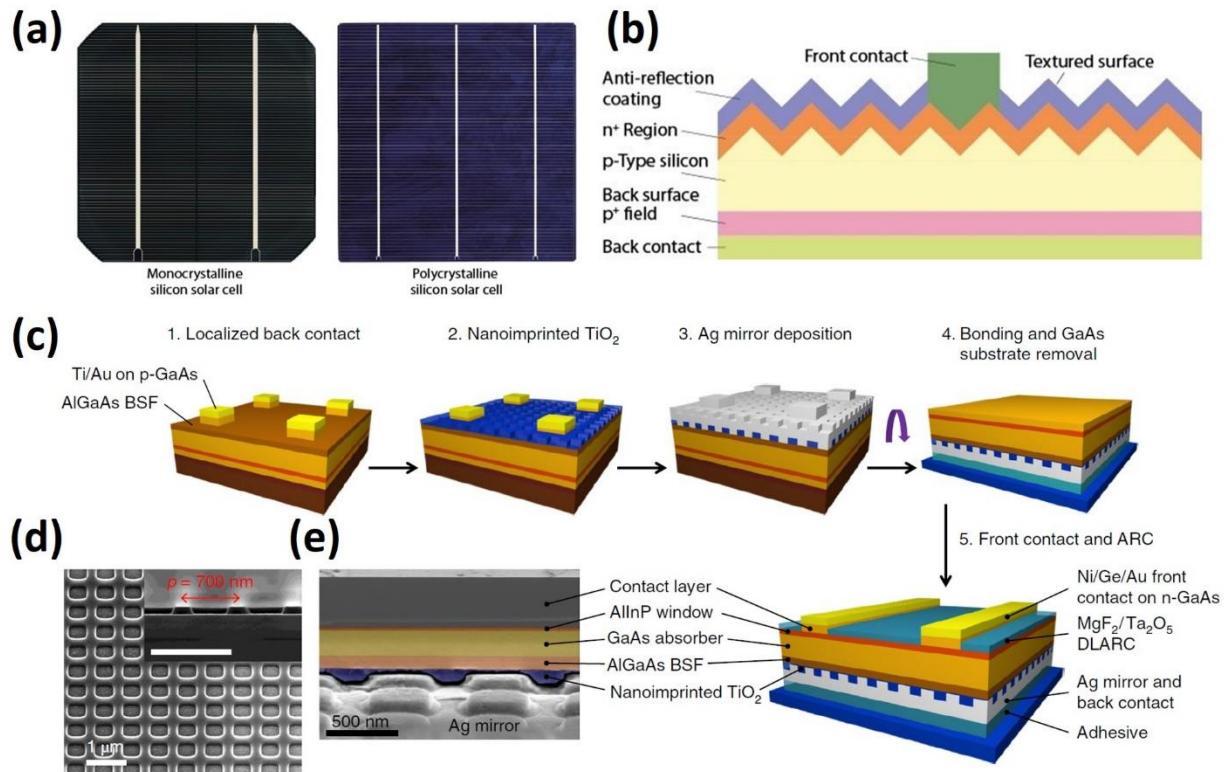


Figure 1.4: (a) Typical mono- and polycrystalline silicon solar cells. (b) Simplified cross-section of a commercial monocrystalline silicon solar cell. Reproduced with permission.^[15] Copyright 2010, Springer Nature. (c) Fabrication process for ultrathin GaAs solar cells with a nanostructured back mirror. (d) SEM image of nano-imprinted TiO₂ periodic structures before Ag mirror deposition. Inset: cross-section of the TiO₂. Scale bar, 1 μm. (e) SEM cross-sectional view after removing the GaAs substrate, showing the Ag nanostructured back mirror. Reproduced with permission.^[16] Copyright 2019, Springer Nature.

1.2.2 The Second Generation

The second generation of solar cells refers to thin-film solar cell technologies, including PV materials such as microcrystalline silicon ($\mu\text{-Si}$), amorphous silicon (a-Si), copper indium gallium selenide (CIGS) and cadmium telluride/cadmium sulphide (CdTe/CdS). To mitigate the costs linked with crystalline silicon solar cells, a-Si was developed and commonly manufactured using plasma-enhanced chemical vapor deposition (PECVD). Due to the absence of long-range order, pure a-Si displays a significant defect density, making it unsuitable for direct use. Consequently, hydrogen doping is necessary to mitigate the dangling bonds, resulting in the formation of hydrogenated amorphous silicon (a-Si:H). The primary limitation of a-Si:H solar cell lies in its low efficiency, with

the world record PCE standing at only 14% after 48 years of development.^[10] In combination with the reduced module costs of c-Si solar cells, the competitiveness of a-Si:H technology was reduced.^[17]

CIGS and CdTe have direct band gaps and high absorption coefficients, resulting in the need for relatively less materials in the manufacturing of their corresponding solar cells (Figure 1.5).^[18, 19] CIGS thin films can be deposited using co-evaporation or sputtering techniques, and they are compatible with various substrates such as glass, metal films and polymers.^[20] The highest-performing CIGS solar cell currently achieves a PCE of 23.6%.^[10] Nonetheless, challenges persist, including elevated material costs and concerns about instability and unreliability arising from the material's sensitivity to temperature fluctuations.^[21] CdTe solar cells exhibit the best PCE of 22.4%.^[10] However, the use of the highly toxic Cd and the limited availability of Te raises concerns about their suitability for large-scale commercial production.^[21]

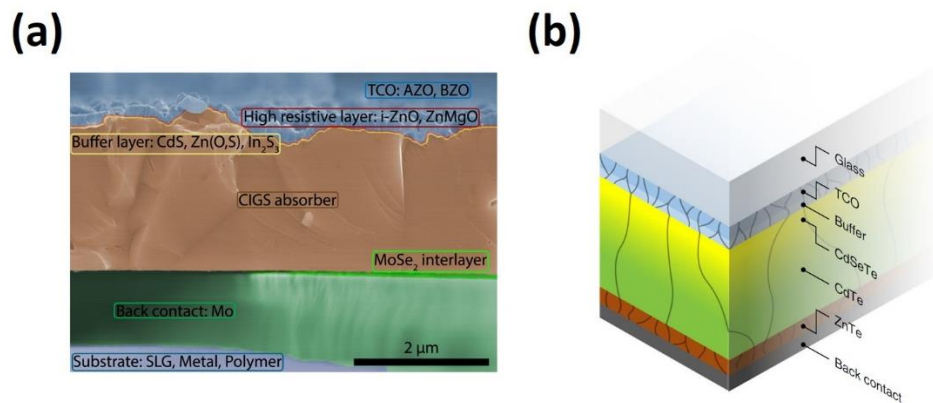


Figure 1.5: (a) Basic structure of a typical copper indium gallium selenide (CIGS) solar cell, with examples of the most commonly used materials. Reproduced with permission.^[18] Copyright 2016, Wiley-VCH. (b) Schematic of a state-of-the-art CdTe solar cell. Reproduced with permission.^[19] Copyright 2019, Springer Nature.

1.2.3 The Third Generation

The third generation of solar cells represents emerging PV technologies including dye-sensitized solar cells (DSSCs), organic solar cells (OSCs), perovskite solar cells (PSCs) and quantum dot solar cells (QDSCs). DSSCs possess unique features like fairly low cost, semi-transparency, easy fabrication and ability to work in less intense light, which makes them an attractive emerging PV technology to supplement the conventional PV device market (Figure 1.6a). Nevertheless, despite over 30 years of development, the highest reported efficiency to date stands at about 13%.^[10] OSCs based on organic bulk heterojunction (BHJ) blends have seen a great development in recent years. Surprisingly and inspiringly, the certified highest efficiency of OSCs has reached 19.2% in 2022^[22], bringing them closer to the leading CdTe solar cells (22.6%) and CIGS solar cells (23.3%).^[10] The advantages of organic photovoltaic materials are their high optical absorption and adjustable energy levels achieved by diverse options of functional organic groups.^[22] Moreover, OSCs have their superiority like low fabrication costs, sustainability of materials, flexibility and light weight, positioning them as strong contenders in the developing photovoltaic market (Figure 1.6b, c). However, the primary challenge impeding the commercialization of such PV devices remains their long-term stability. Colloidal quantum dots (CQDs) such as metal chalcogenides have already been successfully commercialized in the display market, thanks to their exceptional brightness, color purity and color gamut.^[23] In the PV market, CQDs also attracted much attention as a low-cost solution-processable alternative before the appearance of organic and perovskite PV materials (Figure 1.6d). The best QDSCs have achieved a remarkable 19.1% efficiency in 2024.^[10] The development of PSCs will be discussed in Section 1.3.

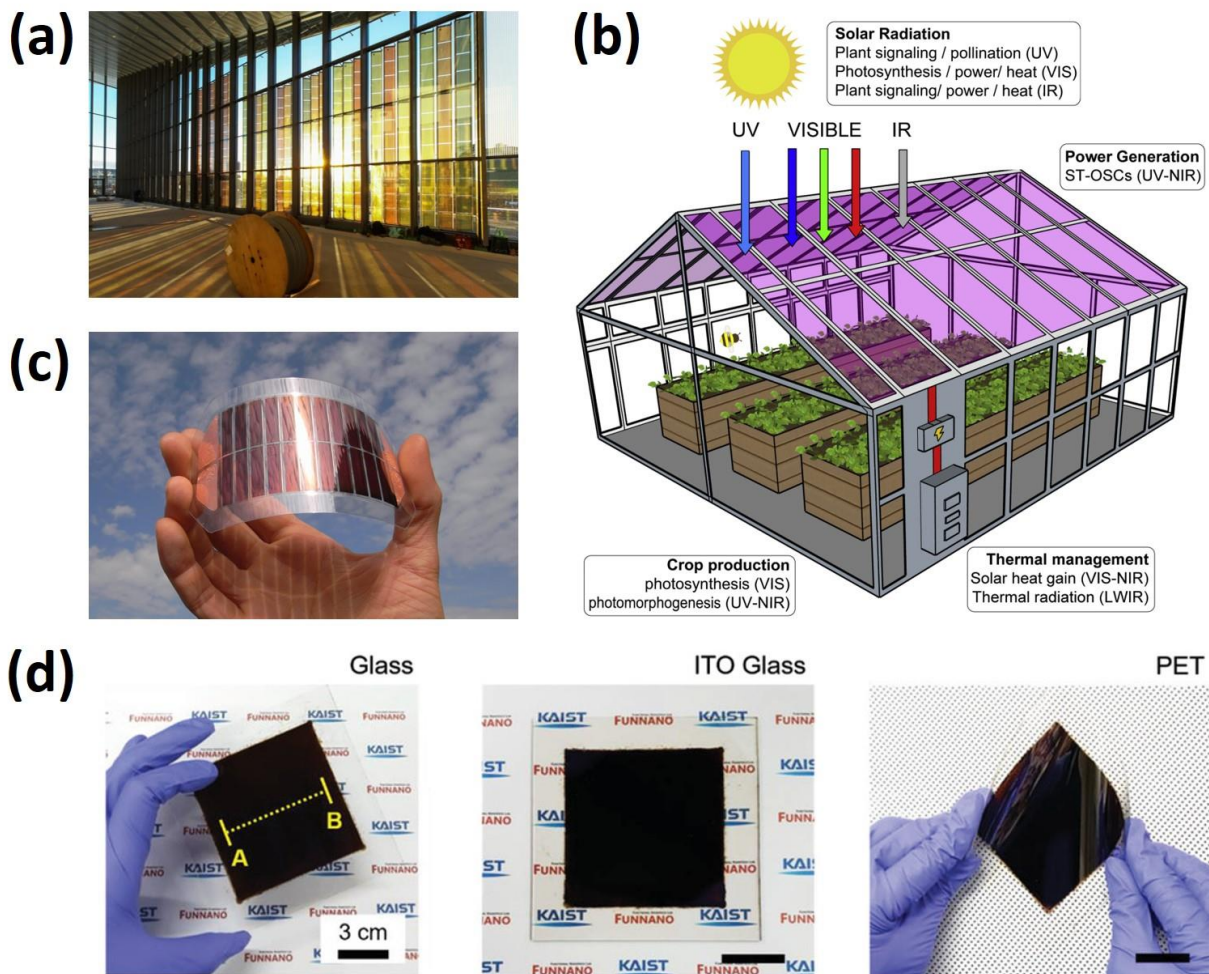


Figure 1.6: (a) Installation featuring dye-sensitized solar cells at the Swiss Tech convention center. Image: École Polytechnique Fédérale de Lausanne (EPFL)/Alain Herzog. (b) Overview of an OSC-integrated greenhouse indicating spectral use of sunlight. Reproduced with permission.^[24] Copyright 2021, Elsevier. (c) Flexible organic solar cell module from Fraunhofer Institute for Solar Energy Systems ISE. (d) Photographs of lead sulfide CQD films (10 cm × 10 cm) on a glass substrate, indium tin oxide (ITO) glass substrate, and PET substrate. Reproduced with permission.^[25] Copyright 2019, Wiley-VCH.

1.3 Perovskite Solar Cells

“Perovskite”, at first referred to a mineral species with the chemical formula of CaTiO_3 . In 1839, the German mineralogist, Gustav Rose (1798 – 1873), first discovered the “perovskite” (CaTiO_3) in the Russian Ural Mountains. In honour of L. A. Perovski (a Russian mineralogist, 1792 – 1856), this type of material was named “perovskite”.^[26] Perovskite oxides with a general formula ABO_3 , which consist of oxide ions (O), tetravalent metal cations (B) and bivalent metal cations (A), and related structures, were a previous research focus due to their high-temperature superconductivity, catalytic properties, magnetocaloric effect and ferroelectricity.^[27] Subsequently, materials exhibiting a crystal structure akin to CaTiO_3 came to be termed “perovskite” in mineralogy, characterized by the chemical formula ABX_3 (see Figure 1.7a). The first research work on metal halide perovskites (MHPs) was conducted in 1893 by Horace Lemuel Wells^[28] and the detailed structures of MHPs were reported by Dieter Weber in the late 1970s^[29-31]. Since the initial application of metal halide perovskites as sensitizers for DSSCs^[32-34], the certified efficiency of PSCs has rapidly surged to 26%^[10] over the last ten years (see Figure 1.3), owing to tremendous efforts in thin-film morphological control^[35], chemical compositional engineering^[36], and interface/device modification^[37, 38], among other factors. Up to this point, metal halide perovskites can be regarded as game changers in photovoltaics.^[39]

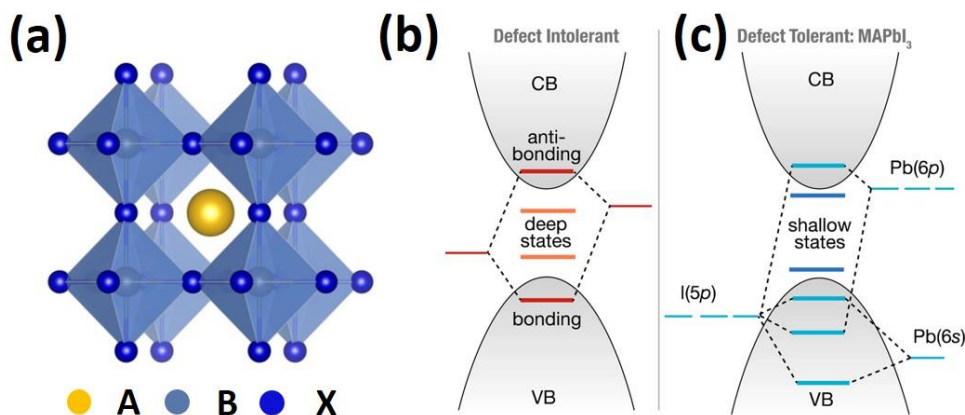


Figure 1.7: Schematic representation of the crystal structure of perovskites. Electronic structure of typical III–V, II–VI or group IV semiconductors (b) compared to that of lead halide perovskite (c). Reproduced with permission.^[40] Copyright 2017, American Chemical Society.

1.3.1 Crystal Structures of Metal Halide Perovskite Materials

As shown in Figure 1.7a, the typical structure of MHPs exhibits a cubic (or somewhat lower, see below) symmetry with a formula of ABX_3 , where A presents an organic or inorganic cation, such as $CH_3NH_3^+$ (methylammonium, MA), $CH(NH_2)_2^+$ (formamidinium, FA), Cs^+ , Rb^+ , etc.; B presents a divalent metal cation, such as Ge^{2+} , Cu^{2+} , Pb^{2+} , Sn^{2+} , etc.; and X presents a halide anion (Cl^- , Br^- , or I^-). The divalent B metal cation is positioned in the center of halide octahedra, and halide anions occupy the vertices of the BX_6 octahedra. Through the sharing of vertex halides, a continuous array is established. The vacancies between BX_6 octahedra are filled with A-site cations, which are typically larger than B-site cations. That is the ideal three-dimensional (3D) framework perovskite structure, but in reality, perovskites tend to distort away from a highly symmetric cubic structure because most cations at A sites are not large enough. For example, $MAPbI_3$ perovskite exhibits several distorted phases featuring symmetries such as $Pm\bar{3}m$, $Pbnm$, $I4/mcm$ and $Pmnb$.^[41] To evaluate the structural stability of perovskite materials comprising different cations and anions, we can use the well-known Goldschmidt's tolerance factor, t , which is defined as^[42]

$$t = \frac{r_A + r_X}{\sqrt{2}(r_B + r_X)} \quad (1.1)$$

where r_A , r_B and r_X correspond to the radii of components A, B and X, respectively. In an ideal condition, the value of t is equal to 1; that is to say, the crystal structure is a cube. Generally, the t value is in the range of around $0.813 \leq t \leq 1.107$ for 3D perovskites. Zeng et al. consider that the range of $0.9 \leq t \leq 1.0$ is ideal for cubic perovskite structure in general. The range of $0.71 \leq t \leq 0.9$ is considered as indicating the likely formation of an orthorhombic or rhombohedral structure due to distortion of BX_6 octahedra. In other cases, that is $t \leq 0.71$ or $t \geq 1$, non-perovskite structures such as NH_4CdCl_3 -type (one-dimensional orthorhombic structures formed by the edge-sharing of octahedra) or $CsNiBr_3$ -type structures (one-dimensional hexagonal structures formed by the face-sharing of octahedra) are formed, respectively.^[43] These non-perovskite materials normally have large band gaps and low electronic conductivity. The other empirical geometric parameter to assess the structural stability of the BX_6 octahedra is the octahedral factor, μ , which is defined as

$$\mu = \frac{r_B}{r_X} \quad (1.2)$$

The stable BX_6 octahedral structure has a μ value between 0.442 and 0.895. These two empirical indicators can effectively describe and predict the putative perovskite's structural stability.

1.3.2 Lead-Based Perovskite Materials

Since the first application of perovskites in photovoltaic devices, lead-based perovskite materials remain the most promising candidates as absorbers for solar cells among the perovskite family. The fundamental mechanisms underlying the good performance of lead-based PSCs are significant. Understanding these mechanisms can guide the community to tap the potential of this material for improved performance in various optoelectronic applications and also to explore other novel photovoltaic semiconductors. The key to the outperformance of lead-based PSCs lies in their stronger optical absorption compared to conventional photovoltaic materials for thin-film solar cells, which reduces the need for materials and minimizes non-radiative recombination that occurs during the transport and collection of photogenerated carriers.^[41] The outstanding optical property originates from the combination of perovskite symmetry and the existence of the lone-pair s orbitals. It results in the direct band gap p - p transition of lead-based MHPs, which is much stronger than p - s transitions commonly seen in thin-film photovoltaic materials such as CIGS and CdTe.^[41] Additionally, solution-processed lead-based MHPs have small effective masses for both electrons and holes^[44], as well as ambipolar transport^[45, 46] with long-range balanced electron-hole diffusion lengths^[47, 48]. These characteristics contribute to efficient charge separation, transport and collection. Furthermore, the properties of dominant shallow trap states and intrinsically benign grain boundaries enable the solution-processed MHPs to achieve high efficiencies and low open-circuit voltage losses.^[41, 49] As shown in Figure 1.7b, for typical III-V, II-VI or group IV semiconductors, the conduction band (CB) and the valence band (VB) have an antibonding and bonding character. Such a property can bring about deep defect states in the band gap when an atom is removed. However, CB and VB both exhibit antibonding character in MHPs. For example, as shown in Figure 1.7c, VB and CB edges of MAPbI₃ are generated from the interaction between Pb 6s and I 5p orbitals, as well as Pb 6p and I 5p orbitals, respectively. The superior defect tolerance of MAPbI₃ is due to the strong Pb 6s orbital and I 5p orbital antibonding coupling such that defects with shallow levels have low formation energies but deep levels have high formation energies. On the other hand, the coupling between Pb 6p orbital and I 5p orbital is very weak. As a result, the CB edge exhibits an ionic character, implying that the energy states are not significantly affected by external defect levels.^[40, 50] Another advantage of MHPs is that the optoelectronic properties can be adjusted through composition engineering. For example, the band gap energy, phase stability and solar cell efficiency can be controlled by choosing different ions in A, B or X sites.^[36] Benefiting from the solution-processibility, low-temperature fabrication, tunable

properties, as well as high photovoltaic efficiency of MHPs, PSCs promise to exhibit substantial competitiveness in the PV market (provided stability and toxicity issues can be addressed).

1.3.3 Device Categories

As previously mentioned, solar cells utilizing perovskites as absorbers have evolved from the realm of DSSCs.^[34] The architecture of DSSCs, as illustrated in Figure 1.8a, is composed of four main parts: i) mesoporous n-type TiO₂, featuring a large internal surface area to absorb sufficient sensitizers for capturing most of the sunlight and transporting the excited electrons to the transparent electrode. ii) sensitizers, such as dyes, inorganic QDs or perovskites, capture the photons and convert them into free electrons and holes at the surface of TiO₂/sensitizer. iii) redox-active electrolyte, which functions as a shuttle for dye regeneration, typically comprises a redox couple involving iodide and triiodide.^[34] iv) electrodes, which serve to collect electrons and reduce positive charges.^[39, 49] Miyasaka et al. first reported the photovoltaic performance of MHPs.^[33, 34] In 2006, they applied CH₃NH₃PbBr₃ on nanoporous TiO₂ as visible light sensitizer for DSSCs, achieving a PCE of 2.2%.^[33] The efficiency was further increased to 3.8% in 2009 by replacing bromine with iodine in the perovskite structure.^[34] However, this type of device is unstable due to dissolution of MHPs in the liquid organic electrolyte containing lithium halide and the corresponding halogen. In 2012, Park et al. introduced a solid hole conductor, 2,2',7,7'-tetrakis(N,N-di-p-methoxyphenylamine)-9,9'-spirobifluorene (*spiro*-MeOTAD), to replace the liquid electrolyte in DSSCs, which not only improved the stability but also boosted the efficiency to 9.7%.^[51] Another milestone in the development of PSCs involved the improvement of PCE by replacing conducting TiO₂ with insulating Al₂O₃ network, which demonstrated that MHPs can function as both absorber and n-type component, transporting electronic charge out of the device.^[45] This work triggered an explosive research effort worldwide in the development of planar PSCs. With enormous effort dedicated to uncovering the intrinsic properties of lead-based MHPs, their high absorption coefficient, small effective masses of both electrons and holes, ambipolar transport featuring long-range balanced electron-hole diffusion lengths and high defect tolerance collectively enable the realization of highly efficient solution-processed planar solar cells with perovskite as a single active layer. The device structures of PSCs can be classified into three main types: regular mesoporous structure (Figure 1.8b), regular planar n-i-p structure (Figure 1.8c) and inverted planar p-i-n structure (Figure 1.8d).

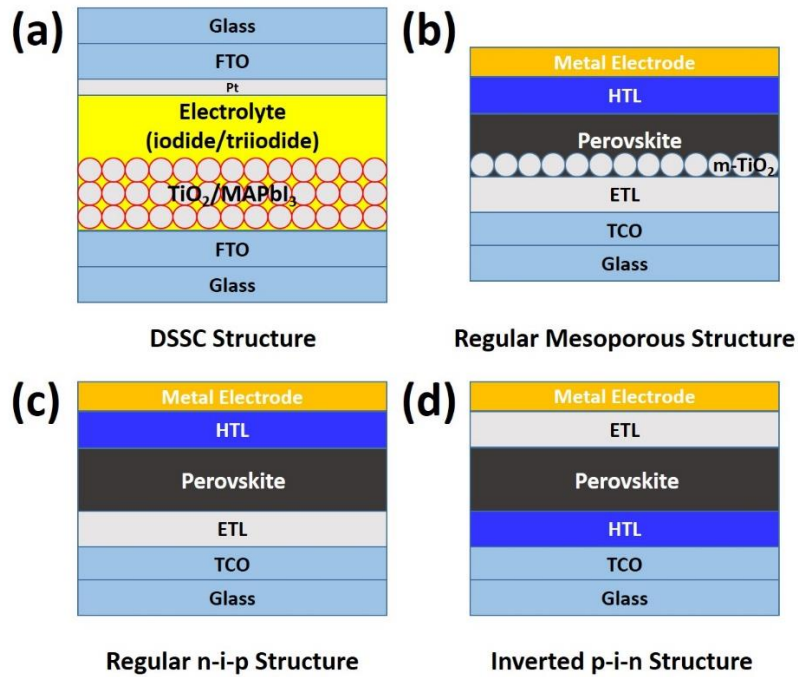


Figure 1.8: Schematic diagrams of perovskite solar cell structures include electrolyte-based mesoscopic DSSC (a), regular mesoporous structure (b), regular planar n-i-p structure (c) and inverted planar p-i-n structure (d). FTO: F-doped SnO_2 ; TCO: transparent conducting oxide; ETL: electron transporting layer; HTL: hole transporting layer.

1.3.4 Working Principle of PSCs

Here, we use the inverted p-i-n solar cell structure as an example to explain the working principle of PSCs (Figure 1.9). In a typical photovoltaic process in PSCs, the photoexcited charge carrier dynamics contain four steps:

i) Exciton generation. The incident light passes through the indium tin oxide (ITO), and photons with energy higher than the band gap of corresponding perovskite are absorbed by the photoactive perovskite film. The ground-state electron can be excited from the VB to the CB, leaving a positively charged electron hole in the VB. This pair of an electron and an electron hole, attracting each other by electrostatic Coulomb force, is termed an exciton.

ii) Exciton dissociation. The dissociation of exciton into free charge carriers depends on the electrostatic force (F), which can be illustrated by Coulomb equation^[52]

$$F = -\frac{1e^2}{4\pi\epsilon r^2} \quad (1.3)$$

where r is the distance between the electron and the hole, ϵ is the dielectric constant of the integral lattice and e is the elementary charge. The energy needed to separate a bonded electron-hole pair is termed as exciton binding energy (E_b). As you can conclude from equation (1.3), in materials with large dielectric constants, the Coulomb interaction between an electron and a hole may be weak. Thus, the radius of exciton is normally larger than the lattice spacing. This type of exciton is called Wannier-Mott exciton. On the contrary, in materials with small dielectric constants, the strong Coulomb force may lead to relatively small excitons. These excitons may locate in the same position, resulting in a Frenkel exciton. The excitons in 3D lead-iodide-based MHPs belong to the type of Wannier-Mott excitons due to their large dielectric constants. Coupled with the properties of small effective masses for both electrons and holes, 3D lead-iodide-based MHPs exhibit small exciton binding energies, with reported values ranging between 2 to 50 meV. Consequently, the separation of excitons into free charge carriers occurs within picoseconds in 3D lead-iodide-based PSCs.^[53] Organic semiconductors serve as a contrasting example, characterized by their typically small dielectric constants and Frenkel excitons. This characteristic implies that they generally exhibit relatively larger E_b . As a consequence, in OSCs, a bulk heterojunction consisting of nanoscale blend of donor and acceptor materials becomes essential, which creates a substantial interface between donor and acceptor materials for efficient dissociation of short-lifetime excitons.^[53]

iii) Charge carrier transport. Due to the properties of ambipolar transport and a long-range balanced electron-hole diffusion length, free electrons/holes can efficiently move to the interfaces between the perovskite layer and the electron/hole transport layer (ETL/HTL) and be extracted by the corresponding transporting layer. Charge transport layers (CTLs) are essential between the perovskite layer and the electrodes. The ETL and HTL have a lower lowest unoccupied molecular orbital (LUMO) and a higher highest occupied molecular orbital (HOMO) than that of perovskite, respectively. These energy differences help reducing energy barrier between perovskite and electrodes, suppress potential interfacial charge recombination, and enhance the photovoltage output.

iv) Charge carrier collection. Electrons and holes in the respective charge selective layers can be transferred to cathode and anode, respectively. In the case of inverted planar p-i-n structure,

electrons will be transferred to the back metal cathode, and holes will be transferred to transparent conducting oxide (TCO).

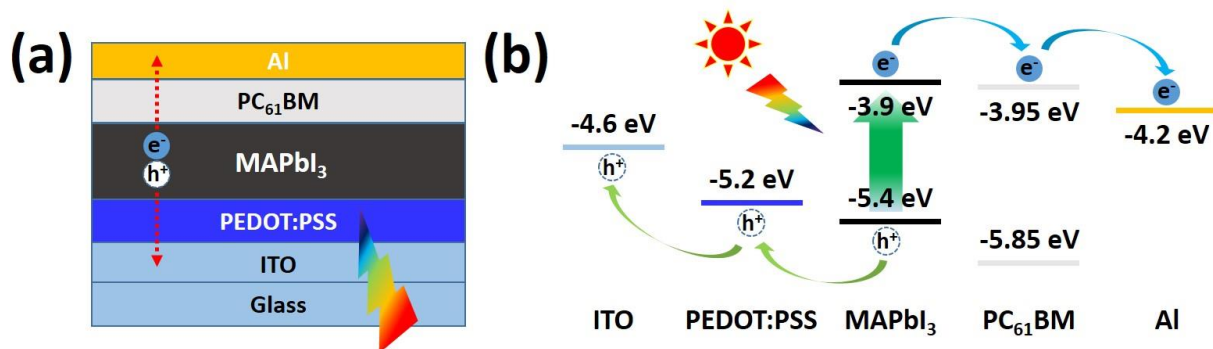


Figure 1.9: Schematic diagram of the working principle in the inverted *p-i-n* PSCs.

1.3.5 The Commercialization of Perovskite Solar Cells: Large-Area Fabrication, Stability and Toxicity Issues

The performance of lead-based single-junction PSCs has reached a certified efficiency of 26.1% over the past decade.^[10] Furthermore, Si/perovskite tandem solar cells have exceeded the Shockly-Queisser limit, achieving a certificated PCE of 33.9% for a 1-cm², 2-terminal, double-junction perovskite/Si cell by LONGi.^[10] Simply assessing the aspect of efficiency, PSCs have already met the requirements for commercialization, coupled with the advantages of a low-cost and easy fabrication process. However, there are still some barriers on the path to real commercialization. The most important obstacles are the large-area fabrication, long-term stability and toxicity issues of lead-based PSCs.

Although high-efficiency PSCs have been achieved on a laboratory scale with small active area (< 1 cm²), the commercialization of PSCs necessitates the development of solar cells with larger areas (> 100 cm²). Recently, several large-area fabrication technologies have been developed, including blade-coating, slot-die coating, spray coating, flexographic printing, gravure printing, screen printing and inkjet printing, which have been proved to be very effective in controlling film formation and improving the PCE to over 21%.^[54] As a single-junction solar cell, a PCE of 25.2 ± 0.8% has been achieved with a designated illumination area of 1 cm².^[55] However, as far as we know, the efficiencies of perovskite photovoltaic devices with active areas larger than 100 cm² are currently lagging behind those of silicon-based solar cells, which can achieve 26.8 ± 0.4 % PCE in an active area of 274.4 cm².^[55]

^{56]} As for perovskite solar modules, Ding et al. reported a record efficiency of $22.4 \pm 0.5\%$ for a perovskite minimodule with a designed illumination area of 26 cm^2 (8 cells) at the Fifth International Conference on Materials & Environmental Science (ICMES-2022).^[57] Inspiringly, Utmolight has recently achieved a $18.6 \pm 0.7\%$ PCE in a small module, combining 39 cells with a designed illumination area of 809.9 cm^2 .^[55, 58] Beyond the perovskite layer, another challenge lies in selecting and depositing CTLs, as well as bottom and top electrodes, regarding cost-effective scalable methods and inexpensive materials. These aspects also require further research effort from both academia and industry.^[59, 60]

Regarding the instability problem of lead-based MHPs, we systematically reviewed the origin of degradation mechanisms for perovskite nanocrystals (PNCs) from three viewpoints, intrinsic crystal structure instability, interface-induced instability and environmental stability. Detailed information can be found in Chapter 3, Section 3.4.^[61] Concerning the stability of lead-based PSCs, the ionic nature of MHPs contributes to the ease of degradation in these active layers. Additionally, other functional layers and interfaces may also suffer from degradation under external stresses, such as moisture, oxygen, light, heat, electric bias and so on.^[62] The major degradation pathways for both perovskite layers and other functional layers can be summarized as the component volatilization, interdiffusion and their induced reactions.^[63] In addressing this concern, significant efforts have been dedicated to enhancing device stability. This involves the development of two-dimensional (2D) perovskites and all-inorganic perovskites, component engineering, defect passivation engineering, interface modification engineering, encapsulation technology and device structure engineering.^[64]

Despite possessing excellent optoelectronic properties and a superior low-cost fabrication process, the toxicity of lead in MHPs remains a serious concern in the context of commercialization. Lead-based perovskites can degrade into water-soluble lead iodide, which has the potential to migrate into the soil as aqueous solution and subsequently enter the ecosystem. Lead ions can enter the human body through various pathways, including ingestion or inhalation from water, food, soil and lead dust.^[65] When entering the human body, Pb may accumulate in the blood, bones, major organs (such as kidney and liver) and even in the brain and skin.^[66] Lead poisoning can affect the human body in various ways. Firstly, lead ions are similar to other biologically essential ions such as Ca^{2+} , Zn^{2+} and Fe^{2+} , thus leading to competition for binding sites and influencing multiple biochemical processes.^[67] Another effect is oxidative stress^[68], which can cause changes in the composition of fatty acids in membranes and affect processes like exocytosis, endocytosis^[69] and signal transduction.^[70] The

accumulation of lead in the human body may also lead to carcinogenicity. Various systems of the human body may be affected, including the hematopoietic system^[71], nervous system^[72], digestive system^[73] and cardiovascular and cerebrovascular systems.

To address this issue, the community has primarily focused on two strategies: developing low-toxicity lead-free perovskite and perovskite-inspired materials as alternatives^[74-77] as well as preventing or reducing lead leakage^[65, 78]. Unfortunately, the photovoltaic performance of lead substitutes has not been satisfactory so far, necessitating further efforts to explore new potential alternatives to lead-based MHPs. The progress and challenges of lead-free perovskite materials will be discussed in the next Section 1.4. Alternatively, another pathway to mitigate the impact of toxic lead is to reduce lead leakage, such as using self-healing polymer encapsulation^[79], low-cost cation-exchange resins^[80], built-in lead-adsorbing resin layer^[81], on-device lead-absorbing tapes^[82], in situ polymerized networks^[83], thiol-functionalized superhydrophobic surfaces^[84] and so on. Simultaneously, the development of specific lead leakage test procedures and the implementation of lead recycling in PSCs are also crucial aspects.^[65, 78, 85-88]

1.4 Lead-Free Perovskite Materials

1.4.1 Single-Element-Substituted Lead-Free Halide Perovskites

As discussed in Section 1.3.2, the outstanding performance of lead-based MHPs is attributed to the octahedral $[\text{PbI}_6]^{4-}$ motif, which determines the electronic band structures and optoelectronic properties. To maintain similar properties, the straightforward idea is to substitute lead with an element that has a similar electronic configuration. Theoretically, the optimal choice is to employ group-14 elements with the same lone-pair s orbital as lead, such as tin (Sn) and germanium (Ge).^[89-91] Tin-based perovskite materials exhibit promising optoelectronic properties such as narrow optical band gaps (~ 1.3 eV), which enables tin-based PSCs to achieve a theoretical efficiency of 33%, as per the Shockley-Queisser limit.^[92] The certificated PCE of tin-based PSCs has reached 14%,^[93] but it still lags behind that of lead-based counterparts. Two main factors account for this disparity.^[94] First, the rapid oxidation of Sn^{2+} to Sn^{4+} in the air or even in the N_2 -filled glovebox leads to the generation of Sn vacancies, which results in unfavourable p-doping, non-radiative recombination and perovskite structural decomposition.^[95] Moreover, the relatively poor morphology caused by fast crystallization of tin-based perovskite hinders the improvement of tin-based device performance.^[96] Additionally,

tin is also a harmful chemical and can be even more toxic than lead (depending on its state), raising concerns about its suitability as an environment-friendly alternative to lead in PSCs.^[97]

Alternatively, examining the electronic configuration of Pb^{2+} ($[\text{Xe}]6s^24f^{14}5d^{10}$), only Tl^+ and Bi^{3+} have the same $6s^26p^0$ electronic configuration, with Bi^{3+} being the only option due to its low toxicity. Moreover, Bi^{3+} has a comparable ionic radius with Pb^{2+} and superior stability compared to Sn^{2+} and Ge^{2+} , making bismuth a promising alternative to lead in PSCs. The substitution of Pb^{2+} with trivalent Bi^{3+} leads to the formation of the $\text{A}_3\text{Bi}_2\text{X}_9$ perovskite-related structure, which can be divided into two types: zero-dimensional (0D) dimer perovskite and 2D layered perovskite. The typical 0D phase ($\text{Cs}_3\text{Bi}_2\text{X}_9$ and $\text{MA}_3\text{Bi}_2\text{X}_9$) is constructed by the Cs^+ or MA^+ cations surrounded by face-sharing octahedral $[\text{Bi}_2\text{X}_9]^{3-}$ clusters (dimer, $\text{P63}/\text{mmc}$).^[98, 99] The 2D phase ($\text{K}_3\text{Bi}_2\text{I}_9$, $\text{Rb}_3\text{Bi}_2\text{I}_9$ and $(\text{NH}_4)_3\text{Bi}_2\text{I}_9$) is constructed by smaller cations (such as K^+ , Rb^+ or NH_4^+) with a corner-sharing $[\text{BiX}_6]^{3-}$ layered octahedral network ($\text{P2}_1/\text{n}$).^[100-102] Similar to Bi-based perovskite-related materials, Sb-based perovskite ($\text{A}_3\text{Sb}_2\text{X}_9$) also has two polymorphs (0D dimer or 2D layered forms), depending on the A-site cations and preparation methods chosen.^[103-105] Unfortunately, so far bismuth- or antimony-based PSCs still face challenges of low PCEs due to wide, indirect band gaps and heavy carrier effective masses.^[106-108]

1.4.2 Lead-Free Halide Double Perovskites

When considering replacing lead with single elements, it turns out that the choice is limited, and the current photovoltaic performance of resulting compounds is far below that of lead-based counterparts. Another approach to broaden the material variety is the conceptual substitution of two Pb^{2+} ions into two heterovalent cations. For example, the combination of monovalent and trivalent cations can be used to form a 3D double perovskite structure with a formula of $\text{A}_2\text{B(I)B(III)X}_6$ (Figure 1.10b).^[109] The $\text{A}_2\text{B(I)B(III)X}_6$ 3D double perovskites are also known as “elpasolites”.^[110] Alternatively, a layered double perovskite structure with the formula $\text{A}_4\text{B(II)B(III)}_2\text{X}_{12}$ can be created through the combination of divalent and trivalent cations (Figure 1.10d).^[111] Another type of double perovskite are the tetravalent-metal vacancy-ordered double perovskites with the formula $\text{A}_2\text{B(IV)}\square\text{X}_6$ (\square = vacancy), where half of the tetravalent atoms are removed and replaced by a vacancy (Figure 1.10c).^[112] This type of double perovskite is also termed “ K_2PtCl_6 -type perovskites” after one of the early compounds to be structurally characterized.^[110] In this section, we only focus on 3D halide double perovskites (HDPs) or elpasolites.

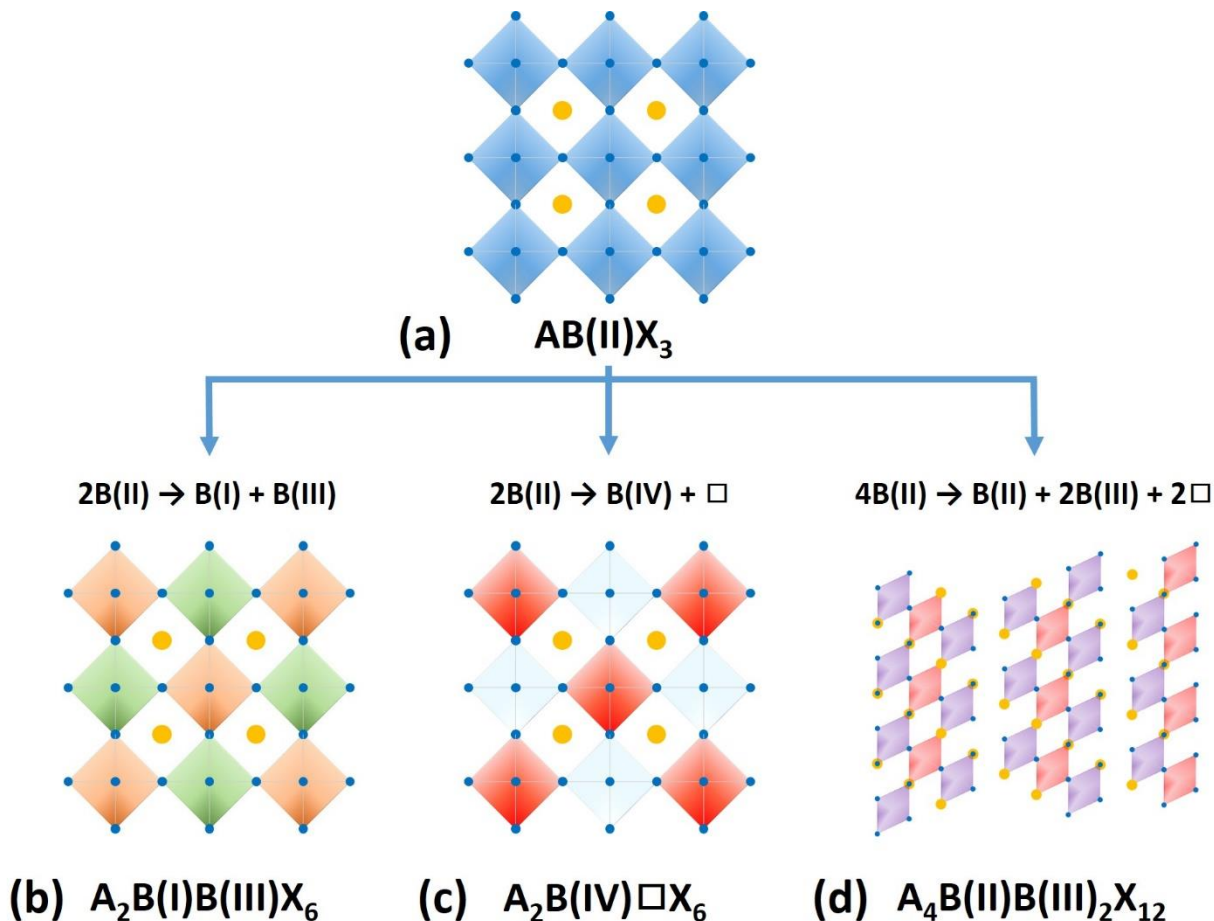


Figure 1.10: The crystal structures of (a) simple halide perovskites ($AB(II)X_3$), (b) halide double perovskites ($A_2B(I)B(III)X_6$), (c) vacancy-ordered halide double perovskites ($A_2B(IV)X_6$) and (d) layered halide double perovskites ($A_4B(II)B(III)_2X_{12}$).

1.4.2.1 A Brief History of Elpasolites

The $A_2B(I)B(III)X_6$ 3D HDPs have been intensively studied both experimentally^[109, 113, 114] and theoretically^[115-117] during the past years. This attention is attributed to the approach of extending material design strategies for lead-free perovskites while maintaining the 3D perovskite structures for better optoelectronic properties. The history of elpasolite dates back to the late 19th century when K_2NaAlF_6 was discovered in El Paso County, Colorado, USA.^[118] In 1922, the first synthesis of an additional elpasolite, $Cs_2Au(I)Au(III)Cl_6$, was reported^[119], which was later demonstrated to exhibit a semiconductor-to-metal transition at high pressures in 1990.^[120] There was no consideration of using elpasolites as photovoltaic materials until 2016 when three groups independently reported the

synthesis and optoelectronic properties of $\text{Cs}_2\text{AgBiX}_6$ ($X = \text{Br}, \text{Cl}$), and $\text{Cs}_2\text{AgBiBr}_6$ was regarded as a promising candidate to substitute lead-based perovskites.^[109, 117, 121] The photovoltaic performance of $\text{Cs}_2\text{AgBiBr}_6$ was reported in the following year by Bein and coworkers. The $\text{Cs}_2\text{AgBiBr}_6$ solar cell with a conventional device structure achieved a PCE of 2.43% and a V_{oc} of around 1 V, which triggered the study on the development of new double perovskite materials for photovoltaic applications.^[113] Recently, a record efficiency of 6.37% has been reported by using a hydrogenation method, where the band gap of $\text{Cs}_2\text{AgBiBr}_6$ films appeared to be tunable from 2.18 eV to 1.64 eV.^[122] Nevertheless, the performance of the most-advanced HDP-based solar cells still lags significantly behind their lead-based counterparts, indicating the necessity for continued effort within the perovskite community.

1.4.2.2 Crystal Structure of Elpasolites

The ideal structure of elpasolite ($\text{A}_2\text{B(I)B(III)X}_6$, Figure 1.10 b) consists of a lattice network where $[\text{B(I)X}_6]^{5-}$ and $[\text{B(III)X}_6]^{3-}$ octahedra are alternately corner-connected in all three directions. A-site cations are positioned within the framework cavities. Here, B(I) can be Ag^+ , Li^+ , Na^+ , K^+ , Rb^+ , Au^+ , Tl^+ or Cu^+ ; B(III) can be Bi^{3+} , Sb^{3+} , Tl^{3+} , In^{3+} , Ti^{3+} , V^{3+} , Fe^{3+} , Co^{3+} , Ni^{3+} , Au^{3+} or rare earth (RE) cations; A can be Cs^+ , Rb^+ , K^+ , NH_4^+ , or MA^+ ; and X represents halide anions. To assess crystallographic stability, the same empirical indicators, Goldschmidt's tolerance factor t and octahedral factor μ , can be applied as for simple perovskites (Figure 1.10a), but with a modification. In this case, r_B represents the average value of ionic radii for B(I) and B(III) cations. Moreover, the decomposition energies (ΔH) or energy above the convex hull (E_{hull}) with respect to the potential decomposition pathways are typically calculated to evaluate the thermodynamic stabilities of HDPs.^[115, 116, 123] Although over 100 elpasolites with structural tolerance factors and octahedral factors in a reasonable range are predicted to be thermodynamically stable, only a few new elpasolites have been successfully synthesized after years of development.^[124]

1.4.2.3 Properties of $\text{Cs}_2\text{AgBiBr}_6$

Of these reported HDPs, $\text{Cs}_2\text{AgBiBr}_6$ stands out among the rest due to its exceptional structural stability and good optoelectronic properties. $\text{Cs}_2\text{AgBiBr}_6$ exhibits a cubic double perovskite structure with the space group $\text{Fm}\bar{3}\text{m}$, where the unit-cell axis ($a = 11.25 \text{ \AA}$) is approximately twice that of MAPbBr_3 ($a = 5.92 \text{ \AA}$).^[109] In terms of crystallographic stability, $\text{Cs}_2\text{AgBiBr}_6$ exhibits values of t and μ of 0.89 and 0.56, respectively, indicating its good structural stability.^[125] The calculated ΔH value for $\text{Cs}_2\text{AgBiBr}_6$ is positive and even higher than that of MAPbI_3 , indicating its superior thermodynamic stability.^[116] Experimentally, $\text{Cs}_2\text{AgBiBr}_6$ single crystals showed negligible changes in crystal

structure and optical properties over a period of 240 days in ambient conditions.^[126] Additionally, $\text{Cs}_2\text{AgBiBr}_6$ possesses a long carrier lifetime and a relatively small carrier effective mass.^[127] Via stroboscopic scattering microscopy, an ambipolar diffusion length of above 1 μm was reported for $\text{Cs}_2\text{AgBiBr}_6$ single crystals.^[128] The time-resolved microwave conductivity (TRMC) of $\text{Cs}_2\text{AgBiBr}_6$ can reach above 1 $\text{cm}^2 (\text{Vs})^{-1}$ ^[129] and up to 5 $\text{cm}^2 (\text{Vs})^{-1}$ ^[130], which is just one order of magnitude lower than that of lead counterparts. Despite considerable efforts in characterizing the material and engineering the devices, PCEs of this material mostly remained just above 3% for single-junction solar cells.^[131]

The major reason for the low efficiency of $\text{Cs}_2\text{AgBiBr}_6$ solar cells is the large indirect band gap of $\text{Cs}_2\text{AgBiBr}_6$. Additionally, the thin-film fabrication method also plays an important role. For instance, in contrast to lead-based perovskite thin films, which have a reproducible band gap value, the band gap of $\text{Cs}_2\text{AgBiBr}_6$ can be varied from 1.95 eV^[109] to 2.25 eV^[132] depending on different fabrication methods. Another bottleneck that limits the PCE of $\text{Cs}_2\text{AgBiBr}_6$ devices is related to unsatisfactory contacts leading to non-radiative recombination.^[133] Engineering the absorbers and contacts towards higher selectivity and aligned energy levels is needed to address this issue.

1.4.2.4 Strategies for Reducing the Band Gaps

Several strategies have been applied to reduce the band gap of $\text{Cs}_2\text{AgBiBr}_6$. The straightforward approach involves replacing Br with I in the crystal structure of $\text{Cs}_2\text{AgBiBr}_6$, which is expected to result in an indirect band gap of 1.08 eV and a direct band gap of 1.79 eV according to theoretical calculations.^[134] However, due to its low thermodynamic stability and unsatisfactory tolerance factor, there has been no report on bulk crystals of $\text{Cs}_2\text{AgBiI}_6$. Inspiringly, these metastable alternative $[\text{AgI}_6]^{5-}$ and $[\text{BiI}_6]^{3-}$ octahedra can be stabilized in lower-dimensional double perovskites with the assistance of ligands^[135] or large cations^[136], which will be discussed in Section 1.5. Besides developing iodide congeners, the absorption of $\text{Cs}_2\text{AgBiBr}_6$ can be extended to the NIR region by doping the B-site with several elements. This method does not change the band edge but forms defect intermediate states in the band gap (sub-band gap states) due to lattice distortion or heterogeneity caused by phase separation.^[137] Furthermore, as mentioned earlier, a band gap value of 1.64 eV can be achieved through the hydrogenation method, where atomic hydrogen is doped into the interstitial sites of the $\text{Cs}_2\text{AgBiBr}_6$ lattice.^[122]

Another promising approach is exploring alternative elements to replace Ag and/or Bi, aiming to reduce the band gap while maintaining the 3D crystal structures. In addition to Ag-based HDPs,

MA₂KBiCl₆^[138], Cs₂LiBiCl₆^[139] Cs₂NaBiX₆ (X = Br, Cl)^[140-142] and Cs₂NaInCl₆^[141] have been successfully synthesized but with even larger band gaps compared to Cs₂AgBiBr₆. Notably, the iodine-containing HDP Cs₂NaBiI₆ has also been synthesized. It showed a smaller indirect band gap (1.66 eV) than that of Cs₂AgBiBr₆, and to date achieved a PCE of 0.42%.^[143] A novel series of Cs₂Ag_xNa_{1-x}FeCl₆ (0 ≤ x ≤ 1) perovskite single crystals have been synthesized, showcasing tunable band gap values ranging from 2.07 eV to 1.55 eV (for pure Cs₂NaFeCl₆ and Cs₂AgFeCl₆, respectively), along with high thermal stability.^[144] Unfortunately, Cs₂AgFeCl₆ crystal exhibits no detectable photoluminescence (PL) even at low temperatures.^[145] Theoretical studies indicate that In(I)-based HDPs, such as Cs₂In(I)SbCl₆ and Cs₂In(I)BiCl₆, are predicted to have narrow direct band gaps of 1.02 and 0.91 eV, respectively.^[116] Nevertheless, these materials are expected to be unstable against oxidation to In(III)-based compounds.^[123] Cs₂AgIn(III)Cl₆ has been successfully synthesized in both bulk and nanocrystal forms; however, it exhibits a large direct band gap ranging from 3.2 to 3.3 eV.^[146, 147] Furthermore, the scarcity and high price of indium may hinder their widespread commercialization. Alternatively, Cu(I)-based double perovskites are also predicted to exhibit narrow band gaps.^[115, 117] Moreover, unlike the noble metals Ag and In, the abundant and cost-effective nature of Cu makes it highly promising for large-scale commercial production. However, experimental reports on bulk crystals of Cu(I)-based 3D HDPs are scarce. To the best of our knowledge, only Cs₂CuSbCl₆ double perovskite nanocrystals (DPNCs) have been successfully synthesized using a modified hot-injection method.^[148]

1.5 Lower-Dimensional Perovskite Materials

1.5.1 Perovskite Nanocrystals

A comprehensive review of perovskite nanocrystals can be found in Chapter 3.

1.5.2 Organic-Inorganic Hybrid Layered Perovskites

As discussed in Section 1.3.5, one of the challenges hindering the commercialization of MHPs is their instability. One potential strategy to enhance the inherent structural stability of MHPs involves introducing large hydrophobic organic cations into the perovskite structure and “cutting” the 3D structure along a certain axis, resulting in the formation of 2D or quasi-2D perovskites. In this section, the term “2D perovskites” specifically denotes organic-inorganic hybrid layered perovskites, excluding all-inorganic layered perovskites.^[149] Lead-based perovskites exhibit superior stability in both 2D and quasi-2D structures, as do the notoriously unstable Sn(II)-based perovskites. As mentioned in Section 1.4.1, Sn²⁺ emerges as a promising alternative to replace Pb²⁺, but suffering from

its susceptibility to oxidation to the Sn⁴⁺ state. The introduction of large organic cations into Sn-based perovskite crystal structures serves to encapsulate the layer, providing protection against moisture and oxygen. Additionally, it helps restrict phase transitions and ion migration, thereby enhancing the stability of Sn-based perovskites.^[150] Beyond the improvement of stability, various unique properties of 2D perovskites have been extensively explored, which stem from the diversity and versatility of organic spacers.

1.5.2.1 Crystal Structures of 2D Hybrid Perovskites

Here, our focus is on $\langle 100 \rangle$ -oriented 2D perovskites, where the slicing of the inorganic layer and the insertion of organic spacers occur along the $\langle 100 \rangle$ direction of the 3D framework. This type of 2D perovskites can be categorized into three types (Figure 1.11a): Ruddlesden-Popper phase (RP), Dion-Jacobson phase (DJ) and the alternating cations in the interlayer space (ACI). The general formula of the RP phase 2D perovskites is $A'_2A_{n-1}B_nX_{3n+1}$, where A' is a large monovalent organic cation, A is a small organic cation, B is a metal ion or a combination of two metal ions (referred to as double perovskites), X presents halide ions and n signifies the number of inorganic layers situated between large organic spacer layers. The organic interlayer between two inorganic layers for the RP phase is a bilayer structure, where the interlayer interactions are mainly characterized by van der Waals forces and hydrogen bonding. The organic interlayer of DJ phase 2D perovskites is a monolayer consisting of divalent organic cations (A''), forming the general structure of $A''A_{n-1}B_nX_{3n+1}$. In general, the DJ phase shows better stability compared to the RP phase owing to the elimination of van der Waals forces. This results from the direct connection of interlayer divalent cations to the adjacent inorganic layers through hydrogen bonds and Coulomb forces. The chemical formula of the ACI phase is $A'''A_nB_nX_{3n+1}$, where the slightly larger cations (A''') and the smaller A-site cations alternate in the interlayer. Consequently, hydrogen bonds and a weak van der Waals forces coexist within the structure.^[151]

Extensive studies have been conducted on 2D perovskites with RP phase among the three structures mentioned above. The RP phase benefits from a higher abundance of monoammonium spacers, which exhibit better self-assembly capabilities, contributing to enhanced film quality in terms of high orientation and crystallinity. DJ and ACI phases usually have shorter interlayer distances and eliminated or reduced van der Waals forces 'crosslinking' the layers, thus enhancing the stability and probably addressing the carrier-transport bottleneck issue (see the detailed discussion on this issue below). However, the diammonium organic cations in the DJ phase leave substantially fewer degrees

of freedom for orientation regulation. As a result, the availability of suitable organic spacers (diammonium) for DJ phase is significantly smaller compared to RP phases. The ACI phase has only been reported with guanidinium cation (GA^+)^[152], acetamidinium cations (ACA^+)^[153] and 1,4-butanediammonium (BDA^{2+})^[154] so far, indicating the difficulty in designing proper organic spacers for ACI phases.

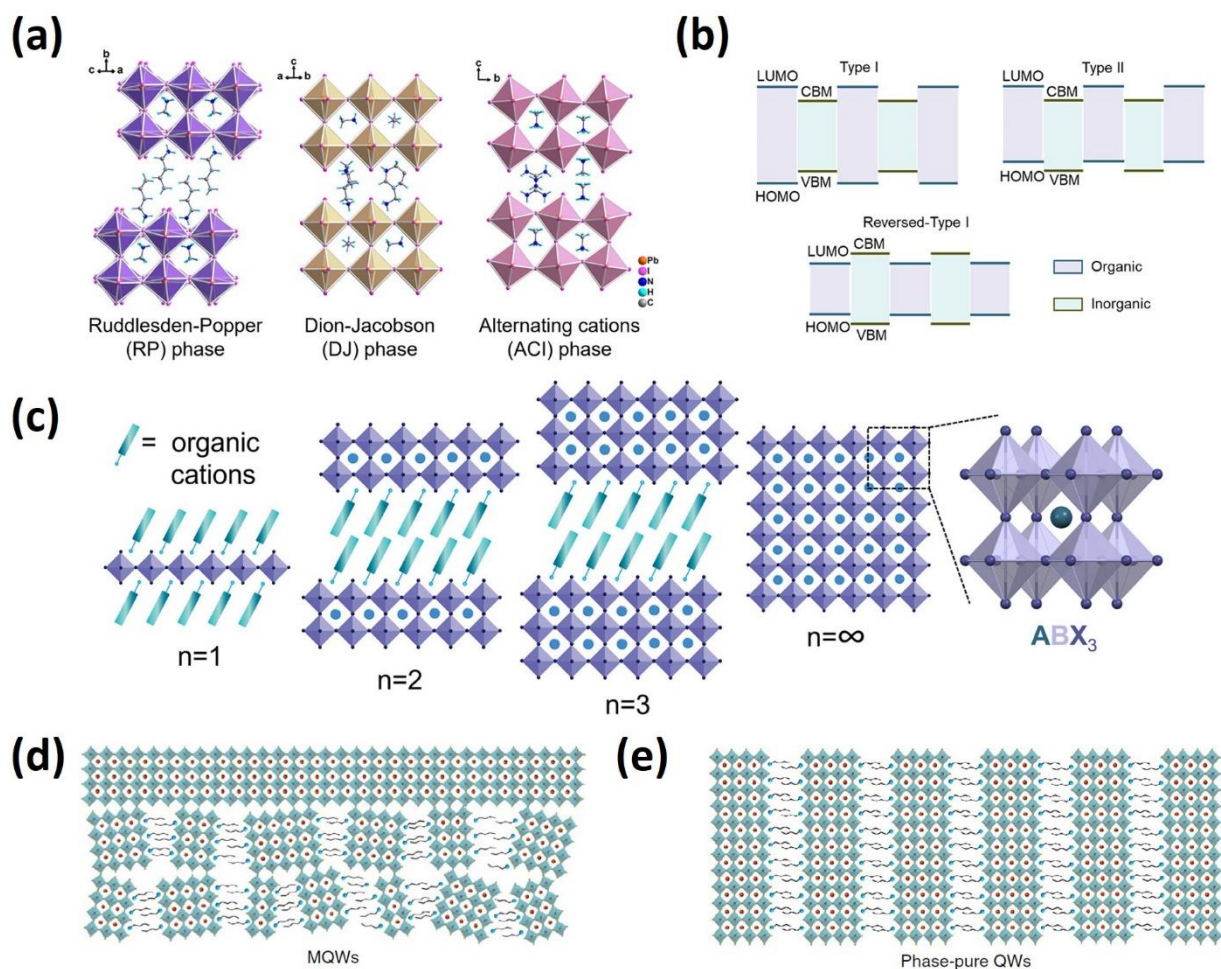


Figure 1.11: (a) RP, DJ, and ACI phases of 2D perovskites. (b) Scheme of perovskite 2D quantum wells with type I, type II, and reversed-type I energy alignment. (c) Schematics of 2D ($n = 1-3$) and 3D perovskites. Reproduced with permission.^[155] Copyright 2023, American Chemical Society. Schematic structure of the MQW film (d) and the phase-pure QW film (e). Reproduced with permission.^[156] Copyright 2021, Springer Nature.

1.5.2.2 Quantum and Dielectric Confinement in 2D Hybrid Perovskites

Recently, a multitude of organic spacers, including aliphatic and single-ring aromatic series cations, have been applied in 2D PSCs. However, the current state-of-the-art performance of these 2D PSCs lags significantly behind their 3D counterparts due to the poor carrier mobility and limited diffusion length.^[157] In the initial examples of 2D perovskites, the extensively studied organic cations for RP or DJ phases, such as butylammonium (BA^+), phenylethylammonium (PEA^+) or 1,3-propanediammonium (PDA^{2+}), possess insulating characteristics and small dielectric constants, which results in a “quantum-well” (QW) band structure with inorganic octahedral layers serving as “well” and organic insulating layers acting as “barrier” (see Figure 1.11b).^[158] Consequently, excitons are quantum confined within the inorganic wells. Combined with the low dielectric screening from the surrounding organic spacers, this configuration yields much larger band gaps and E_b (typically in the range of a few hundred meV). In comparison, their 3D counterparts, such as iodine-based 3D perovskites (with E_b values ranging from 2 to 50 meV)^[159] and bromine-based 3D perovskites (with E_b values ranging from 67 to 150 meV)^[160], demonstrate superior light absorption, charge carrier separation and transport. Nonetheless, in case of the ACI phase, such as $(\text{GA})(\text{MA})_n\text{Pb}_n\text{I}_{3n+1}$, the degree of photogenerated carrier dissociation is generally higher due to their much smaller interlayer distance and E_b .^[152, 161]

Although these hydrophobic cations can improve the stability, their electronically insulating nature can inhibit charge transfer across the organic layer. Transient absorption spectroscopic (TAS) studies have confirmed that both electrons and holes can transfer between perovskite QWs, but this process occurs on a timescale of several picoseconds. This phenomenon explains the overall slow carrier mobility observed in such systems.^[162-164] Time-resolved terahertz (THz) spectroscopies have investigated the transient photoconductivity of 2D perovskites and verified that charge conduction predominantly occurred along the inorganic slabs, supporting the asymmetric confinement of charge carriers in 2D perovskites.^[165] The performance of optoelectronic devices based on 2D perovskites is highly dependent on the phase purity and orientation of the corresponding thin films, owing to the anisotropic structure of 2D perovskites. Achieving precise control over these factors through common solution-processing methods remains challenging, as discussed in detail below.^[166]

1.5.2.3 Phase Purity of 2D Hybrid Perovskites

As the value of n increases, the band gap and E_b of 2D perovskites can be reduced due to the weakened quantum and dielectric confinement effect with higher number of inorganic layers (Figure 1.11c).^[158]

For example, the excitonic properties of the high-quality $(\text{BA})_2(\text{MA})_{n-1}\text{Pb}_n\text{I}_{3n+1}$ ($n = 3$ and $n = 4$) crystals are very close to those of 3D perovskite ($n = \infty$).^[167] However, the introduction of large cations into 3D perovskites can lead to challenges in maintaining phase purity for these quasi-2D perovskites, where $n > 1$. The common reaction and deposition of perovskite precursors often result in an uneven distribution of inorganic slabs.^[168, 169] For example, as illustrated in Figure 1.11d, the film of $(\text{BA})_2(\text{MA})_3\text{Pb}_4\text{I}_{13}$, fabricated by spin-coating from a stoichiometric precursor solution, exhibits a broad distribution of inorganic slabs, including 3D MAPbI_3 ($n = \infty$).^[156] The different formation energy of these different phases is the main reason of this phenomenon. Specifically, MAPbI_3 possesses a lower formation energy and tends to crystallize firstly at the surface where rapid evaporation occurs at the air-liquid interface. This results in a decrease in the ratio of MA^+ to BA^+ for the target phase in the residual solution. Consequently, 2D perovskite phases with lower values of n can be formed in the bottom portion.^[169] Compositional heterogeneity, especially that involving $n = 1$ or 2 phases, can significantly obstruct charge transport and influence charge recombination in 2D perovskites due to the formation of multiple quantum wells (MQWs) by insulating organic layers.^[168] Therefore, maintaining the phase purity of quasi-2D perovskite (Figure 1.11e) is crucial for achieving both efficient and stable solar cells but challenging in reality.^[170]

1.5.2.4 Crystal Orientation of 2D Hybrid Perovskites

Besides the challenge of achieving phase purity in 2D perovskites, crystal orientation is also crucial for the development of high-performance solar cells.^[170, 171] As mentioned above, once the insulating organic spacers cut the 3D perovskite framework and hinder the charge transport between two inorganic layers normal to the layers, the mobility and conductivity are significantly better along the direction of inorganic layers than normal to the inorganic layers. Depending on the deposition process, the organic and inorganic layers in 2D perovskites can be oriented either parallel or normal to the substrate, or they may exhibit random orientation with small crystalline grains (Figure 1.12). For photovoltaic applications, which normally involve a layer-by-layer sandwich structure, it is favorable for 2D perovskite films to possess a vertical orientation with respect to the electrodes. Similar to conventional 2D materials, pure 2D perovskites ($n = 1$) exhibit preferential growth parallel to the substrate, as large organic cations tend to self-assemble laterally.^[171] The preferred vertical orientation can be achieved by a handful of deposition techniques, such as hot casting,^[167, 169] solvent engineering^[172-174] and additive engineering^[175-178]. Moreover, the type of organic cations and substrates both play important roles in the crystallization process due to the distinct interactions

among solvents, organic cations and substrates.^[174, 179, 180] Given the diversity of organic cations, contributing to different complicated interactions during the film deposition process, there is still no general conclusion on specific control of the orientation of 2D perovskite films.

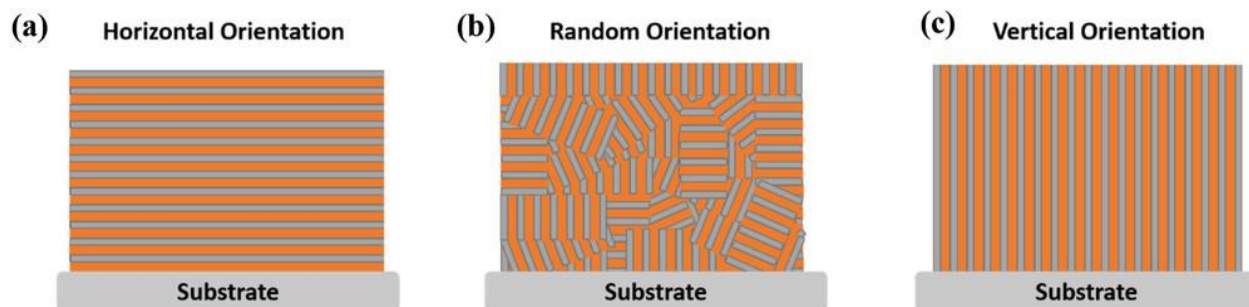


Figure 1.12: Orientation of 2D perovskite thin films. Schemes illustrating 2D perovskite films with organic and inorganic layers. (a) Preferentially oriented parallel to the substrate, (b) randomly oriented, and (c) preferentially oriented perpendicular to the substrate. Reproduced with permission.^[170] Copyright 2021, Wiley-VCH.

1.5.2.5 Functionality of Organic Cations: Quantum Well Breaking and Out-of-Plane Conductivity

In contrast to 3D perovskites, the optoelectronic properties of 2D perovskites are influenced not only by the inorganic octahedra but also by the large organic ammonium cations. As explained in Section 1.5.2.2, the natural QWs can form in 2D perovskites and further affect their properties. Thanks to the diversity and versatility of organic cations, the optoelectronic properties of the corresponding 2D perovskites can be adjusted by elaborately designing organic spacers,^[155, 181, 182] causing this type of material to show great potential in various applications such as white light-emitting devices (WLED)^[183], nonlinear optics^[184, 185], spintronic devices^[186, 187] and SCs^[157].

The reduction of E_b and the increase of exciton diffusion length in 2D perovskites can contribute to improving the charge separation and collection in 2D perovskite SCs. The reduction of E_b in 2D perovskites can be achieved by introducing organic components with a strong dipole moment (high dielectric constant) into 2D perovskite structures^[188, 189], designing suitable organic cations to maintain the ideal inorganic octahedra with less distortion^[190, 191], or incorporating organic charge transfer complexes in the organic layer^[192, 193]. Recently, researchers have been focusing on introducing organic spacers with extended conjugation to finely tune the 2D QW structure from type I to type II (Figure 1.11 b) band alignment, which can break the QWs and reduce E_b .^[194]

Given that most 2D perovskites prefer to possess parallel orientation relative to the substrate, an alternative strategy for enhancing the performance of 2D perovskite optoelectronic device involves improving intrinsic out-of-plane conductivity.^[195, 196] The out-of-plane conductivity in 2D perovskites is determined by factors such as the inorganic-to-inorganic interlayer spacing, intra and intermolecular electronic coupling of the organic spacers, as well as the tuning of the barrier height of the QWs.^[195, 197] The DJ and ACI phase 2D perovskites usually have shorter interlayer distance, thus showing relatively better out-of-plane conductivity.^[198] For example, it has been revealed that carrier or exciton transport along the out-of-plane direction in the DJ phase (4AMP)(MA)Pb₂I₇ (4AMP = 4-(aminomethyl)piperidinium) perovskite is comparable to that along the in-plane direction.^[199] Efficient strategies for enhancing intra and intermolecular electronic coupling include introducing hydrogen bond and π - π stacking interactions of the organic spacers, as well as improving energy alignment between the organic layers and inorganic layers. For example, in the case of RP phase perovskites, fluorine substitution on the para position in PEA to form 4-fluorophenethylammonium (F-PEA) results in shorter average phenyl ring centroid–centroid distances in the organic layer. This leads to better aligned stacking of perovskite sheets, enhancing intermolecular electronic coupling and improving the out-of-plane conductivity.^[200] Therefore, the rational molecular design and understanding of organic spacers with novel functionalities for 2D perovskites are crucial to promote the performance of their corresponding optoelectronic devices.^[155]

1.5.3 The Merits of Reduced Dimension for Metastable Double Perovskite Materials

Some double perovskites have been predicted to feature excellent optoelectronic properties but with metastable phases. The synthesis and stabilization of these metastable double perovskites can enrich the double perovskite family and benefit the screening of high-performance lead-free halide double perovskite materials. The reduction of dimensionality at both morphological and molecular levels can stabilize metastable double perovskite structures with the assistance of long-chain organic ligands or large organic cations, which can form DPNCs and layered double perovskites, respectively. As an example of morphological level dimensional reduction, Cs₂AgBiI₆ is challenging to synthesize directly; however, its DPNCs have been obtained by the post-treatment of Cs₂AgBiBr₆ DPNCs via anion exchange.^[135] This thermodynamically unstable phase can be kinetically stabilized by introducing additional control of surface energy. In terms of molecular level dimensional reduction, AgBiI₃-based layered DPs have also been successfully synthesized recently, such as (AE2T)₂AgBiI₈ (AE2T = 5,5'-diylbis(aminoethyl)-[2,2'-bithiophene])^[201], (C₆H₁₆N₂)₂AgBiI₈ (C₆H₁₆N₂ = 1,4-

cyclohexanediamine)^[202] and (4FPEA)₄AgBiI₈ (4FPEA = 4-fluorophenethylammonium)^[203], where the octahedra are strongly distorted but still maintain layered double perovskite phases.

Another example regards Cu(I)-based HDPs, which have been rarely reported experimentally. The ground-state structure of Cu(I) halides favors three- or four- rather than six-fold coordination, which is also suggested by theoretical calculations.^[110] However, Cu(I)-based perovskite structures containing [CuX₆]⁵⁻ octahedra can be obtained via non-equilibrium methods. Besides the aforementioned example of Cs₂CuSbCl₆ nanocrystals (Section 1.4.2.4), the double perovskite structure with six-fold coordination of Cu(I) can also be stabilized through dimensional reduction to layered perovskites. Recently, some Cu(I)-based layered double perovskites have been successfully synthesized where Cu(I) displays an extremely distorted six-fold coordination while still maintaining the perovskite structure, for instance, (C₆H₁₆N₂)₂CuBiI₈^[202], (PPDA)₂CuRuCl₈^[204], (PEA)₄CuInCl₈^[205, 206] and (BA)₄CuInCl₈^[206] (PPDA = para-phenylenediammonium). It is evident that both the long-chain organic ligands and large organic cations can stabilize the Cu(I)-based double perovskite structure by morphological and molecular level dimensional reduction, providing opportunities to investigate their optoelectronic properties. The successful stabilization of these metastable phases has inspired and guided the scientific community to explore other unknown lead-free halide double perovskites, potentially revealing fascinating performance characteristics.

1.6 Outline of the Thesis

In this work, several metastable double perovskite structures were successfully stabilized by morphological and molecular level dimensional reduction. The synthesis, optoelectronic properties and applications of these novel double perovskite materials were investigated.

In Chapter 3, we comprehensively reviewed the recent progress of PNCs. The synthetic methods and stability issues of the PNCs are introduced first, followed by the introduction of the strategies for improving their stability by encapsulation. The applications of PNCs in various optoelectronic devices are then briefly presented. Finally, the remaining challenges in improving the stability of PNCs towards PNC-based optoelectronics with high performance and great durability are addressed.

In Chapter 4, we synthesize $\text{Cs}_2\text{CuSbCl}_6$ double perovskite nanocrystals (DPNCs) at ambient conditions by a facile and fast synthesis method, namely, a modified ligand-assisted reprecipitation (LARP) method. This metastable $\text{Cs}_2\text{CuSbCl}_6$ double perovskite structure can be stabilized through the solution-based nanocrystal synthesis. Using an anion-exchange method, $\text{Cs}_2\text{CuSbBr}_6$ DPNCs are obtained for the first time, featuring a strikingly narrow band gap of 0.9 eV. Finally, taking advantage of the solution processability of DPNCs, smooth and dense $\text{Cs}_2\text{CuSbCl}_6$ and $\text{Cs}_2\text{CuSbBr}_6$ DPNC films are successfully fabricated. We prove that these metastable $\text{Cs}_2\text{CuSbCl}_6$ and $\text{Cs}_2\text{CuSbBr}_6$ double perovskite structures can be successfully stabilized by morphological level dimensional reduction.

In Chapter 5, we establish that the metastable Ag-Bi-I and Cu-Bi-I systems can be stabilized by molecular level dimensional reduction, which implies introducing large hydrophobic organic cations into double perovskite structures and “cutting” the 3D structures along a certain plane to form 2D perovskites. Here, we report that both Ag-Bi-I and Cu-Bi-I systems are thermodynamically stable with the structures of $(\text{aromatic-}O\text{-linker-NH}_3)_4\text{AgBiI}_8$ and $(\text{aromatic-}O\text{-linker-NH}_3)_4\text{CuBiI}_8$, respectively, where the aromatic moiety is naphthalene or pyrene and the linker is ethyl or propyl. The intrinsic electronic challenges of double perovskites are investigated and the electronic anisotropy of two-dimensional perovskites is modulated. With extended conjugated systems, $(\text{pyrene-}O\text{-ethyl-NH}_3)_4\text{AgBiI}_8$ was isolated from a total of eight new 2D double perovskites, exhibiting an electronic band structure forming a type IIb multiple quantum well system with favorable intraorganic layer arrangement for out-of-plane conductivity, leading to a photocurrent response ratio of almost three orders of magnitude under AM1.5G illumination. Finally, $(\text{pyrene-}O\text{-ethyl-NH}_3)_4\text{AgBiI}_8$ was integrated

into a sandwich structure to construct the first pure $n = 1$ Ruddlesden-Popper 2D double perovskite solar cell.

1.7 References

- [1] IPCC, *Climate Change 2022: Mitigation of Climate Change. Contribution of Working Group III to the Sixth Assessment Report of the Intergovernmental Panel on Climate Change*. Cambridge University Press, Cambridge, UK and New York, NY, USA **2022**.
- [2] M.B. Hayat, D. Ali, K.C. Monyake, L. Alagha, N. Ahmed, *Int. J. Energy Res.* **2019**, *43*, 1049.
- [3] C. Wu, K. Wang, M. Batmunkh, A.S.R. Bati, D. Yang, Y. Jiang, Y. Hou, J.G. Shapter, S. Priya, *Nano Energy* **2020**, *70*, 104480.
- [4] *United Nations Development Programme and World Energy Council* **2017**.
- [5] IEA, *Electricity Information: Overview*, IEA, Paris <https://www.iea.org/reports/electricity-information-overview>, License: CC BY 4.0 **2021**.
- [6] IEA, *World Energy Outlook 2022*, IEA, Paris <https://www.iea.org/reports/world-energy-outlook-2022>, License: CC BY 4.0 (report); CC BY NC SA 4.0 (Annex A) **2022**.
- [7] A.E. Becquerel, *C. R. Acad. Sci.* **1839**, *9*, 145.
- [8] C.E. Fritts, *Am. J. Sci.* **1883**, *26*, 465.
- [9] R.S. Ohl, *U.S. Patent US2402662A* **1941**.
- [10] <https://www.nrel.gov/pv/cell-efficiency.html> **National Renewable Energy Laboratory, Best Research-Cell Efficiencies chart**.
- [11] D. Chapin, C. Fuller, G. Pearson, *Semiconductor Devices: Pioneering Papers*, World Scientific 1991, pp. 969.
- [12] J. Pastuszak, P. Węgierek, *Materials* **2022**, *15*, 5542.
- [13] I. Massiot, A. Cattoni, S. Collin, *Nat. Energy.* **2020**, *5*, 959.
- [14] S. Ghosh, R. Yadav, *Sustain. Energy Technol. Assess.* **2021**, *47*, 101410.
- [15] T. Saga, *NPG Asia Mater.* **2010**, *2*, 96.
- [16] H.-L. Chen, A. Cattoni, R. De Lépinau, A.W. Walker, O. Höhn, D. Lackner, G. Siefer, M. Faustini, N. Vandamme, J. Goffard, B. Behaghel, C. Dupuis, N. Bardou, F. Dimroth, S. Collin, *Nat. Energy.* **2019**, *4*, 761.
- [17] M. Stuckelberger, R. Biron, N. Wyrsh, F.-J. Haug, C. Ballif, *Renew. Sustain. Energy Rev.* **2017**, *76*, 1497.
- [18] T. Feurer, P. Reinhard, E. Avancini, B. Bissig, J. Löckinger, P. Fuchs, R. Carron, T.P. Weiss, J. Perrenoud, S. Stutterheim, S. Buecheler, A.N. Tiwari, *Prog Photovolt Res Appl.* **2017**, *25*, 645.
- [19] W.K. Metzger, S. Grover, D. Lu, E. Colegrove, J. Moseley, C.L. Perkins, X. Li, R. Mallick, W. Zhang, R. Malik, J. Kephart, C.S. Jiang, D. Kuciauskas, D.S. Albin, M.M. Al-Jassim, G. Xiong, M. Gloeckler, *Nat. Energy.* **2019**, *4*, 837.
- [20] K. Otte, L. Makhova, A. Braun, I. Konovalov, *Thin Solid Films* **2006**, *511-512*, 613.
- [21] Suman, P. Sharma, P. Goyal, *Mater. Today Proc.* **2020**, *28*, 1593.
- [22] L. Zhu, M. Zhang, J. Xu, C. Li, J. Yan, G. Zhou, W. Zhong, T. Hao, J. Song, X. Xue, Z. Zhou, R. Zeng, H. Zhu, C.-C. Chen, R.C.I. MacKenzie, Y. Zou, J. Nelson, Y. Zhang, Y. Sun, F. Liu, *Nat. Mater.* **2022**, *21*, 656.

- [23] Q. Zhao, R. Han, A.R. Marshall, S. Wang, B.M. Wieliczka, J. Ni, J. Zhang, J. Yuan, J.M. Luther, A. Hazarika, G.-R. Li, *Adv. Mater.* **2022**, *34*, 2107888.
- [24] E. Ravishankar, M. Charles, Y. Xiong, R. Henry, J. Swift, J. Rech, J. Calero, S. Cho, R.E. Booth, T. Kim, A.H. Balzer, Y. Qin, C. Hoi Yi Ho, F. So, N. Stingelin, A. Amassian, C. Saravitz, W. You, H. Ade, H. Sederoff, B.T. O'Connor, *Cell Rep. Phys. Sci.* **2021**, *2*, 100381.
- [25] M.-J. Choi, Y. Kim, H. Lim, E. Alarousu, A. Adhikari, B.S. Shaheen, Y.H. Kim, O.F. Mohammed, E.H. Sargent, J.Y. Kim, Y.S. Jung, *Adv. Mater.* **2019**, *31*, 1805886.
- [26] M. Lyu, J.-H. Yun, P. Chen, M. Hao, L. Wang, *Adv. Energy Mater.* **2017**, *7*, 1602512.
- [27] Y. Wei, Z.Y. Cheng, J. Lin, *Chem. Soc. Rev.* **2019**, *48*, 310.
- [28] H.L. Wells, *Zeitschrift für anorganische Chemie* **1893**, *3*, 195.
- [29] D. Weber, *Zeitschrift für Naturforschung B* **1979**, *34*, 939.
- [30] D. Weber, *Zeitschrift für Naturforschung B* **1978**, *33*, 862.
- [31] D. Weber, *Zeitschrift für Naturforschung B* **1978**, *33*, 1443.
- [32] Akihiro Kojima, Kenjiro Teshima, Tsutomu Miyasaka, Y. Shirai, *ECS Meeting Abstracts* **2006**, MA2006-02, 397.
- [33] A. Kojima, K. Teshima, T. Miyasaka, Y. Shirai, *ECS Meeting Abstracts*, IOP Publishing, 2006, pp. 397.
- [34] A. Kojima, K. Teshima, Y. Shirai, T. Miyasaka, *J. Am. Chem. Soc.* **2009**, *131*, 6050.
- [35] M. Jung, S.-G. Ji, G. Kim, S.I. Seok, *Chem. Soc. Rev.* **2019**, *48*, 2011.
- [36] B. Saparov, D.B. Mitzi, *Chem. Rev.* **2016**, *116*, 4558.
- [37] A. Fakharuddin, L. Schmidt-Mende, G. Garcia-Belmonte, R. Jose, I. Mora-Sero, *Adv. Energy Mater.* **2017**, *7*, 1700623.
- [38] T. Webb, S.J. Sweeney, W. Zhang, *Adv. Funct. Mater.* **2021**, *31*, 2103121.
- [39] S. Kazim, M.K. Nazeeruddin, M. Gratzel, S. Ahmad, *Angew. Chem. Int. Ed.* **2014**, *53*, 2812.
- [40] R.E. Brandt, J.R. Poindexter, P. Gorai, R.C. Kurchin, R.L.Z. Hoye, L. Nienhaus, M.W.B. Wilson, J.A. Polizzotti, R. Sereika, R. Žaltauskas, L.C. Lee, J.L. MacManus-Driscoll, M. Bawendi, V. Stevanović, T. Buonassisi, *Chem. Mater.* **2017**, *29*, 4667.
- [41] W.-J. Yin, T. Shi, Y. Yan, *Adv. Mater.* **2014**, *26*, 4653.
- [42] V.M. Goldschmidt, *Naturwissenschaften* **1926**, *14*, 477.
- [43] M.-G. Ju, J. Dai, L. Ma, X.C. Zeng, *J. Am. Chem. Soc.* **2017**, *139*, 8038.
- [44] K. Galkowski, A. Mitioglu, A. Miyata, P. Plochocka, O. Portugall, G.E. Eperon, J.T.-W. Wang, T. Stergiopoulos, S.D. Stranks, H.J. Snaith, R.J. Nicholas, *Energy Environ. Sci.* **2016**, *9*, 962.
- [45] M.M. Lee, J. Teuscher, T. Miyasaka, T.N. Murakami, H.J. Snaith, *Science* **2012**, *338*, 643.
- [46] L. Etgar, P. Gao, Z. Xue, Q. Peng, A.K. Chandiran, B. Liu, M.K. Nazeeruddin, M. Grätzel, *J. Am. Chem. Soc.* **2012**, *134*, 17396.
- [47] G. Xing, N. Mathews, S. Sun, S.S. Lim, Y.M. Lam, M. Grätzel, S. Mhaisalkar, T.C. Sum, *Science* **2013**, *342*, 344.

- [48] S.D. Stranks, G.E. Eperon, G. Grancini, C. Menelaou, M.J.P. Alcocer, T. Leijtens, L.M. Herz, A. Petrozza, H.J. Snaith, *Science* **2013**, *342*, 341.
- [49] H.J. Snaith, *J. Phys. Chem. Lett.* **2013**, *4*, 3623.
- [50] W.-J. Yin, T. Shi, Y. Yan, *Appl. Phys. Lett.* **2014**, *104*.
- [51] H.S. Kim, C.R. Lee, J.H. Im, K.B. Lee, T. Moehl, A. Marchioro, S.J. Moon, R. Humphry-Baker, J.H. Yum, J.E. Moser, M. Gratzel, N.G. Park, *Sci. Rep.* **2012**, *2*, 591.
- [52] R. Chakraborty, A. Nag, *Phys. Chem. Chem. Phys.* **2021**, *23*, 82.
- [53] J. Wu, H. Cha, T. Du, Y. Dong, W. Xu, C.T. Lin, J.R. Durrant, *Adv. Mater.* **2022**, *34*, 2101833.
- [54] B. Parida, A. Singh, A.K.K. Soopy, S. Sangaraju, M. Sundaray, S. Mishra, S.Z. Liu, A. Najjar, *Adv. Sci.* **2022**, *9*.
- [55] M.A. Green, E.D. Dunlop, M. Yoshita, N. Kopidakis, K. Bothe, G. Siefer, X. Hao, *Prog Photovolt Res Appl.* **2024**, *32*, 3.
- [56] M. Yang, X. Ru, S. Yin, WCPEC-8, 8th World Conference on Photovoltaic Energy Conversion (LONGi, 2022), 2022.
- [57] B. Ding, Y. Zhang, Y. Ding, H. Kanda, K. Hobeom, K. Brooks, G. Xiaoxin, X. Jianxing, M.K. Nazeeruddin, The 5th International Conference on Materials & Environmental Science, ICMES-2022, Saïdia, 2022.
- [58] <https://www.nrel.gov/pv/assets/pdfs/champion-module-efficiencies.pdf> **National Renewable Energy Laboratory, Champion Module Efficiencies.**
- [59] F. Yang, D. Jang, L. Dong, S. Qiu, A. Distler, N. Li, C.J. Brabec, H.-J. Egelhaaf, *Adv. Energy Mater.* **2021**, *11*, 2101973.
- [60] J.M.C. da Silva, A.D. Gonçalves, F.C. Marques, J.N. de Freitas, *Solar RRL* **2022**, *6*, 2100865.
- [61] S. Wang, A.A. Yousefi Amin, L. Wu, M. Cao, Q. Zhang, T. Ameri, *Small Struct.* **2021**, *2*, 2000124.
- [62] C.C. Boyd, R. Cheacharoen, T. Leijtens, M.D. McGehee, *Chem. Rev.* **2019**, *119*, 3418.
- [63] S.S. Zhang, Z.H. Liu, W.J. Zhang, Z.Y. Jiang, W.T. Chen, R. Chen, Y.Q. Huang, Z.C. Yang, Y.Q. Zhang, L.Y. Han, W. Chen, *Adv. Energy Mater.* **2020**, *10*, 2001610.
- [64] C. Wang, X. Dong, F. Chen, G. Liu, H. Zheng, *Mater. Chem. Front.* **2023**, *7*, 5786.
- [65] C.-H. Chen, S.-N. Cheng, L. Cheng, Z.-K. Wang, L.-S. Liao, *Adv. Energy Mater.* **2023**, *13*, 2204144.
- [66] T. Luo, M. Shen, J. Zhou, X. Wang, J. Xia, Z. Fu, Y. Jin, *Environ. Toxicol.* **2019**, *34*, 521.
- [67] I.R. Benmessaoud, A.-L. Mahul-Mellier, E. Horváth, B. Maco, M. Spina, H.A. Lashuel, L. Forró, *Toxicol. Res.* **2016**, *5*, 407.
- [68] Z. Chen, X. Huo, G. Chen, X. Luo, X. Xu, *Environ. Sci. Pollut. Res.* **2021**, *28*, 28833.
- [69] Z.-K. Wang, X.-L. Zhou, X.-B. Song, D.-M. Zhuang, Z.-Y. Wang, D.-B. Yang, L. Wang, *Biol. Trace Elem. Res.* **2016**, *174*, 166.
- [70] X. Jin, Z. Xu, X. Zhao, M. Chen, S. Xu, *Chemosphere* **2017**, *180*, 259.
- [71] A. Lukačínová, O. Rácz, E. Lovássová, F. Ništiar, *Ecotoxicol. Environ. Saf.* **2011**, *74*, 1747.
- [72] K. Czubowicz, H. Ješko, P. Wencel, W.J. Lukiw, R.P. Strosznajder, *Mol. Neurobiol.* **2019**, *56*, 5436.

- [73] A. Mabrouk, *J Biochem Mol Toxicol.* **2019**, *33*, e22238.
- [74] Z. Shi, J. Guo, Y. Chen, Q. Li, Y. Pan, H. Zhang, Y. Xia, W. Huang, *Adv. Mater.* **2017**, *29*, 1605005.
- [75] S.Z. Wang, J.T. Wang, Y.H. Lou, Y.H. Zhou, Z.K. Wang, *Adv. Mater. Interfaces* **2022**, *9*, 2200772.
- [76] Y. Zhang, Y. Ma, Y. Wang, X. Zhang, C. Zuo, L. Shen, L. Ding, *Adv. Mater.* **2021**, *33*, 2006691.
- [77] G.K. Grandhi, D. Hardy, M. Krishnaiah, B. Vargas, B. Al-Anesi, M.P. Suryawanshi, D. Solis-Ibarra, F. Gao, R.L.Z. Hoye, P. Vivo, *Adv. Funct. Mater.* **2023**, *n/a*, 2307441.
- [78] P. Wu, S. Wang, X. Li, F.J.M. Zhang, *Matter* **2022**, *5*, 1137.
- [79] Y. Jiang, L. Qiu, E.J. Juarez-Perez, L.K. Ono, Z. Hu, Z. Liu, Z. Wu, L. Meng, Q. Wang, Y. Qi, *Nat. Energy.* **2019**, *4*, 585.
- [80] S. Chen, Y. Deng, H. Gu, S. Xu, S. Wang, Z. Yu, V. Blum, J. Huang, *Nat. Energy.* **2020**, *5*, 1003.
- [81] S. Chen, Y. Deng, X. Xiao, S. Xu, P.N. Rudd, J. Huang, *Nat. Sustain* **2021**, *4*, 636.
- [82] X. Li, F. Zhang, J. Wang, J. Tong, T. Xu, K. Zhu, *Nat. Sustain* **2021**, *4*, 1038.
- [83] B. Niu, H. Wu, J. Yin, B. Wang, G. Wu, X. Kong, B. Yan, J. Yao, C.-Z. Li, H. Chen, *ACS Energy Lett.* **2021**, *6*, 3443.
- [84] H. Zhang, K. Li, M. Sun, F. Wang, H. Wang, A.K.-Y. Jen, *Adv. Energy Mater.* **2021**, *11*, 2102281.
- [85] F. Yang, S. Wang, P. Dai, L. Chen, A. Wakamiya, K. Matsuda, *J. Mater. Chem. A* **2021**, *9*, 2612.
- [86] F.-W. Liu, G. Biesold, M. Zhang, R. Lawless, J.-P. Correa-Baena, Y.-L. Chueh, Z. Lin, *Mater. Today* **2021**, *43*, 185.
- [87] M. Ren, Y. Miao, T. Zhang, Z. Qin, Y. Chen, N. Wei, X. Qian, T. Wang, Y. Zhao, *ACS Sustain. Chem. Eng.* **2021**, *9*, 16519.
- [88] M.L. Parisi, A. Sinicropi, *Nat. Sustain* **2021**, *4*, 754.
- [89] F. Hao, C.C. Stoumpos, D.H. Cao, R.P.H. Chang, M.G. Kanatzidis, *Nat. Photon.* **2014**, *8*, 489.
- [90] T. Krishnamoorthy, H. Ding, C. Yan, W.L. Leong, T. Baikie, Z. Zhang, M. Sherburne, S. Li, M. Asta, N. Mathews, S.G. Mhaisalkar, *J. Mater. Chem. A* **2015**, *3*, 23829.
- [91] N. Ito, M.A. Kamarudin, D. Hirotsu, Y. Zhang, Q. Shen, Y. Ogomi, S. Iikubo, T. Minemoto, K. Yoshino, S. Hayase, *J. Phys. Chem. Lett.* **2018**, *9*, 1682.
- [92] Z. Zhao, F. Gu, Y. Li, W. Sun, S. Ye, H. Rao, Z. Liu, Z. Bian, C. Huang, *Adv. Sci.* **2017**, *4*, 1700204.
- [93] B.B. Yu, Z. Chen, Y. Zhu, Y. Wang, B. Han, G. Chen, X. Zhang, Z. Du, Z. He, *Adv. Mater.* **2021**, *33*, 2102055.
- [94] Z.H. Zhang, Y.F. Huang, J.L. Jin, Y.T. Jiang, Y.L. Xu, J.W. Zhu, D.W. Zhao, *Angew. Chem. Int. Ed.* **2023**, *135*, e202308093.
- [95] W.J. Ke, C.C. Stoumpos, M.G. Kanatzidis, *Adv. Mater.* **2019**, *31*, 1803230.
- [96] B. Li, B. Chang, L. Pan, Z. Li, L. Fu, Z. He, L. Yin, *ACS Energy Lett.* **2020**, *5*, 3752.
- [97] A. Babayigit, D. Duy Thanh, A. Ethirajan, J. Manca, M. Muller, H.-G. Boyen, B. Conings, *Sci. Rep.* **2016**, *6*, 18721.
- [98] N. Tewari, S.B. Shivarudraiah, J.E. Halpert, *Nano Lett.* **2021**, *21*, 5578.

- [99] Z. Zhang, X. Li, X. Xia, Z. Wang, Z. Huang, B. Lei, Y. Gao, *J. Phys. Chem. Lett.* **2017**, *8*, 4300.
- [100] U.H. Hamdeh, B.J. Ryan, R.D. Nelson, M. Zembrzuski, J. Slobidsky, K.J. Prince, I. Cleveland, A. Vela-Ramirez, A.C. Hillier, M.G. Panthani, *J. Phys. Chem. Lett.* **2019**, *10*, 3134.
- [101] X. Huang, S. Huang, P. Biswas, R. Mishra, *J. Phys. Chem. C* **2016**, *120*, 28924.
- [102] S.J. Sun, S. Tominaka, J.H. Lee, F. Xie, P.D. Bristowe, A.K. Cheetham, *APL Mater.* **2016**, *4*, 031101.
- [103] J.-C. Hebig, I. Kühn, J. Flohre, T. Kirchartz, *ACS Energy Lett.* **2016**, *1*, 309.
- [104] P.C. Harikesh, H.K. Mulmudi, B. Ghosh, T.W. Goh, Y.T. Teng, K. Thirumal, M. Lockrey, K. Weber, T.M. Koh, S. Li, S. Mhaisalkar, N. Mathews, *Chem. Mater.* **2016**, *28*, 7496.
- [105] B. Saparov, F. Hong, J.-P. Sun, H.-S. Duan, W. Meng, S. Cameron, I.G. Hill, Y. Yan, D.B. Mitzi, *Chem. Mater.* **2015**, *27*, 5622.
- [106] F. Jiang, D. Yang, Y. Jiang, T. Liu, X. Zhao, Y. Ming, B. Luo, F. Qin, J. Fan, H. Han, L. Zhang, Y. Zhou, *J. Am. Chem. Soc.* **2018**, *140*, 1019.
- [107] B.-W. Park, B. Philippe, X. Zhang, H. Rensmo, G. Boschloo, E.M.J. Johansson, *Adv. Mater.* **2015**, *27*, 6806.
- [108] C. Zuo, L. Ding, *Angew. Chem. Int. Ed.* **2017**, *56*, 6528.
- [109] A.H. Slavney, T. Hu, A.M. Lindenberg, H.I. Karunadasa, *J. Am. Chem. Soc.* **2016**, *138*, 2138.
- [110] N.R. Wolf, B.A. Connor, A.H. Slavney, H. Karunadasa, *Angew. Chem. Int. Ed.* **2021**, *133*, 16400.
- [111] B. Vargas, E. Ramos, E. Perez-Gutierrez, J.C. Alonso, D. Solis-Ibarra, *J. Am. Chem. Soc.* **2017**, *139*, 9116.
- [112] Y. Zhao, K. Cruse, M. Abdelsamie, G. Ceder, C.M. Sutter-Fella, *Matter* **2021**, *4*, 1801.
- [113] E. Greul, M. Petrus, A. Binek, P. Docampo, T. Bein, *J. Mater. Chem. A* **2017**, *5*, 19972.
- [114] M.T. Sirtl, R. Hooijer, M. Armer, F.G. Ebadi, M. Mohammadi, C. Maheu, A. Weis, B.T. van Gorkom, S. Häringer, R.A.J. Janssen, T. Mayer, V. Dyakonov, W. Tress, T. Bein, *Adv. Energy Mater.* **2022**, *12*, 2103215.
- [115] Z. Xiao, K.-Z. Du, W. Meng, D.B. Mitzi, Y. Yan, *Angew. Chem.* **2017**, *129*, 12275.
- [116] X.G. Zhao, J.H. Yang, Y.H. Fu, D.W. Yang, Q.L. Xu, L.P. Yu, S.H. Wei, L.J. Zhang, *J. Am. Chem. Soc.* **2017**, *139*, 2630.
- [117] G. Volonakis, M.R. Filip, A.A. Haghighirad, N. Sakai, B. Wenger, H.J. Snaith, F. Giustino, *J. Phys. Chem. Lett.* **2016**, *7*, 1254.
- [118] W. Cross, W.F. Hillebrand, *Am. J. Sci.* **1883**, *s3-26*, 271.
- [119] H.L. Wells, *Am. J. Sci.* **1922**, *s5-3*, 315.
- [120] N. Kojima, H. Kitagawa, T. Ban, F. Amita, M. Nakahara, *Solid State Commun.* **1990**, *73*, 743.
- [121] E.T. McClure, M.R. Ball, W. Windl, P.M. Woodward, *Chem. Mater.* **2016**, *28*, 1348.
- [122] Z. Zhang, Q. Sun, Y. Lu, F. Lu, X. Mu, S.-H. Wei, M. Sui, *Nat. Commun.* **2022**, *13*, 3397.
- [123] Z. Xiao, K.-Z. Du, W. Meng, J. Wang, D.B. Mitzi, Y. Yan, *J. Am. Chem. Soc.* **2017**, *139*, 6054.
- [124] T. Zhang, Z. Cai, S. Chen, *ACS Appl. Mater. Interfaces* **2020**, *12*, 20680.

- [125] J. Su, T. Mou, J. Wen, B. Wang, *J. Phys. Chem. C* **2020**, *124*, 5371.
- [126] F. Ji, J. Klarbring, F. Wang, W. Ning, L. Wang, C. Yin, J.S.M. Figueroa, C.K. Christensen, M. Etter, T. Ederth, L. Sun, S.I. Simak, I.A. Abrikosov, F. Gao, *Angew. Chem. Int. Ed.* **2020**, *59*, 15191.
- [127] H.W. Lei, D. Hardy, F. Gao, *Adv. Funct. Mater.* **2021**, *31*, 2105898.
- [128] M. Delor, A.H. Slavney, N.R. Wolf, M.R. Filip, J.B. Neaton, H.I. Karunadasa, N.S. Ginsberg, *ACS Energy Lett.* **2020**, *5*, 1337.
- [129] D. Bartesaghi, A.H. Slavney, M.C. Gelvez-Rueda, B.A. Connor, F.C. Grozema, H.I. Karunadasa, T.J. Savenije, *J. Phys. Chem. C* **2018**, *122*, 4809.
- [130] M.T. Sirtl, M. Armer, L.K. Reb, R. Hooijer, P. Dörflinger, M.A. Scheel, K. Tvingstedt, P. Rieder, N. Glück, P. Pandit, S.V. Roth, P. Müller-Buschbaum, V. Dyakonov, T. Bein, *ACS Appl. Energy Mater.* **2020**, *3*, 11597.
- [131] W. Tress, M.T. Sirtl, *Solar RRL* **2022**, *6*, 2100770.
- [132] Z. Li, S.R. Kavanagh, M. Napari, R.G. Palgrave, M. Abdi-Jalebi, Z. Andaji-Garmaroudi, D.W. Davies, M. Laitinen, J. Julin, M.A. Isaacs, R.H. Friend, D.O. Scanlon, A. Walsh, R.L.Z. Hoye, *J. Mater. Chem. A* **2020**, *8*, 21780.
- [133] M.T. Sirtl, F. Ebadi, B.T. van Gorkom, P. Ganswindt, R.A.J. Janssen, T. Bein, W. Tress, *Adv. Opt. Mater.* **2021**, *9*, 2100202.
- [134] C.N. Savory, A. Walsh, D.O. Scanlon, *ACS Energy Lett.* **2016**, *1*, 949.
- [135] S.E. Creutz, E.N. Crites, M.C. De Siena, D.R. Gamelin, *Nano Lett.* **2018**, *18*, 1118.
- [136] B.A. Connor, L. Leppert, M.D. Smith, J.B. Neaton, H.I. Karunadasa, *J. Am. Chem. Soc.* **2018**, *140*, 5235.
- [137] W. Yu, Y. Zou, H. Wang, B. Qu, Z. Chen, L. Xiao, *J. Phys. Chem. Lett.* **2023**, *14*, 5310.
- [138] F. Wei, Z. Deng, S. Sun, F. Xie, G. Kieslich, D.M. Evans, M.A. Carpenter, P.D. Bristowe, A.K. Cheetham, *Mater. Horiz.* **2016**, *3*, 328.
- [139] Y.M. Sun, A.J. Fernandez-Carrion, Y.H. Liu, C.L. Yin, X. Ming, B.M. Liu, J. Wang, H. Fu, X.J. Kuang, X.R. Xing, *Chem. Mater.* **2021**, *33*, 5905.
- [140] J.D. Majher, M.B. Gray, T.A. Strom, P.M. Woodward, *Chem. Mater.* **2019**, *31*, 1738.
- [141] J. Zhou, X. Rong, P. Zhang, M.S. Molokeev, P. Wei, Q. Liu, X. Zhang, Z. Xia, *Adv. Opt. Mater.* **2019**, *7*, 1801435.
- [142] W. Lee, D. Choi, S. Kim, *Chem. Mater.* **2020**, *32*, 6864.
- [143] C. Zhang, L. Gao, S. Teo, Z. Guo, Z. Xu, S. Zhao, T. Ma, *Sustainable Energy & Fuels* **2018**, *2*, 2419.
- [144] Y. Xian, H. Yin, Y. Bao, Y. Xiao, S. Yuan, N.U. Rahman, Y. Yuan, Y. Zhang, X. Meng, S. Jin, W. Li, J. Fan, *J. Phys. Chem. Lett.* **2020**, *11*, 9535.
- [145] H. Yin, Y. Xian, Y. Zhang, W. Chen, X. Wen, N.U. Rahman, Y. Long, B. Jia, J. Fan, W. Li, *Adv. Funct. Mater.* **2020**, *30*, 2002225.
- [146] G. Volonakis, A.A. Haghighirad, R.L. Milot, W.H. Sio, M.R. Filip, B. Wenger, M.B. Johnston, L.M. Herz, H.J. Snaith, F. Giustino, *J. Phys. Chem. Lett.* **2017**, *8*, 772.

- [147] F. Locardi, M. Cirignano, D. Baranov, Z. Dang, M. Prato, F. Drago, M. Ferretti, V. Pinchetti, M. Fanciulli, S. Brovelli, L. De Trizio, L. Manna, *J. Am. Chem. Soc.* **2018**, *140*, 12989.
- [148] W. Zhou, P. Han, X. Zhang, D. Zheng, S. Yang, Y. Yang, C. Luo, B. Yang, F. Hong, D. Wei, R. Lu, K. Han, *J. Phys. Chem. Lett.* **2020**, *11*, 6463.
- [149] H.A. Evans, L. Mao, R. Seshadri, A.K. Cheetham, *Annu. Rev. Mater. Res.* **2021**, *51*, 351.
- [150] J.B. Zhao, Z.H. Zhang, G.X. Li, M.H. Aldamasy, M. Li, A. Abate, *Adv. Energy Mater.* **2023**, *13*, 2204233.
- [151] J. Gong, M.W. Hao, Y.L. Zhang, M.Z. Liu, Y.Y. Zhou, *Angew. Chem. Int. Ed.* **2022**, *61*, e202112022.
- [152] C.M.M. Soe, C.C. Stoumpos, M. Kepenekian, B. Traoré, H. Tsai, W. Nie, B. Wang, C. Katan, R. Seshadri, A.D. Mohite, J. Even, T.J. Marks, M.G. Kanatzidis, *J. Am. Chem. Soc.* **2017**, *139*, 16297.
- [153] Q. Wei, H. Ren, J. Liu, Q. Liu, C. Wang, T.W. Lau, L. Zhou, T. Bian, Y. Zhou, P. Wang, Q. Lei, O.F. Mohammed, M. Li, J. Yin, *ACS Energy Lett.* **2023**, *8*, 4315.
- [154] P. Li, C. Liang, X.-L. Liu, F. Li, Y. Zhang, X.-T. Liu, H. Gu, X. Hu, G. Xing, X. Tao, Y. Song, *Adv. Mater.* **2019**, *31*, 1901966.
- [155] J. Sun, K. Wang, K. Ma, J.Y. Park, Z.-Y. Lin, B.M. Savoie, L. Dou, *J. Am. Chem. Soc.* **2023**, *145*, 20694.
- [156] C. Liang, H. Gu, Y. Xia, Z. Wang, X. Liu, J. Xia, S. Zuo, Y. Hu, X. Gao, W. Hui, L. Chao, T. Niu, M. Fang, H. Lu, H. Dong, H. Yu, S. Chen, X. Ran, L. Song, B. Li, J. Zhang, Y. Peng, G. Shao, J. Wang, Y. Chen, G. Xing, W. Huang, *Nat. Energy.* **2021**, *6*, 38.
- [157] Q. Cao, P. Li, W. Chen, S. Zang, L. Han, Y. Zhang, Y. Song, *Nano Today* **2022**, *43*, 101394.
- [158] X. Hong, T. Ishihara, A. Nurmikko, *Phys. Rev. B* **1992**, *45*, 6961.
- [159] V. D'innocenzo, G. Grancini, M.J. Alcocer, A.R.S. Kandada, S.D. Stranks, M.M. Lee, G. Lanzani, H.J. Snaith, A. Petrozza, *Nat. Commun.* **2014**, *5*, 3586.
- [160] K. Tanaka, T. Takahashi, T. Ban, T. Kondo, K. Uchida, N. Miura, *Solid State Commun.* **2003**, *127*, 619.
- [161] Y. Zhang, P. Wang, M.-C. Tang, D. Barrit, W. Ke, J. Liu, T. Luo, Y. Liu, T. Niu, D.-M. Smilgies, Z. Yang, Z. Liu, S. Jin, M.G. Kanatzidis, A. Amassian, S.F. Liu, K. Zhao, *J. Am. Chem. Soc.* **2019**, *141*, 2684.
- [162] M. Yuan, L.N. Quan, R. Comin, G. Walters, R. Sabatini, O. Voznyy, S. Hoogland, Y. Zhao, E.M. Beauregard, P. Kanjanaboos, Z. Lu, D.H. Kim, E.H. Sargent, *Nat. Nanotechnol.* **2016**, *11*, 872.
- [163] J. Liu, J. Leng, K. Wu, J. Zhang, S. Jin, *J. Am. Chem. Soc.* **2017**, *139*, 1432.
- [164] Q. Shang, Y. Wang, Y. Zhong, Y. Mi, L. Qin, Y. Zhao, X. Qiu, X. Liu, Q. Zhang, *J. Phys. Chem. Lett.* **2017**, *8*, 4431.
- [165] R.L. Milot, R.J. Sutton, G.E. Eperon, A.A. Haghighirad, J. Martinez Hardigree, L. Miranda, H.J. Snaith, M.B. Johnston, L.M. Herz, *Nano Lett.* **2016**, *16*, 7001.
- [166] J.V. Milić, *J. Mater. Chem. C* **2021**, *9*, 11428.
- [167] H. Tsai, W. Nie, J.-C. Blancon, C.C. Stoumpos, R. Asadpour, B. Harutyunyan, A.J. Neukirch, R. Verduzco, J.J. Crochet, S. Tretiak, L. Pedesseau, J. Even, M.A. Alam, G. Gupta, J. Lou, P.M. Ajayan, M.J. Bedzyk, M.G. Kanatzidis, A.D. Mohite, *Nature* **2016**, *536*, 312.

- [168] R. Quintero-Bermudez, A. Gold-Parker, A.H. Proppe, R. Munir, Z. Yang, S.O. Kelley, A. Amassian, M.F. Toney, E.H. Sargent, *Nat. Mater.* **2018**, *17*, 900.
- [169] Y. Lin, Y. Fang, J. Zhao, Y. Shao, S.J. Stuard, M.M. Nahid, H. Ade, Q. Wang, J.E. Shield, N. Zhou, A.M. Moran, J. Huang, *Nat. Commun.* **2019**, *10*, 1008.
- [170] X. Zhao, T. Liu, Y.-L. Loo, *Adv. Mater.* **2021**, *34*, 2105849.
- [171] G. Wu, R. Liang, Z. Zhang, M. Ge, G. Xing, G. Sun, *Small* **2021**, *17*, 2103514.
- [172] X. Zhao, T. Liu, A.B. Kaplan, C. Yao, Y.-L. Loo, *Nano Lett.* **2020**, *20*, 8880.
- [173] W.T.M. Van Gompel, R. Herckens, P.-H. Denis, M. Mertens, M.C. Gélvez-Rueda, K. Van Hecke, B. Ruttens, J. D'Haen, F.C. Grozema, L. Lutsen, D. Vanderzande, *J. Mater. Chem. C* **2020**, *8*, 7181.
- [174] C.M.M. Soe, W. Nie, C.C. Stoumpos, H. Tsai, J.-C. Blancon, F. Liu, J. Even, T.J. Marks, A.D. Mohite, M.G. Kanatzidis, *Adv. Energy Mater.* **2018**, *8*, 1700979.
- [175] X. Zhang, G. Wu, S. Yang, W. Fu, Z. Zhang, C. Chen, W. Liu, J. Yan, W. Yang, H. Chen, *Small* **2017**, *13*, 1700611.
- [176] W. Fu, J. Wang, L. Zuo, K. Gao, F. Liu, D.S. Ginger, A.K.Y. Jen, *ACS Energy Lett.* **2018**, *3*, 2086.
- [177] J. Qing, X.-K. Liu, M. Li, F. Liu, Z. Yuan, E. Tiukalova, Z. Yan, M. Duchamp, S. Chen, Y. Wang, S. Bai, J.-M. Liu, H.J. Snaith, C.-S. Lee, T.C. Sum, F. Gao, *Adv. Energy Mater.* **2018**, *8*, 1800185.
- [178] X. Zhang, G. Wu, W. Fu, M. Qin, W. Yang, J. Yan, Z. Zhang, X. Lu, H. Chen, *Adv. Energy Mater.* **2018**, *8*, 1702498.
- [179] P. Kovaricek, P. Nadazdy, E. Pluharova, A. Brunova, R. Subair, K. Vegso, V.L.P. Guerra, O. Volochanskyi, M. Kalbac, A. Krasnansky, P. Pandit, S.V. Roth, A. Hinderhofer, E. Majkova, M. Jergel, J. Tian, F. Schreiber, P. Siffalovic, *Adv. Funct. Mater.* **2021**, *31*, 2009007.
- [180] Y. Chen, Y. Sun, J. Peng, W. Zhang, X. Su, K. Zheng, T. Pullerits, Z. Liang, *Adv. Energy Mater.* **2017**, *7*, 1700162.
- [181] J.-W. Lee, S. Tan, S.I. Seok, Y. Yang, N.-G. Park, *Science* **2022**, *375*, eabj1186.
- [182] X. Li, J.M. Hoffman, M.G. Kanatzidis, *Chem. Rev.* **2021**, *121*, 2230.
- [183] M.D. Smith, H.I. Karunadasa, *Acc. Chem. Res.* **2018**, *51*, 619.
- [184] F.O. Saouma, C.C. Stoumpos, J. Wong, M.G. Kanatzidis, J.I. Jang, *Nat. Commun.* **2017**, *8*, 742.
- [185] I. Abdelwahab, G. Grinblat, K. Leng, Y. Li, X. Chi, A. Rusydi, S.A. Maier, K.P. Loh, *ACS Nano* **2018**, *12*, 644.
- [186] X. Chen, H. Lu, K. Wang, Y. Zhai, V. Lunin, P.C. Sercel, M.C. Beard, *J. Am. Chem. Soc.* **2021**, *143*, 19438.
- [187] K. Leng, L. Wang, Y. Shao, I. Abdelwahab, G. Grinblat, I. Verzhbitskiy, R.L. Li, Y.Q. Cai, X. Chi, W. Fu, P. Song, A. Rusydi, G. Eda, S.A. Maier, K.P. Loh, *Nat. Commun.* **2020**, *11*, 5483.
- [188] Q. Li, Y. Dong, G. Lv, T. Liu, D. Lu, N. Zheng, X. Dong, Z. Xu, Z. Xie, Y. Liu, *ACS Energy Lett.* **2021**, *6*, 2072.
- [189] B. Cheng, T.-Y. Li, P. Maity, P.-C. Wei, D. Nordlund, K.-T. Ho, D.-H. Lien, C.-H. Lin, R.-Z. Liang, X. Miao, I.A. Ajia, J. Yin, D. Sokaras, A. Javey, I.S. Roqan, O.F. Mohammed, J.-H. He, *Commun. Phys.* **2018**, *1*, 80.

- [190] D. Pariari, S. Mehta, S. Mandal, A. Mahata, T. Pramanik, S. Kamilya, A. Vidhan, T.N. Guru Row, P.K. Santra, S.K. Sarkar, F. De Angelis, A. Mondal, D.D. Sarma, *J. Am. Chem. Soc.* **2023**, *145*, 15896–15905.
- [191] J.M. Hoffman, C.D. Malliakas, S. Sidhik, I. Hadar, R. McClain, A.D. Mohite, M.G. Kanatzidis, *Chem. Sci.* **2020**, *11*, 12139.
- [192] J.V. Passarelli, C.M. Mauck, S.W. Winslow, C.F. Perkinson, J.C. Bard, H. Sai, K.W. Williams, A. Narayanan, D.J. Fairfield, M.P. Hendricks, W.A. Tisdale, S.I. Stupp, *Nat. Chem.* **2020**, *12*, 672.
- [193] M.C. Gélvez-Rueda, W.T.M. Van Gompel, R. Herckens, L. Lutsen, D. Vanderzande, F.C. Grozema, *J. Phys. Chem. Lett.* **2020**, *11*, 824.
- [194] X. Dong, M. Chen, R. Wang, Q. Ling, Z. Hu, H. Liu, Y. Xin, Y. Yang, J. Wang, Y. Liu, *Adv. Energy Mater.* **2023**, *13*, 2301006.
- [195] S. Shao, M.A. Loi, *Adv. Energy Mater.* **2021**, *11*, 2003907.
- [196] J.V. Passarelli, D.J. Fairfield, N.A. Sather, M.P. Hendricks, H. Sai, C.L. Stern, S.I. Stupp, *J. Am. Chem. Soc.* **2018**, *140*, 7313.
- [197] C.Z. Li, J. Yang, F.H. Su, J.J. Tan, Y. Luo, S.J. Ye, *Nat. Commun.* **2020**, *11*, 5481.
- [198] L. Mao, E.E. Morgan, A. Li, R.M. Kennard, M.J. Hong, Y. Liu, C.J. Dahlman, J.G. Labram, M.L. Chabinyk, R. Seshadri, *ACS Energy Lett.* **2022**, *7*, 2801.
- [199] Z. Shi, Z. Ni, J. Huang, *ACS Energy Lett.* **2022**, *7*, 984.
- [200] F. Zhang, D.H. Kim, H. Lu, J.-S. Park, B.W. Larson, J. Hu, L. Gao, C. Xiao, O.G. Reid, X. Chen, Q. Zhao, P.F. Ndione, J.J. Berry, W. You, A. Walsh, M.C. Beard, K. Zhu, *J. Am. Chem. Soc.* **2019**, *141*, 5972.
- [201] M.K. Jana, S.M. Janke, D.J. Dirkes, S. Dovletgeldi, C. Liu, X. Qin, K. Gundogdu, W. You, V. Blum, D.B. Mitzi, *J. Am. Chem. Soc.* **2019**, *141*, 7955.
- [202] L.-Y. Bi, Y.-Q. Hu, M.-Q. Li, T.-L. Hu, H.-L. Zhang, X.-T. Yin, W.-X. Que, M.S. Lassoued, Y.-Z. Zheng, *J. Mater. Chem. A* **2019**, *7*, 19662.
- [203] R. Hooijer, A. Weis, A. Biewald, M.T. Sirtl, J. Malburg, R. Holfueer, S. Thamm, A.A.Y. Amin, M. Righetto, A. Hartschuh, L.M. Herz, T. Bein, *Adv. Opt. Mater.* **2022**, *10*, 2200354.
- [204] P. Vishnoi, J.L. Zuo, X. Li, D.C. Binwal, K.E. Wyckoff, L. Mao, L. Kautzsch, G. Wu, S.D. Wilson, M.G. Kanatzidis, R. Seshadri, A.K. Cheetham, *J. Am. Chem. Soc.* **2022**, *144*, 6661.
- [205] M.L. Aubrey, A. Saldivar Valdes, M.R. Filip, B.A. Connor, K.P. Lindquist, J.B. Neaton, H.I. Karunadasa, *Nature* **2021**, *597*, 355.
- [206] B.A. Connor, R.W. Smaha, J. Li, A. Gold-Parker, A.J. Heyer, M.F. Toney, Y.S. Lee, H.I. Karunadasa, *Chem. Sci.* **2021**, *12*, 8689.

2 Characterization Techniques

This chapter briefly introduces the theoretical background of the main characterization techniques used in this work for analyzing the optoelectronic properties and device performance of low-dimensional perovskites.

2.1 X-ray Diffraction (XRD)

X-ray diffraction (XRD) is a common non-destructive analytical technique to identify the structure of crystalline substances, including inorganic, organic and inorganic-organic hybrid materials. Operating on the fundamental principle of Bragg's law (equation 2.1, where n is the order of diffraction, λ is the wavelength of the X-rays, d is the crystal lattice spacing, and θ is the incident angle.^[1]

), this technique involves the diffraction of X-rays by crystal planes, resulting in a diffraction pattern that can be used to analyze the crystal structure of a material. The Bragg equation can be described as follows,

$$n \lambda = 2 d \sin(\theta) \quad (2.1)$$

where n is the order of diffraction, λ is the wavelength of the X-rays, d is the crystal lattice spacing, and θ is the incident angle.^[1]

The X-rays are usually generated in an X-ray tube, consisting of a cathode filament (normally tungsten) and an anode target (usually molybdenum (Mo), copper (Cu), iron (Fe) or chromium (Cr)). These components are enclosed in a vacuum chamber. Electrons are produced through the process of thermionic emission, achieved by heating the cathode filament. Subsequently, these electrons are accelerated towards the anode material when a high voltage is applied. The monochromatic radiation can be attained through filtration, a process that involves selectively allowing certain wavelengths of X-rays to pass while blocking others. This filtration step enhances the quality and specificity of the X-ray beam, providing a more controlled and refined source for analysis in X-ray diffraction

experiments. The wavelength (λ) of X-ray can be adjusted by selecting different anode materials. Common choices include 0.7 Å (Mo- K_α), 1.54 Å (Cu- K_α), 2 Å (Fe- K_α) and 2.3 Å (Cr- K_α). These values are approximately within the same order of magnitude as the interplanar spacings of the crystal lattice, allowing for optimal interaction with the sample's structure. Then, the incident electromagnetic radiation, arriving at different angles (θ), interacts with the electrons of the atoms within the sample. This interaction leads to the formation of a diffraction pattern when the Bragg condition is fulfilled.^[2] The diffraction pattern serves as a distinctive signature that provides valuable information about the crystal structure of the material under examination.

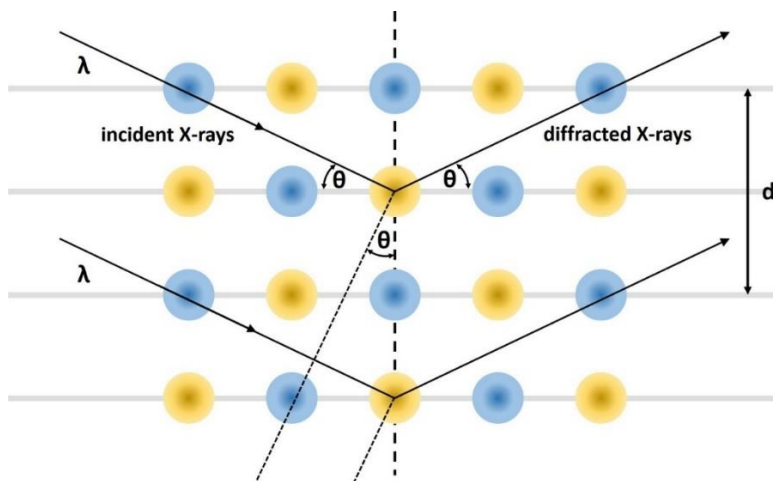


Figure 2.1: Schematic illustration of Bragg's law.

The XRD experiment can be conducted in either transmission mode (Debye-Scherrer geometry) or in reflection mode (Bragg-Brentano geometry). In transmission mode, a STOE STADI P diffractometer is used, featuring a Ge(111) single crystal monochromator for either Cu- K_α ($\lambda = 1.54$ Å) or Mo- K_α ($\lambda = 0.71$ Å) radiation and a solid-state strip detector (DECTRIS MYTHEN 1K). The powder sample is placed in a transparent sample holder (such as polymer foil or glass tube) and can be rotated during the measurement. The X-ray beam is focused onto the sample, while the detector moves in a circle around the sample position to detect reflections within the 2θ range. In reflection mode, a BRUKER D8 DISCOVER diffractometer equipped with Ni-filtered Cu- K_α radiation and a position-sensitive detector (LynxEye) is used. The sample, whether in powder or thin film form, is placed on a substrate such as glass or silicon wafer. In reflection mode, both the X-ray source and the detector are moved in synchronized steps, scanning all angles θ between them and the sample surface. This method

ensures that only reflections caused by crystallographic planes oriented parallel to the substrate are detected.

2.2 Grazing Incidence Wide Angle X-Ray Scattering (GIWAXS)

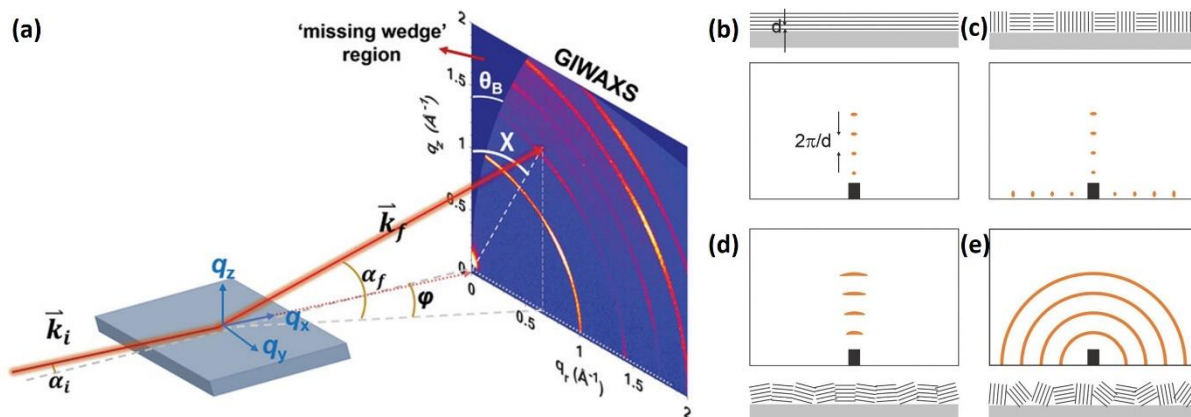


Figure 2.2: (a) Scattering geometry of GIWAXS. The incident beam of the wave vector \vec{k}_i hits the sample with a shallow incident angle of α_i , producing a scattered wave \vec{k}_f with an outgoing angle α_f with respect to the sample surface. The outgoing plane has an azimuthal angle φ with respect to the incident beam plane. The direct beam points to the origin of the reciprocal space. The polar angle χ is the angle between the q_z axis and the projection of the scattering wave vector \vec{q} on the q_x - q_z plane, while the polar angle θ_B corresponds to the minimum detectable χ . Reproduced with permission.^[3] Copyright 2021, Wiley-VCH. Sketch of film crystallinity and corresponding 2D GIWAXS data in case of (b) vertical lamellar stacking, (c) crystallites with vertical and horizontal orientation, (d) oriented domains and (e) full rotational disorder of crystallites. The GISAXS signal is blocked by a beam stop (black box). Reproduced with permission.^[4] Copyright 2014, Wiley-VCH.

Grazing incidence wide angle X-ray scattering (GIWAXS) is an advanced X-ray scattering technology designed to determine the crystal structure and the orientation of the crystalline regions with respect to the substrate. As shown in Figure 2.2a, the geometry of GIWAXS is similar to the aforementioned reflection mode. However, in GIWAXS, a distinctive feature is that the position of the X-ray source stays constant at a very low incident angle ($< 1^\circ$) while only the detector is moved by 2θ (or a 2D detector is used). Indeed, due to the low incident angles employed in GIWAXS, the X-ray radiation has a relatively longer footprint and interacts with a rather higher volume of film material, resulting in a stronger signal. Another advantage of the GIWAXS technique is the use of a 2D detector. Compared to point-like or 1D detectors, a 2D detector allows simultaneous signal collection

in both the in-plane (q_{xy}) and out-of-plane (q_z) directions, leading to a 2D GIWAXS pattern (as illustrated in Figure 2.2). If the crystalline film is highly oriented with crystal planes parallel to the substrate, well-pronounced Bragg peaks (dots) appear on the detector (Figure 2.2b). If both parallel and perpendicular orientations exist in the film, Bragg peaks (dots) appear both in the q_z and q_{xy} directions (Figure 2.2c). In scenarios where the film is less oriented, with domains exhibiting an angular distribution along the horizontal direction, Bragg peaks appear broad along the q_z direction (partial rings, Figure 2.2d). For randomly oriented films, Debye-Scherrer rings with a homogeneous intensity distribution can manifest on the 2D detector (Figure 2.2e).^[4] As shown in Figure 2.2a, an inaccessible region (missing wedge) exists in the GIWAXS pattern due to the curvature of the Ewald sphere. Thus, diffraction signals may be hidden in this inaccessible region.

2.3 Inductively Coupled Plasma-Optical Emission Spectroscopy (ICP-OES)

Inductively coupled plasma optical emission spectroscopy (ICP-OES) is an analytical technique employed for both qualitative and quantitative determination of elements within a sample. The process typically involves dissolving the sample in a strong acid or a mixture of acids. Subsequently, the solution is injected into a radiofrequency-induced argon plasma in the form of a fine aerosol, achieved by using a nebulizer. Upon injection into the plasma, the sample aerosol undergoes rapid drying and vaporization, with the atoms being energized by collisional excitation at high temperatures. As these energized atoms return to a lower energy level, they emit photons of characteristic energies. These emitted photons, specific to each element, are recorded by a wavelength-selective device. The detected wavelengths are unique to each element, and the intensity of the emitted radiation corresponds to the concentration of the respective element within the sample.^[5]

2.4 Electron Microscopy

The electron microscope operates on a fundamentally different principle compared to optical microscopes. While the optical microscope uses visible light (photons) to magnify images, the electron microscope uses a focused beam of electrons and applies their wave-like characteristics to magnify the sample image, which makes it a powerful tool for studying the micro- and nanostructured morphology of materials.

The key advantage of electron microscopy lies in the fact that the wavelength of electrons in the focused beam is significantly smaller than that of visible light. This allows the electron microscope to

achieve much higher resolution (typically around 0.1 nm in practice) than what is attainable with a classical optical microscope (usually around 200 nm), which can be explained by the Abbe resolution limit (equation 2.2).

$$d = \frac{\lambda}{2NA} \quad (2.2)$$

The minimum resolvable distance d depends on the numerical aperture NA of the optical system and on the wavelength λ of the photons or electrons. The wavelength of the electron beam is determined by equation 2.3,

$$\lambda = \frac{h}{\sqrt{2m_e E_{acc}}} \quad (2.3)$$

where h is Planck's constant, m_e is the electron mass and E_{acc} is the acceleration energy. The ability to accelerate the electron beam in electron microscopes over a range from 1 kV to 300 kV or higher enables imaging at the nanoscale, which is based on the equations 2.2 and 2.3. Additionally, the electron beam can interact with the specimen in various ways, producing different signals as shown in Figure 2.3. These interactions offer a great deal of information, which can be obtained through techniques such as:

- 1) Scanning Electron Microscopy (SEM) and Transmission Electron Microscopy (TEM): These techniques involve the study of the scattering or diffraction of the electron beam as it interacts with the specimen, providing detailed imaging at the micro- and nanoscale.
- 2) Electron Energy Loss Spectroscopy (EELS): EELS is a spectroscopic technique that analyzes the energy lost by electrons as they interact with the specimen, offering insights into the material's composition and electronic structure.
- 3) Energy-Dispersive X-ray Spectroscopy (EDS) or Wavelength-Dispersive X-ray Spectroscopy (WDS): These spectroscopic techniques involve the detection of X-rays or electrons produced by the excitation of atoms in the specimen. EDS and WDS are commonly used in electron microprobe analysis and Auger electron spectroscopy, providing both imaging and elemental analysis capabilities.

These diverse methods allow researchers to obtain a comprehensive understanding of the morphology, composition and electronic structure of materials at the atomic and nanoscale levels.

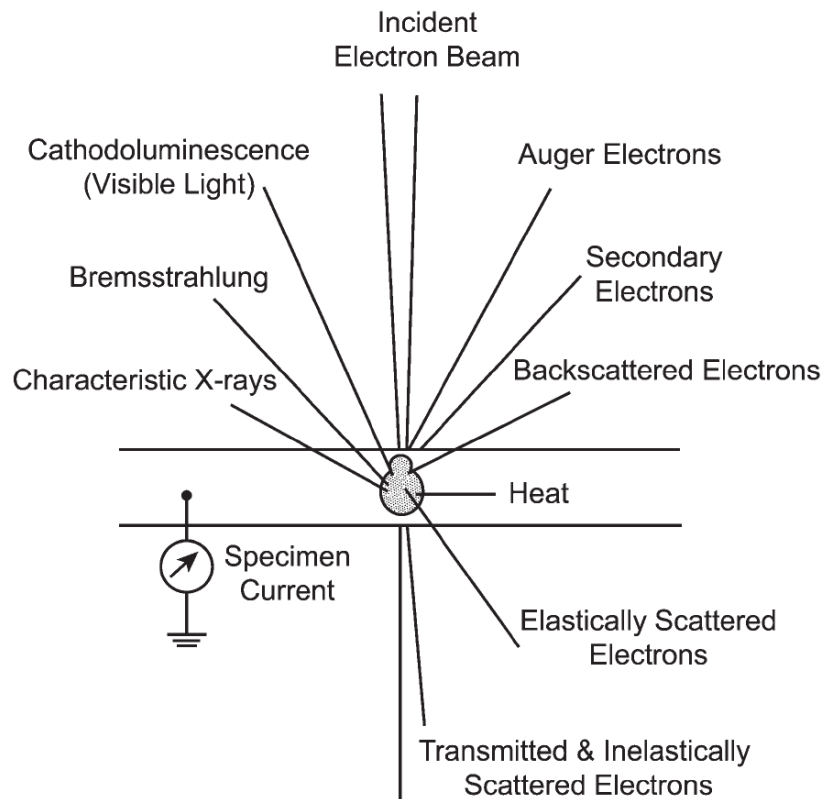


Figure 2.3: Interactions of the electron beam with matter in electron microscopy. Reproduced with permission.^[6] Copyright 2005, Wiley-VCH.

2.4.1 Scanning Electron Microscopy (SEM)

SEM is a powerful tool for probing surface morphology and topography at the nanometer scale. In a typical SEM setup (as illustrated in Figure 2.4a), an electron beam is emitted and accelerated by an electron gun within a high vacuum environment. The energy of the electron beam typically ranges from 1 to 40 keV. The beam is then focused by condenser lenses and an objective lens, achieving a diameter as small as a few nanometers. Upon reaching the sample surface, the electron beam initiates multiple interactions, as depicted in Figure 2.3. Here, the secondary electrons ($E < 50$ eV) or the backscattered electrons ($E > 50$ eV) carry the main information about the morphology of the samples. These electrons are detected and transformed into images that reveal topological contrast and chemical composition. In this thesis, all the samples were measured by using an FEI Helios G3 UC instrument equipped with an additional concentric backscattered electron detector.

2.4.2 Energy Dispersive X-ray Spectroscopy (EDX)

EDX, when coupled with SEM, is commonly used for elemental mapping, allowing for spatial resolution of the elemental composition with an SEM. EDX uses characteristic X-rays generated by inelastic scattering of the incident electron beam on the sample (Figure 2.3). In detail, the incident electron beam has the ability to displace the electrons in the inner atomic shell, creating vacancies that can be filled by electrons from outer shell at higher energy levels. This process leads to the emission of characteristic X-rays with distinct energies corresponding to specific elements. The EDX detector then captures these X-rays, and the data are processed by software to generate a spectrum that reveals both the composition of the sample and the spatial distribution of its elemental components.

2.4.3 Transmission Electron Microscopy (TEM)

TEM uses transmitted electrons (as shown in Figure 2.3) to obtain information about the internal structure of a sample. To facilitate electron transmission, the sample must be thin enough (typically less than 100 nm) to allow the electron beam to penetrate through the sample. In addition, the electron beam is accelerated to a higher energy range compared to that for SEM, typically 60 to 300 kV. It is then focused by electromagnetic condenser lenses. As shown in Figure 2.4b, the transmitted electrons are displayed on a fluorescent screen or recorded with a CCD camera, transforming into images that provide insights into the morphology and crystal structure of the sample.

High-Resolution Transmission Electron Microscopy (HRTEM) is a specialized mode that can achieve a minimum resolvable distance of less than 1 Å, owing to the electron's wavelength, which can be less than 5 pm. In HRTEM, the mode can be switched from imaging to diffraction by altering the optical path. This allows for the generation of a diffraction pattern from the sample, aiding in the identification of its crystal phase.

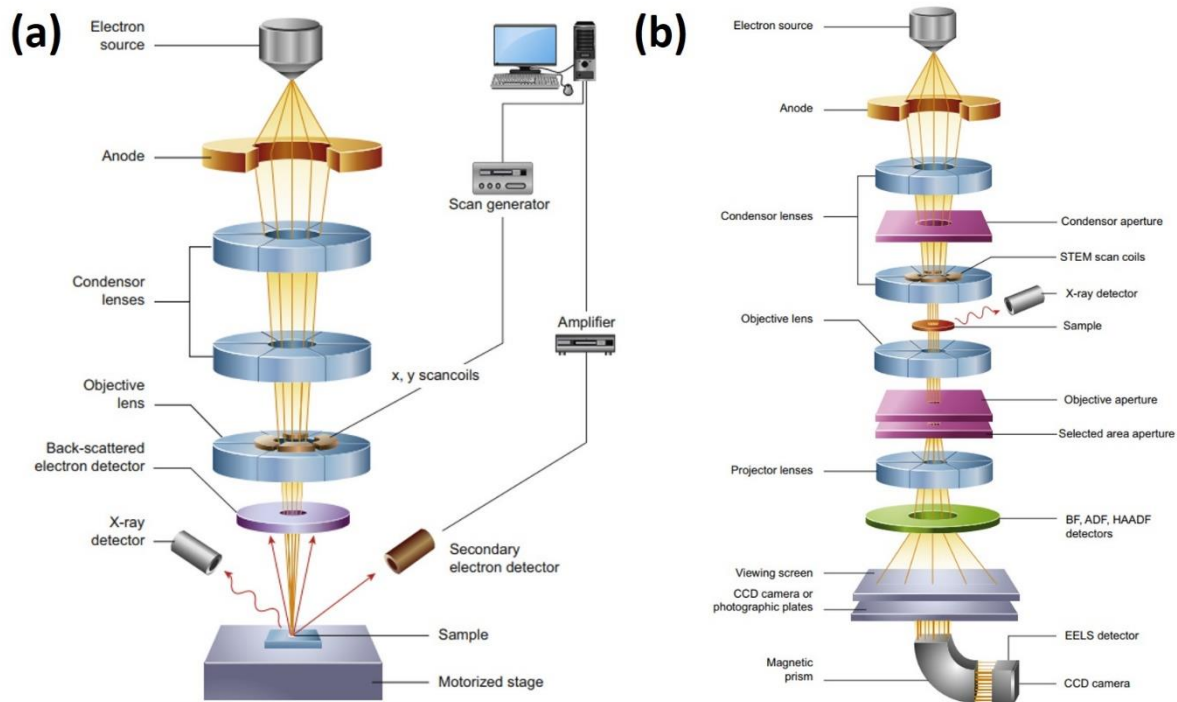


Figure 2.4: Schematic representation of the microscope column of (a) scanning electron microscope and (b) transmission electron microscopy. Reproduced with permission.^[7] Copyright 2016, Elsevier Ltd.

2.5 Atomic Force Microscopy (AFM)

Atomic force microscopy (AFM) is a high-resolution imaging technique used for studying the surface morphology and properties of materials at the nanoscale. However, it is rather different from other microscopes like an optical or electron microscope, as it does not focus photon or electron onto a sample surface to obtain an image. Instead, AFM builds up a map of the height (or other properties, such as phase properties) of the sample surface by scanning a sharp tip (usually at the end of a cantilever) very close to the surface of a sample, as shown in Figure 2.5.^[8] The attractive or repulsive forces between the tip and the sample surface are measured based on the deflection of the cantilever. This deflection is monitored by a laser beam, and any shift in the reflected laser beam is detected by an array of photodiodes. By recording the (x, y, z) position of the tip with respect to the sample and the corresponding force, the surface topography and properties of the sample surface can be obtained.

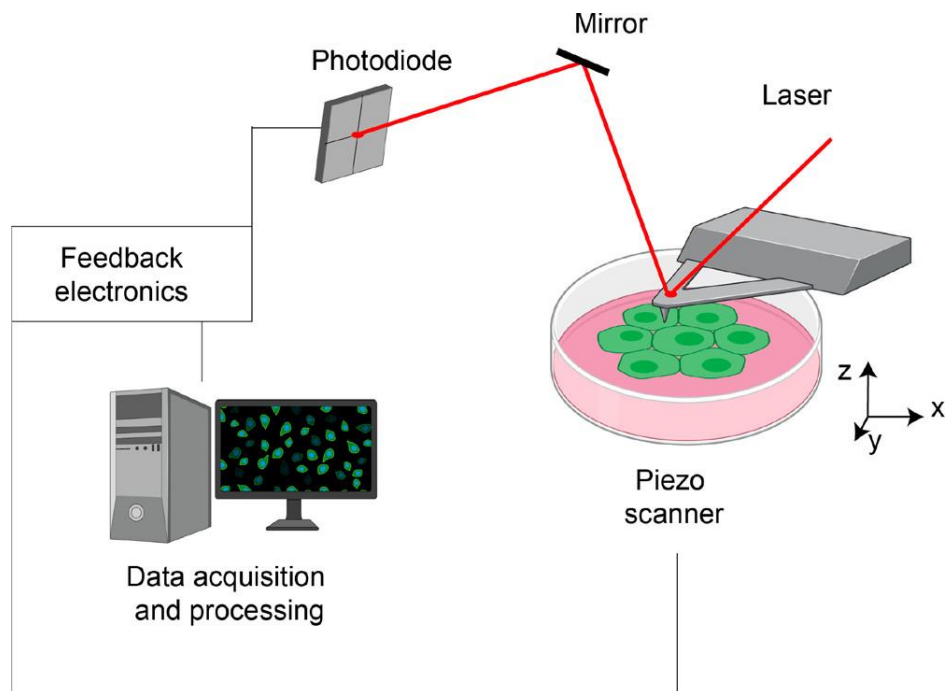


Figure 2.5: Schematic representation of the operational principle of an atomic force microscope. Reproduced with permission.^[9] Copyright 2021, American Chemical Society.

2.6 Photoelectron Spectroscopy (PES)

Photoelectron spectroscopy (PES) is a surface-sensitive tool employed to determine the relative energies of electrons in atoms and molecules under ultrahigh vacuum conditions, revealing the elemental composition and electronic states of the surface or near surface region of a sample. PES is based on the principle of the photoelectric effect, where the sample is ionized by high-energy radiation such as UV or X-rays. The kinetic energy (KE) of the ejected electrons (photoelectrons) is then recorded by an energy analyzer. The number of photoelectrons at various KE can be counted by the detector. The energy required to liberate electrons from their bound state in the atomic shell is known as the electron binding energy (E_{BE}), which can be calculated by equation 2.4,

$$E_{BE} = h\nu - KE \quad (2.4)$$

where $h\nu$ is the energy of the radiation. Plots of photoelectron count versus E_{BE} (eV) are obtained from PES experiments, where the E_{BE} of a peak represents the energy required to liberate an electron from the subshell, and the intensity of the peak indicates the relative number of electrons in the subshell.

Depending on the energy of the radiation used, PES can be categorized into X-ray photoelectron spectroscopy (XPS) and ultraviolet photoelectron spectroscopy (UPS).

In XPS, soft X-rays (with energy in the range of 200 eV to 2 keV) can be used to obtain information about the elemental composition and the corresponding oxidation states, through their distinctive E_{BE} values. Moreover, the E_{BE} peak intensities in XPS are proportional to the atomic concentration, facilitating the quantification of the relative amount of elements in the sample.

In UPS, UV radiation with a relatively lower energy (in the range of 10 to 45 eV) is used to determine the ionization energy of the electrons in the outermost shell (valence electrons). Since these electrons are more shielded and farther from the nucleus on average, they have the lowest E_{BE} among all the electrons in an atom. Consequently, the valence band energy of the probed sample can be determined.^[10]

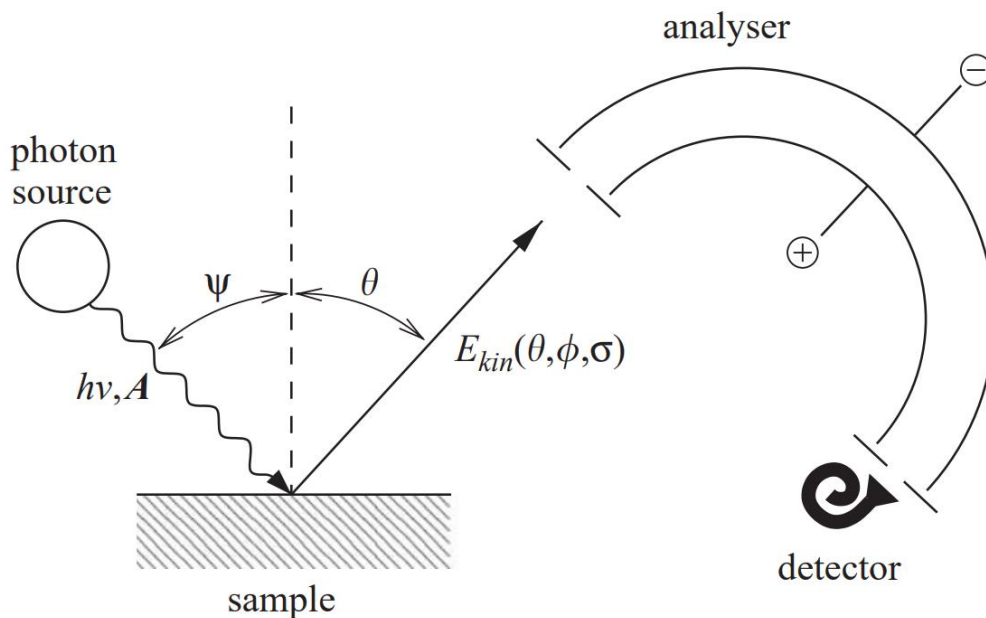


Figure 2.6: Schematic representation of a typical photoelectron spectrometer. Reproduced with permission.^[11] Copyright 2005, Elsevier.

2.7 Nuclear Magnetic Resonance Spectroscopy (NMR)

Nuclear magnetic resonance (NMR) spectroscopy is a powerful analytical technique that permits, among many other features, the determination of molecular structures. When certain nuclei with an

odd number of protons or neutrons are placed in an external magnetic field, they behave like tiny magnets leading to the splitting of spin states, a phenomenon known as Zeeman effect. Upon exposure to a radiofrequency (RF) pulse, these nuclei absorb energy, resulting in spectroscopic information.

In isolated atomic nuclei, the same type of nucleus in the same strength of an external magnetic field is sensitive to only a specific frequency of RF field. However, when these atomic nuclei are part of molecular structures, various factors such as the distribution of electron clouds within the molecule can lead to variation in the actual strength of the external magnetic field experienced by each nucleus. Moreover, atomic nuclei at different positions within the molecular structure may perceive different intensities of the additional magnetic field. The influence of the electron cloud on the external magnetic field intensity in the molecule results in different positions of atomic nuclei being sensitive to different frequencies of the RF field, which can be used to resolve molecular structures. The distribution of chemical bonds and electron clouds near atomic nuclei is referred to as the chemical environment of that nucleus. Changes in the frequency position of NMR signals due to the influence of the chemical environment are termed chemical shift. The chemical shift provides valuable information about the local environment of specific nuclei within a molecule, aiding in the elucidation of molecular structures.

In NMR spectra, the intensity of the NMR signal is also an important factor. Atomic nuclei in the same chemical environment in the NMR spectrum appear as the same signal peak. Analyzing the intensity of these signal peaks provides information about the quantity of these atomic nuclei, offering crucial information for the analysis of molecular structures. The characterization of signal peak intensity is achieved through the integration of the area under the curve of the signal peak. This information is particularly important for ^1H -NMR spectra, where the intensity of peaks corresponds to the number of hydrogen nuclei. However, ^{13}C -NMR spectroscopy has inferior receptivity compared to ^1H -NMR spectroscopy due to the lower abundance of ^{13}C compared to ^1H . In such cases, the focus is often on the chemical shifts and coupling patterns to derive structural information.

2.8 Ultraviolet-Visible Spectroscopy (UV-Vis)

Ultraviolet-visible (UV-Vis) spectroscopy is an effective technique used to measure the absorption or transmission of discrete wavelengths of UV, visible or near-infrared light by a sample (liquid or solid) in comparison to a reference or blank sample. When the energy of the incident photons is sufficient

to excite an electron from the valence band to the conduction band of the sample, absorption of photons occurs, which can be described by the Lambert-Beer law (equation 2.5),

$$A = -\log_{10}\left(\frac{I}{I_0}\right) = \varepsilon \times c \times d \quad (2.5)$$

where A is absorbance, I is the measured intensity of transmitted light, I_0 is the intensity of incident light, ε is the extinction coefficient of the sample, c is the concentration of the absorbing species and d is the path length of light travelling through the sample.

The nature and energy of the optical bandgap are of great importance in semiconductors. The Tauc plot method is commonly employed to approximate the optical bandgap of a semiconductor based on its absorption spectrum.^[12] The Tauc plot is typically presented as equation 2.6,

$$(\alpha h\nu)^{\frac{1}{\gamma}} = B(h\nu - E_g) \quad (2.6)$$

where α is the absorption coefficient, $h\nu$ is the photon energy, B is a constant, E_g is the band gap energy. The γ factor accounts for the nature of the electron transition, where $\gamma = 0.5$ for direct allowed transition, $\gamma = 1.5$ for direct forbidden transition, $\gamma = 2.0$ for indirect allowed transition and $\gamma = 3.0$ for indirect forbidden transition.

2.9 Photoluminescence Spectroscopy (PL)

Photoluminescence (PL) spectroscopy is a non-destructive and contactless optical method used for the characterization of the electronic structure and dynamics of materials. PL measurements are based on different types of luminescence such as fluorescence. When a semiconductor absorbs photons, electrons are excited from the valence band to the conduction band, followed by relaxation to a lower energy state, leading to the emission of photons. These emitted photons can be collected by a photodiode array, and the PL spectrum is recorded as a plot of the intensity of emitted photons as a function of the emitted wavelength. However, the relaxation process can occur through either radiative or non-radiative pathways. The radiative process typically involves band-to-band recombination, resulting in the emission of light. In reality, imperfections such as defects or disorder may be present due to variations in chemical composition, leading to trap states in the band structures. If trap-assisted recombination processes are non-radiative, the surplus energy is dissipated *via* vibrations (phonons) in the solid. By measuring steady-state PL spectra, information

about the energy of the bandgap, charge transfer efficiency and the recombination process can be obtained.

Extending this technique by measuring over time, time-resolved PL (TRPL) methods, such as time-correlated single photon counting (TCSPC), are often used to investigate the recombination and decay processes of photo-excited charge carriers. In TRPL experiments, a short laser pulse is used to excite the material, often generating excitons (bound electron-hole pairs). The subsequent emission of photons is detected and monitored over time using a sensitive detector with a high temporal resolution, typically at the femto-, pico- or nanosecond timescale. The decay of the photoluminescence signal is then analyzed by fitting the decay curve from the TCSPC method with an appropriate function, usually following an exponential decay. This analysis provides valuable information about carrier lifetimes and recombination dynamics. By studying how quickly excited carriers recombine or decay to their ground state, we can gain insights into the material's electronic properties, such as trap states, defects, and the efficiency of charge carrier transport in semiconductors. Time-resolved techniques enhance our understanding of the temporal aspects of electronic processes in materials, offering a more comprehensive characterization of their behavior.

2.10 Current-Voltage (J - V) Measurements

The performance of solar cells is usually assessed by measuring the current-voltage (J - V) curves under both illumination and dark conditions. To characterize the working performance of photovoltaic devices, a solar simulator is normally used as the source of illumination. The simulator can provide a standard air mass 1.5 global (AM1.5G) spectrum with an incident power of 100 mW cm^{-2} . In a typical measurement, the device is illuminated, and the J - V curve is obtained by scanning with an applied external voltage in a certain range with a certain speed while recording the corresponding current density of the device. The current density is determined by the absolute current measured and the overall area of the solar cell. Figure 2.7 shows a typical J - V curve and its characteristic photovoltaic parameters, which will be discussed below.

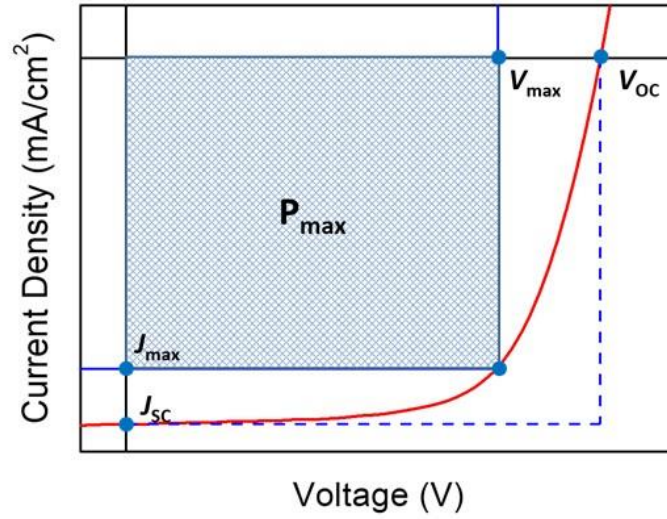


Figure 2.7: A typical J-V curve and performance parameters of solar cells.

The most important parameter of the device performance is power conversion efficiency (PCE), which can be described as how efficiently the power of incident light (P_{in}) can be converted into electric power (equation 2.7),

$$PCE = \frac{P_{max}}{P_{in}} = \frac{J_{max} \times V_{max}}{P_{in}} = \frac{V_{oc} \times J_{sc} \times FF}{P_{in}} \quad (2.7)$$

where P_{max} is the maximum power that a solar cell generates, which is given by the product between current density at maximum power point (J_{max}) and voltage at maximum power point (V_{max}). The current at $V = 0$ (short-circuit) is noted J_{sc} , while the voltage at $J = 0$ (open-circuit) is noted V_{oc} . The fill factor (FF) can be defined as the ratio of P_{max} of the solar cell and the product of J_{sc} and V_{oc} (equation 2.8), which is a key parameter to evaluate the performance of device, regarding how well it can convert solar energy into output power.

$$FF = \frac{P_{max}}{V_{oc} \times J_{sc}} = \frac{J_{max} \times V_{max}}{V_{oc} \times J_{sc}} \quad (2.8)$$

Generally, the FF does not have a physical meaning, but its value is a reflection of all carrier dynamic processes within the device, such as the diffusion and separation of photo-generated excitons, as well as the transit and collecting efficiency of free charge carriers.^[13] Besides, FF is also related to bulk and

interfacial non-radiative recombination, deriving from ubiquitous trap-assisted recombination processes.^[14]

The PCE of solar cells is determined, among other factors, by the recombination process of photo-excited charge carriers. The charge carriers can recombine radiatively or non-radiatively, where the energy of recombined excess electrons and holes is eventually transferred as either a photon or phonon, respectively. The V_{OC} of a solar cell can be affected by various factors but is mainly determined by the bandgap of the active material. According to the Shockley–Queisser limit theory, the achievable value of V_{OC} is determined by the difference between quasi-Fermi levels of electrons (E_{Fn}) and holes (E_{Fp}), shown in equation 2.9,

$$V_{OC} = \frac{E_{Fn} - E_{Fp}}{q} \quad (2.9)$$

where q is the elementary charge. Besides, the non-radiative recombination also plays a significant role in limiting the V_{OC} . Non-radiative recombination can occur at various sites within the device, including intragap recombination centers (defects and traps) within a single absorber (e.g., perovskite) layer and heterojunctions between the perovskite layer and the adjacent transport layers.^[15]

The J_{SC} is mainly affected by the efficiency of charge carrier generation and extraction. This efficiency depends on several factors, including the incident light intensity, the material's absorption and reflection characteristics, and the quality of the active layer and the interfaces within the solar cell.

2.11 Quantum Efficiency (QE)

Quantum efficiency (QE) is strongly related with photo-generated current and can be divided into external quantum efficiency (EQE) and internal quantum efficiency (IQE), where the former describes the incident photon to charge carrier conversion efficiency and the latter describes the absorbed photon to charge carrier conversion efficiency for each wavelength. First of all, the spectral responsivity (SR) has to be measured before calculating the EQE value (equation 2.10), which can be accomplished by measuring the current density of a device at short circuit conditions over different wavelengths (J_{sa}) and then comparing to a reference diode current density (J_{ref}).

$$SR(\lambda) = \frac{J_{sa}(\lambda)}{J_{ref}(\lambda)} \quad (2.10)$$

The EQE can be calculated by equation 2.11,

$$EQE(\lambda) = \frac{hc}{q\lambda} \times SR(\lambda) \quad (2.11)$$

where h is Planck's constant, c is the light speed, q is elementary charge, and λ is the wavelength.^[16]

The IQE can be calculated by equation 2.12, when only considering reflectance (R) without other loss mechanisms such as scattering.

$$IQE(\lambda) = \frac{EQE(\lambda)}{1 - R(\lambda)} \quad (2.12)$$

Furthermore, the integrated photocurrent density (J_{int}) can be derived from EQE, which is obtained by integration of the EQE curve and the photon flux (ϕ) at one sun (equation 2.13).

$$J_{int} = q \int_0^{\infty} \phi(\lambda)EQE(\lambda)d\lambda \quad (2.13)$$

The J_{int} can be used to justify and understand J_{sc} values obtained from J - V measurements of the solar cells.

2.12 References

- [1] B.E. Warren, Courier Corporation**1990**.
- [2] W.L. Bragg, *Proceedings of the Royal Society of London. Series A, Containing Papers of a Mathematical Physical Character* **1914**, 89, 468.
- [3] M. Qin, P.F. Chan, X. Lu, *Adv. Mater.* **2021**, 33, 2105290.
- [4] P. Müller-Buschbaum, *Adv. Mater.* **2014**, 26, 7692.
- [5] M. Thompson, Springer Science & Business Media**2012**.
- [6] J. D'amore, S. Al-Abed, K. Scheckel, J. Ryan, *J. Environ. Qual.* **2005**, 34, 1707.
- [7] B.J. Inkson, in: G. Hübschen, I. Altpeter, R. Tschuncky, H.-G. Herrmann (Eds.) *Materials Characterization Using Nondestructive Evaluation (NDE) Methods*, Woodhead Publishing**2016**, pp. 17.
- [8] P. Eaton, P. West, Oxford university press**2010**.
- [9] D.J. Müller, A.C. Dumitru, C. Lo Giudice, H.E. Gaub, P. Hinterdorfer, G. Hummer, J.J. De Yoreo, Y.F. Dufrêne, D. Alsteens, *Chem. Rev.* **2021**, 121, 11701.
- [10] S. Béchu, M. Ralaiarisoa, A. Etcheberry, P. Schulz, *Adv. Energy Mater.* **2020**, 10, 1904007.
- [11] S. Hüfner, S. Schmidt, F. Reinert, *Nucl. Instrum. Methods Phys. Res.* **2005**, 547, 8.
- [12] J. Tauc, R. Grigorovici, A. Vancu, *Phys. Status Solidi B* **1966**, 15, 627.
- [13] J. Huang, Y. Yuan, Y. Shao, Y. Yan, *Nat. Rev. Mater.* **2017**, 2, 17042.
- [14] L. Wu, H. Zang, Y.-C. Hsiao, X. Zhang, B. Hu, *Appl. Phys. Lett.* **2014**, 104.
- [15] Z. Guo, A.K. Jena, G. Kim, T. Miyasaka, *Energy Environ. Sci.* **2022**, 15, 3171.
- [16] W. Ananda, 2017 15th International Conference on Quality in Research (QiR) : International Symposium on Electrical and Computer Engineering, **2017**, pp. 450.

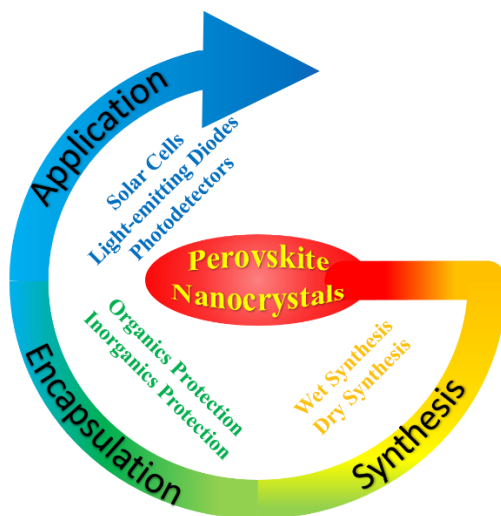
3 Review Article: Perovskite Nanocrystals: Synthesis, Stability and Optoelectronic Applications

This chapter is based on the following publication:

Shizhe Wang*, Amir Abbas Yousefi Amin, Linzhong Wu, Muhan Cao, Qiao Zhang*, and Tayebbeh Ameri*, *Small Struct.* **2021**, 2, 2000124.

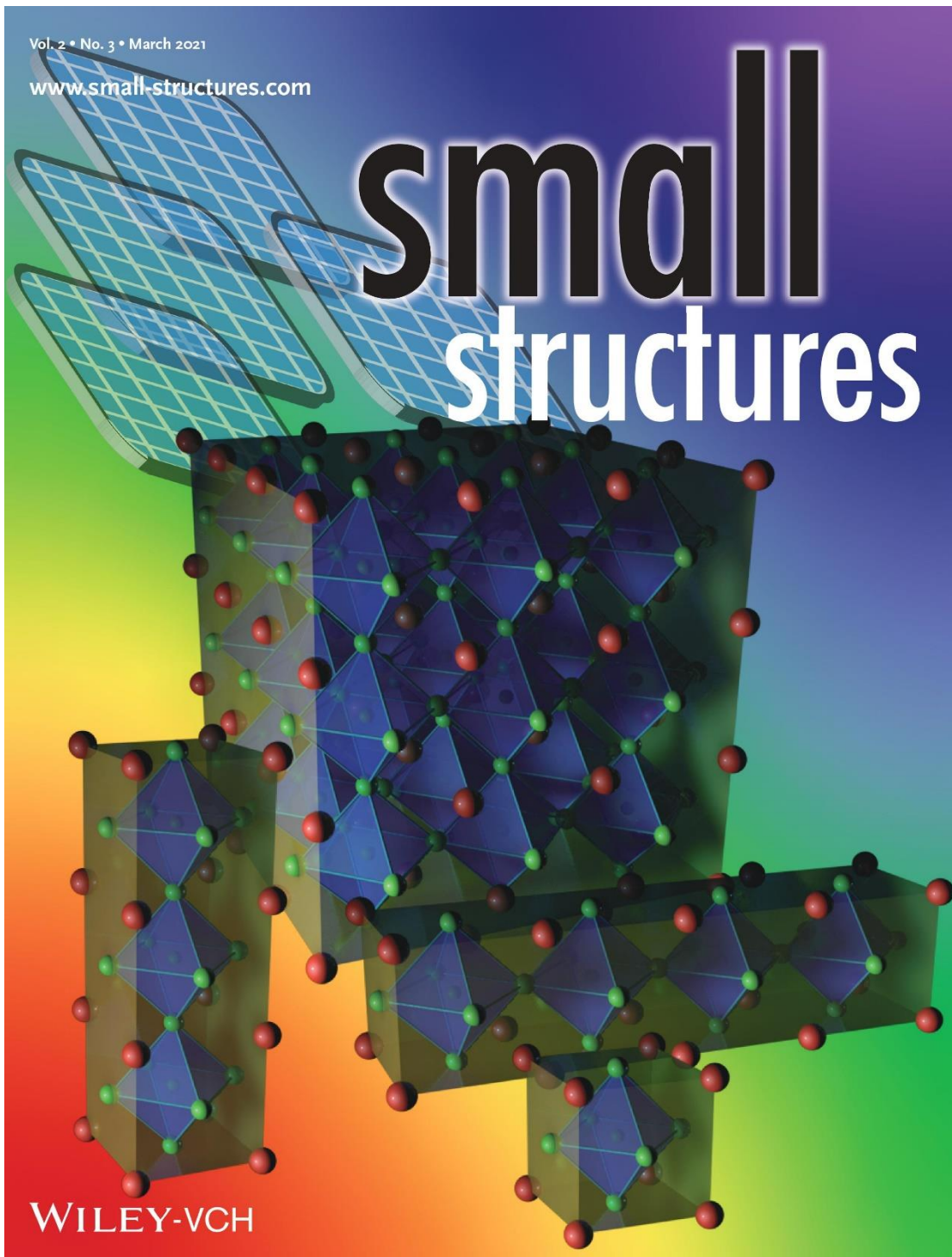
Reprinted from *Small Struct.* **2021**, 2, 2000124., with the permission of John Wiley and Sons Publishing.

Link to the published article: <https://onlinelibrary.wiley.com/doi/full/10.1002/sstr.202000124>



This review was structured by S.W.. The coordination work with Prof. Dr. Qiao Zhang's group was conducted by S.W.. S.W. wrote the initial draft of the manuscript and edited until the final version.

Keywords: Perovskite nanocrystals, stability, encapsulation of perovskite nanocrystals, perovskite solar cells, light-emitting diodes, photodetectors



Back cover image in *Small Structures* designed by Shizhe Wang.

3.1 Abstract

Metal halide perovskite (MHP) materials, named as the game changers, have attracted researchers' attention worldwide for over a decade. Among them, nanometer-scale perovskite nanocrystals (PNCs) have exhibited attractive photophysical properties, such as tunable bandgaps, narrow emission, strong light-absorption coefficients, and high defect tolerance, because they combined the excellent optoelectronic properties of bulk perovskite materials with strong quantum confinement effects of the nanoscale. These materials possess a great potential to be applied in the optoelectronic devices. For commercial applications in devices like solar cells (SCs), light-emitting diodes (LEDs), and photodetectors (PDs), the stability of PNCs against ambient atmosphere like oxygen and moisture, as well as light and high temperature is crucial. In this review, the synthetic methods and stability issues of the PNCs are introduced first, followed by the introduction of the strategies for improving their stability by encapsulation. The applications of PNCs in various optoelectronic devices are then briefly presented. Finally, the remained challenges in improving the stability of PNCs towards the PNC-based optoelectronics with high performance and great durability are addressed.

3.2 Introduction

Perovskite materials have attracted broad attention from different academic circles over a decade. Regarded as the game changer in photovoltaics^[1], these materials achieved a skyrocketing improvement of the power conversion efficiency (PCE), increasing from 3.81%^[2] to 23.3%^[3] within 10 years, and hitting to 25.5% currently.^[4] Except the photovoltaic applications^[5-12], these superstar materials have also been developed for light-emitting diodes (LEDs)^[13-16], photodetectors (PDs)^[17-19], and as catalysts for photocatalysis^[20-25], to name but a few. The perovskite materials possess great potential to be applied in various commercial products in the future.

“Perovskite”, at first, referred to a mineral species with the chemical formula of CaTiO_3 . In 1839, the German mineralogist, Gustav Rose (1798 – 1873), first discovered the “perovskite” (CaTiO_3) in the Russian Ural Mountains. In honour of L. A. Perovski (a Russian mineralogist, 1792 – 1856), this type of material is named as “perovskite”. Later on, materials with a similar CaTiO_3 crystal structure are called “perovskite” in mineralogy, which have a chemical formula of ABX_3 (see Figure 3.1a). The high-temperature superconductivity, catalytic properties, magnetocaloric effect and ferroelectricity of perovskite consisting of oxygen, named as perovskite oxides, are the previous research center. The B site of perovskite oxides can be bivalent or tetravalent metal cations.^[14] Due to the successful

application of metal halide perovskite (MHPs) in photovoltaic devices^[2, 26], the scholars of different research areas have focused on this type of material and made it one of the most studied research subjects worldwide over the last ten years. MHPs are composed of monovalent organic or inorganic cations (such as CH₃NH₃⁺ (methylammonium, MA), CH(NH₂)₂⁺ (formamidinium, FA), Cs⁺, Rb⁺, etc.) in the A site, divalent metal cations (such as Ge²⁺, Cu²⁺, Pb²⁺, Sn²⁺, etc.) in the B site, as well as halide anions (Cl⁻, Br⁻ or I⁻) in the X site.

With numerous achievements in bulk perovskite materials, research of MHPs has been extended to nanoscale. Since the first report in 2014^[27], perovskite nanocrystals (PNCs) have also aroused the interest due to their specialties, which possess the excellent optoelectronic properties of bulk perovskite materials and the quantum confinement effects of materials in nanoscale, showing the properties of tunable bandgaps, narrow emission and strong light-absorption coefficients. The notable advantage of PNCs over traditional quantum dots (QDs), like sulphide and selenide QDs, is their high defect tolerance. The dimensions and shapes of PNCs can be facily adjusted to 0D QDs, 1D nanowires (NWs) and nanorods (NRs), 2D nanosheets (NSs) and nanoplatelets (NPLs), and 3D nanocubes (NCus) by modifying the reaction conditions.^[28] Figure 3.1b shows a good example of adjusting the dimensionality of CsPbX₃ (where X = I, Br, Cl) NCs by using different organic ligands.

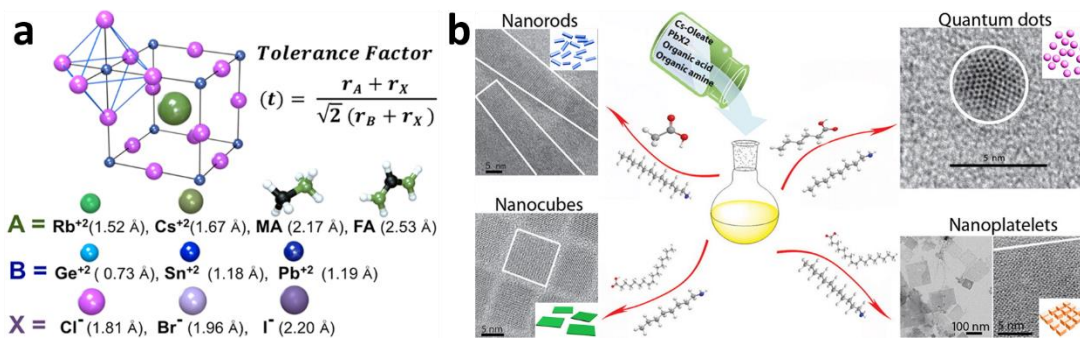


Figure 3.1: a) Cubic perovskite crystal structure (α -phase) showing the flexibility in the choice of cation (A), metal (B), and anion (X). The ionic radii of different ions are also shown. The tolerance factor (t) for 3D perovskites should be approximately 1 to attain an ideal close-packed cubic perovskite phase, where r_A , r_B , and r_X are the effective ionic radii for A, B, and X ions, respectively. Reproduced with permission.^[29] Copyright 2019, American Chemical Society. b) Tuning the dimensionality of inorganic CsPbX₃ (X = Cl, Br, I) NCs by varying the organic ligands used. Hexanoic acid and octylamine for spherical quantum dots; oleic acid and dodecylamine for nanocubes; acetate acid and dodecylamine for nanorods; oleic acid and octylamine for few-unit-cell-thick nanoplatelets. Reproduced with permission.^[30] Copyright 2016, American Chemical Society.

Although PNCs have shown outstanding properties and considerable potential for various applications in the future, the stability issue of these materials is still the main challenge hindering their roads towards commercialization. Researchers have devoted substantial efforts to understand the degradation mechanisms of PNCs^[31-34] and develop effective strategies to protect PNCs for highly-efficient performance and long-term lifetime.^[35-37]

This review comprehensively summarizes the latest advances of the synthesis methods for both lead-based and lead-free PNCs. Moreover, elements that impact on the stability of the PNCs are introduced. Strategies of encapsulation to protect PNCs are reviewed afterwards. Importantly, various applications of the PNCs in optoelectronics are briefly reviewed. And finally, the challenges remained for improving the stability of PNCs and the outlook to possible directions in developing PNC-based devices with high performance and great operation durability are addressed.

3.3 Synthesis of Perovskite Nanocrystals

The facile methods for synthesizing PNCs with different dimensions and shapes have aroused huge research interest in recent years.^[38, 39] In this section, we discuss the wet synthesis processes, including hot injection method, ligand-assisted reprecipitation (LARP) method, emulsion process, ultrasonic and microwave-based methods, solvothermal method, microfluidic method, template assisted method, and electrospinning or electrospray method, as well as the dry synthesis processes, chemical vapour deposition (CVD). In addition, the synthesis methods for lead-free PNCs are presented in this section, which is also an important research branch of PNCs in the process of commercialization. Finally, the anion-exchange reaction, an important post-synthetic method, is introduced and discussed.

3.3.1 Wet Synthesis Processes of PNCs

3.3.1.1 Hot Injection Method

Hot injection method is a traditional synthesis method for metal chalcogenide or fluoride NCs.^[40] Figure 3.2a shows the schematic of hot injection method.^[41] Typically, a cation precursor is prepared separately before the injection, for example, Cs-oleate and methylamine are normally chosen for Cs⁺ ions and MA⁺ ions, respectively. Then, a solution of metal halide salt and organic ligands is dried under vacuum and heated to a certain reaction temperature under nitrogen before injection. Alkyl chain acid and amine are usually chosen as ligands. Upon quick injecting the cation precursor into the mixture of metal halide salt and ligands, the PNCs form immediately owing to their fast nucleation and growth kinetics. In 2015, Kovalenko et al. first used this method to synthesize PNCs, CsPbX₃ (X= Cl, Br, I or halide mixture).^[42] For that, the Cs-oleate precursor was injected into PbX₂ precursor containing organic ligands at a specific high temperature (up to 250 °C) and operated under protective gas, like nitrogen and argon. Then the reaction was instantly quenched by putting the flask into an ice-water bath. The reacting mixture became gel when the temperature suddenly fell, and the growth of PNCs stopped at the same time. By modifying the temperature and time of reaction, PNCs with different sizes and shapes can be obtained.

The as-fabricated CsPbX₃ NCs with 4 - 15 nm lengths of edge exhibited adjustable bandgaps and emission spectra covering the full visible spectral area of 410 - 700 nm (Figure 3.2b), as a result of the compositional modulations and quantum confinement. The photoluminescence (PL) of CsPbX₃ NCs was characterized by narrow full width at half maximum (FWHM) of 12 - 42 nm, radiative lifetimes

in the range of 1 - 29 ns, high quantum yields (QYs) of up to 90%, and wide color gamut covering up to 140% of the National Television System Committee (NTSC) color standard.^[42]

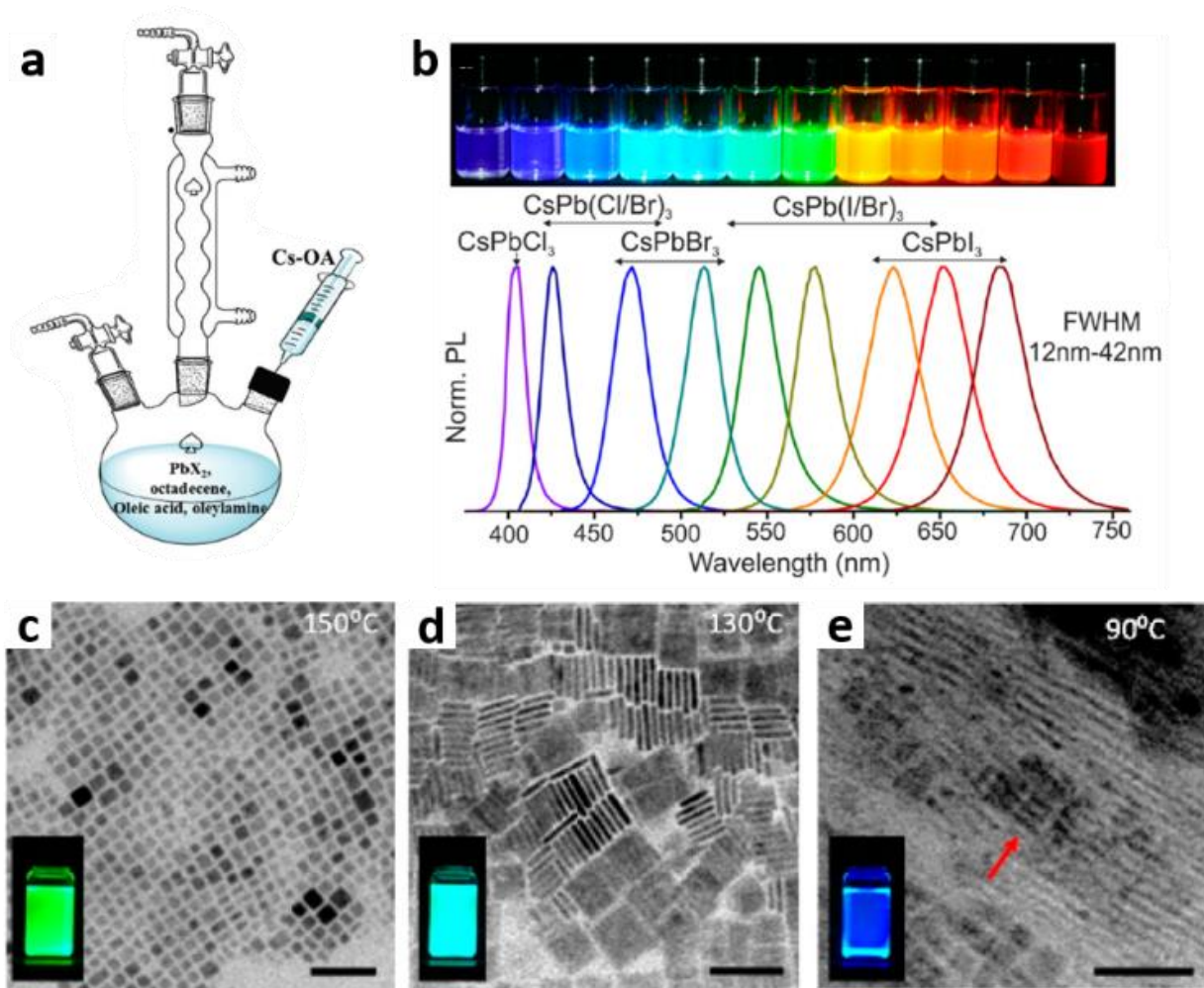


Figure 3.2: a) Schematic of hot injection method. Reproduced with permission.^[41] Copyright 2017, Wiley-VCH. b) CsPbX_3 NCs ($X = \text{Cl}, \text{Br}, \text{I}$) colloidal solutions in toluene under UV lamp ($\lambda = 365 \text{ nm}$); representative PL spectra ($\lambda_{\text{exc}} = 400 \text{ nm}$ for all but 350 nm for CsPbCl_3 samples). Reproduced with permission.^[42] Copyright 2015, American Chemical Society. Study of the influence of reaction temperature in CsPbBr_3 colloidal synthesis: c) At 150°C , green emitting 8 - 10 nm NCs are formed; d) At 130°C , cyan emitting NPLs with lateral dimensions of 20 nm and thickness of a few unit cells ($\sim 3 \text{ nm}$) are formed; e) At 90°C , blue emitting thin NPLs are observed, along with several-hundred nanometers lamellar structures. NPLs growth along the lamellae (red arrow) (c - d, scale bars are 50 nm). Reproduced with permission.^[46] Copyright 2015, American Chemical Society

The reaction temperature can affect the quality of final products. When the temperature is too high, some unwanted variants can be obtained. For example, CsPb_2Br_5 and CsPb_2Cl_5 would be produced when the synthesis of CsPbBr_3 and CsPbCl_3 NCs was operated at $260\text{ }^\circ\text{C}$.^[43] In addition, some reactants will precipitate when the temperature of solution is too high. For example, the reaction temperature for synthesizing CsPbBr_3 is around $190\text{ }^\circ\text{C}$. However, further increasing the temperature to a threshold temperature of $195\text{ }^\circ\text{C}$ leads to PbBr_2 precipitation.^[42] While the precipitation temperature of reactant PbBr_2 can rise above $195\text{ }^\circ\text{C}$ by adding more ligands into the solution.^[44] At low reaction temperature, large CsPbBr_3 NPLs form with broad edge length distribution.^[45] Alivisatos et al. studied the reaction temperature effect on the morphology of PNCs. They discovered that reactions at lower temperatures between 90 and $130\text{ }^\circ\text{C}$ tended to favour asymmetric growth of PNCs, producing quasi 2D materials (Figure 3.2c and Figure 3.2d).^[46] The reaction time is another sensitive factor for hot-injection method. Normally, the reaction is completed within 10 seconds due to the fast nucleation and growth kinetics of PNCs, like CsPbX_3 and MAPbI_3 .

Capping ligands are often used in the hot injection method. They can solvate the metal halide precursors effectively, alter the kinetic pathways to obtain PNCs with various morphology, and stabilize the final products. The alkyl chain acids and amines play an important role on the crystal growth and surface properties of PNCs. Figure 3.3b shows the dynamic ligands binding on the surface of CsPbBr₃ NCs, where oleate or bromide anions bound to the surface caesium or lead ions, and alkyl chain ammonium cations bound to surface bromides with weak hydrogen bonds or electrostatic interactions.^[47] To study the surface chemistry, Liu et al. have systematically changed alkyl chain composition of amines and carboxylic acids. They realized that the amine and acid show independent influence on the shape and size of NCs (see Figure 3.3a). At a relatively higher temperature of 170 °C, larger size CsPbBr₃ NCs could be obtained when using a shorter chain acid. However, at the same injecting temperature, a shorter chain amine resulted in a different shape of NPLs comparing to NCs by using longer chain amine. At a relatively lower temperature of 140 °C, the length of acid had little impact on the thickness of NPLs, but shorter chain amine led to thinner NPLs. Figure 3.3c-f show low- and high-resolution transmission electron microscopy (TEM) images of CsPbBr₃ NCs synthesized by using different ligands at the temperature of 170 °C (Figure 3.3c-e) and 140 °C (Figure 3.3f). Based on ¹H NMR and IR spectroscopic results, they indicated that both ammonium and carboxylate bound to the as-fabricated PNCs' surface. However, the final composition of surface ligand was dependent on purification processing. When more polar acetone was used during purification cycles, ammonium ligands tended to leave the surface, but would remain upon the utilization of nonpolar hexane solvent. It confirmed that ammonium ions bound more weakly to the surface than carboxylate ligands did. Additionally, the utilization of a more soluble caesium acetate (CsOAc) instead of commonly used Cs₂CO₃ led to smaller particle sizes and improved processability without any detrimental influence on the optoelectronic properties.^[45] Recently, Manna et al. reported a novel route for the synthesis of both hybrid organic-inorganic and all-inorganic PNCs by choosing benzoyl halides as halide precursor to be injected into the solution. The halide ions can be released swiftly, following by nucleation and growth of PNCs. The final product synthesized by this method exhibited a good phase stability, uniform particle sizes, and outstanding optical properties.^[48]

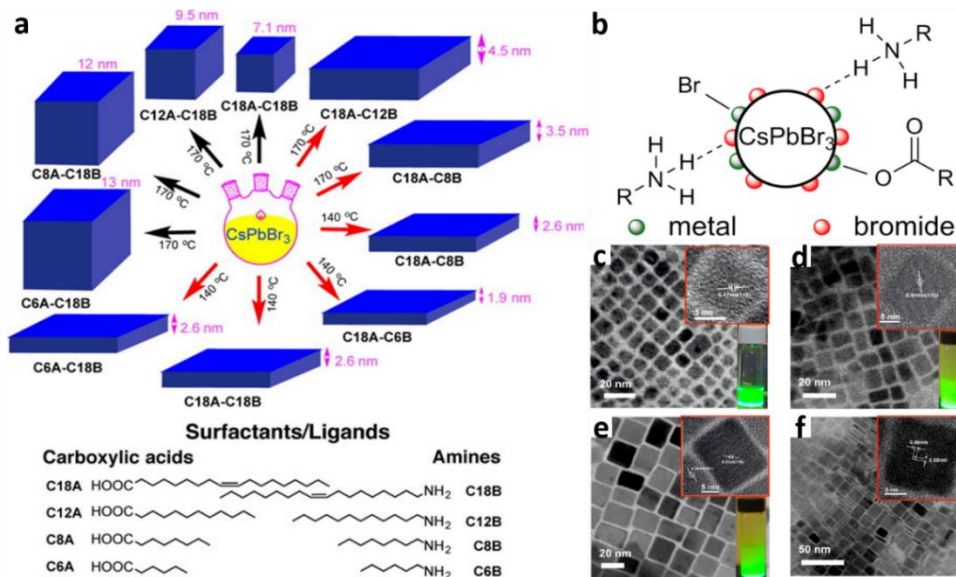


Figure 3.3: a) Schematic of CsPbBr₃ with different sizes and shapes synthesized under temperature of 140 °C or 170 °C and with different length of ligands. Reproduced with permission.^[45] Copyright 2016, American Chemical Society. b) The surface chemical environment of typical CsPbBr₃ NCs. Reproduced with permission.^[47] Copyright 2016, American Chemical Society. Low- and high-resolution TEM images of CsPbBr₃ NCs from 170 °C reactions using (c) C12A-C18B, (d) C8A-C18B, and (e) C6A-C18B, respectively. Insets in (c-e): Photographs of CsPbBr₃ NCs colloidal solutions in hexane under UV light; f) Low- and high-resolution TEM images of CsPbBr₃ NPLs from the 140 °C reaction using C6A-C18B. Reproduced with permission.^[45] Copyright 2016, American Chemical Society.

3.3.1.2 Ligand-assisted Reprecipitation Method (LARP)

Although hot injection method gives the best morphology control on the synthesis of PNCs so far, the high cost of this method is not proper for commercial production. Consequently, other alternative procedures should be developed to address this problem. LARP method is the most common used method to synthesize PNCs at room temperature (RT). Figure 3.4a shows the representative schematic of the LARP method, in which the precursor is a mixture of perovskite reactants and ligands in N,N-dimethylformamide (DMF). Then, a certain volume of precursor is dropped into toluene or 1-octadecene (ODE), which initiates PNCs formation and aggregation. Apparently, the types of ligands and solvents in precursors are critical factors to control the sizes and shapes of PNCs. The LARP technique is a low-cost and scalable process, which is suitable for fabricating both all-inorganic and hybrid organic-inorganic PNCs.^[38]

In 2014, Pérez-Prieto et al. reported the synthesis method of nanometer-sized, organolead halide MAPbBr_3 perovskites. By using medium-length alkyl chain ammonium cations (e.g., octadecylammonium) as ligands, they obtained PNCs with an average size of 6 nm. The PNCs were stable for at least three months in solution and solid state. This process also allowed to fabricate PNCs thin films via spin-coating. Notably, they obtained luminescent PNCs both in solution and in film, though the photoluminescence quantum yield (PLQY) was only $\sim 20\%$.^[27] In 2015, Zhong et al. further optimized the LARP technique by changing octadecylammonium bromide and octylammonium bromide ligands to n-octylamine and oleic acid (OA) in the synthesis. The n-octylamine can help to avoid the fast crystallization and aggregation, and the oleic acid can also suppress the QD aggregation effects and make the colloidal solution stable. The colloidal MAPbBr_3 QDs showed great enhancement in luminescent with absolute PLQYs up to 70%. They also illustrated that the size reduction and appropriate chemical passivation of Br-rich surface can increase exciton binding energy and PL.^[49] Later on, Deng et al. adopted this strategy for synthesis of all-inorganic CsPbX_3 ($X = \text{Cl}, \text{Br}, \text{I}$) PNCs with controlled shape and achieved PLQY values up to $>80\%$. By using different types of ligands in LARP process, CsPbX_3 NCs could be modified into NCs, 1D NRs, and 2D NPLs with precise morphology.^[30] Rogach et al. studied the size-tunability of the bandgap of MAPbBr_3 perovskite quantum dots (PQDs) by adjusting temperature to control over the LARP synthesis. The PL peaks of as-synthesized PQDs can be tuned between 475 and 520 nm (see Figure 3.4b).^[50]

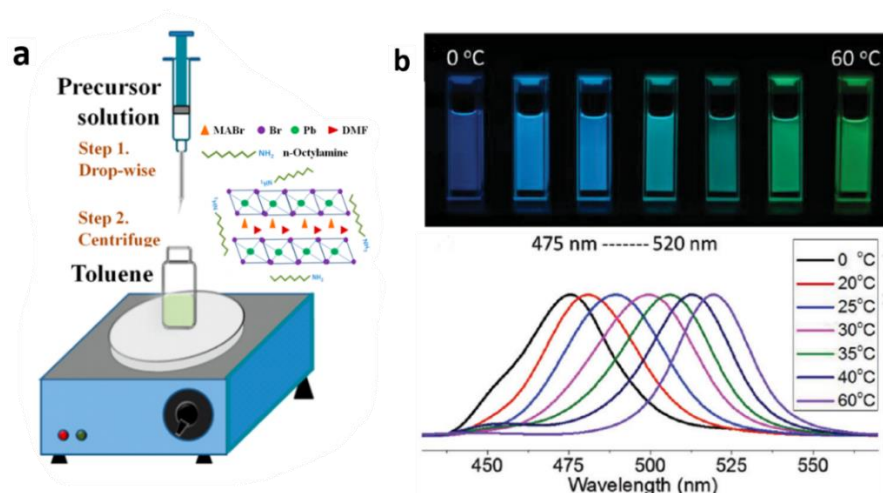


Figure 3.4: a) Schematic of LARP method (Inset: starting materials in the precursor solution). Reproduced with permission.^[49] Copyright 2015, American Chemical Society. b) photograph of colloidal MAPbBr_3 PQDs solutions in toluene under UV lamp excitation ($\lambda = 365 \text{ nm}$) and size-tunable PL spectra over the range of wavelengths. Reproduced under the terms of the CC-BY license.^[50] Copyright 2015, Wiley-VCH.

Inspired by Zhong's work, Zeng et al. created a RT supersaturated recrystallization (SR) procedure to fabricate CsPbX₃ (X = Cl, Br, I) NCs (see Figure 3.5). The process doesn't require heating, inert gas, and injection operation, thus can be completed very fast. They dissolved PbX₂ and CsX (X = Cl, Br, I, or their mixture) in dimethyl sulfoxide (DMSO) or DMF, and added OA and oleylamine (OAm) as surface ligands. Toluene was chosen as an anti-solvent due to the poor solubility for these ions (< 10⁻⁷ g mL⁻¹). Then, the precursor was dropped into toluene. Owing to the huge solubility difference, a highly supersaturated state was produced at once and, consequently, fast recrystallization occurred under stirring condition. OAm and OA worked as dispersants for these PNCs and also helped to control the particle size.^[51]

However, polar solvents, like DMF, as reaction medium can severely degrade or form defective PNCs and, therefore, decrease the production yield. For example, CsPbX₃ NCs often lose colloidal stability and brightness of PL when polar solvents are added to separate them.^[47] To address this issue, Pan et al. reported a room-temperature and gram-scale synthetic strategy, based on a homogeneous reaction in various nonpolar organic solvents by using precursors containing long alkyl chain acid salts of caesium and lead and quaternary ammonium bromides. The as-prepared PNCs exhibited a tunable PL in the region from 440 nm to 682 nm and PLQYs of 50 to 85%.^[52] Recently, Macdonald et al. reported an oleic and amine-acid-free RT synthesis of CsPbBr₃ and FAPbBr₃ NCs by using a mixture of diisooctylphosphinic acid and trioctylphosphine oxide. This mixture of ligands provided a stable platform for the polar-solvent-free synthesis of fully inorganic CsPbBr₃ (FWHM ≈ 14 nm, emission = 519 nm) and hybrid organic-inorganic FAPbBr₃ (FWHM ≈ 19 nm, emission = 532 nm) NCs in the air. In addition, it was shown that compared to a traditionally used ligand combination, phosphine ligands could be washed off easily, which would benefit the future development of optoelectronic devices.^[53]

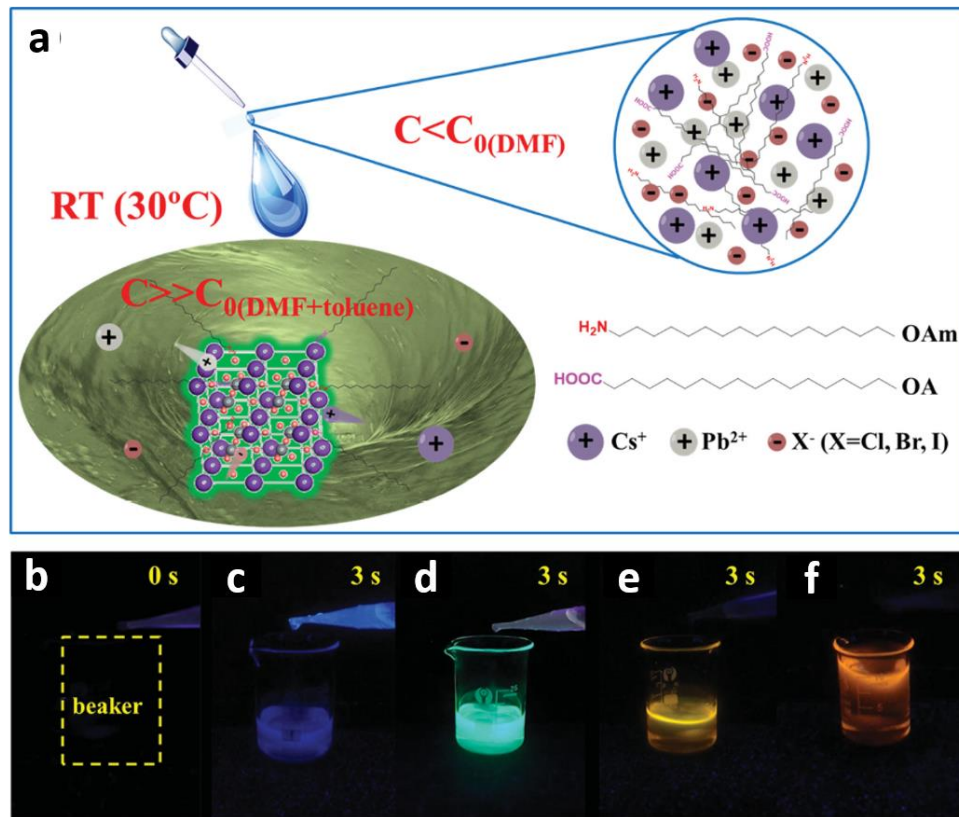


Figure 3.5: a) The SR can be finished within 10 s through transferring the Cs^+ , Pb^{2+} , and X^- ions from the soluble to insoluble solvents at RT without any protecting atmosphere and heating [C : ion concentration in different solvents. C_0 : saturated solubilities in DMF, toluene, or mixed solvents (DMF + toluene)]. b) Clear toluene under a UV light. Snapshots of four typical samples after the addition of precursor ion solutions for 3 s, blue (c, Cl:Br = 1), green (d, pure Br), yellow (e, I:Br = 1), and red (f, I:Br = 1.5), respectively. Reproduced with permission.^[51] Copyright 2016, Wiley-VCH.

3.3.1.3 Emulsion Method

As shown in Figure 3.6a and Figure 3.6b, Zhong et al. developed a facile non-aqueous emulsion synthesis of PNCs by mixing a demulsifier with an emulsion of precursors. First, they created an emulsion system by mixing DMF and n-hexane, which were immiscible to each other. Then, they subsequently added tert-butanol into the initialized solvent mixture, which worked as the demulsifier and induced the crystallization process. By using this method, they could control the crystallization process and the size of PNCs by varying the amount of demulsifier, and they succeeded in obtaining monodisperse MAPbBr_3 QDs with size between 2 and 8 nm (Figure 3.6c-f) and PLQYs of 80 to 92%,

which were higher than samples fabricated by LARP methods.^[49] They also used the same method to synthesize inorganic CsPbBr₃ PNCs and obtained CsPbBr₃ NCs with the size between 9 - 20 nm.^[54]

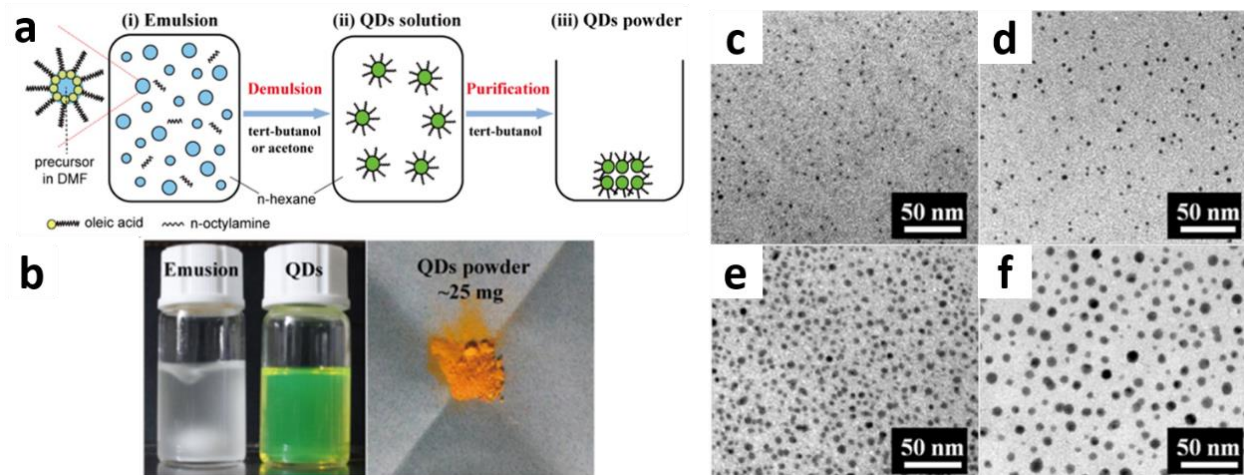


Figure 3.6: a) Schematic illustration of the QD emulsion synthesis, (i) formation of the emulsion, (ii) demulsification by adding demulsifier, and redispersing into colloidal solution, (iii) purification into solid-state powder. b) Optical photographs of typical MAPbBr₃ emulsion, resultant colloidal solution, and solid-state powder of MAPbBr₃ QDs. (c-f) Low-resolution TEM image of MAPbBr₃ QDs with diameters of 2.6 ± 0.6 , 3.3 ± 0.7 , 4.6 ± 1.1 , and 7.2 ± 1.7 nm. The amount of tert-butanol used were 1.5 mL, 2 mL, 4 mL, 6 mL, and 8 mL, respectively. Reproduced with permission.^[54] Copyright 2015, American Chemical Society.

3.3.1.4 Ultrasonic and Microwave-based Method

The ultrasonic and microwave-assisted methods show potential for large scale production due to the polar solvent-free fabrication. Song et al. first reported ultrasound-assisted synthesis of colloidal APbX₃ NCs, where A represents Cs⁺, MA, or FA, and X represents I⁻, Br⁻, or Cl⁻. Figure 3.7a shows CsPbBr₃ NCs with the size of 10 nm. They added PbX₂, MAX (or FAX, CsX), and OAm to toluene to make a precursor. The reaction vessel of precursor was placed in a high-density probe-type ultrasonicator. The reaction temperature was kept at 20 °C by immersing it in a water jacket connected to a circulator with a temperature controller. Furthermore, they used the same method to produce a series of mixed halides PNCs.^[55] Bals, Urban, Polavarapu and their colleagues developed a polar-solvent-free synthesis method of CsPbX₃ (X = Cl⁻, Br⁻, and I⁻) PNCs (Figure 3.7b-d) with high quality, which was based on direct tip sonication of the combination of capping ligands (OAm and OA) and precursor salts (Cs₂CO₃ and PbX₂) in a nonpolar solvent under ambient atmospheric conditions. The average

crystal sizes were between 10 and 15 nm for CsPbBr₃ and between 8 and 12 nm for CsPbI₃. It was interesting that lower caesium content reduced reaction rate and strongly support 2D growth, thereby synthesizing NPLs.^[56]

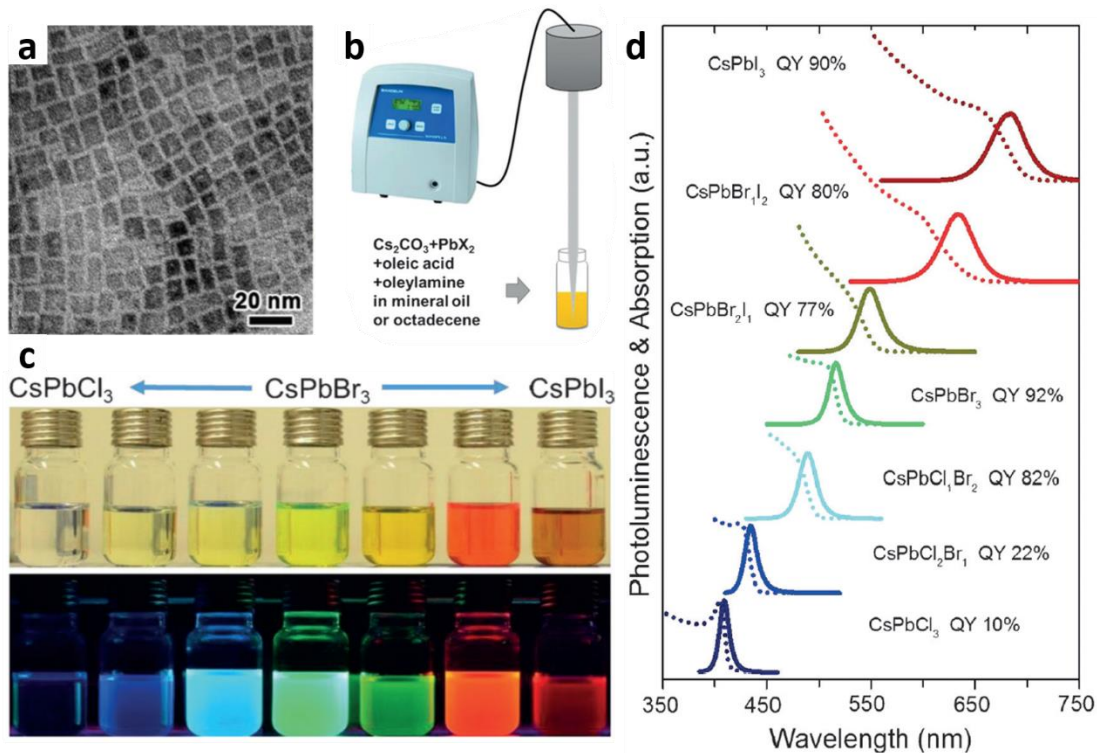


Figure 3.7 a) High-resolution transmission electron microscopy (HRTEM) image of monodisperse 10 nm CsPbBr₃ NCs. Reproduced with permission.^[55] Copyright 2016, Royal Society of Chemistry. b) Synthesis of CsPbX₃ NCs through single-step tip sonication. c) Photograph of colloidal dispersions of CsPbX₃ NCs with different halide (X = Cl, Br, and I) compositions in hexane under room light (top) and 367 nm UV light (bottom). d) Corresponding UV/Vis and PL spectra and PLQYs of the samples shown in c). Reproduced with permission.^[56] Copyright 2016, Wiley-VCH.

Zhang et al. reported a rapid and efficient microwave-assisted process to produce CsPbX₃ NCs with controllable morphology and high quality. The microwave heating has some advantages like low energy cost and high heating rate, which are favoured by industrial communities. In addition, the as-obtained materials possessed superior photophysical properties. The emission peak could be adjusted in the region of 410 nm to 694 nm by altering the anion composition. The FWHM were very narrow (9 - 34 nm), which showed their potential in lighting and display application.^[57] Nearly at the same time, Na et al. used a simple microwave irradiation to synthesize CsPbX₃ PNCs with adjustable

properties and morphology (NCus, NRs, NWs, quadrate NPLs and hexagonal NPLs). The precursor was a solid-liquid mixture containing PbX_2 ($X = \text{Cl, Br, I}$), Cs_2CO_3 , ODE, OA and OAm, which was placed into a glass vessel and positioned in the microwave oven. Finally, CsPbX_3 PNCs were produced via static microwave irradiation for ~ 4 min.^[58] Zhang et al. modified the previous method by using caesium acetate (CsOAc) and bis(2,4,4-trimethylpentyl) phosphinic acid (TMPPA) as Cs precursor and capping ligand, rather than commonly used Cs_2CO_3 and OA. The mixture of OA and TMPPA could solvate CsOAc completely at RT, while Cs_2CO_3 precursor was insoluble. The reason was that carbonic acid was less acidic than acetic acid, correspondingly, it was harder for Cs_2CO_3 than CsOAc to coordinate and form soluble Cs-ligand complex monomers. Consequently, more soluble monomers could be released by CsOAc, resulting in supersaturation, nucleation, and growth of NCs.^[59]

3.3.1.5 Solvothermal Method

Solvothermal methods are one of the most used techniques to obtain well-defined NCs under increased pressure and modest temperature. This method shows a relatively slow reaction, comparing to the traditional hot-injection and LARP. Therefore, it can control the kinetics of nucleation and growth process during the PNCs' synthesis. In addition, this method has the feature of high crystallinity and uniformity, controllable size and shape, as well as simple, low-cost and scalable synthesis. Typically, the precursor solution is added into a Teflon liner, which is held by a stainless-steel autoclave. Then, the sealed tank is put into an oven and heated at a specific temperature. The reaction is normally conducted at high temperature and pressure.

Zhang et al. first reported the successful production of high-quality all-inorganic CsPbX_3 NCs through a simple solvothermal approach. The as-prepared PNCs are shown in Figure 3.8a-e. CsPbX_3 NCs were cube-like shape with an average edge length of around 10 nm. They also found that the growth of CsPbI_3 NCs was faster than the other halides perovskite, leading to the relatively larger size (≈ 12.5 nm). The optimized CsPbX_3 NCus showed a high PLQYs of over 80%. More importantly, $\text{CsPb}(\text{Br/I})_3$ ultrathin NWs could also be prepared through this approach with a high yield (Figure 3.8f-g). The concentration and aging effect of precursors determined the morphology of PNCs. As illustrated in Figure 3.8i, the concentration of precursor ions was relatively low when precursor was directly heated without predissolving. Then, precursors were gradually dissolved when the temperature increased and little amount of PNCs nucleated at specific concentration. Under this condition, the nuclei grew into NCus finally. In opposite, when precursors were predissolved and the concentration

of ions were high at the beginning, more nuclei were formed, resulting in smaller nuclei. Here, by increasing the reaction time, the morphology of NCs could change from NCs to NWs.^[60]

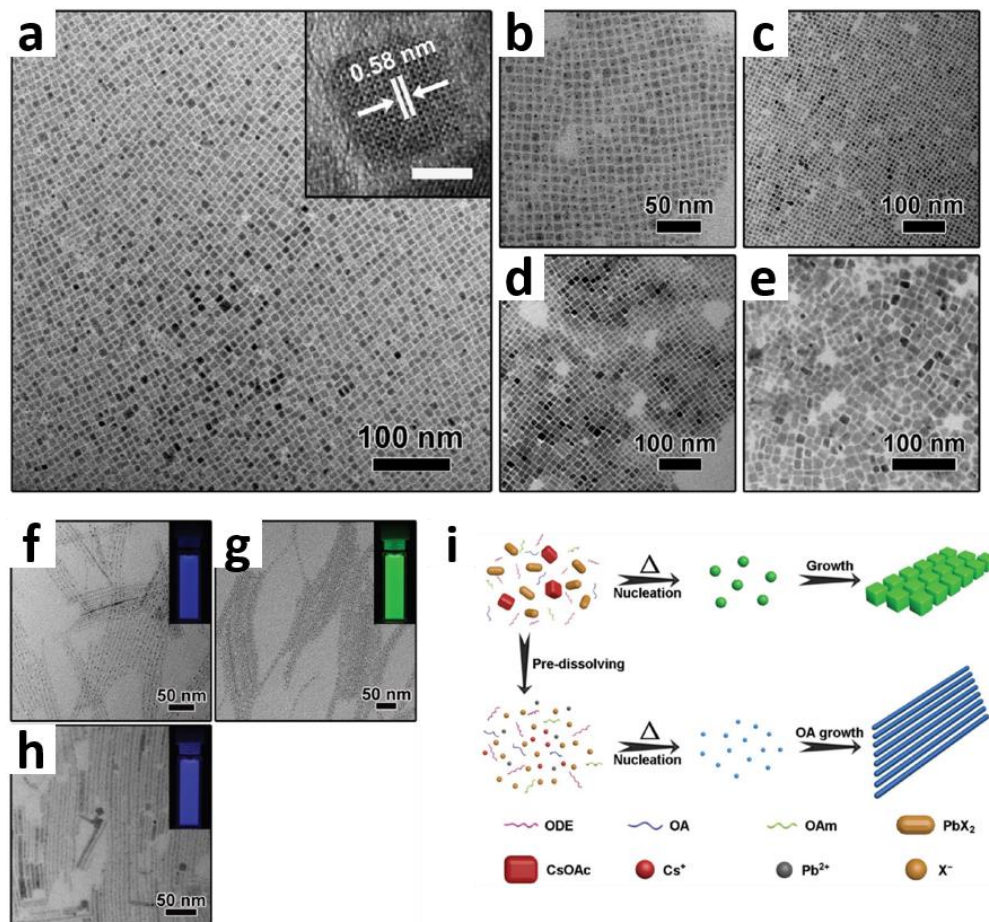


Figure 3.8: TEM images of a) CsPbBr_3 , b) CsPbCl_3 , c) $\text{CsPb}(\text{Cl}/\text{Br})_3$, d) $\text{CsPb}(\text{Br}/\text{I})_3$, and e) CsPbI_3 NCs. (The inset in (a) is the HRTEM image of CsPbBr_3 nanocrystals. The scale bar in the inset is 5 nm.) TEM images of ultrathin f) CsPbBr_3 , g) $\text{CsPb}(\text{Br}/\text{I})_3$, and h) $\text{CsPb}(\text{Cl}/\text{Br})_3$ nanowires. Insets show the bright emission color of colloidal CsPbX_3 solution in hexane under UV illumination ($\lambda = 365 \text{ nm}$). i) the proposed growth process of CsPbBr_3 NCs without and with pre-dissolving step. Reproduced with permission.^[60] Copyright 2017, Wiley-VCH.

Zheng et al.^[61] and Chen et al.^[62] also reported a solvothermal synthesis process of Mn-doped CsPbCl_3 PNCs nearly at the same time. Zheng et al. reported 2D Mn-doped CsPbCl_3 NPLs accompanied with the phenomenon of a gradual phase segregation of pure CsMnCl_3 from Mn: CsPbCl_3 NPLs by spinodal decomposition.^[61] Chen et al. systematically studied the effect of Cs/Pb ratio on crystal structure of Mn-doped CsPbCl_3 product. When the Cs/Pb ratio was low (0.3:1 or 0.6:1), rhombohedral Cs_4PbCl_6

phase coexisted with cubic CsPbCl₃ phase. When the ratio increased (0.9:1 and 1.2:1), the as-synthesized products were pure cubic CsPbCl₃ phase without any obvious impurities. PNCs still remained as the cubic CsPbCl₃ phase when further increasing the ratio (1.5:1 and 1.8:1). When the Cs/Pb ratio was fixed at 1.2:1, undoped sample showed tetragonal CsPbCl₃ phase while all the Mn-doped PNCs were pure cubic CsPbCl₃ phase, which indicated that Mn²⁺ dopants could modify crystal structure. In addition, Mn-doped CsPbCl₃ NCs synthesized by this method showed better stability than those synthesized by hot-injection method.^[63] Except lead-based PNCs, the solvothermal method could also be applied to synthesize lead-free PNCs, like CsSnX₃^[64, 65], CsGeX₃^[66], etc.

3.3.1.6 Microfluidic Method

Microfluidic method is suitable for rapid mass and energy transfer, which allows to create or homogenize both temperature and reagent on ultrashort time scales. This method can provide researchers with the fabrication of NCs with diverse and complex composition, and a fast, accurate and economical testing of parameters via varying volumetric flow rates of the precursor and controlling sequentially addition of the reagents.^[67, 68]

In 2015, just after the first successful synthesis of PNCs by hot injection method, Kovalenko et al. used microfluidic reaction systems to study the kinetics and factors on the formation of CsPbX₃ NCs. As shown in Figure 3.9a, the setup was relatively simple for studying the formation of PNCs. The precursors, which were put into precision syringe pumps, were mixed rapidly via a cross-mixing junction and formed droplets that can be heated to a certain reaction temperature rapidly. The obtained materials showed tunable PL and narrow FWHM (Figure 3.9b and Figure 3.9c). Benefiting from this simple and economic synthesis method, months-to-years of time and between 10 and 100 kg of reagents cost were saved compared to standard batch-by-batch screening routes. Depending on the synthesis methods, they studied the rapid reaction kinetics and formation mechanism for mixed-halide PNCs. Only a really short time (within 5 seconds) was needed to complete the nucleation and growth of CsPbX₃ NCs, so the time couldn't be used to control the size of NCs in traditional batch syntheses. In addition, the temperature used in hot injection method was between 1 and 10 °C lower than that in microfluidic method.^[69]

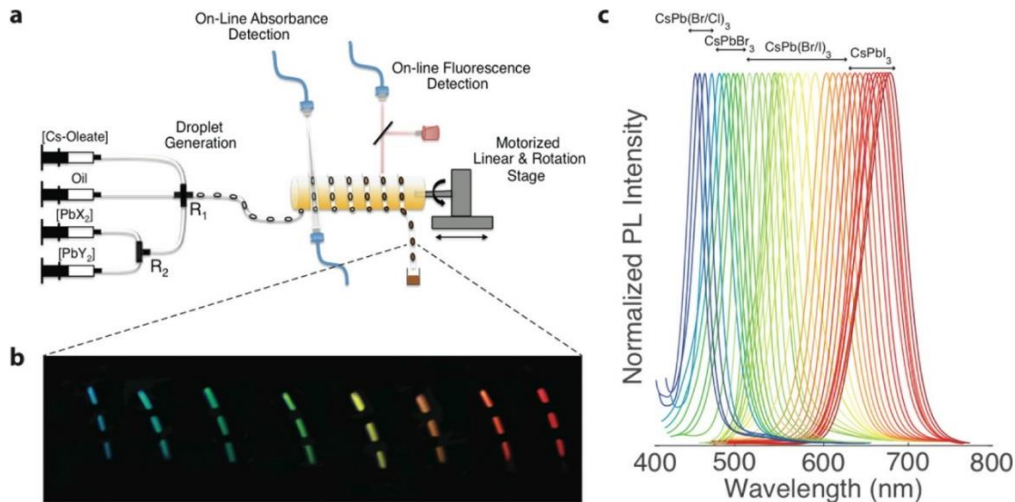


Figure 3.9: a) Illustration of the droplet-based microfluidic platform integrated with online absorbance and fluorescence detection for the synthesis and real time characterization of CsPbX_3 PNCs. b) Image of the generated droplets after exiting the heating zone taken under UV excitation ($\lambda_{\text{ex}} = 405 \text{ nm}$), showing bright PL of CsPbX_3 NCs. c) Online fluorescence spectra of CsPbX_3 NCs (X : Cl, Br, I and Cl/Br and Br/I mixed halide systems) spanning the whole visible spectral region with narrow emission linewidths. Reproduced with permission.^[69] Copyright 2016, American Chemical Society.

3.3.1.7 Template-assisted Synthesis

Template-assisted approach is a versatile and straightforward method to grow monodisperse PNCs. The crystallization kinetics and NCs formation are conducted on a particular template instead of using capping ligands. Yamauchi et al. used mesoporous silica templates to synthesize $\text{MAPbBr}_{x-1}\text{I}_{x-3}$ NCs. The particle size was controlled by the pore sizes of the templates, which showed quantum confinement effect as the samples' color changed by adjusting particle size.^[70] Kaltenbrunner et al. used nanoporous alumina and silicon thin films as templates to synthesize PNCs directly without the utilization of stabilizers.^[71] Recently, Li et al. used mesoporous Al_2O_3 as the template and developed a high temperature solid-state confined growth strategy to prepare highly emissive CsPbBr_3 NCs. The obtained CsPbBr_3 NCs possessed excellent optical properties comparable with colloidal CsPbBr_3 NCs, such as high PLQY (70%), narrow emission line width (FWHM = 25 nm), and much better thermal stability. It is worth noting that large amounts of expensive and toxic organic solvents can be avoided by using this method, which paves a new route for economical synthesis of high quality PNCs.^[72]

3.3.1.8 Electrospinning or Electrospray Method

Ogale et al. used electrospinning or electrospray method to synthesize MAPbX₃ NCs successfully, where instead of a solid substrate a bath of the antisolvent (without or with a capping agent) in a metal-electrode container was used as the substrate. It was quite like LARP method but applying the high electric field to the droplets of precursor solution, which broke them into a jet of nanodroplets. The nanodroplets fell into antisolvent (toluene) bath, resulting in rapid crystallization of the perovskite leading to uncapped 0D NCs. Interestingly, the capping agent, OAm, also contributed to the formation of 2D sheet-like layered perovskites by intercalation via host-guest chemistry.^[73]

3.3.1.9 Other Wet Synthesis Methods

Except the methods mentioned above, some novel wet synthesis methods have been also reported recently. Kovalenko et al. developed wet ball milling method to synthesis APbBr₃ NCs (A = Cs, FA). In detail, bulk CsPbBr₃ or FAPbBr₃ was added into a zirconia bowl with zirconia balls. The diameters of the balls are 4 mm and 5 mm. Then, OAmBr (ligand) and mesitylene (solvent) were added into the mixture. After milling at a certain speed for certain time, CsPbBr₃ or FAPbBr₃ NCs could be obtained. The optoelectronic quality of the products was as good as that synthesized by hot-injection method. However, this method was not applicable to iodide systems like CsPbI₃ and MAPbI₃.^[74] To form heterostructures, Xing et al. reported an in-situ solution growth method to decorate MAPbBr₃ NCs on the surface of MXene (Ti₃C₂T_x) NSs, which was achieved by an optimal mixed solvent ratio. The surface terminations of MXene NSs, such as fluorine, oxygen, and hydroxyl groups, are prone to interact with OA and OAm, which would form kinetically favorable nucleation points. Then, MAPbBr₃ NCs can grow on these points.^[75]

3.3.2 Dry Synthesis Processes of PNCs

3.3.2.1 Chemical Vapor Deposition

Chemical vapor deposition (CVD) is an effective method for fabricating traditional semiconductor nanocrystals. In 2014, Xiong et al. first used this method to synthesize PNCs (MAPbX₃, X = I, Br, Cl or halide mixture) in shape of NPLs, which possessed lateral dimensions from 5 to 30 μm and thicknesses from some atomic layers to hundred nanometers. The NPLs were fabricated via a two-step CVD process. First, they grew PbX₂ NPLs on muscovite mica utilizing van der Waals epitaxy in a vapour transport chemical deposition system. Next, the as-fabricated platelets were turned into perovskites by a gas-solid hetero-phase reaction with MAX. In addition, MAPbCl₃ NWs were also

fabricated as by-products during this process.^[76] To obtain perovskite NWs, Xiong et al. used silicon oxide rather than mica as substrates and succeeded in synthesizing the single-crystalline $\text{MAPbI}_x\text{Cl}_{3-x}$, MAPbBr_3 , MAPbI_3 and NWs via a two-step vapour phase synthesis process.^[77] Song et al. reported that the inorganic perovskite NWs of CsPbCl_3 , CsPbBr_3 , and CsPbI_3 were synthesized by vapour transport method. The NWs consisted of a single-crystalline cubic or pseudocubic phase with a uniform [100] growth direction and straight surfaces. The bandgap of perovskite NW was successfully adjusted covering a broad range by using three different compositions of halides.^[78] Pan's group used vapor phase deposition method to grow all-inorganic halide alloy perovskite NRs. They placed an alumina boat with a combination of CsX and PbX_2 at the heating area of the vapor deposition system and placed some SiO_2/Si substrates at the downstream of the quartz tube to synthesize the CsPbX_3 products. The as-grown CsPbX_3 NRs had a single crystalline structure with super smooth surface and precise triangular facets.^[78] Yan et al. synthesized composition-graded $\text{CsPbBr}_x\text{I}_{3-x}$ NWs via desynchronized deposition of PbX_2 and temperature controlled halide exchange reaction.^[79]

3.3.3 Synthesis Methods of Lead-free PNCs

Despite the excellent optoelectronic properties of lead-based perovskite materials, the toxicity of lead element remains a serious issue in the view of commercialization. The lead-based perovskites can degrade to water-soluble lead ions, which bind strongly to sulfhydryl groups on proteins and damage the central nervous system.^[80] Thus, great effort has been also devoted to synthesize lead-free PNCs. Here, we briefly introduce the synthesis method for lead-free PNCs.

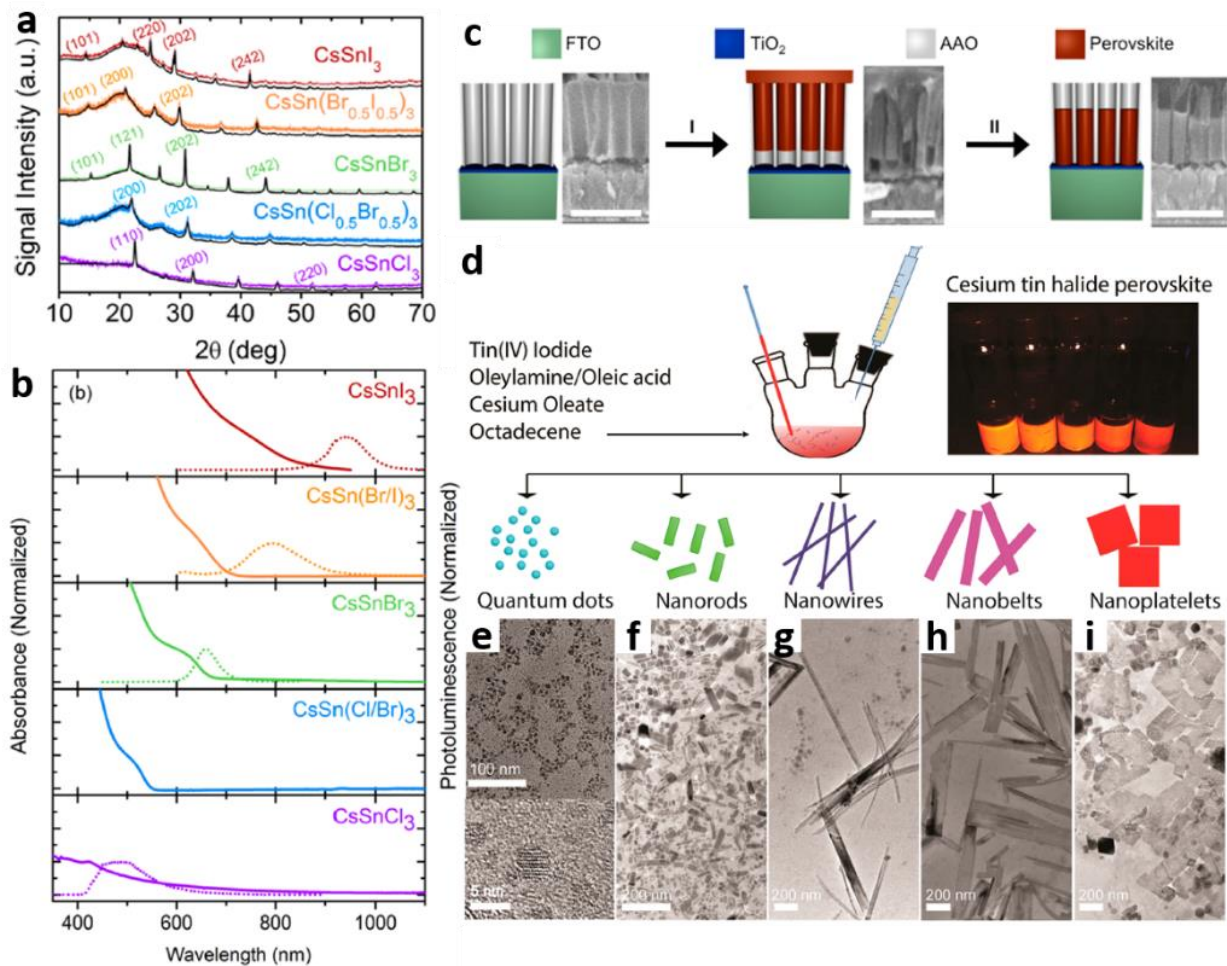


Figure 3.10: a) PXRD spectra of CsSnX_3 ($X = \text{Cl}, \text{Cl}_{0.5}\text{Br}_{0.5}, \text{Br}, \text{Br}_{0.5}\text{I}_{0.5}, \text{I}$) perovskite nanocrystals. (b) Absorbance and steady-state PL of nanocrystals containing pure and mixed halides. The PL spectrum of $\text{CsSn}(\text{Cl}_{0.5}\text{Br}_{0.5})_3$ particles was identical to the pure chloride-containing nanocrystals. Reproduced with permission.^[81] Copyright 2016, American Chemical Society. c) Synthesis of perovskite nanowire arrays in AAO. perovskite precursor solution penetrates the AAO pores, followed by spin coating and annealing (I). Sample is exposed to a DMSO/chlorobenzene solution followed by a short annealing step (II). Reproduced with permission.^[82] Copyright 2016, American Chemical Society. d) Schematic of procedures for the controlled synthesis of perovskite Cs_2SnI_6 nanocrystals (left panel) and photograph of the as-prepared Cs_2SnI_6 samples under UV light (right panel). (e-i) TEM images of Cs_2SnI_6 nanocrystals with different shapes (the inset of e gives an HRTEM image of Cs_2SnI_6 spherical quantum dots). Reproduced with permission.^[83] Copyright 2016, American Chemical Society.

Same as Pb, Sn and Ge belong to Group 14 and can fulfil the coordination and balance the charge to form a conventional perovskite structure. The tin-based PNCs (CsSnX_3 , $X = \text{Cl}, \text{Cl}_{0.5}\text{Br}_{0.5}, \text{Br}, \text{Br}_{0.5}\text{I}_{0.5}, \text{I}$)

are also the first reported lead-free PNCs (Figure 3.10a).^[81] The absorbance and emission of the as-fabricated PNCs showed that bandgaps could be extended from visible to near-IR area by adjusting the amount of different halides (Figure 3.10b). Here, the hot injection method was a little different with lead-based PNCs. The tin precursor was dissolved in tri-n-octylphosphine, a mildly reducing and coordinating solvent, to avoid the precipitation of CsX during its injection into the Cs₂CO₃ precursor solution.^[81] However, the easy oxidation of Sn²⁺ to Sn⁴⁺ makes tin-based material hard to be directly used in the environment. The tin(IV)-based PNCs, like Cs₂SnX₆ PNCs, are attractive as the substitutions to tin(II)-based PNCs due to their stability in the air. The first Cs₂SnI₆ NWs were synthesised by anodized aluminum oxide (AAO) templates (Figure 3.10c). So that, the perovskite precursor solution was added and allowed to penetrate the pores of AAO. Then, the excess liquid was removed from the surface followed by annealing to evaporate the solvent and obtain the final perovskite NWs.^[82] Deng et al. obtained Cs₂SnX₆ NCs with various morphology via a simple hot-injection method without using phosphine (Figure 3.10d-i). The Cs-oleate precursor was swiftly injected into tin precursor containing OA and OAm in ODE at 220 °C. At the initial stage, the shapes of the samples were QDs. Then NRs were obtained after 5 minutes of reaction. The NRs grew into NWs and the length extended after 10 minutes' reaction time. After 30-minute reaction period, NWs assembled side by side and nanobelts were formed, which could also be transformed into NPLs.^[83] The germanium-based perovskite is another candidate to substitute lead in metal halide perovskite. As far as we know, there is only one report about Ge-based NCs, CsGeX₃, which was synthesised by the hot-injection approach.^[84]

Due to the easy oxidation of lead-substitution from 14 group, $A_3B_2X_9$ PNCs, where B represents trivalent oxidation state of Bi or Sb, have been considered as another choice for replacing lead-based PNCs. $MA_3Bi_2X_9$ ($X = Cl, Br, I$) QDs were first reported by Tang's group synthesised by LARP method (Figure 3.11a-d). Ethyl acetate and DMF were used as good solvents to solvate $BiBr_3$ and $MABr$ and octane as poor solvent to precipitate $MA_3Bi_2X_9$ QDs. Additionally, n-octylamine was used to control the rate of crystallization and OA was used to stabilize the colloidal solution.^[85] Based on this achievement, further study was carried out on the Cl-passivation of $MA_3Bi_2Br_9$ QDs, which led to a bright blue emission with PLQY up to 54.1% at the wavelength of 422 nm. Unlike the lead-based PNCs, the halide exchange in $MA_3Bi_2Br_9$ is not so fast that the core-shell or locally concentrated Cl- onto $MA_3Bi_2Br_9$ QDs can be achieved.^[86] Gamelin et al. systematically studied the Cs-Bi-X compositions by using a combination of hot-injection and post-synthetic anion exchange methods. $Cs_3Bi_2X_9$ ($X = Cl, Br$) NPs, Cs_3BiX_6 ($X = Cl, Br$) NCs, and $Cs_3Bi_2I_9$ (Dimer Modification) NCs were obtained by injecting trimethylsilyl halide (TMSX) reagents into the hot precursors of Cs and Bi acetate salts. The $Cs_3Bi_2X_9$ ($X = Cl, Br$) NPs could be formed when a high Bi/Cs ratio and a large excess of OA were used. However, higher Cs/Bi ratios and less OA favored the formation of Cs_3BiCl_6 over $Cs_3Bi_2Cl_9$. Interestingly, Cs_3BiBr_6 NCs synthesized by hot injection method suffered from a persistent CsBr impurity comparing to the one obtained by anion exchange using TMSBr.^[87] The $Cs_3Sb_2X_9$ and $Rb_3Sb_2X_9$ PNCs were synthesized by hot-injection for the first time in 2017 (Figure 3.11e-g).^[88] Nag et al. reported that the NPLs and NRs morphology of the $Cs_3Sb_2I_9$ NCs could be obtained by varying the reaction temperature, which was also reported for $CsPbBr_3$ NCs. By using the same synthesis method, the 2D layered structure of $Rb_3Sb_2I_9$ NCs were obtained. All these samples showed emissions in the yellow-red region.^[88]

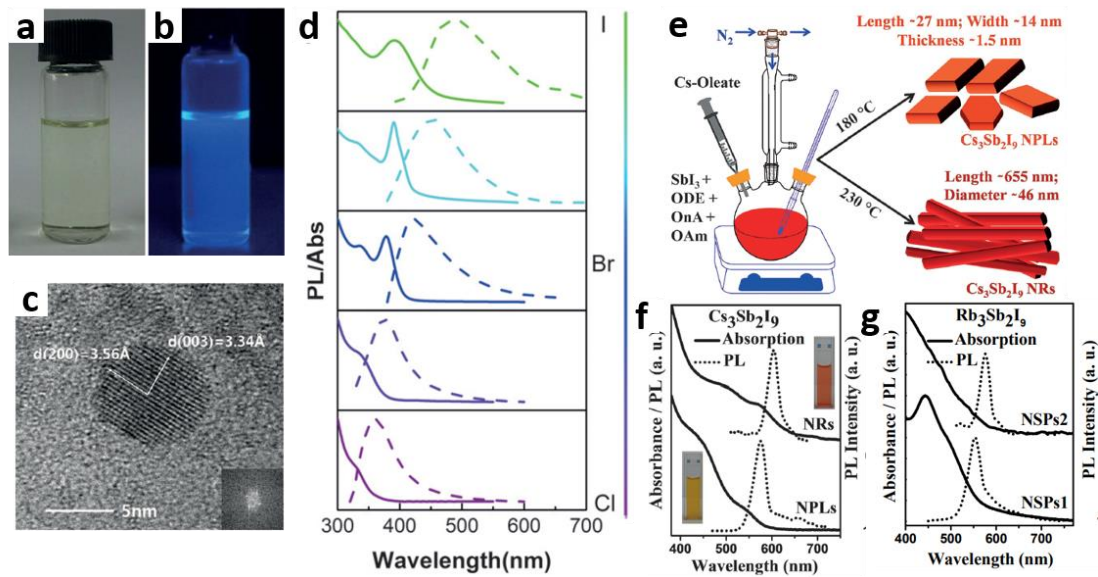


Figure 3.11: Optical image of a colloidal $MA_3Bi_2Br_9$ solution under a) visible light and b) 365 nm UV light. c) HRTEM image of a typical QD. The inset in the bottom right corner is the corresponding fast Fourier transform (FFT) image. d) Composition-tunable absorption and PL spectra of perovskite $MA_3Bi_2X_9$ QDs by halide substitution. Reproduced with permission.^[85] Copyright 2016, Wiley-VCH. e) Schematic representation of the synthesis of $Cs_3Sb_2I_9$ NPLs and $Cs_3Sb_2I_9$ NRs. ODE=1-octadecene, OnA=octanoic acid, OAm=oleylamine. f) UV/Vis absorption and PL spectra of $Cs_3Sb_2I_9$ NPLs and $Cs_3Sb_2I_9$ NRs. Insets: photographs of colloidal $Cs_3Sb_2I_9$ NPLs (yellow) and $Cs_3Sb_2I_9$ NRs (red) under visible light. g) UV-visible and PL spectrum of $Rb_3Sb_2I_9$ NSPs1 (reaction temperature 180 °C) with the diameter of around 7.5 nm and $Rb_3Sb_2I_9$ NSPs2 (reaction temperature 230 °C) with the diameter of around 17 nm. Reproduced with permission.^[88] Copyright 2017, Wiley-VCH.

3.3.4 Anion-Exchange Reaction

By virtue of ionic property and structural instability of PNCs, the anion-exchange reaction is a simple and effective method to adjust the optical properties of PNCs. For example, the bandgap and the absorption spectra of PNCs can be adjusted easily for different applications in SCs, LEDs, and PDs.^[38] Park et al. first reported the finding of reversible anion-exchange reaction of $MAPbX_3$ (where X = Cl, Br, and I). The mixed halide $MAPbBr_{3-x}Cl_x$ or $MAPbBr_{3-x}I_x$ NCs can be synthesized by adding a starting material ($MAPbBr_3$) into $MACl$ or MAI solution, respectively. The composition of the final products can be controlled easily by adjusting the molar ratio of starting material and MAX, enabling the absorption and PL spectra of PNCs to cover a wide range.^[89]

The anion-exchange reaction for all-inorganic CsPbX₃ was also demonstrated by Manna et al, where different halide precursors, such as oleylammonium halides (OLAM-X), octadecylammonium halides (ODA-X), tetrabutylammonium halides (TBA-X), and lead halide salts (PbX₂), were tested in the exchange reactions. Interestingly, when TBA-X was chosen as halide precursor, anion-exchange reactions didn't work from Cl to Br or from Br to I, but worked from Br to Cl or from I to Br. For other halide precursor tested in this work, the reversible anion-exchange reaction could be achieved. The hard/soft acid/base interaction can explain this phenomenon. TBA cation prefers binding to softer halide ions because it is a soft acid. The Br⁻ (or I⁻) ions are softer than Cl⁻ (or Br⁻) ions, thereby remaining associated with TBA.^[90]

Previous anion-exchange reactions were commonly performed by using OAm-halide precursors, which needed to prepare in a Schlenk line at high temperature. Additionally, the optical performance was prone to be damaged due to unstable crystal structures of PNCs. Wang et al. reported a novel precursor, which was consisted of OAm-copper halide complexes. The reaction could be operated at RT and the final products showed good structural stability and crystallinity improvement. The PLQY and stability of PNCs treated with CuX₂ showed an obvious improvement.^[91] Chen et al. first used MgX₂ as a halide precursor to study the anion-exchange reaction in CsPbBr₃ NCs. The morphology and crystal phase of the original CsPbBr₃ NCs retained after the reaction. Also, the final products showed good stability and tunable bandgap. Furthermore, they selected a series of metal halide salts MX₂ (M = Cd, Pb, Sn, Zn, Sr, Ca, Cu, Ba, Mn, Ba) as precursors for halide-exchange reaction to find a predication rule of precursors. After comprehensive study, they concluded that the similar bonding dissociation energy (BDE) values within the precursor and host lattice can make the halide exchange proceed easily.^[92]

3.4 Stability of Perovskite Nanocrystals

Stability is one of the critical issues for commercialization of PNCs. To solve the instability problem of PNCs, we should have a deep understanding of the origin of degradation mechanisms. This section reviews crystal structural stability, interface-induced stability, and environmental stability such as oxygen, moisture, light, and thermal stability.

3.4.1 Crystal Structural Stability

As shown in Figure 3.1a, the typical structure of halide perovskite is a cube, where the divalent metal cation is placed in the center, and monovalent cations and halide anions occupy the vertexes and face-centers, respectively. The center B-site cation coordinates with six halides and forms a BX_6 octahedral configuration. By sharing the corner halides, a continuous array can be obtained. And A-site cations, which are bigger than B-site cations, occupy the vacancy between BX_6 octahedra. That is the ideal 3D framework perovskite structure. However, under normal conditions, perovskites tend to distort away from a highly symmetric cubic structure, thereby forming an orthorhombic phase. Some reason can cause this transformation (*vide infra*). Obviously, this distortion leads to different electronic and optical properties and we will discuss them below.

To evaluate structural stability of perovskite materials comprising different cations and anions, we can use the well-known Goldschmidt's tolerance factor, t , which is defined as^[93]

$$t = \frac{r_A + r_X}{\sqrt{2}(r_B + r_X)} \quad (3.1)$$

where r_A , r_B and r_X correspond to the radius of components A, B, and X, respectively. In an ideal condition, the value of t equals to 1, that is to say, the crystal structure is a cube. Generally, the t value is in the range of around $0.813 \leq t \leq 1.107$ for 3D perovskites. Zeng et al. consider that the range of $0.9 \leq t \leq 1.0$ is ideal for cubic perovskite structure in general. The range of $0.71 \leq t \leq 0.9$ is considered as likely formation of orthorhombic or rhombohedral structure due to distortion of BX_6 octahedrons. In other cases, that is $t \leq 0.71$ or $t \geq 1$, non-perovskite structures such as NH_4CdCl_3 -type (1D orthorhombic structures formed by the edge-sharing of octahedra) or $CsNiBr_3$ -type structures (1D hexagonal structures formed by the face-sharing of octahedra) are formed.^[94] These non-perovskite materials normally have large bandgaps and low electronic conductivity. The other semiempirical geometric parameter to assess the structural stability of the BX_6 octahedra is octahedral factor, μ , which can be defined as

$$\mu = \frac{r_B}{r_x} \quad (3.2)$$

The stable BX_6 octahedral structure has μ value between 0.442 and 0.895. These two empirical indicators can effectively describe and predict the putative perovskite's structural stability, leading to the conclusion that ionic radii of components play a crucial role in the crystal structural stability.

Both $MAPbCl_3$ and $MAPbBr_3$ have cubic structures, and $MAPbI_3$ has a tetragonal structure at RT. As for $CsPbI_3$, the cubic perovskite phase can be obtained at high temperature (315 °C), however, this material changes to the non-perovskite phase at the temperature below 315 °C, which accompanies with bandgap changed from direct to indirect with value from 1.73 eV to 2.82 eV, respectively.^[95-97] $CsPbBr_3$ is one of the most studied PNCs which also shows superior stability to $CsPbI_3$. However, the binding energy and the effective Bohr diameter of Wannier-Mott exciton of $CsPbBr_3$ are 40 meV and 7 nm, respectively, which are inferior to $CsPbI_3$ (20 meV, 12 nm). In addition, the bandgap of $CsPbBr_3$ is 2.0 eV which is also inferior to $CsPbI_3$ (1.44 eV) in terms of photovoltaic applications. For FA-based PNCs, they have been synthesized by hot injection method and LARP method. Indeed, a tolerance factor closer to 1 can be achieved with FA cation than MA and Cs ones,^[98] although the sizes of MA ($R_A = 2.17 \text{ \AA}$) and FA ($R_A = 2.53 \text{ \AA}$) are similar. The fact is that the crystal structures of $MAPbI_3$ is tetragonal but $FAPbI_3$ is trigonal or pseudocubic. It's because that FA^+ is more prone to form hydrogen bonds than MA^+ , thus more stable pseudocubic structure can be obtained.^[99] However, it has been reported that $FAPbI_3$ exists in two kinds of polymorphs: one is a perovskite-type material with trigonal symmetry ($P3m1$); the other is a yellow hexagonal non-perovskite material ($P6_3mc$).^[100]

Currently, using a mixture of different cations, like Cs/MA^[101, 102], Cs/FA^[103-106], MA/FA^[107], Cs/Rb^[108-110], etc., as the monovalent cations in A-site of perovskite structure is widely adopted by researchers, which can adjust the value of tolerance factor close to 1 to make PNCs stable. Besides stability, optoelectronic properties and shapes of PNCs can also be modified. A great review published recently has comprehensively summarized the effect of doping and substitution in metal halide PNCs.^[98] Therefore, we don't unfold this topic here.

Low-dimensional perovskites, like 2D perovskites arranged in the Ruddlesden-Popper phase, have become the research hotspot recently due to their excellent environmental stability. 2D perovskites have a general formula $R_2A_{n-1}B_nX_{3n+1}$, where R is an additional bulky organic cation (such as an aliphatic or aromatic alkylammonium) as a spacer between the inorganic sheets and n defines the number of inorganic layers held together. These 2D perovskites are much more stable than 3D

perovskites owing to the van der Waals interactions existed among organic molecules and consequently, increased formation energy. In addition, unlike 3D perovskites which limit the radius of the A-site cations to around 2.6 Å^[111], a wide choice of organic cations is available for 2D perovskites, which can also benefit the designing of new types of perovskite with desired properties for various optoelectronic applications.

Importantly, structural stability of PNCs is slightly different from bulk perovskite. On the one hand, the large specific surface area could speed up decomposition.^[112] On the other hand, the large surface energy can stabilize the cubic phase.^[113] For instance, as mentioned before, bulk CsPbI₃ with a cubic phase is only stable at high temperature, and it tends to transform into a non-perovskite phase with a larger bandgap by reducing the temperature. However, CsPbI₃ NCs can maintain cubic crystal structure for some months in air.^[113]

Pressure can significantly induce a structural phase transition, thereby changing the optoelectronic properties of the corresponding perovskite materials, such as bandgap, carrier lifetime, photocurrent, electrical resistance, etc.^[114-117] For example, 0D Cs₄PbBr₆ NCs which show initially nonfluorescent property can obtain a distinct emission at high pressure (above 3.01 GPa). The reason is the large distortion of [PbBr₆]⁴⁻ octahedra due to the structural phase transition from rhombohedral to monoclinic. Moreover, the excited-state structural reorganization, which is required to trap an exciton, is considered to be smaller than the one of the ambient-pressure. Thus, Cs₄PbBr₆ NCs with high-pressure monoclinic structural phase exhibit photoluminescence.^[114]

3.4.2 Interface-Induced Instability

Perovskite interface is crucial for stability and performance of devices like solar cells (SCs), PDs, and LEDs. Here, we only focus on the interface between PNCs and their environments. The PNCs show high ionicity and structural instability. So, the interaction between the surfaces of PNCs and the capping ligands is ionic and labile, which is crucial to the stability of structure. First, we want to introduce the Covalent Bond Classification (CBC) to classify metal-ligand interactions, which was developed by Green.^[118, 119] According to CBC, ligands are classified as L-type, X-type, or Z-type, which depend on the amount of electrons that the neutral ligand contributes to the metal-ligand bond (2, 1 or 0, respectively).

Hens and Kovalenko et al. first studied the surface chemistry of CsPbX₃.^[47] They used ¹H solution nuclear magnetic resonance (NMR) spectroscopy to characterize the purity of sample, clarify the

surface chemistry, and estimate the influence of purification process on the surface composition. In short, they found that surface ligands binding to the CsPbBr₃ NC surface are highly dynamic, that is to say, ligands are lost during isolation and purification in an easy way. Both carboxylic acids and long-chain amines were required to stabilize the surface during purification, as well as sustaining optical and material integrity. They also measured the diffusion coefficient D of a molecule in NC suspension to further study the dynamic surface by using Diffusion Ordered NMR Spectroscopy (DOSY), because the diffusion coefficient of a bound ligand can be considered as the same as that of the whole object (PNC core with ligand shell). The diffusion coefficient D is associated with molecule size via the Stokes-Einstein equation with k_B the Boltzmann constant, T the absolute temperature, and f the friction coefficient:

$$D = \frac{K_B T}{f} \quad (3.3)$$

The value of D for oleylammonium bromide without CsPbBr₃ NCs and in the suspension was measured to be 361 and $166 \pm 18 \mu\text{m}^2 \text{s}^{-1}$, respectively. This indicated that surface ligands in the PNCs' solutions were not tightly attached on the surface but undergo a rapid exchange between free state and bound. This dynamic stabilization mechanism with oleylammonium bromide can well elucidate the fast halide exchange reaction during device fabrication.

3.4.3 Environmental Stability

The environmental stability of PNCs has become a primary concern for their applications in the real world. A comprehensive understanding of the degradation mechanism of PNCs including the degradation under moisture, oxygen and light exposure, allows for a rational design of stable PNCs implemented in quantum dot solar cells (QDSCs), Quantum dot light-emitting diodes (QLEDs), etc.

3.4.3.1 Moisture

Moisture, which exists everywhere in our life, is considered to be harmful to the stability of PNCs. Although some groups have reported that water can be valuable for perovskite device fabrication^[120-122], it is considered as a "toxicant" to PNCs, regardless of the duration of exposure and amount of water.^[123-125] The large perovskite crystals can be obtained with the assistant of moisture, because it can be absorbed within grain boundaries and then induce grain boundary creep and merge the adjacent grains together, as well as enhance the ion diffusion length by providing the aqueous environment.^[126] However, when exposed to the moisture atmosphere, the perovskite structure

showed a fast degradation, characterized by color change from black to yellow for perovskite structure like $\text{MAPbI}_{3-x}\text{Cl}_x$. Snaith et al. attributed the color change to the transformation of perovskite crystal structure to 0D system, where compounds are present as isolated octahedral. When water molecules are introduced into the crystal structure, they form weak hydrogen bonds to hydroscopic MA^+ , which lead to a bond dissociation between the crystal constituents.^[125] Although there are some discrepancies, an evident conclusion is that water worked as a catalysis in the process of degradation. Therefore, water only speeds up the decomposition of PNCs by carrying the proton of MA^+ to I^- and liberating CH_3NH_2 . Alberti et al. found that MAPbI_3 undergo a comparable degradation dynamics pathway, where the crystal structure of MAPbI_3 changed from tetragonal to cubic without hydration taking place.^[127] For all-inorganic perovskite materials like CsPbI_3 , water also catalyzed the conversion of $\gamma\text{-CsPbI}_3$ to $\delta\text{-CsPbI}_3$ illustrated by in-suit powder X-ray diffraction (PXRD) measurement.^[128]

3.4.3.2 Oxygen

The ground state lead-based perovskites show good stability in oxygen atmospheres. Li et al. reported that PL of CsPbBr_3 NCs showed no obvious decrease when exposed to the relative humidity (RH) levels of 60 and 80% for 8 hours.^[126] However, PL intensity increased under oxygen atmospheres, which was called the ‘oxygen boost’ effects.^[14] It was revealed by density functional theory (DFT) modelling that oxygen molecules effectively inactivated deep hole traps related to iodide interstitials by forming reasonably stable oxidized products in MAPbI_3 . Upon illumination in an inert atmosphere, some sub-band gap states are formed in MAPbI_3 .^[129] Then, the oxygen molecules could attenuate the trap density. Thus, suppression of traps led to brighter PL emission under oxidizing conditions.

However, the temporal “oxygen boost” effects only occurred at the beginning of illumination. Upon continuous illumination, the green film of CsPbBr_3 NCs would change to yellow soon (within 1 hour).^[126] Haque et al. combined experimental and computational methods and proposed the probable degradation mechanism as (see Figure 3.12a): (a) Oxygen diffusion and incorporation into the lattice, (b) photoexcitation of MAPbI_3 to create holes and electrons (c) superoxide formation from oxygen, and (d) reaction and degradation to layered PbI_2 , H_2O , I_2 and CH_3NH_2 .^[130]

3.4.3.3 Light

The stability issues against moisture and oxygen can be avoided by using encapsulation strategies, but the light stability of perovskite materials is still a serious topic.^[131] For the application as absorber

in SCs to capture solar energy and as convertor in LEDs to change the blue/UV light into various visible light, PNCs need a long-term stability under continue illumination. Thus, a deep understanding of the original reason for the photo-degradation of PNCs is of great importance to enhance the performance and lifetime of the PNCs-based optoelectronic devices.

The phenomenon of photo-induced “brightening” of the perovskite PL, called the light soaking effect, is widely reported in perovskite-based SCs and LEDs. For bulk perovskite, PL intensity of MAPbI₃ film would increase up to three orders of magnitude and PL lifetime would increase from several nanoseconds to several hundred nanoseconds upon light irradiation with an excitation power density of 0.01 to 1 W cm⁻². In addition, light-induced PL enhancement is reversibly enabled by switching off excitation light. The most interesting discovery is that switching the atmosphere between nitrogen and oxygen would also reverse the photo-induced “brightening” (Figure 3.12b).^[132] However, Mohite et al. have observed that the oxygen had minor effects on photo-induced ‘brightening’ due to the large-grain perovskite structures, preventing direct exposition to the external atmosphere.^[131] McGehee et al. has reported a similar phenomenon in MAPbI_{3-x}Br_x films. They also observed the X-ray diffraction (XRD) diffraction peaks split with light soaking, which means the crystal segregated into two crystalline phases (Figure 3.12c). After leaving for a few minutes in the dark, the XRD pattern reverted to their original shape.^[32]

The photo-induced ‘brightening’ of emission can be associated with an order-of magnitude decrease in density of trap state, which was caused by ion migration under illumination. Stranks et al. used confocal PL microscopy and time-of-flight secondary ion-mass spectrometry to study this phenomenon. From time-of-flight secondary ion mass spectrometry (ToF-SIMS) image of iodide distribution mapping and line scan (Figure 3.12d and Figure 3.12e), the areas exposed to high radiation showed depleted levels of iodide (lower than the background iodide levels), while the adjacent areas showed iodide-rich levels compared with the background iodide levels. This work provides obvious evidence for photo-induced halide migration in MAPbI₃. Thus, field-induced both vertical and lateral migration allowed a large number of iodide to occupy the vacancies and yield a decrease in density of vacancies, which can suppress the non-radiative recombination and enhance the intensity of PL.^[33]

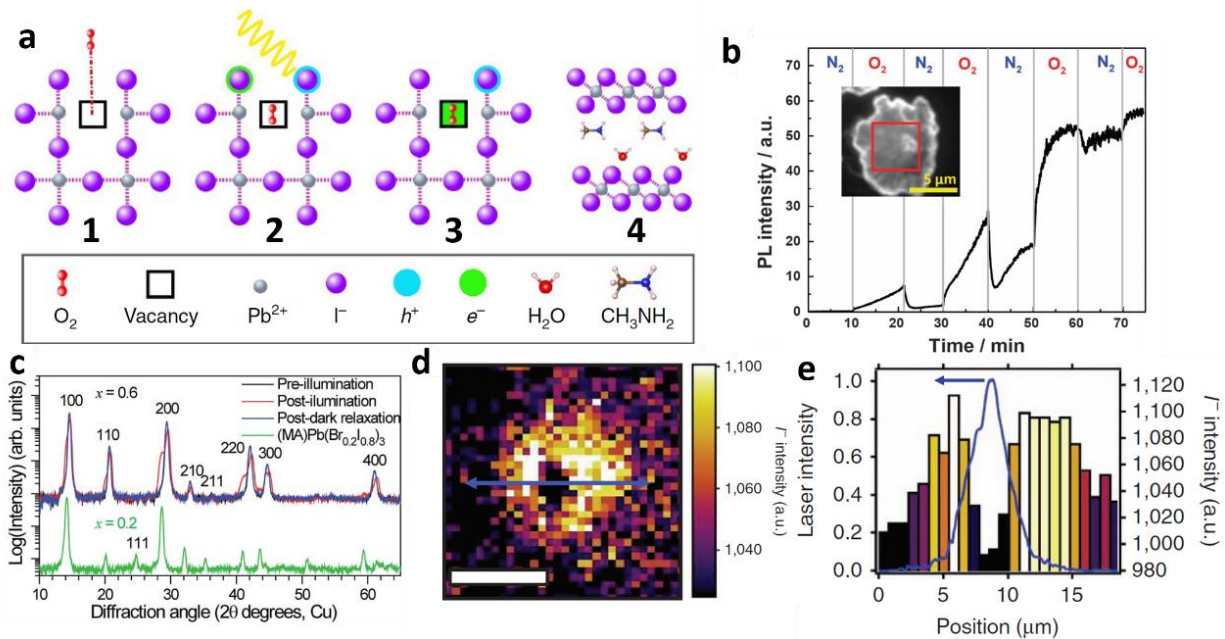


Figure 3.12: a) Oxygen-induced photo-degradation. Schematic representation of the reaction steps of O₂ with MAPbI₃. Reproduced under the terms of the CC-BY license.^[130] Copyright 2017, Springer Nature. b) The atmosphere effect on the PL enhancement of MAPbI₃. The atmosphere was switched between N₂ and O₂ at the time moments indicated by the gray vertical lines. The sample was continuously irradiated by 0.2 W cm⁻². Inset shows the PL micrograph of the sample and the selected region (red square) taken for the analysis. The sample was kept in N₂ for 5 min before the experiment. Reproduced with permission.^[132] Copyright 2015, Royal Society of Chemistry. c) XRD pattern of an x = 0.6 film before (black) and after (red) white-light soaking for 5 minutes at ~ 50 mW cm⁻², and after 2 h in the dark (blue). The XRD pattern of an x = 0.2 film (green) is offset for comparison. Reproduced under the terms of the CC-BY license.^[32] Copyright 2014, Royal Society of Chemistry. d) ToF-SIMS image of the iodide (I⁻) distribution summed through the film depth (the image has been adjusted to show maximum contrast), scale bar, 10 μm. e) Line scan of the blue arrow in c to show the iodide distribution (right axis). The measured spatial profile of the illumination laser (blue) is shown on the left axis. Reproduced under the terms of the CC-BY license.^[33] Copyright 2016, Springer Nature.

3.4.3.4 Temperature

Temperature is another factor that causes the degradation of PNCs. The all-inorganic PNCs have shown better thermal stability than organic-inorganic hybrid PNCs. For example, according to thermogravimetric analysis (TGA) measurements, the sublimation of HX and CH₃NH₂ for MAPbBr₃ and MAPbI₃ is around 220 °C^[133] and 250 °C^[134], respectively. But for CsPbX₃, the decomposition

temperature is over 500 °C because of the collapse of crystal structures.^[134] In addition, high temperature can even accelerate the degradation caused by oxygen and moisture.^[125] Interestingly, Schaller et al. studied the reversibility of PL intensity of CsPbBr₃ QDs under the operations of multiple heating and cooling steps. The sample lost ~5% of original PL intensity at 300 K when heated to 400 K and lost ~20% for 450 K. However, when the sample was heated to a higher temperature, the PL quenching was irreversible. The reason might be the desorption and decomposition of organic ligands above 450 K.^[135] The reversible PL feature is favoured by LED application, in which the operation of devices always caused a certain amount of temperature increase.

3.5 Encapsulation for improving the stability

Encapsulation is one of the most potential strategies to enhance the stability of PNCs. Recently, some great articles about encapsulation of PNCs have been published, introducing different methods and materials. Chen and Huang et al. have reviewed these works and present a nice summary as you can see in Figure 3.13.^[36] In this section, we focus on the most used materials for encapsulation.

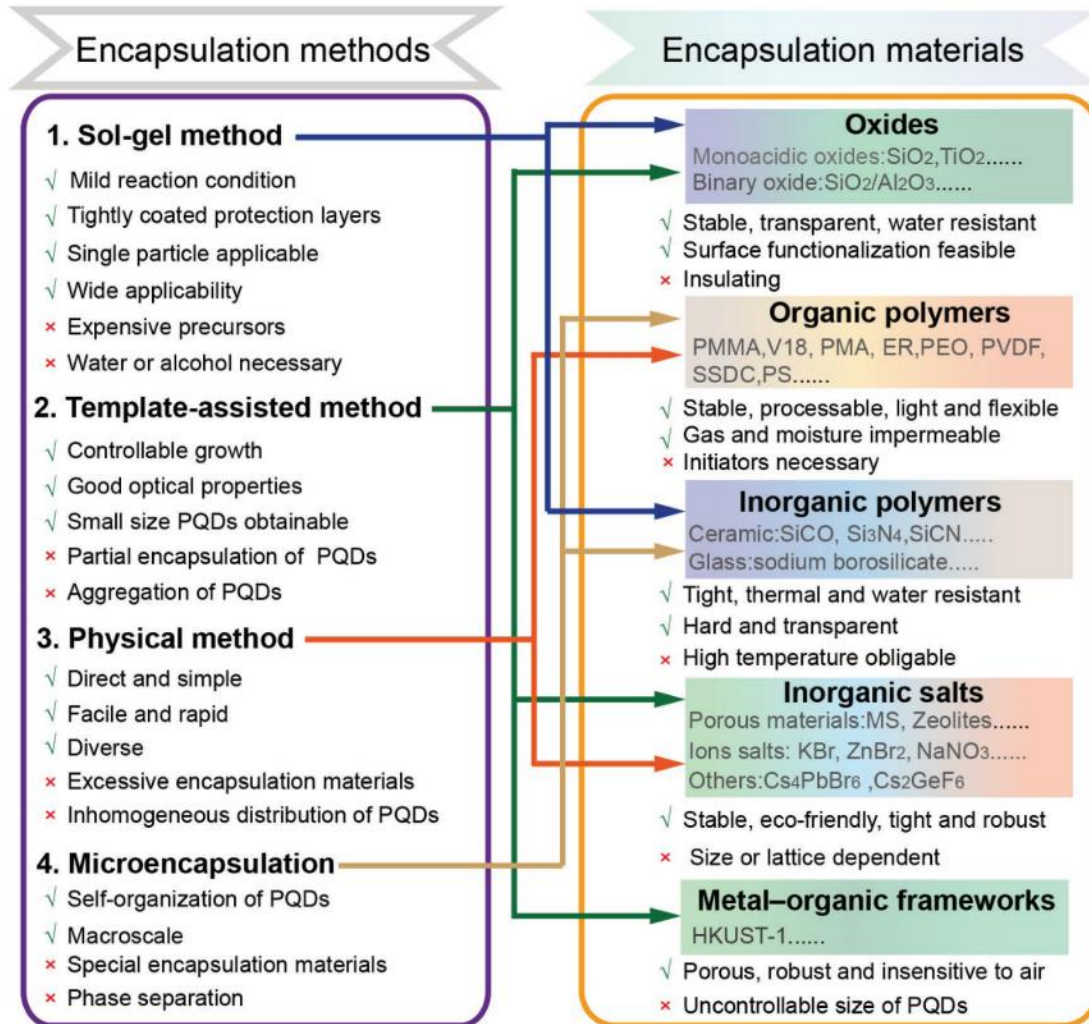


Figure 3.13: Relations between encapsulation methods and materials as well as their advantages and disadvantages. Reproduced with permission.^[36] Copyright 2019, Wiley-VCH.

3.5.1 Organics Protection

The mixture of NPs and polymers as composite material has been practiced for decades.^[136] In the early 1990s, Kamigaito et al. reported that the addition of mica to nylon can produce a five-fold increase in the tensile strength and yield of the material.^[137, 138] Actually, polymers can also work as surface coating to enhance the stability of PNCs.

Kovalenko et al. embedded CsPbX₃ NCs into poly(methyl methacrylate) (PMMA) polymer by a RT photo-induced polymerization and fabricated multi shapes of PNCs-PMMA composite material (Figure 3.14a). They also reported that CsPbX₃ NCs accelerated the rate of photopolymerization when comparing to the experiment with pure MMA.^[42] Zhong et al. reported an in-situ synthesis method of MAPbX₃ NCs, which were embedded in polyvinylidene fluoride (PVDF) matrix. They dissolved MAX, PbX₂ and PVDF in DMF. Subsequently, DMF solvent was dried under low pressure and MAPbX₃ NCs crystallized in PVDF film. A variety of composite films with colorful emissions on glass substrates were successfully fabricated (Figure 3.14b). Figure 3.14c and Figure 3.14d show the transmittance and PL emission spectra of these MAPbX₃/PVDF composite films.^[139] Polyvinyl pyrrolidone (PVP) was also used as capping ligand to protect PNCs, which was physically adsorbed and wrapped on the surface of PNCs.^[140, 141] Fu et al. synthesized CsPbBr₃ NCs via a simple one-step solution self-assembly process and used biocompatible PVP as ligand to control the co-precipitation of Cs⁺, Pb²⁺, and X⁻ species.^[140] Recently, He et al. used hundred-nanometer cellulose nanocrystal (CNC) instead of traditional ligands to synthesize MAPbBr₃ PQDs paper using a vacuum filtration growth method. The cellulose has a large amount of -HSO₃⁻ and -O⁻, which can work as ligands to control the formation of PNCs. After the solvent was removed, MAPbBr₃ PQDs were crystalized with the assistance of surface ligands. In addition, the MAPbBr₃ PQDs were also protected by CNC and their relative PL intensity remained at around 80% after exposure to an environment of 60% RH and 20 °C for 8 months.^[142]

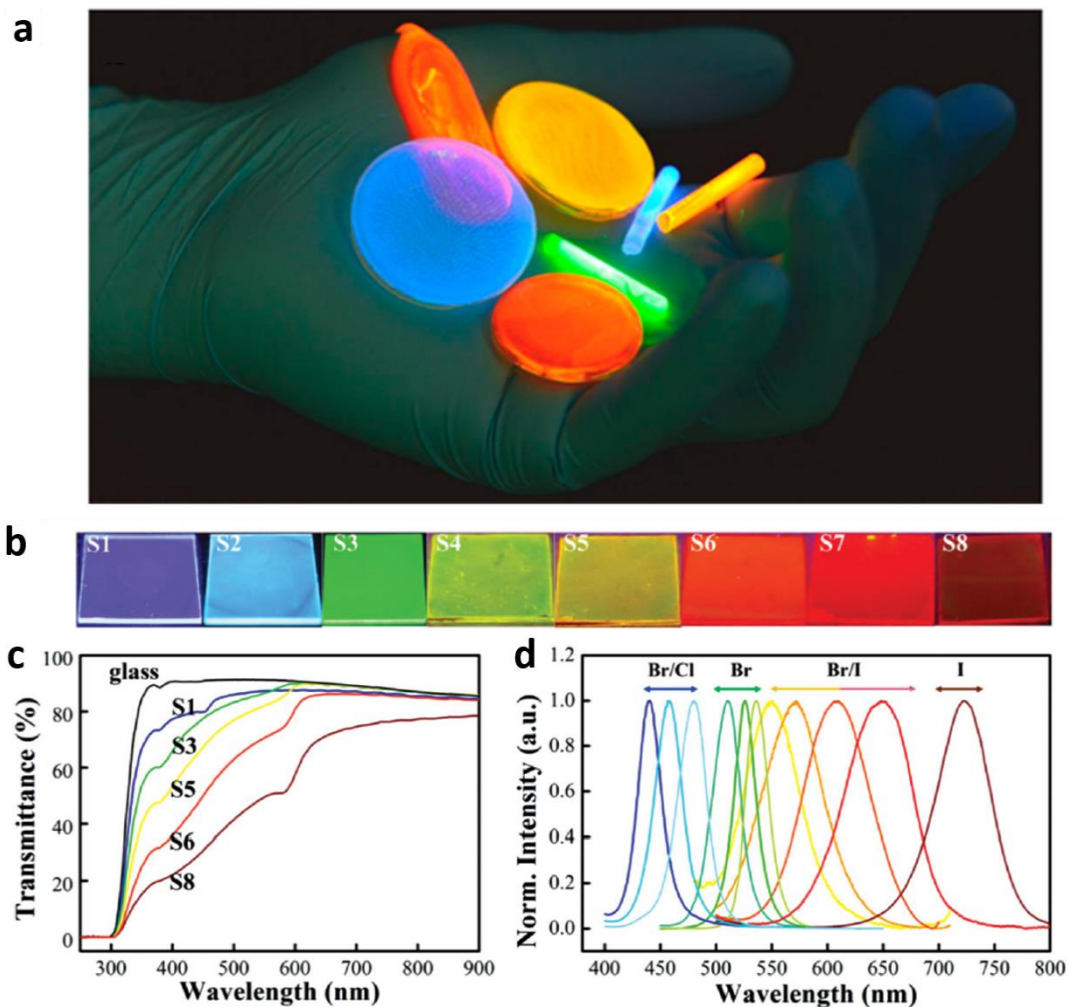


Figure 3.14: a) Photograph ($\lambda_{exc} = 365$ nm) of highly luminescent $CsPbX_3$ NCs-PMMA polymer monoliths obtained with Irgacure 819 as photoinitiator for polymerization. Reproduced with permission.^[42] Copyright 2015, American Chemical Society. b) Optical images under a UV lamp (365 nm) of color-tunable $MAPbX_3$ /PVDF composite films with different halogen constitutions on glass substrates (S1: $MAPbClBr_2$, S2: $MAPbCl_{0.5}Br_{2.5}$, S3: $MAPbBr_3$, S4: $MAPbBr_{2.7}I_{0.3}$, S5: $MAPbBr_{2.5}I_{0.5}$, S6: $MAPbBr_2I$, S7: $MAPbBr_{1.5}I_{1.5}$, S8: $MAPbI_3$). c) Transmittance spectra of the correlated composite films on glass substrate. d) PL spectra of the composite films. Reproduced with permission.^[139] Copyright 2016, Wiley-VCH.

3.5.2 Inorganics Protection

3.5.2.1 Silica

Among inorganic materials, silica is one of the best choices to cover the PNCs. Silica is widely distributed in nature and also possess excellent stability in the environment. It can work as a template and serve via a facile, complementary, non-colloidal, and ligand-free preparation route.^[143] In addition, silica with an excellent compatibility is accepted as “Generally Recognized As Safe” (GRAS) by the Food and Drug Administration (FDA). This material has been broadly utilized in cosmetics and also as food additives approved by FDA, which can make application of PNCs in bio-applications possible.

Liu et al. first used silica to protect PNCs. They mixed CsPbBr₃ QDs solution with the commercial mesoporous silica particles in hexane to synthesize CsPbBr₃-mesoporous silica composites (Figure 3.15a). The pore sizes of mesoporous silica are approximately 12 – 15 nm. This treatment can avoid halide exchange and increase the stability of QDs, which is of great importance for LED packaging.^[144] Kovalenko et al. used a related approach to introduce perovskite precursor into the pores of mesoporous silica, where PNCs can crystallize there (Figure 3.15b). In addition, the sizes of PNCs could be adjusted by mesoporous silica’s pore sizes, which also improved the uniformity of PNCs.^[143] Li et al. developed a novel SiO₂ encapsulation method by choosing tetramethyl orthosilicate (TMOS) as precursor to synthesize silica cover on the MAPbX₃ PNCs. TMOS was used as the precursor, and its hydrolysis rate is much quicker than that of tetraethyl orthosilicate (TEOS). Thus, it can avoid a higher water consumption rate, which can damage perovskite’s phase structure. After 4 days, the green light emission of the pure PQDs solution totally disappeared, but the PQDs solutions with TEOS and TMOS still emitted green light, in which TMOS-modified sample showed better stability (Figure 3.15c).^[37] Yu et al. chose (3-aminopropyl) triethoxysilane (APTES) as both capping agent for inorganic PQDs and precursor for silica matrix. They mixed APTES with PbX₂ precursor in a water-free system to synthesize PNCs. But after crystallization of PNCs, the system was opened to air and stirred for three hours for the hydrolytic reaction (Figure 3.15d and Figure 3.15e). The stability of the PNCs improved that the luminescence of PNC with silica showed no obvious reduction after exposure to air for ninety days.^[145]

Zhang et al. developed an interfacial synthesis of CsPbX₃/SiO₂ Janus NCs by treating a mixture of Cs₄PbX₆ NCs and alkoxide with water. The as-obtained material exhibited significantly enhanced PL stability against damages by air, water, and light treatment. However, the CsPbX₃ NCs were partially

covered with oxides, the long-term stability of product remained as an issue.^[146] Zhang's group focused on the PNCs/Silica combination strategies and designed a facile one-pot synthesis of CsPbBr₃@SiO₂ core-shell NPs. They injected a mixture of CsBr, PbBr₂, OA, OAm, DMF, and ammonia solution into toluene containing TMOS and successfully obtained monodisperse CsPbBr₃@SiO₂ core-shell NPs, which showed excellent stability in humid air or even under ultrasonication in water.^[147]

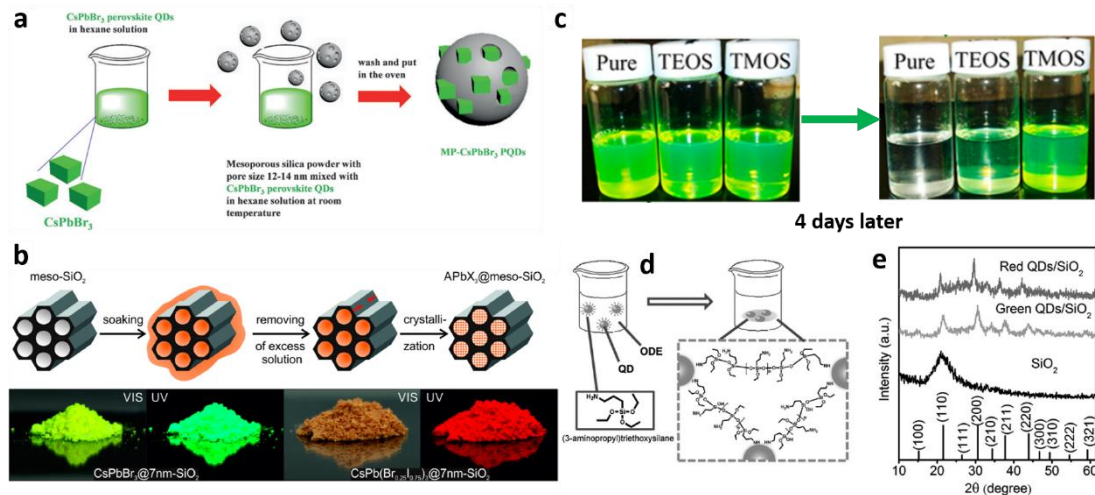


Figure 3.15: a) The synthesis process of mesoporous silica green PQD nanocomposite (MP-PQDs). Reproduced with permission.^[144] Copyright 2016, Wiley-VCH. b) Schematic of the template-assisted synthesis of APbX₃ NCs (A = Cs⁺, MA⁺ or FA⁺; X = Br or I) in the pores of mesoporous silica (up) and the photographs of mesoporous silica impregnated with CsPbBr₃ (left) and CsPb(Br_{0.25}I_{0.75})₃ NCs (right) under daylight and under UV illumination (down). Reproduced with permission.^[143] Copyright 2016, American Chemical Society. c) Optical images of the colloidal MAPbBr₃-QD solutions with TEOS and TMOS before and after 4 days. Reproduced with permission.^[37] Copyright 2016, American Chemical Society. d) Schematic illustration of formation of QD/silica composites. e) XRD patterns of SiO₂, Red QDs/SiO₂, and Green QDs/SiO₂. Reproduced with permission.^[145] Copyright 2016, American Chemical Society.

3.5.2.2 Salts

Except for silica, Zhong et al. used NaNO₃ as the matrix to protect MAPbBr₃ PNCs owing to the virtue of its transparency, low refractive index, and non-toxicity. The NaNO₃ could also be dissolved in DMF, which made the one-step reprecipitation procedure achievable for fabrication of MAPbBr₃/NaNO₃ nanocomposites (Figure 3.16a). This strategy was extremely fast, facile and efficient that the MAPbBr₃/NaNO₃ composites could be formed immediately after pouring the poor solvent toluene

into the precursor. The sizes of MAPbBr₃ NCs were 30 to 50 nm and they were homogeneously distributed in the matrix. The NaNO₃ matrix made PNCs highly resistant to heat, light, and polar solvent, like chloroform.^[148] Chen et al. realized the in-situ crystallization of CsPbBr₃ QDs among a particularly designed TeO₂-based glass matrix (Figure 3.16b). In addition, the melting temperature of TeO₂-based glass could be lowered down to 650 °C, comparing to high melting temperature (up to 1100 °C) of other commonly used glass hosts, which could avoid the volatilization of Br sources and increase the amount of crystallized CsPbBr₃ QDs in the glass. The CsPbBr₃ QD-embedded glasses (QDs@glass) showed a high PLQY of ~70%, superior photo/thermal stability and excellent water resistance.^[149]

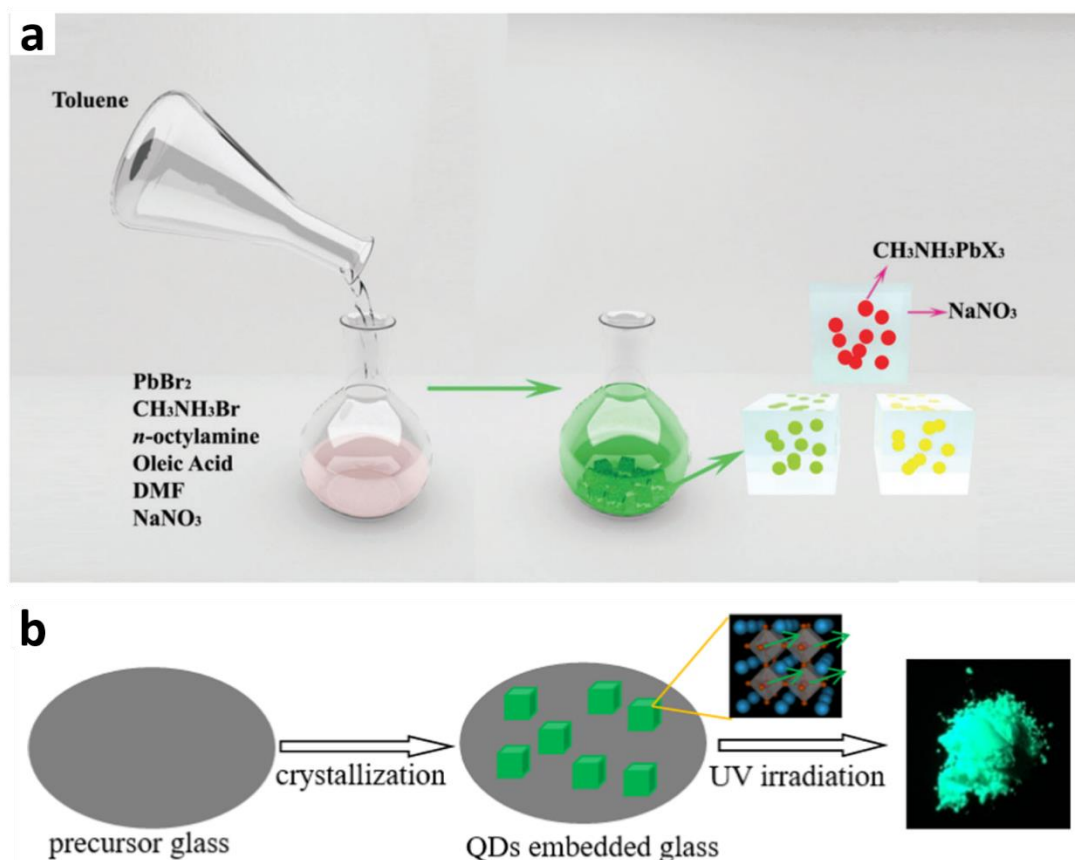


Figure 3.16: a) Scheme of a one-step reprecipitation procedure for synthesis of MAPbBr₃/NaNO₃ nanocomposites. Reproduced with permission.^[148] Copyright 2016, Royal Society of Chemistry. b) Glass crystallization strategy to fabricate QD-embedded glass: CsPbX₃ crystal structure and luminescent photograph of QDs@glass powder under irradiation of UV lamp (365 nm) are also provided. Reproduced with permission.^[149] Copyright 2018, American Chemical Society.

Hou et al. chose magnesium silicate as the protector for MAPbX₃ PQDs because this material is a transparent and ecofriendly inorganic material, with a unique structure and good thermal stability. They developed a simple strategy that incorporated MAPbX₃ PQDs into magnesium silicate hollow spheres (MSHSs) in toluene via a modified ligand-assisted reprecipitation method at ambient condition. These nanocomposites (MAPbX₃ QDs-MSHSs) showed outstanding PL that the emission peaks were broadly tunable in the blue-to-red region and the quantum yields (QY) was above 50%, which also had surprisingly high thermal stability and high photostability (Figure 3.17).^[150]

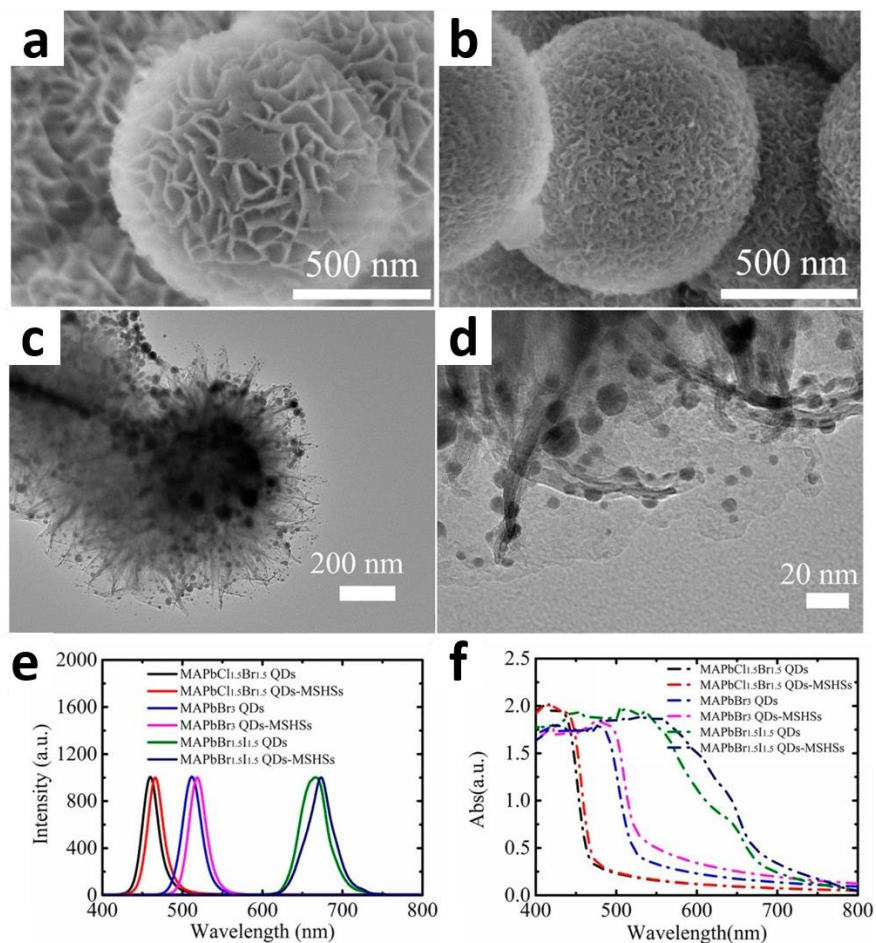


Figure 3.17: a) Scanning electron microscope (SEM) photograph of magnesium silicate hollow spheres (MSHSs). b) SEM photograph of MAPbBr₃ QDs-MSHSs nanocomposites. c) TEM and d) HRTEM photographs of MAPbBr₃ QDs-MSHSs nanocomposites. e) PL spectra and f) optical absorption of MAPbX₃ QDs and MAPbX₃ QDs-MSHSs nanocomposites with different halide components. Reproduced with permission.^[150] Copyright 2018, American Chemical Society.

3.5.2.3 Perovskite

Some stable perovskite materials can also serve as protectors for PNCs. Sun and Zeng et al. reported a ligand-free low-temperature solution-growth CsPbBr₃/Cs₄PbBr₆ perovskite nanocomposites (Figure 3.18). They incorporated CsPbBr₃ QDs into matrix of Cs₄PbBr₆ PNCs by low temperature solution-phase synthesis, which could significantly improve the thermal stability and photostability of PQDs. CsPbBr₃/Cs₄PbBr₆ nanocomposites showed high PLQY of up to ~55% and CsPbBr₃ QDs exhibited a steady stimulated emission profile irrespective of temperature change, which was beneficial to long-term stable operating optoelectronic devices.^[151] Zhong et al. also used a slow-cooling method to grow Cs₄PbBr₆ assisted by HBr. They found the nonstoichiometry of original Cs₄PbBr₆ crystals led to the formation of CsPbBr₃ NCs in Cs₄PbBr₆ matrix, which was supported by evolution process and structural characterizations. They combined highly luminescent Cs₄PbBr₆ crystals with embedded CsPbBr₃ NCs as green emitters, K₂SiF₆:Mn⁴⁺ (KSF) phosphor as red emitters, and GaN chips as blue emitters to fabricate White LED devices, which generated white lights of high quality with luminous efficiency of ~151 lm W⁻¹ and color gamut of 90.6% Rec. 2020 at 20 mA. These devices had improved efficiency and stability than LEDs based on traditional PNCs with comparable color quality.^[152]

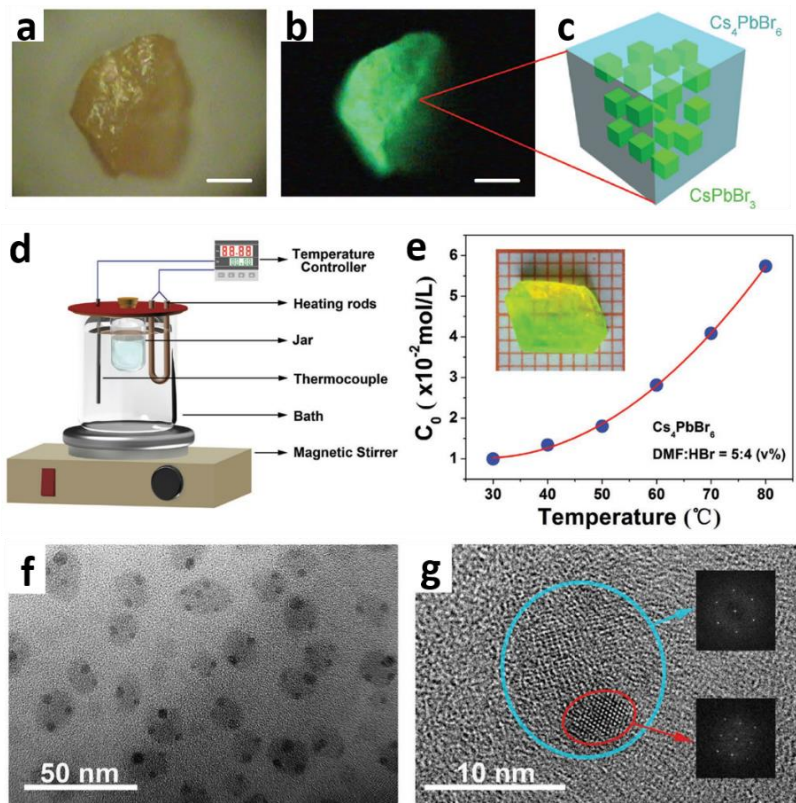


Figure 3.18: a) The optical image of a representative CsPbBr₃/Cs₄PbBr₆ nanocomposite microcrystal. Scale bar: 50 μm. b) The PL image of the CsPbBr₃/Cs₄PbBr₆ nanocomposite microcrystal. Scale bar: 50 μm. c) The schematic structure of CsPbBr₃ nanocrystals embedded in Cs₄PbBr₆ host matrix for CsPbBr₃/Cs₄PbBr₆ perovskite nanocomposites. Reproduced with permission.^[151] Copyright 2017, Wiley-VCH. d) Schematic illustration of the setup for crystal growth. e) Solubility curves of Cs₄PbBr₆ in mixed HBr-DMF solution, inset: the as-fabricated green emissive crystal. The grid in the inset is 1 mm. f) Typical TEM images of the particles processed from green emissive Cs₄PbBr₆ crystals with embedded CsPbBr₃ NCs. g) HRTEM image of a typical particle. The inset in the bottom right corner is the corresponding FFT image of CsPbBr₃ and the top right corner is the corresponding FFT image of Cs₄PbBr₆ crystals with embedded CsPbBr₃ NCs. Reproduced with permission.^[152] Copyright 2018, Wiley-VCH.

3.6 Application

Perovskite nanocrystals possess excellent optoelectronic properties, i.e., tunable bandgaps, narrow emission, strong light-absorption coefficients, high PLQYs, and high defect tolerance, which paved the way for designing highly efficient PNC-based optoelectronic devices, for example, laser^[153, 154], field-effect transistor (FET)^[155-158], SCs, LEDs, and PDs. The promising progress and recently reported achievements in the application fields of SCs, LEDs, and PDs are briefly reviewed in the following sections.

3.6.1 Solar Cells (SCs)

Perovskite photovoltaic technology achieved a rapid and breakthrough development since 2006 that the first application of these materials in SCs was reported.^[26] The power conversion efficiency (PCE) of single-junction perovskite solar cells (PSCs) has hit 25.5%^[4], which is comparable to the performance of other photovoltaic technologies (23.35% for copper indium gallium selenide, 26.7% for crystalline silicon, and 29.1% for GaAs solar cells^[159]). Significantly, the low-cost solution-processed fabrication of PSCs shows priority to those traditional photovoltaic devices, which appeals to both academic communities and industrial corporations. However, different issues such as, most importantly, the stability needs to be addressed towards PSCs commercialization. As already discussed in section 3, the main problem of instability is the perovskite structure, originating from their low lattice energies and intrinsic ionic bond properties. In this regard, applying the PNCs instead of bulk perovskite as light-absorber in solar cells can be a potential route towards increasing stability. For example, CsPbI₃ QDs with a high specific surface area have more stable cubic structure at RT comparing to bulk CsPbI₃, due to the large surface energy.^[42] The performance of PNC-based SCs reported in recent years is summarized in Table 3.1.

Luther et al. led the research on substituting bulk perovskite materials with PNCs as light-absorber in PSCs. They used the hot-injection method, which was developed by Kovalenko et al.^[42], to synthesize cubic-phase CsPbI₃ NCs and improve the purification method via the utilization of methyl acetate (MeOAc) as anti-solvent to wash off excess unreacted precursors without causing agglomeration. The purified CsPbI₃ QDs retained the cubic structure in air and even at low temperatures for some months, and also showed efficient dot-to-dot electronic transport. First, the CsPbI₃ QDs dispersed in octane were spin coated to deposit the photo-active-layer films. Then, films were dipped in a saturated MeOAc solution of Pb(NO₃)₂ or Pb(OAc)₂ to enhance the surface

passivation. The champion solar cell possessed an open-circuit voltage (V_{oc}) of 1.23 V and a PCE of 10.77% with an active area of 0.10 cm² cell characterized in ambient conditions.^[113] The same group further optimized the quality of QDs-based photo-active layers via A-site cation halide salt (AX) treatments, where A represents FA⁺, MA⁺, or Cs⁺ and X represents I⁻ or Br⁻. This post-treatment tuned and greatly enhanced electronic coupling among QDs. Consequently, the carrier mobility and therefore the short-circuit current density (J_{sc}) of device were enhanced. The FAI treated device obtained the highest PCE of 13.4%, which was a record-efficiency for QDSCs at that time. A notably reduced hysteresis between reverse and forward scans and a better agreement between the stabilized power output (SPO) and reverse J - V scan were obtained after the FAI post-treatment.^[160] To better understand the surface chemistry of PQDs in this system, they employed various spectroscopic techniques to present a molecular picture of QD surface according to the results. Interestingly, they found that controlling the atmospheric moisture was paramount for fabricating high-efficiency QDSCs because water assisted the process by hydrolysis of MeOAc to make methanol and acetic acid. Then, oleate ligands on the surface of QDs were replaced by acetic acid, while the native oleylammonium ligands remain until exchanged with smaller FA⁺ during the final treatment. They also realized that the time for the final treatment should be controlled because the treatment led to a tighter coupled QD regime, which would turn into a perovskite film after longer treatment.^[161]

Using a different strategy, Liu et al. used high mobility micrometer-sized graphene (μ GR) sheets to crosslink CsPbI₃ QDs. The conductivity was enhanced by designing an effective channel for carrier transport. Meanwhile, the stability against moisture and high temperature was also improved by keeping QDs from agglomeration. Consequently, the performance of the CsPbI₃ QDs- μ GR was improved by over 12%, reaching an 11.4% PCE compared to 10.17% PCE for control device. In regard to stability, over 98% of the initial efficiency of optimized device remained after one-month storage in N₂ atmosphere. For moisture stability, when exposed to relative humidity of 60%, PCE of control devices decreased by 90% of initial PCE while the μ GR/CsPbI₃ device decreased by 10% only. For thermal stability, optimized μ GR/CsPbI₃ solar cells maintained 85% of its initial PCE after they were heated at 100 °C for 3 hours while the reference cell performance decreased to only 20% of the initial value after the same treatment.^[162]

However, the Cs-based PNCs have a relatively larger bandgap and short carrier lifetime compared to the organic-inorganic hybrid ones. For photovoltaic application, the FAPbI₃ has a more desirable bandgap of around 1.5 eV.^[163-165] Yang et al. developed the FAPbI₃ QDSCs for the first time. The

absorption edge of FAPbI₃ QDs is 1.55 eV, which is superior to CsPbI₃ QDs (1.80 eV). Furthermore, the time-resolved photoluminescence (TRPL) decay showed the FAPbI₃ QDs has a longer carrier lifetime. By solvent-treatment to control ligands of FAPbI₃ QDs, the best device yielded a PCE of 8.38% with the SPO of 8.05%. Surprisingly, FAPbI₃ QDs and devices showed better stability than bulk FAPbI₃ film and devices, which can turn to yellow phase easily under ambient atmospheres.^[163] In another work published by Yang et al., the PCE of FAPbI₃ QDSCs was boosted to 12.7% by adding a conjugated small molecule 2,2'-[[[6,6,12,12-tetrakis(4-hexylphenyl)-6,12-dihydrodithieno[2,3-d:2',3'-d']-s-indaceno[1,2-b:5,6-b']dithiophene-2,8-diyl]bis[methyldiylidene(3-oxo-1H-indene-2,1(3H)-diylidene)]]bis[propanedinitrile] (ITIC) into QDs film, which can effectively enhance charge separation.^[164]

Perovskite materials are tunable in A, B, or X sites, which gives them exceptional optoelectronic versatility. For the X-site, Konstantatos et al. synthesized mixed-halide (CsPbBrI₂) NCs by using halide exchange reactions of concentrated CsPbBr₃ NCs solutions with I-. To study their photovoltaic performance, solar cells were fabricated by coating CsPbBr_xI_{3-x} NCs layer through either a single-step method or layer-by-layer coating method. The best device showed the PCE of 5.3% along with a V_{oc} of 1.31 V via the single-step deposition of CsPbBrI₂ NCs. However, the devices were current-limited confirmed by the external quantum efficiency (EQE) spectrum, and also showed an obvious hysteresis in both types of devices.^[166]

Luther et al. reported the tunable A-site alloys of Cs_{1-x}FA_xPbI₃ NCs by the cation-exchange approach. The Cs_{1-x}FA_xPbI₃ NCs showed adjustable emission in the red and near-infrared region from 650 and 800 nm as the value of X increases from 0 to 1. They estimated the activation energy related to the alloying process to be ~0.65 eV, which is higher than that associated with halide exchange.^[165] A controllable synthesis of Cs_{1-x}FA_xPbI₃ QDs film with the whole composition range, even in the form of spatial heterostructure, was achieved by using Cs_{1-x}FA_xPbI₃ QDs solution. In this regard, Luther et al. used a layer-by-layer deposition method to fabricate PQSCs. They demonstrated SCs with abrupt compositional changes throughout the perovskite film, by which they can control the composition of the photo-active layer to form an internal heterojunction. By optimizing composition of each heterostructure-component, more efficient charge separation at interface was achieved, resulting in enhanced photocarrier harvesting. As a result, they obtained a record PCE of 17.39% with a SPO of 15.52%.^[167] Wang et al. reported an OA ligand-assisted cation-exchange strategy to synthesize Cs_{1-x}FA_xPbI₃ QDs with high quality. They found that cross-exchange of cations is facilitated in an OA-rich

environment, enabling a fast formation of $\text{Cs}_{1-x}\text{FA}_x\text{PbI}_3$ QDs with decreased defect density. The best $\text{Cs}_{1-x}\text{FA}_x\text{PbI}_3$ QDSCs achieved a certified PCE of 16.6% without obvious hysteresis.^[168] Finally, it is worthwhile to mention that the PNCs are also used in dye sensitized solar cells as an absorber.^[169-171]

Besides directly serving as the absorber in a photovoltaic device, PNCs are also used as raw materials to fabricate bulk films.^[161, 172-176] Kamat et al. deposited CsPbBr_3 QDs layer by layer, followed by annealing to cast stable films of desired thickness, which solve the problem of CsPbBr_3 deposition via solution processing due to the poor solubility of CsBr .^[175] In addition, PNCs have been used as the interface modifier to engineer the band alignment.^[177-179] Liu et al. developed a bulk–nanosheet–quantum dots or 3D–2D–0D dimension profiled interface, which promoted carrier extraction by introducing an electric field in the device, leading to increased current and a PCE as high as 12.39% for bulk CsPbBr_2 PSCs.^[178]

Table 3.1 Performance of representative PNC-based solar cells.

PNCs	Synthesis Method	Nanocrystal size (nm)	Device Structure	Scan direction	V _{oc} (eV)	J _{sc} (mA cm ⁻²)	FF (%)	PCE (%)	SPO (%)	Area (cm ²)	Ref.
CsPbI ₃	Hot injection	10	FTO/TiO ₂ /CsPbI ₃ /Spiro-OMeTAD/MoO _x /Al	R	1.23	13.47	65	10.77	8.16	0.1	[113]
CsPbI ₃	Hot injection	30	FTO/TiO ₂ /FAI-coated CsPbI ₃ /Spiro-OMeTAD/MoO _x /Al	R	1.16	15.25	76.6	13.58	13.43	0.058	[160]
CsPbI ₃	Hot injection	~ 20	FTO/TiO ₂ /CsPbI ₃ /Spiro-OMeTAD/Au	R	1.18	15.5	73.0	13.47	12.37	0.058	[165]
				F	1.17	15.2	66.0	11.75			
CsPbI ₃	Hot injection	10	FTO/TiO ₂ /CsPbI ₃ -μGR/PTAA/Au	-	1.18	13.59	72.6	11.64	-	0.09	[162]
CsPbI ₃	Hot injection	~ 8	FTO/TiO ₂ /CsPbI ₃ /PTB7/MoO ₃ /Ag	-	1.27	12.39	80.0	12.55	12.35	0.0725	[180]
CsPbI ₃	Hot injection	9.86	FTO/c-TiO ₂ /α-CsPbI ₃ /Spiro-OMeTAD/Au	R	1.04	16.98	67.2	11.87	11.00	-	[181]
				F	1.03	16.64	62.2	10.70			
CsPbI ₃	Hot injection	-	FTO/TiO ₂ /CsPbI ₃ /PTAA/MoO ₃ /Ag	R	1.25	14.96	75.6	14.10	13.90	0.0725	[182]
				F	1.25	14.89	75.3	14.00			
CsPbI ₃	Hot injection	10	FTO/TiO ₂ /Yb-doped CsPbI ₃ /PTB7/MoO ₃ /Ag	-	1.25	14.18	74.0	13.12	-	0.0725	[183]
CsPbI ₃	Hot injection	12	FTO/TiO ₂ /CsPbI ₃ /Spiro-OMeTAD/Au	-	1.11	14.80	74.0	12.15	-	0.16	[184]
CsPbI ₃	Hot injection	9.3	FTO/c-TiO ₂ /CsPbI ₃ /Spiro-OMeTAD/Au	-	1.10	11.30	66.0	8.10	-	0.11	[185]
CsPbI ₃	Hot injection	10	FTO/TiO ₂ /CsPbI ₃ /Spiro-OMeTAD/Au	-	1.11	14.40	70.0	11.20	10.60	0.12	[186]
CsPbI ₃	Hot injection	9	ITO/PTAA/CsPbI ₃ /C60/BCP/Ag	R	1.11	11.80	73.5	9.60	9.20	0.054	[187]
				F	1.10	11.62	73.9	9.42			
			ITO/PTAA/CsPbI ₃ /C60/BCP/Graphene	R	1.09	10.90	57.5	6.80	6.40		
				F	1.08	10.79	57.7	6.73			
CsPbI ₃	Hot injection	10	FTO/c-TiO ₂ /CsPbI ₃ /Spiro-OMeTAD/MoO _x /Au	-	1.18	15.21	74.2	13.3	-	0.096	[188]
CsPbI ₃	Hot injection	9.1	FTO/c-TiO ₂ /s-m-TiO ₂ /CsPbI ₃ /Spiro-OMeTAD/Au	R	1.06	17.77	75.8	14.32	13.87	-	[189]
				F	1.06	17.73	74.0	13.89			

PNCs	Synthesis Method	Nanocrystal size (nm)	Device Structure	Scan direction	V_{oc} (eV)	J_{sc} (mA cm ⁻²)	FF (%)	PCE (%)	SPO (%)	Area (cm ²)	Ref.
CsPbI ₃	Hot injection	9.5	FTO/NiO _x /CsPbI ₃ /C60/ZnO/Ag	-	1.19	14.25	77.6	13.10	-	0.056	[190]
CsPbI ₂ Br	Hot injection	13	FTO/TiO ₂ /CsPbI ₂ Br/Spiro-OMETAD/Au	-	1.30	5.32	77.0	5.34	-	0.0314	[166]
CsPbI ₂ Br	Hot injection	10.3	ITO/TiO ₂ /CsPbI ₂ Br/P3HT/Au	R	1.20	14.22	71.3	12.2	10.20	-	[191]
				F	1.13	13.07	58.0	8.5			
CsPbBr ₃	One-step injection	15 - 20	FTO/c-TiO ₂ /CsPbBr ₃ /Spiro-OMeTAD/Au	R	1.54	5.65	62.4	5.42	~3.60	0.0935	[192]
				F	1.31	4.77	38.1	2.37			
CsPbBr ₃	Hot injection	10	FTO/c-TiO ₂ /CsPbBr ₃ /Spiro-OMeTAD/MoO ₃ /Au	-	0.90	7.38	40.0	2.65	-	0.06	[193]
FAPbI ₃	Hot injection	~20	FTO/TiO ₂ /FAPbI ₃ /Spiro-OMeTAD/Au	R	1.12	11.81	64.0	8.52	8.83	0.058	[165]
				F	1.12	11.85	68.0	9.01			
FAPbI ₃	Hot injection	12.8 - 17.7	ITO/SnO ₂ /FAPbI ₃ /Spiro-OMeTAD/Au	-	1.10	11.83	64.4	8.38	8.05	-	[163]
FAPbI ₃	Hot injection	14	ITO/SnO ₂ /FAPbI ₃ (ITIC mixed)/Spiro-OMeTAD/Ag	-	1.10	15.40	74.8	12.7	12.70	-	[164]
Cs _{0.75} FA _{0.25} PbI ₃	Hot injection	~ 20	FTO/TiO ₂ /Cs _{0.75} FA _{0.25} PbI ₃ /Spiro-OMeTAD/Au	R	1.15	14.36	68.0	11.14	10.93	0.058	[165]
				F	1.14	14.23	66.0	10.77			
CsPbI ₃ /FAPbI ₃	Hot injection	-	FTO/TiO ₂ /CsPbI ₃ /FAPbI ₃ /PTAA/MoO ₃ /Ag	R	1.22	17.26	74.0	15.60	15.10	0.0725	[194]
				F	1.20	17.21	72.0	14.90			
Cs _{0.25} FA _{0.75} PbI ₃ /CsPbI ₃	Hot injection	-	ITO/TiO ₂ /Cs _{0.25} FA _{0.75} PbI ₃ /CsPbI ₃ /Spiro-OMeTAD/MoO ₃ /Al	-	1.20	18.91	76.0	17.39	15.52	0.059	[167]
Cs _{1-x} FA _x PbI ₃	Hot injection	14	ITO/SnO ₂ /Cs _{1-x} FA _x PbI ₃ /Spiro-OMeTAD/Au	-	1.17	18.30	78.3	16.60	-	0.058	[168]

3.6.2 Light-emitting Diodes (LEDs)

In the past few years, wurtzite or zinc blende Cd-based QDs, for example, CdS, CdSe, CdTe, Cu-doped ZnInS, and InP@ZnSeS, have been the dominant materials for quantum dot based light-emitting diodes (QLEDs), which cost lots of time and efforts to synthesize.^[195] PNCs have the merit of facile synthesis procedure and superior optical performance, like adjustable emission wavelength, high brightness and color purity, and high defect tolerance. These advantages make PNCs a promising alternative to conventional materials. Comparing to the bulk perovskite LEDs, where the excitons formed by injected carriers (in electrical excitation) are able to dissociate back to free charge carriers easily, the charge carriers are confined in a small domain by the grain boundary and surface ligands in PNCs with particle size from several to tens of nanometers. This importance can significantly increase the luminescence efficiency.

The initial attempts to fabricate perovskite-based light-emitting diodes (PeLEDs) should date back to over twenty years ago; however, electroluminescence could only be obtained at liquid nitrogen temperature^[196] and at very high applied voltage.^[197] The massive research on PSCs triggered a huge progress also in the field of PeLED, started from 2009. In 2014, Friend et al. highlighted the truth that an efficient photovoltaic material can also be a good light emitter. They reported high-brightness LEDs based on solution-processed perovskites and demonstrated electroluminescence in the near-infrared, red and green by adjusting the anion compositions of perovskite.^[13] This work started intensive research on PeLEDs. Table 3.2 summarizes the performance of PNC-based LEDs in recent publications. In the following, just a few examples of important strategies and achievements are reviewed.

In 2015, for the first time, Zeng et al. reported the QLED based on all-inorganic perovskite cesium lead halide (CsPbX_3 , X = Cl, Br, I) nanocrystals. The typical QLED device composed of ITO/PEDOT:PSS/poly(9-vinylcarbazole)(PVK)/QDs/TPBi/LiF/Al exhibited blue, green, and yellow electroluminescence, which was achieved by controlling the particle sizes and varying the anion element composition. In more details, PL peak shifted to shorter or longer wavelength sides when the size of QDs was decreased or increased, respectively, and the PL peak shifted to longer or shorter wavelength sides when the I anions or Cl anions were introduced into the CsPbBr_3 PNCs. These devices showed the luminance of 742 cd m^{-2} , 946 cd m^{-2} , and 528 cd m^{-2} , with EQE of 0.07%, 0.12%, and 0.09% for the blue, green, and red LEDs, respectively.^[198]

The surface ligands of PNCs play a crucial role in the performance of QLEDs. Normally, surface ligands of PNCs have double-side effects on QLEDs, for instance, a certain amount of ligands are required to provide sufficient surface passivation but excessive ligands will lead to low conductivity. Bakr et al. introduced a halide ion pair (e.g., di-dodecyl dimethyl ammonium bromide (DDAB)) to cap CsPbX₃ QDs by ligand-exchange strategy. DDAB is a relatively short ligand, thereby facilitating carrier transport in the QD film to obtain high-performance PeLEDs. As a result, the device based on these halide-ion-pair-capped CsPbBr₃ QDs achieved a maximum EQE of 3.0% and luminance of 330 cd m⁻², which is much better comparing to all-inorganic PQD LEDs without ligand exchange.^[199] Except for replacing longer ligand with shorter ligand, Zeng et al. succeeded in controlling the ligand density of QDs film to balance surface passivation and carrier injection by a highly efficient solution-processed treatment. After screening various solvents, they chose the combination of hexane and ethyl acetate as solvent for QDs treatment to control surface ligand density. With proper treatment, the QDs solution stability, PLQYs, film uniformity, and microstructure were all improved. At the same time, the EQE and current efficiency were also increased from 0.12% to 6.27% and from 0.43 cd A⁻¹ to 13.3 cd A⁻¹, respectively, comparing to the QDs using one cycle of acetone treatment.^[200]

On the other hand, PNCs are believed to be potential alternative down-conversion materials in phosphor-converted light-emitting diodes (pc-LEDs) for lighting and next-generation display technology. The advantageous properties such as narrow emission bandwidth and high PLQYs, enable PNCs to work as color converters in pc-LEDs. In 2015, Dong et al. used the LARP method to synthesize brightly luminescent and color-adjustable MAPbX₃ (X = Br, I, Cl) QDs with absolute QY up to 70% at RT and low excitation fluencies. The as-fabricated MAPbBr₃ QDs with the particle size of 3.3 nm had a Br-rich surface with the Br/Pb molar ratio of 3.5. Through analysing the temperature-dependent emission spectra, they reported that the MAPbBr₃ QDs possess an exciton binding energy of ~375 meV and an optical phonon energy of ~42 meV. They also fabricated the wide-color gamut prototype pc-WLED devices via the combination of green emissive MAPbBr₃ QDs, red emissive rare-earth phosphor K₂SiF₆:Mn⁴⁺ (KSF), and blue emissive GaN chips.^[49] Zeng's group developed a facile method to synthesize CsPbX₃ (X = Cl, Br, I) inorganic PQDs, which based on supersaturated recrystallization could be carried out at RT in a fast and simple way, without inert gas and injection operation. The synthesized PQDs had the QYs of 80%, 95%, 70%, and FWHM of 35, 20, and 18 nm for the red, green, and blue emissions, respectively. They also measured the exciton binding energy of CsPbBr₃ QDs as 40 meV, which was found to be much higher than those of GaN (25 meV) and RT thermal

disturbance energy (26 meV). This means that excitons in CsPbBr₃ QDs can have a rapid recombination at RT, inducing excellent PL properties.^[51]

Table 3.2 Performance of representative PNC-based light-emitting diodes.

PNCs	Synthesis Method	Device Structure	Morphology	EL/FWHM	V_T	EQE_{max}	Current efficiency	Peak luminance	Refs
				(nm)	(V)	(%)	($cd A^{-1}$)	($cd m^{-2}$)	
$(FA)_{1-x}(MA)_xPbBr_3$	LARP	ITO/PEDOT:PSS/ $(FA)_{1-x}(MA)_xPbBr_3$ NPs without electrolyte matrix and with electrolyte matrix/Al	NPs	550/~20	~17	-	0.013	2	[201]
MAPbBr ₃	Emulsion Synthesis	ITO/PEDOT/MAPbBr ₃ /TPBi/CsF/Al	QDs	524/~26	2.9	1.1	4.5	2503	[54]
MAPbBr ₃	-	SOCP/MAPbBr ₃ /TPBi/LiF/Al	NPs	~547/20	~3.6	8.53	42.9	-	[202]
CsPbX ₃	Hot injection	ITO/PEDOT:PSS/PVK/CsPbX ₃ /TPBi/LiF/Al	QDs	455/23	5.1	0.07	14	742	[198]
				516/29	4.2	0.12	0.43	946	
				586/21	4.6	0.09	0.08	528	
MAPbBr _{3-x} I _x	RT solution growth	ITO/PEDOT:PSS/ MAPbBr _{3-x} I _x /F8/Ca/Ag	NRs	533/26	-	-	-	-	[203]
MAPbBr ₃	LARP	ITO/PEDOT:PSS/MAPbBr ₃ /TPBi/LiF/Al	NPLs	436/~30	3.5	2.31	8.1	8.5	[204]
MAPbX ₃	LARP	ITO/PEDOT:PSS/PVK/MAPbBr ₃ /TPBi/LiF/Al	QDs	520/21	7.8	1.06	3.72	2398	[205]
CsPbBr ₃	Hot injection	ITO/PEDOT:PSS/Poly-TPD/PFI/CsPbBr ₃ /TPBi/LiF/Al	NCus	516/18	2.5	0.06	0.19	1377	[206]
CsPbBr ₃ -CsPb ₂ Br ₅	Hot injection	ITO/PEDOT:PSS/CsPbBr ₃ -CsPb ₂ Br ₅ /TPBi/LiF/Al	NPs	527/24	4.6	2.21	8.98	3853	[207]
CsPbX ₃	Hot injection	ITO/ZnO/PEI/CsPbX ₃ /CBP/TCTA/MoO _x /Au	QDs	688/36	1.9	7.25	0.49	435	[208]
				648/33	1.9	6.3	3.42	2216	
				516/20	2.4	0.4	1.32	3019	
				404/14	3.4	0.61	0.0049	11	
CsPbBr _x Cl _{3-x}	Hot injection	ITO/PEDOT:PSS/PVK/DDAB-OA-CsPbX ₃ /TPBi/LiF/Al	NCus	515/19	3	3	-	330	[199]
				490/19	3	1.9	-	35	
CsPbX ₃	Hot injection	ITO/ZnO/CsPbX ₃ -TMA/TFB/MoO ₃ /Ag	NCus	698/31	-	5.7	-	206	[209]
				619/29	-	1.4	-	1559	
				523/19	-	0.19	-	2335	

PNCs	Synthesis Method	Device Structure	Morphology	EL/FWHM	V_T	EQE_{max}	Current efficiency	Peak luminance	Refs
				(nm)	(V)	(%)	($cd A^{-1}$)	($cd m^{-2}$)	
				480/17	-	0.0074	-	8.7	
$CsPb_{1-x}Sn_xBr_3$	Hot injection	ITO/PEDOT:PSS/poly-TPD/ $CsPb_{1-x}Sn_xBr_3$ /TPBi/LiF/Al	QDs	508/-	5	-	3.6	5495	[210]
$CsPbX_3$	Hot injection	ITO/TiO ₂ / $CsPbX_3$ /F8/MoO ₃ /Au	QDs	650/35	2.6	0.05	-	90-930	[211]
				510/25	2.8	0.325	-	-	
				495/21	4.1	0.075	-	-	
$CsPbBr_3$	Hot injection	ITO/PEDOT:PSS/poly-TPD/ $CsPbBr_3$ /TPBi/LiF/Al	QDs	512/20	3.4	6.27	13.3	15185	[200]
$CsPbX_3$	Hot injection	ITO/PEDOT:PSS/NPB/ $CsPbX_3$ /BCP/LiF/Al	QDs	445/-	4	-	0.025	15.2	[212]
				510/-	5	-	0.308	51.7	
				640/-	4	-	0.027	21.7	
$CsPbBr_3$	-	ITO/PEDOT:PSS/Ag rods/NPB/ $CsPbBr_3$ /TPBi/LiF/Al	QDs	Green	3.8	0.43	1.42	8911	[213]
$CsPbBr_3$	LARP	ITO/ZnO/ $CsPbBr_3$ /TFB/MoO _x /Au	QDs	510/20	3	0.06	-	-	[214]
$CsPbBr_3$	Hot injection	ITO/NiO/ $CsPbBr_3$ /ZnO/Al	QDs	516/21	2.4	0.11	0.57	3091	[215]
$CsPbBr_3$	Hot injection	ITO/PEDOT:PSS/PVK/ $CsPbBr_3$ -PMMA/TPBi/LiF/Al	QDs	Green	-	0.25	0.96	637	[216]
$CsPbBr_3$	Hot injection	ITO/PEDOT:PSS/poly-TPD/ $CsPbBr_3$ /TPBi/Liq/Al	QDs	512/17	2.6	8.73	26.2	1660	[217]
$CsPbBr_3$	Hot injection	ITO/PEDOT:PSS/poly-TPD/ $CsPbBr_3$ /TPBi/LiF/Al	QDs	515/18	4.6	1.194	3.1	12090	[218]
$CsPbX_3$	Hot injection	ITO/PEDOT:PSS/poly-TPD/ $CsPbX_3$:Mn/TPBi/LiF/Al	QDs	511/20	4.2	1.49	6.4	9971	[219]
				685/42	4.1	1.04	0.15	132	
$CsPbBr_3$	Hot injection	ITO/ZnO/MZO/ $CsPbBr_3$ /CBP/TCTA/MoO _x /Au	QDs	Green	2.9	1.1	3.66	3059	[220]
$CsPbBr_3$	Microwave	ITO/PEDOT:PSS/PTPD/ $CsPbBr_3$ /PVK/ZnO/Al	NBs	520/17	2.2	1.1	-	590	[221]
$CsPb_{0.67}Sn_{0.33}Br_3$	Hot-injection	ITO/PEDOT:PSS/TFB/ $CsPb_{0.67}Sn_{0.33}Br_3$ /TPBi/LiF/Al	QDs	517/-	3.6	4.13	11.63	12500	[222]
PEABr: $CsPbBr_3$	-	ITO/PEDOT:PSS/PEABr: $CsPbBr_3$ /TPBi/Ca/Al	quasi-2D	514/20	3	1.97	6.16	9957	[223]

PNCs	Synthesis Method	Device Structure	Morphology	EL/FWHM	V_T	EQE_{max}	Current efficiency	Peak luminance	Refs
				(nm)	(V)	(%)	($cd A^{-1}$)	($cd m^{-2}$)	
CsPbI ₃	Hot-injection	ITO/PEDOT:PSS/CsPbI ₃ /TPBi/LiF/Al	QDs	693/32	3	0.21	0.012	7.2	[224]
CsPb ₂ X ₅	-	ITO/PEDOT:PSS/TFB/CsPb ₂ X ₅ /TPBi/LiF/Al	quasi-2D	520/20	3.8	1.1	-	7317	[225]
				693/30	4	0.14	-	-	
IDA-CsPbI ₃	Hot-injection	ITO/PEDOT:PSS/poly-TPD/IDA-CsPbI ₃ /TPBi/LiF/Al	NCs	688/33	4.1	5.02	-	748	[226]
OPA-CsPbBr ₃	Hot-injection	ITO/PEDOT:PSS/poly-TPD/OPA-CsPbBr ₃ /TPBi/LiF/Al	QDs	516/19	2.8	6.5	18.13	7085	[227]
CsPbBr ₃	Hot-injection	ITO/NiO/CsPbBr ₃ /Zn _{1-x} Mg _x O/Al	QDs	519/19	2.8	3.79	7.96	6093.2	[228]
Ce ³⁺ -Doped CsPbBr ₃	Hot-injection	ITO/PEDOT:PSS/poly-TPD/Ce-doped CsPbBr ₃ /TPBi/LiF/Al	NCs	515/19	2.5	4.4	14.2	>3000	[229]
CsPbBr ₃	LARP	ITO/ZnO/CsPbBr ₃ /TCTA/MoO ₃ /Au	NCs	460/-	-	1.7	5.8	4428	[230]
CsPbBr ₃	Self-assembly	ITO/PEDOT:PSS/PVK/CsPbBr ₃ /TPBi/Liq/Al	core/shell QDs	510/21	3.9	15.17	40	18600	[231]
CsPbBr ₃	Hot-injection	ITO/Li:TiO ₂ /CsPbBr ₃ /TiO ₂ /Au	QDs	530/25	2.3	2.38	3	2210	[232]
CsPbBr ₃	LARP	ITO/PEDOT:PSS/PTAA/CsPbBr ₃ /TPBi/LiF/Al	QDs	515/18	2.75	11.6	45.4	55800	[233]
FAPbBr ₃	Self-assembly	ITO/PEDOT:PSS/FAPbBr ₃ /PO-TOT/Ca/Al	NCs	528-532/25-26	2.2	13.4	57.6	56000	[234]
CsPbBr ₃	Hot-injection	ITO/PEDOT:PSS/Poly-TPD/CsPbBr ₃ /TPBi/Liq/Al	QDs	508/18	5.6	0.17	-	-	[235]
		ITO/PEDOT:PSS/Poly-TPD/CsPbBr ₃ + OAM-I /TPBi/Liq/Al		649/31	2.8	21.3	10.6	500	
		ITO/PEDOT:PSS/Poly-TPD/CsPbBr ₃ + An-HI /TPBi/Liq/Al		644/29	2.7	14.1	11.6	794	
Cs _x FA _{1-x} PbBr ₃	-	ITO/NiO/TFB/PVK/Cs _x FA _{1-x} PbBr ₃ /TPBi/LiF/Al	NPs	483/-	3.3	9.5	12	700	[236]
(PEA) ₂ PbBr ₄	LARP	ITO/PEDOT:PSS/PVK:TAPC/(PEA) ₂ PbBr ₄ /TPBi/Ca/Ag	NPLs	408.8/18	4.2	0.31	0.19	147.6	[237]
CsPbBr _x Cl _{3-x}	Directly mixing	ITO/PEDOT:PSS/Poly-TPD/CsPbBr _x Cl _{3-x} /TPBi/Ca/Ag	NCs	469	3.8	0.65	0.47	30	[238]
				479	3.2	1	0.94	119	
				489	3.4	1.8	2.4	182	
				496	3.2	2.6	4.5	603	

3.6.3 Photodetectors (PDs)

The PDs have the functions of capturing optical signals and converting them into electrical signals, which are crucial for various industrial and scientific applications, including biomedical sensing, imaging, defence, and optical communications.^[239-241] Perovskite material has the merits of excellent optoelectronic properties, such as highly efficient absorption, ambipolar charge-transport characteristics, long carrier diffusion length, high dielectric constant, and ferroelectric polarization, making it a potential candidate for PDs application. Additionally, the low-cost solution-processed fabrication methods benefit the large-scale production and commercialization, to some extent, which makes it more competitive comparing to the most widespread inorganic semiconductors such as Si and GaN.^[19]

The PDs can be classified into three types: photodiodes, photoconductors and phototransistors. Figure 3.19 shows the two-terminal devices including photodiodes and photoconductors, and the three-terminal devices including phototransistors, which have the source, drain and gate electrodes. Regarding the spatial layout, the photodetectors can also be classified as vertical and lateral types. For photodiodes and phototransistors, they only show vertical and lateral types, respectively. However, photoconductors have two kinds of types.^[242] Depending on the width of the spectral response window, the photodetectors can also be classified as spectrally broadband or narrowband PDs. Broadband PDs can sense a broad spectrum of light, for instance, X-rays, UV-light, and visible light, while narrowband PDs can only sense a narrow range of light, for instance, red, green, blue, etc. PNCs have a narrow spectrum, which is really suitable for narrowband PDs. The spectrally selective PDs are favoured by the market, where only a small spectral range of light can be detected.

The photodiodes show similar device structures as solar cells, but work under reverse applied field with low dark currents. Both electrons and holes can be extracted through a built-in potential, inducing a high responsivity and a rapid response speed. In contrast, the photoconductors only transfer a single carrier. A long response time is one of the most critical restrictions of photoconductors. In photoconductors, potentially, if the opposite photo-generated carriers get trapped by inner defects or material surface, transporting photo-generated carriers recirculate multiple times during the lifetime of the trapped ones, inducing a high photoconductive gain. Unluckily, a photoconductive gain is beneficial for achieving a high responsivity but also drives to a slow response.^[17] In this case, the high responsivity of the photoconductors may result from the generation of a

secondary photocurrent and photoconductive gain. Furthermore, the detectivity in photoconductors is usually small due to their high dark currents and noises. As mentioned above, photoconductors have vertical and lateral device structures. It could be challenging to implement the PNCs in the vertical type devices because of the high requirement of film uniformity to perfectly cover the surface of active layer. In contrast, the lateral structure devices can be simply fabricated using 1D nanowires and 2D nanosheet perovskite. Table 3.3 presents a summary of the performance of recent PNC-based PDs.

The 1D architecture of perovskite NWs has provided a well-confined carrier transport channel for application as PDs due to their less grain boundary, morphological anisotropy, and good mechanical flexibility.^[243] However, the large surface area of MAPbI₃ NWs could cause much easier carrier recombination and material decomposition, which would be detrimental to the performance and stability of the device. Tang et al. used OA soaking to passivate MAPbI₃ NWs' surface defects to enhance the stability and sensitivity of the perovskite NW-based PDs. By this treatment, the carrier lifetime was improved from 28.1 to 51.3 ns. As a result, a high responsivity of 4.95 A W⁻¹, detectivity of 2×10^{13} Jones, and response time of less than 0.1 ms were achieved.^[244]

In 2016, Lee et al. first demonstrated the all-inorganic PNCs-based PDs. They chose CsPbI₃ NCs as active material for PDs, which is a red emitter. The as-obtained PNC solution was drop-casted on a doped Si substrate with pre-patterned gold electrodes. The device showed good photosensitivity with an on/off photocurrent ratio of 10⁵ and relatively fast rise ($t_{\text{rise}} = 24$ ms) and decay times ($t_{\text{decay}} = 29$ ms).^[245] Zeng et al. applied the 2D CsPbBr₃ NSs for solution-processed flexible PDs for the first time. These CsPbBr₃ NSs with a thickness of ~ 3.3 nm and edge length of ~ 1 μm are proper to be assembled into high-quality, large-area films via a solution process. The flexible, 2D CsPbBr₃ visible-light PDs showed excellent charge transport properties, a high photosensitivity with an on/off ratio higher than 10³.^[246] Liu et al. used a simple two-step vapour transport chemical deposition method to grow MAPbI₃ NPLs with lateral dimension of about 5 \sim 20 μm on SiO₂/Si substrates. The thickness of these 2D materials was distributed in the region of 5 \sim 300 nm, which depended on the controlled growing time. They further studied the thickness-dependent photoresponse of the devices and concluded that the sample with a thickness of around 30 nm exhibits the best performance due to the dominant longest lifetime of perovskite excitons (≈ 4.5 ns).^[247]

Review Article: Perovskite Nanocrystals: Synthesis, Stability and Optoelectronic Applications

And finally, to obtain compact and smooth carrier channels for the PD devices, Zeng et al. reported a recyclable dissolution-recrystallization method for CsPbBr₃ PNCs. Specifically, the large particles could be gradually dissolved from the surface, and the PNCs could be obtained by adjusting the ratio of the dissolved part. In addition to the size decreasing behaviour, the PNCs would aggregate after washing off the highly dynamic surface species. The as-fabricated films exhibited large numbers of holes and gaps. Then, they used a combination of toluene and ethanol as washing solvent to form a liquid circumstance in films. The surface and sharp parts dissolved, and the liquid matters filled the holes and gaps. After solvent evaporation, the dissolved species between isolated particles would be attached on the surfaces of particle and recrystallized. The film treated by this micro-self-healing method showed decreased hole size and smooth morphologies, which benefited the performance of PD devices.^[248]

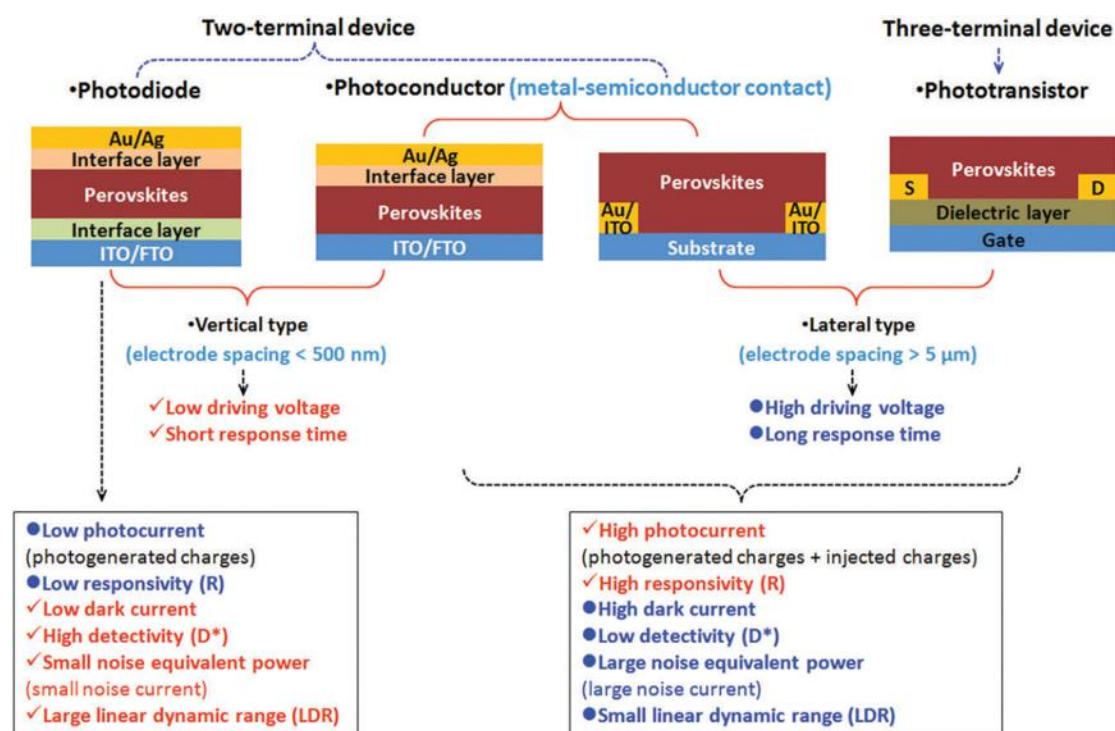


Figure 3.19: Schematic of architectures for perovskite-based photodetectors and the characteristics of photodetection performance for different devices. Reproduced with permission.^[18] Copyright 2017, Royal Society of Chemistry.

Table 3.3 Performance of representative PNC-based photodetectors.

PNCs	Synthesis Method	Morphology	Devices Structure	Input light intensity & wavelength	Bias voltage	Responsivity	On/off ratio	Rise/decay time	Detectivity	Ref
				(mW cm ⁻² /nm)	(V)	(A W ⁻¹)		(ms)	(Jones)	
CsPbI ₃	Hot injection	NCs	Au/CsPbI ₃ /Au	1.98, 405	1	-	10 ⁵	24/29	-	[245]
MAPbI ₃	One-step self-assembly	NWs	Au/MAPbI ₃ /Au	2.36, 530	1	4.95	250	< 0.1	2 × 10 ¹³	[244]
CsPbBr ₃	Hot injection	NSs	ITO/CsPbBr ₃ /ITO	10, 442	5	0.64	>10 ⁴	0.019/0.024	-	[246]
CsPbBr ₃	Dissolution-recrystallization	NCs	Au/CsPbBr ₃ /Au	1.01, 442	3	0.18	8 × 10 ³	1.8/1.0	6.1 × 10 ¹⁰	[248]
MAPbI ₃	Solution process & vapor-phase conversion	NSs	Ti&Au/MAPbI ₃ /Ti&Au	-, 405	1	22	10 ²	< 20 / < 40	-	[249]
				-, 532		12				
MAPbI ₃	Vapor phase deposition	NPLs	Cr&Au/MAPbI ₃ /Cr&Au	60, 633	1	23.3	-	150	-	[247]
MAPbI ₃	Dissolution-recrystallization	NWs	Ag/MAPbI ₃ /Ag	1, 532	3	-	13	120/210	-	[250]
CsPb(Br/I) ₃	Hot injection	NRs	Au/CsPb(Br/I) ₃ /Au	20, 532	1	-	2000	680/660	-	[251]
CsPbBr ₃	LARP	micro	CsPbBr ₃ /CNTs	-, 400	10	31.1	10 ⁵	0.016/0.38	-	[252]
MAPbI ₃	Saturated vapor-assisted crystallization	NWs	Au/MoO ₃ /MAPbI ₃ /MoO ₃ /Au	-	-	460	-	0.18/0.33	2.6 × 10 ¹³	[253]
CsPbI _{3-x} Br _x	Oxygen-assisted chemical vapor deposition	QDs	Au/CsPbI _{3-x} Br _x /MoS ₂ /Au	-, 532	0.1	7.7×10 ⁴	10 ⁴	590/320	5.6 × 10 ¹¹	[254]
CsPbCl ₃ -graphen	Hot injection	NCs	Au/CsPbCl ₃ -graphen/Au	8.17×10 ⁻³ , 400	0.5	10 ⁶	-	0.3 × 10 ³ /1.35 × 10 ³	2 × 10 ¹³	[156]

3.7 Summary and Outlook

Metal halide perovskite nanocrystals possess excellent optoelectronic properties, which make them a competitive candidate for the next-generation optoelectronics and photonics. This article briefly reviewed the synthesis methods, stability issues, encapsulation strategies, and few photoelectronic applications of PNCs. Although great contributions from worldwide multidisciplinary researchers have made this field more and more mature, there are still different critical issues to be addressed in further research, which will be briefly discussed here.

Various processes for synthesis of PNCs are described here, among which the ligands are always necessary to form nanoscale structures. However, it is not still well-understood how surface passivation and stability of PNCs are affected by different types of ligands. Comparing to conventional nanoscale semiconductors, the precise control of the size and shape of PNCs needs further effort. In addition, the mechanisms of how ligands control the size and shape of the PNCs are needed to be elaborated. A systematic exploration of the novel ligands for the sake of stable surface termination in PNCs and a deep understanding of their functionality are highly demanded. Besides, it is also of great interest to study the impact of ligands on the electronic band structure of PNCs.

Lead-based PNCs are the most studied due to their better optoelectronic properties comparing to other MHPs; however, the ever-growing concerns about the toxicity of these materials has encouraged many research groups to develop lead-free PNCs substitutes. Unfortunately, replacing the lead by other single metal elements has limited choices. Most of the “single metal” lead-free perovskite materials show inferior properties when comparing to lead-based one. Despite tin(II)-based perovskites have a suitable bandgap, their easy oxidation from Sn(II) to Sn(VI) impedes the application of these materials. In recent years, the so-called double perovskite materials appear on the scene, represented by $\text{Cs}_2\text{AgBiX}_6$ perovskite. Supported by computational studies on the elements screening for a possible combination of A^+ , B^+ , B^{3+} , and X^- ions, eleven optimal materials were screened out and three of them showed the appropriate direct band gaps of 1.68, 1.77 and 1.83 eV (for $\text{Cs}_2\text{AgSbI}_6$, $\text{Cs}_2\text{AgBiI}_6$, and $\text{Cs}_2\text{AuBiBr}_6$, respectively).^[255] To date, just a few new double perovskite materials have been reported, but not in the nano-sized form. This is also an exciting direction for future research.

One of the most significant challenges for the commercialization of PNCs is their stability. The interior and exterior factors that may cause the degradation of PNCs are summarized in this review. For the

interior factors like perovskite structural stability, doping a small amount of other metal cations into perovskite structure is an effective way to improve stability. However, the structure-property relationship needs further investigation both in theoretical and experimental fields, especially for the lead-free PNCs. The function of ligands working as the surface passivators, on the other hand, needs to be systematically studied in order to achieve stable surface passivation with least effect on the optoelectronic properties of PNCs.

Numerous studies on coating and encapsulation of PNCs with various materials have been discussed in this review. However, these protectors are mostly chemical and environment stable but insulated. That means even if the stability can be improved dramatically, these materials act as barriers for charges at the same time and could be detrimental to the optoelectronic properties of PNCs. To address this issue, novel strategies should be explored, for instance, reducing the protector's amount and doping the insulated protectors might improve the carriers transport.

Although they are still in the development phase, PNCs have shown high potential in various optoelectronic and photonic applications. However, a much longer lifetime and durable performance are required to ensure a bright industrial future for PNC-based technologies. Additionally, the toxicity issue of the lead-based PNCs should be ideally resolved no matter what fields these materials are used for. Exploring the novel PNCs with non-toxic properties and soluble in water will extend their application to further fields such as bio-application and water-splitting. With numerous efforts from the researchers and global cooperation among the chemists, physicists, materials scientists and engineers, this field has shown great progress with the skyrocketing numbers of research works in recent years and the breaking record presented in every few days. We believe that the PNCs have very high potential to be implemented as one of the most-used materials in different technologies in the near future.

3.8 Conflict of Interest

The authors declare no conflict of interest.

3.9 Acknowledgements

The authors gratefully acknowledge funding by the Deutsche Forschungsgemeinschaft (DFG, German Research Foundation) under Germany's Excellence Strategy – EXC 2089/1 – 390776260 (e-conversion) and funding by the Bavarian Ministry of Science (Solar Technologies go Hybrid – SolTech). T. A. acknowledges the financial support of the German Research Foundation (DFG project with grant number of AM 519/1-1). S. W. and L. W. acknowledge the financial support of China Scholarship Council (CSC).

3.10 References

- [1] S. Kazim, M. K. Nazeeruddin, M. Gratzel, S. Ahmad, *Angew. Chem. Int. Ed.* **2014**, *53*, 2812.
- [2] A. Kojima, K. Teshima, Y. Shirai, T. Miyasaka, *J. Am. Chem. Soc.* **2009**, *131*, 6050.
- [3] Q. Jiang, Y. Zhao, X. Zhang, X. Yang, Y. Chen, Z. Chu, Q. Ye, X. Li, Z. Yin, J. You, *Nat. Photonics* **2019**, *13*, 460.
- [4] <https://www.nrel.gov/pv/cell-efficiency.html> **National Renewable Energy Laboratory, Best Research-Cell Efficiencies chart.**
- [5] J. You, L. Meng, T.-B. Song, T.-F. Guo, Y. Yang, W.-H. Chang, Z. Hong, H. Chen, H. Zhou, Q. Chen, Y. Liu, N. De Marco, Y. Yang, *Nat. Nanotechnol.* **2016**, *11*, 75.
- [6] H. S. Kim, C. R. Lee, J. H. Im, K. B. Lee, T. Moehl, A. Marchioro, S. J. Moon, R. Humphry-Baker, J. H. Yum, J. E. Moser, M. Gratzel, N. G. Park, *Sci. Rep.* **2012**, *2*, 591.
- [7] M. Liu, M. B. Johnston, H. J. Snaith, *Nature* **2013**, *501*, 395.
- [8] Y. Hu, J. Schlipf, M. Wussler, M. L. Petrus, W. Jaegermann, T. Bein, P. Müller-Buschbaum, P. Docampo, *ACS Nano* **2016**, *10*, 5999.
- [9] J. You, L. Meng, T.-B. Song, T.-F. Guo, Y. Yang, W.-H. Chang, Z. Hong, H. Chen, H. Zhou, Q. Chen, Y. Liu, N. De Marco, Y. Yang, *Nat. Nanotechnol.* **2015**, *11*, 75.
- [10] P. Wang, X. Zhang, Y. Zhou, Q. Jiang, Q. Ye, Z. Chu, X. Li, X. Yang, Z. Yin, J. You, *Nat. Commun.* **2018**, *9*, 2225.
- [11] C. Zuo, L. Ding, *Nanoscale* **2014**, *6*, 9935.
- [12] Y. Gao, Y. Dong, K. Huang, C. Zhang, B. Liu, S. Wang, J. Shi, H. Xie, H. Huang, S. Xiao, J. He, Y. Gao, R. A. Hatton, J. Yang, *ACS Photonics* **2018**, *5*, 4104.
- [13] Z.-K. Tan, R. S. Moghaddam, M. L. Lai, P. Docampo, R. Higler, F. Deschler, M. Price, A. Sadhanala, L. M. Pazos, D. Credgington, F. Hanusch, T. Bein, H. J. Snaith, R. H. Friend, *Nat. Nanotechnol.* **2014**, *9*, 687.
- [14] Y. Wei, Z. Y. Cheng, J. Lin, *Chem. Soc. Rev.* **2019**, *48*, 310.
- [15] Q. Van Le, H. W. Jang, S. Y. Kim, *Small Methods* **2018**, *2*, 1700419.
- [16] P. Docampo, T. Bein, *Acc. Chem. Res.* **2016**, *49*, 339.
- [17] J. P. Deng, J. L. Li, Z. Yang, M. Q. Wang, *J. Mater. Chem. C* **2019**, *7*, 12415.
- [18] H. Wang, D. H. Kim, *Chem. Soc. Rev.* **2017**, *46*, 5204.
- [19] M. Ahmadi, T. Wu, B. Hu, *Adv. Mater.* **2017**, *29*, 1605242.
- [20] S. Park, W. J. Chang, C. W. Lee, S. Park, H.-Y. Ahn, K. T. Nam, *Nat. Energy* **2016**, *2*, 16185.
- [21] X. L. Zhu, Y. X. Lin, Y. Sun, M. C. Beard, Y. Yan, *J. Am. Chem. Soc.* **2019**, *141*, 733.
- [22] W. Wang, M. O. Tade, Z. P. Shao, *Chem. Soc. Rev.* **2015**, *44*, 5371.
- [23] S. Shyamal, N. Pradhan, *J. Phys. Chem. Lett.* **2020**, *11*, 6921.
- [24] S. Shyamal, S. K. Dutta, T. Das, S. Sen, S. Chakraborty, N. Pradhan, *J. Phys. Chem. Lett.* **2020**, *11*, 3608.

- [25] S. Shyamal, S. K. Dutta, N. Pradhan, *J. Phys. Chem. Lett.* **2019**, *10*, 7965.
- [26] A. Kojima, K. Teshima, T. Miyasaka, Y. Shirai, *210th ECS Meeting* **2006**, MA2006-02, 397.
- [27] L. C. Schmidt, A. Pertegás, S. González-Carrero, O. Malinkiewicz, S. Agouram, G. Mínguez Espallargas, H. J. Bolink, R. E. Galian, J. Pérez-Prieto, *J. Am. Chem. Soc.* **2014**, *136*, 850.
- [28] A. B. Yusoff, M. K. Nazeeruddin, *Adv. Energy Mater.* **2018**, *8*, 1702073.
- [29] A. O. El-Ballouli, O. M. Bakr, O. F. Mohammed, *Chem. Mater.* **2019**, *31*, 6387.
- [30] S. Sun, D. Yuan, Y. Xu, A. Wang, Z. Deng, *ACS Nano* **2016**, *10*, 3648.
- [31] F. Lang, O. Shargaieva, V. V. Brus, H. C. Neitzert, J. Rappich, N. H. Nickel, *Adv. Mater.* **2018**, *30*, 1702905.
- [32] E. T. Hoke, D. J. Slotcavage, E. R. Dohner, A. R. Bowring, H. I. Karunadasa, M. D. McGehee, *Chem. Sci.* **2015**, *6*, 613.
- [33] D. W. deQuilettes, W. Zhang, V. M. Burlakov, D. J. Graham, T. Leijtens, A. Osherov, V. Bulović, H. J. Snaith, D. S. Ginger, S. D. Stranks, *Nat. Commun.* **2016**, *7*, 11683.
- [34] S. Draguta, O. Sharia, S. J. Yoon, M. C. Brennan, Y. V. Morozov, J. S. Manser, P. V. Kamat, W. F. Schneider, M. Kuno, *Nat. Commun.* **2017**, *8*, 200.
- [35] D. D. Yang, X. M. Li, H. B. Zeng, *Adv. Mater. Interfaces* **2018**, *5*, 1701662.
- [36] W. Z. Lv, L. Li, M. C. Xu, J. X. Hong, X. X. Tang, L. G. Xu, Y. H. Wu, R. Zhu, R. F. Chen, W. Huang, *Adv. Mater.* **2019**, *31*, 1900682.
- [37] S. Huang, Z. Li, L. Kong, N. Zhu, A. Shan, L. Li, *J. Am. Chem. Soc.* **2016**, *138*, 5749.
- [38] M. N. Liu, H. C. Zhang, D. Gedamu, P. Fourmont, H. Rekola, A. Hiltunen, S. G. Cloutier, R. Nechache, A. Priimagi, P. Vivo, *Small* **2019**, *15*, 29.
- [39] H. Y. Fu, *J. Mater. Chem. A* **2019**, *7*, 14357.
- [40] C. D. Donega, P. Liljeroth, D. Vanmaekelbergh, *Small* **2005**, *1*, 1152.
- [41] X. Li, F. Cao, D. Yu, J. Chen, Z. Sun, Y. Shen, Y. Zhu, L. Wang, Y. Wei, Y. Wu, H. Zeng, *Small* **2017**, *13*, 1603996.
- [42] L. Protesescu, S. Yakunin, M. I. Bodnarchuk, F. Krieg, R. Caputo, C. H. Hendon, R. X. Yang, A. Walsh, M. V. Kovalenko, *Nano Lett.* **2015**, *15*, 3692.
- [43] A. Dutta, R. K. Behera, S. K. Dutta, S. Das Adhikari, N. Pradhan, *J. Phys. Chem. Lett.* **2018**, *9*, 6599.
- [44] G. Almeida, L. Goldoni, Q. Akkerman, Z. Y. Dang, A. H. Khan, S. Marras, I. Moreels, L. Manna, *ACS Nano* **2018**, *12*, 1704.
- [45] A. Pan, B. He, X. Fan, Z. Liu, J. J. Urban, A. P. Alivisatos, L. He, Y. Liu, *ACS Nano* **2016**, *10*, 7943.
- [46] Y. Bekenstein, B. A. Koscher, S. W. Eaton, P. Yang, A. P. Alivisatos, *J. Am. Chem. Soc.* **2015**, *137*, 16008.
- [47] J. De Roo, M. Ibáñez, P. Geiregat, G. Nedelcu, W. Walravens, J. Maes, J. C. Martins, I. Van Driessche, M. V. Kovalenko, Z. Hens, *ACS Nano* **2016**, *10*, 2071.
- [48] M. Imran, V. Caligiuri, M. Wang, L. Goldoni, M. Prato, R. Krahne, L. De Trizio, L. Manna, *J. Am. Chem. Soc.* **2018**, *140*, 2656.

- [49] F. Zhang, H. Zhong, C. Chen, X.-g. Wu, X. Hu, H. Huang, J. Han, B. Zou, Y. Dong, *ACS Nano* **2015**, *9*, 4533.
- [50] H. Huang, A. S. Susha, S. V. Kershaw, T. F. Hung, A. L. Rogach, *Adv. Sci.* **2015**, *2*, 1500194.
- [51] X. Li, Y. Wu, S. Zhang, B. Cai, Y. Gu, J. Song, H. Zeng, *Adv. Funct. Mater.* **2016**, *26*, 2435.
- [52] S. Wei, Y. Yang, X. Kang, L. Wang, L. Huang, D. Pan, *Chem. Commun.* **2016**, *52*, 7265.
- [53] F. Ambroz, W. D. Xu, S. Gadipelli, D. J. L. Brett, C. T. Lin, C. Contini, M. A. McLachlan, J. R. Durrant, I. P. Parkin, T. J. Macdonald, *Part. Part. Syst. Charact.* **2020**, *37*, 1900391.
- [54] H. Huang, F. Zhao, L. Liu, F. Zhang, X.-g. Wu, L. Shi, B. Zou, Q. Pei, H. Zhong, *ACS Appl. Mater. Interfaces* **2015**, *7*, 28128.
- [55] D. M. Jang, D. H. Kim, K. Park, J. Park, J. W. Lee, J. K. Song, *J. Mater. Chem. C* **2016**, *4*, 10625.
- [56] Y. Tong, E. Bladt, M. F. Aygüler, A. Manzi, K. Z. Milowska, V. A. Hintermayr, P. Docampo, S. Bals, A. S. Urban, L. Polavarapu, J. Feldmann, *Angew. Chem. Int. Ed.* **2016**, *55*, 13887.
- [57] Q. Pan, H. Hu, Y. Zou, M. Chen, L. Wu, D. Yang, X. Yuan, J. Fan, B. Sun, Q. Zhang, *J. Mater. Chem. C* **2017**, *5*, 10947.
- [58] Z. Long, H. Ren, J. Sun, J. Ouyang, N. Na, *Chem. Commun.* **2017**, *53*, 9914.
- [59] H. Liu, Z. Wu, H. Gao, J. Shao, H. Zou, D. Yao, Y. Liu, H. Zhang, B. Yang, *ACS Appl. Mater. Interfaces* **2017**, *9*, 42919.
- [60] M. Chen, Y. Zou, L. Wu, Q. Pan, D. Yang, H. Hu, Y. Tan, Q. Zhong, Y. Xu, H. Liu, B. Sun, Q. Zhang, *Adv. Funct. Mater.* **2017**, *27*, 1701121.
- [61] Z.-J. Li, E. Hofman, A. H. Davis, A. Khammang, J. T. Wright, B. Dzikovski, R. W. Meulenberg, W. Zheng, *Chem. Mater.* **2018**, *30*, 6400.
- [62] A. L. Antaris, H. Chen, K. Cheng, Y. Sun, G. S. Hong, C. R. Qu, S. Diao, Z. X. Deng, X. M. Hu, B. Zhang, X. D. Zhang, O. K. Yaghi, Z. R. Alamparambil, X. C. Hong, Z. Cheng, H. J. Dai, *Nat. Mater.* **2016**, *15*, 235.
- [63] D. Q. Chen, G. L. Fang, X. Chen, L. Lei, J. S. Zhong, Q. A. Mao, S. Zhou, J. N. Li, *J. Mater. Chem. C* **2018**, *6*, 8990.
- [64] L.-J. Chen, C.-R. Lee, Y.-J. Chuang, Z.-H. Wu, C. Chen, *J. Phys. Chem. Lett.* **2016**, *7*, 5028.
- [65] L. J. Chen, J. H. Dai, J. D. Lin, T. S. Mo, H. P. Lin, H. C. Yeh, Y. C. Chuang, S. A. Jiang, C. R. Lee, *ACS Appl. Mater. Interfaces* **2018**, *10*, 33307.
- [66] L. J. Chen, *RSC Adv.* **2018**, *8*, 18396.
- [67] K. S. Elvira, X. C. i Solvas, R. C. R. Wootton, A. J. deMello, *Nat. Chem.* **2013**, *5*, 905.
- [68] S.-Y. Teh, R. Lin, L.-H. Hung, A. P. Lee, *Lab Chip* **2008**, *8*, 198.
- [69] I. Lignos, S. Stavarakis, G. Nedelcu, L. Protesescu, A. J. deMello, M. V. Kovalenko, *Nano Lett.* **2016**, *16*, 1869.
- [70] V. Malgras, S. Tominaka, J. W. Ryan, J. Henzie, T. Takei, K. Ohara, Y. Yamauchi, *J. Am. Chem. Soc.* **2016**, *138*, 13874.
- [71] S. Demchyshyn, J. M. Roemer, H. Groß, H. Heilbrunner, C. Ulbricht, D. Apaydin, A. Böhm, U. Rütt, F. Bertram, G. Hesser, M. C. Scharber, N. S. Sariciftci, B. Nickel, S. Bauer, E. D. Głowacki, M. Kaltenbrunner, *Sci. Adv.* **2017**, *3*, e1700738.

- [72] B. Wang, C. Y. Zhang, W. L. Zheng, Q. G. Zhang, Z. Q. Bao, L. Kong, L. Li, *Chem. Mater.* **2020**, *32*, 308.
- [73] R. Naphade, S. Nagane, G. S. Shanker, R. Fernandes, D. Kothari, Y. Zhou, N. P. Pature, S. Ogale, *ACS Appl. Mater. Interfaces* **2016**, *8*, 854.
- [74] L. Protesescu, S. Yakunin, O. Nazarenko, D. N. Dirin, M. V. Kovalenko, *ACS Applied Nano Materials* **2018**, *1*, 1300.
- [75] Z. P. Zhang, Y. Li, C. Liang, G. N. Yu, J. F. Zhao, S. J. Luo, Y. Huang, C. L. Su, G. C. Xing, *Small* **2020**.
- [76] S. T. Ha, X. Liu, Q. Zhang, D. Giovanni, T. C. Sum, Q. Xiong, *Adv. Opt. Mater.* **2014**, *2*, 838.
- [77] J. Xing, X. F. Liu, Q. Zhang, S. T. Ha, Y. W. Yuan, C. Shen, T. C. Sum, Q. Xiong, *Nano Lett.* **2015**, *15*, 4571.
- [78] K. Park, J. W. Lee, J. D. Kim, N. S. Han, D. M. Jang, S. Jeong, J. Park, J. K. Song, *J. Phys. Chem. Lett.* **2016**, *7*, 3703.
- [79] L. Huang, Q. Gao, L.-D. Sun, H. Dong, S. Shi, T. Cai, Q. Liao, C.-H. Yan, *Adv. Mater.* **2018**, *30*, 1800596.
- [80] H. Needleman, *Annu. Rev. Med.* **2004**, *55*, 209.
- [81] T. C. Jellicoe, J. M. Richter, H. F. J. Glass, M. Tabachnyk, R. Brady, S. E. Dutton, A. Rao, R. H. Friend, D. Credgington, N. C. Greenham, M. L. Böhm, *J. Am. Chem. Soc.* **2016**, *138*, 2941.
- [82] M. J. Ashley, M. N. O'Brien, K. R. Hedderick, J. A. Mason, M. B. Ross, C. A. Mirkin, *J. Am. Chem. Soc.* **2016**, *138*, 10096.
- [83] A. Wang, X. Yan, M. Zhang, S. Sun, M. Yang, W. Shen, X. Pan, P. Wang, Z. Deng, *Chem. Mater.* **2016**, *28*, 8132.
- [84] X. Wu, W. Song, Q. Li, X. Zhao, D. He, Z. Quan, *Chem. Asian J.* **2018**, *13*, 1654.
- [85] M. Leng, Z. Chen, Y. Yang, Z. Li, K. Zeng, K. Li, G. Niu, Y. He, Q. Zhou, J. Tang, *Angew. Chem. Int. Ed.* **2016**, *55*, 15012.
- [86] M. Leng, Y. Yang, Z. Chen, W. Gao, J. Zhang, G. Niu, D. Li, H. Song, J. Zhang, S. Jin, J. Tang, *Nano Lett.* **2018**, *18*, 6076.
- [87] S. E. Creutz, H. B. Liu, M. E. Kaiser, X. S. Li, D. R. Gamelin, *Chem. Mater.* **2019**, *31*, 4685.
- [88] J. Pal, S. Manna, A. Mondal, S. Das, K. V. Adarsh, A. Nag, *Angew. Chem. Int. Ed.* **2017**, *56*, 14187.
- [89] D. M. Jang, K. Park, D. H. Kim, J. Park, F. Shojaei, H. S. Kang, J. P. Ahn, J. W. Lee, J. K. Song, *Nano Lett.* **2015**, *15*, 5191.
- [90] Q. A. Akkerman, V. D'Innocenzo, S. Accornero, A. Scarpellini, A. Petrozza, M. Prato, L. Manna, *J. Am. Chem. Soc.* **2015**, *137*, 10276.
- [91] Y.-C. Chen, H.-L. Chou, J.-C. Lin, Y.-C. Lee, C.-W. Pao, J.-L. Chen, C.-C. Chang, R.-Y. Chi, T.-R. Kuo, C.-W. Lu, D.-Y. Wang, *J. Phys. Chem. C* **2019**, *123*, 2353.
- [92] W. Lv, X. Tang, L. Li, L. Xu, M. Li, R. Chen, W. Huang, *J. Phys. Chem. C* **2019**, *123*, 24313.
- [93] V. M. Goldschmidt, *Naturwissenschaften* **1926**, *14*, 477.
- [94] M.-G. Ju, J. Dai, L. Ma, X. C. Zeng, *J. Am. Chem. Soc.* **2017**, *139*, 8038.

- [95] R. E. Beal, D. J. Slotcavage, T. Leijtens, A. R. Bowring, R. A. Belisle, W. H. Nguyen, G. F. Burkhard, E. T. Hoke, M. D. McGehee, *J. Phys. Chem. Lett.* **2016**, *7*, 746.
- [96] T. Leijtens, E. T. Hoke, G. Grancini, D. J. Slotcavage, G. E. Eperon, J. M. Ball, M. De Bastiani, A. R. Bowring, N. Martino, K. Wojciechowski, M. D. McGehee, H. J. Snaith, A. Petrozza, *Adv. Energy Mater.* **2015**, *5*, 1500962.
- [97] S. Z. Wang, Y. Hua, M. K. Wang, F. Y. Liu, L. M. Ding, *Mater. Chem. Front.* **2019**, *3*, 1139.
- [98] C. H. Lu, G. V. Biesold, Y. J. Liu, Z. T. Kang, Z. Q. Lin, *Chem. Soc. Rev.* **2020**, *49*, 4953.
- [99] A. Amat, E. Mosconi, E. Ronca, C. Quarti, P. Umari, M. K. Nazeeruddin, M. Grätzel, F. De Angelis, *Nano Lett.* **2014**, *14*, 3608.
- [100] T. M. Koh, K. Fu, Y. Fang, S. Chen, T. C. Sum, N. Mathews, S. G. Mhaisalkar, P. P. Boix, T. Baikie, *J. Phys. Chem. C* **2014**, *118*, 16458.
- [101] B. Xu, W. Wang, X. Zhang, W. Cao, D. Wu, S. Liu, H. Dai, S. Chen, K. Wang, X. Sun, *J. Mater. Chem. C* **2017**, *5*, 6123.
- [102] J. J. Gallardo, E. Blanco, A. Sánchez-Coronilla, J. C. Pinero, J. Navas, *Appl. Mater. Today* **2020**, *18*, 100488.
- [103] L. Protesescu, S. Yakunin, S. Kumar, J. Bär, F. Bertolotti, N. Masciocchi, A. Guagliardi, M. Grotevent, I. Shorubalko, M. I. Bodnarchuk, C.-J. Shih, M. V. Kovalenko, *ACS Nano* **2017**, *11*, 3119.
- [104] C. Wang, Y. Zhang, A. Wang, Q. Wang, H. Tang, W. Shen, Z. Li, Z. Deng, *Chem. Mater.* **2017**, *29*, 2157.
- [105] X. Zhang, H. Liu, W. Wang, J. Zhang, B. Xu, K. L. Karen, Y. Zheng, S. Liu, S. Chen, K. Wang, X. W. Sun, *Adv. Mater.* **2017**, *29*, 1606405.
- [106] I. Lignos, V. Morad, Y. Shynkarenko, C. Bernasconi, R. M. Maceiczky, L. Protesescu, F. Bertolotti, S. Kumar, S. T. Ochsenbein, N. Masciocchi, A. Guagliardi, C.-J. Shih, M. I. Bodnarchuk, A. J. deMello, M. V. Kovalenko, *ACS Nano* **2018**, *12*, 5504.
- [107] K. Hills-Kimball, Y. Nagaoka, C. Cao, E. Chaykovsky, O. Chen, *J. Mater. Chem. C* **2017**, *5*, 5680.
- [108] M. R. Linaburg, E. T. McClure, J. D. Majher, P. M. Woodward, *Chem. Mater.* **2017**, *29*, 3507.
- [109] D. Amgar, T. Binyamin, V. Uvarov, L. Etgar, *Nanoscale* **2018**, *10*, 6060.
- [110] P. Todorović, D. Ma, B. Chen, R. Quintero-Bermudez, M. I. Saidaminov, Y. Dong, Z.-H. Lu, E. H. Sargent, *Adv. Opt. Mater.* **2019**, *7*, 1901440.
- [111] G. Grancini, M. K. Nazeeruddin, *Nat. Rev. Mater.* **2019**, *4*, 4.
- [112] C. Wu, Y. Zou, T. Wu, M. Ban, V. Pecunia, Y. Han, Q. Liu, T. Song, S. Duhm, B. Sun, *Adv. Funct. Mater.* **2017**, *27*, 1700338.
- [113] A. Swarnkar, A. R. Marshall, E. M. Sanehira, B. D. Chernomordik, D. T. Moore, J. A. Christians, T. Chakrabarti, J. M. Luther, *Science* **2016**, *354*, 92.
- [114] Z. W. Ma, Z. Liu, S. Y. Lu, L. R. Wang, X. L. Feng, D. W. Yang, K. Wang, G. J. Xiao, L. J. Zhang, S. A. T. Redfern, B. Zou, *Nat. Commun.* **2018**, *9*, 4506.
- [115] L. Zhang, C. M. Liu, L. R. Wang, C. L. Liu, K. Wang, B. Zou, *Angew. Chem. Int. Ed.* **2018**, *57*, 11213.
- [116] L. Zhang, K. Wang, Y. Lin, B. Zou, *J. Phys. Chem. Lett.* **2020**, *11*, 4693.

- [117] G. Liu, L. P. Kong, W. G. Yang, H. K. Mao, *Mater. Today* **2019**, *27*, 91.
- [118] M. L. H. Green, G. Parkin, *J. Chem. Educ.* **2014**, *91*, 807.
- [119] M. L. H. Green, *J. Organomet. Chem.* **1995**, *500*, 127.
- [120] J. You, Y. Yang, Z. Hong, T.-B. Song, L. Meng, Y. Liu, C. Jiang, H. Zhou, W.-H. Chang, G. Li, Y. Yang, *Appl. Phys. Lett.* **2014**, *105*, 183902.
- [121] H. Zhou, Q. Chen, G. Li, S. Luo, T.-b. Song, H.-S. Duan, Z. Hong, J. You, Y. Liu, Y. Yang, *Science* **2014**, *345*, 542.
- [122] K. K. Bass, R. E. McAnally, S. Zhou, P. I. Djurovich, M. E. Thompson, B. C. Melot, *Chem. Commun.* **2014**, *50*, 15819.
- [123] J. Zhao, B. Cai, Z. Luo, Y. Dong, Y. Zhang, H. Xu, B. Hong, Y. Yang, L. Li, W. Zhang, C. Gao, *Sci. Rep.* **2016**, *6*, 21976.
- [124] J. A. Christians, P. A. Miranda Herrera, P. V. Kamat, *J. Am. Chem. Soc.* **2015**, *137*, 1530.
- [125] S. N. Habisreutinger, T. Leijtens, G. E. Eperon, S. D. Stranks, R. J. Nicholas, H. J. Snaith, *Nano Lett.* **2014**, *14*, 5561.
- [126] S. Huang, Z. Li, B. Wang, N. Zhu, C. Zhang, L. Kong, Q. Zhang, A. Shan, L. Li, *ACS Appl. Mater. Interfaces* **2017**, *9*, 7249.
- [127] A. Alberti, I. Deretzis, G. Pellegrino, C. Bongiorno, E. Smecca, G. Mannino, F. Giannazzo, G. G. Condorelli, N. Sakai, T. Miyasaka, C. Spinella, A. La Magna, *ChemPhysChem* **2015**, *16*, 3064.
- [128] D. B. Straus, S. Guo, R. J. Cava, *J. Am. Chem. Soc.* **2019**, *141*, 11435.
- [129] D. Meggiolaro, E. Mosconi, F. De Angelis, *ACS Energy Lett.* **2017**, *2*, 2794.
- [130] N. Aristidou, C. Eames, I. Sanchez-Molina, X. Bu, J. Kosco, M. S. Islam, S. A. Haque, *Nat. Commun.* **2017**, *8*, 15218.
- [131] W. Nie, J.-C. Blancon, A. J. Neukirch, K. Appavoo, H. Tsai, M. Chhowalla, M. A. Alam, M. Y. Sfeir, C. Katan, J. Even, S. Tretiak, J. J. Crochet, G. Gupta, A. D. Mohite, *Nat. Commun.* **2016**, *7*, 11574.
- [132] Y. Tian, M. Peter, E. Unger, M. Abdellah, K. Zheng, T. Pullerits, A. Yartsev, V. Sundström, I. G. Scheblykin, *Phys. Chem. Chem. Phys.* **2015**, *17*, 24978.
- [133] A. Dualeh, P. Gao, S. I. Seok, M. K. Nazeeruddin, M. Grätzel, *Chem. Mater.* **2014**, *26*, 6160.
- [134] M. Kulbak, S. Gupta, N. Kedem, I. Levine, T. Bendikov, G. Hodes, D. Cahen, *J. Phys. Chem. Lett.* **2016**, *7*, 167.
- [135] B. T. Diroll, G. Nedelcu, M. V. Kovalenko, R. D. Schaller, *Adv. Funct. Mater.* **2017**, *27*, 1606750.
- [136] A. C. Balazs, T. Emrick, T. P. Russell, *Science* **2006**, *314*, 1107.
- [137] A. Usuki, Y. Kojima, M. Kawasumi, A. Okada, Y. Fukushima, T. Kurauchi, O. Kamigaito, *J. Mater. Res.* **2011**, *8*, 1179.
- [138] Y. Kojima, A. Usuki, M. Kawasumi, A. Okada, Y. Fukushima, T. Kurauchi, O. Kamigaito, *J. Mater. Res.* **2011**, *8*, 1185.
- [139] Q. Zhou, Z. Bai, W.-g. Lu, Y. Wang, B. Zou, H. Zhong, *Adv. Mater.* **2016**, *28*, 9163.
- [140] H. Zhang, X. Wang, Q. Liao, Z. Xu, H. Li, L. Zheng, H. Fu, *Adv. Funct. Mater.* **2017**, *27*, 1604382.

- [141] Y. Guo, K. Shoyama, W. Sato, E. Nakamura, *Adv. Energy Mater.* **2016**, *6*, 1502317.
- [142] T. Y. Li, X. Z. Xu, C. H. Lin, X. W. Guan, W. H. Hsu, M. L. Tsai, X. S. Fang, T. Wu, J. H. He, *Adv. Sci.* **2020**, 1902439.
- [143] D. N. Dirin, L. Protesescu, D. Trummer, I. V. Kochetygov, S. Yakunin, F. Krumeich, N. P. Stadie, M. V. Kovalenko, *Nano Lett.* **2016**, *16*, 5866.
- [144] H.-C. Wang, S.-Y. Lin, A.-C. Tang, B. P. Singh, H.-C. Tong, C.-Y. Chen, Y.-C. Lee, T.-L. Tsai, R.-S. Liu, *Angew. Chem. Int. Ed.* **2016**, *55*, 7924.
- [145] C. Sun, Y. Zhang, C. Ruan, C. Y. Yin, X. Y. Wang, Y. D. Wang, W. W. Yu, *Adv. Mater.* **2016**, *28*, 10088.
- [146] H. Hu, L. Wu, Y. Tan, Q. Zhong, M. Chen, Y. Qiu, D. Yang, B. Sun, Q. Zhang, Y. Yin, *J. Am. Chem. Soc.* **2018**, *140*, 406.
- [147] Q. Zhong, M. Cao, H. Hu, D. Yang, M. Chen, P. Li, L. Wu, Q. Zhang, *ACS Nano* **2018**, *12*, 8579.
- [148] G. Yang, Q. Fan, B. Chen, Q. Zhou, H. Zhong, *J. Mater. Chem. C* **2016**, *4*, 11387.
- [149] S. Yuan, D. Chen, X. Li, J. Zhong, X. Xu, *ACS Appl. Mater. Interfaces* **2018**, *10*, 18918.
- [150] Z. F. Zhao, Z. H. Wu, J. Cheng, L. Jing, Y. F. Hou, *J. Phys. Chem. C* **2018**, *122*, 16887.
- [151] Y. Wang, D. Yu, Z. Wang, X. Li, X. Chen, V. Nalla, H. Zeng, H. Sun, *Small* **2017**, *13*, 1701587.
- [152] X. M. Chen, F. Zhang, Y. Ge, L. F. Shi, S. Huang, J. L. Tang, Z. Lv, L. Zhang, B. S. Zou, H. Z. Zhong, *Adv. Funct. Mater.* **2018**, *28*, 1706567.
- [153] Q. Liao, X. Jin, H. B. Fu, *Adv. Opt. Mater.* **2019**, *7*, 25.
- [154] Q. Wei, X. J. Li, C. Liang, Z. P. Zhang, J. Guo, G. Hong, G. C. Xing, W. Huang, *Adv. Opt. Mater.* **2019**, *7*, 1900080.
- [155] P. Rastogi, A. Chu, C. Greboval, J. L. Qu, U. N. Nounbe, S. S. Chee, M. Goyal, A. Khalili, X. Z. Xu, H. Cruguel, S. Ithurria, B. Gallas, J. F. Dayen, L. Dudy, M. G. Silly, G. Patriarche, A. Degiron, G. Vincent, E. Lhuillier, *Nano Lett.* **2020**, *20*, 3999.
- [156] M. G. Gong, R. Sakidja, R. Goul, D. Ewing, M. Casper, A. Stramel, A. Elliot, J. Z. Wu, *ACS Nano* **2019**, *13*, 1772.
- [157] E. A. Gaulding, J. Hao, H. S. Kang, E. M. Miller, S. N. Habisreutinger, Q. Zhao, A. Hazarika, P. C. Sercel, J. M. Luther, J. L. Blackburn, *Adv. Mater.* **2019**, *31*, 1902250.
- [158] Y. Wang, Z. Y. Lv, Q. F. Liao, H. Q. Shan, J. R. Chen, Y. Zhou, L. Zhou, X. L. Chen, V. A. L. Roy, Z. P. Wang, Z. X. Xu, Y. J. Zeng, S. T. Han, *Adv. Mater.* **2018**, *30*, 1800327.
- [159] M. A. Green, E. D. Dunlop, J. Hohl-Ebinger, M. Yoshita, N. Kopidakis, X. Hao, *Prog Photovolt* **2020**, *28*, 629.
- [160] E. M. Sanehira, A. R. Marshall, J. A. Christians, S. P. Harvey, P. N. Ciesielski, L. M. Wheeler, P. Schulz, L. Y. Lin, M. C. Beard, J. M. Luther, *Sci. Adv.* **2017**, *3*, eaao4204.
- [161] L. M. Wheeler, E. M. Sanehira, A. R. Marshall, P. Schulz, M. Suri, N. C. Anderson, J. A. Christians, D. Nordlund, D. Sokaras, T. Kroll, S. P. Harvey, J. J. Berry, L. Y. Lin, J. M. Luther, *J. Am. Chem. Soc.* **2018**, *140*, 10504.

- [162] Q. Wang, Z. Jin, D. Chen, D. Bai, H. Bian, J. Sun, G. Zhu, G. Wang, S. Liu, *Adv. Energy Mater.* **2018**, *8*, 1800007.
- [163] J. Xue, J.-W. Lee, Z. Dai, R. Wang, S. Nuryyeva, M. E. Liao, S.-Y. Chang, L. Meng, D. Meng, P. Sun, O. Lin, M. S. Goorsky, Y. Yang, *Joule* **2018**, *2*, 1866.
- [164] J. Xue, R. Wang, L. Chen, S. Nuryyeva, T.-H. Han, T. Huang, S. Tan, J. Zhu, M. Wang, Z.-K. Wang, C. Zhang, J.-W. Lee, Y. Yang, *Adv. Mater.* **2019**, *31*, 1900111.
- [165] A. Hazarika, Q. Zhao, E. A. Gauding, J. A. Christians, B. J. Dou, A. R. Marshall, T. Moot, J. J. Berry, J. C. Johnson, J. M. Luther, *ACS Nano* **2018**, *12*, 10327.
- [166] S. Christodoulou, F. Di Stasio, S. Pradhan, A. Stavrinadis, G. Konstantatos, *J. Phys. Chem. C* **2018**, *122*, 7621.
- [167] Q. Zhao, A. Hazarika, X. Chen, S. P. Harvey, B. W. Larson, G. R. Teeter, J. Liu, T. Song, C. Xiao, L. Shaw, M. Zhang, G. Li, M. C. Beard, J. M. Luther, *Nat. Commun.* **2019**, *10*, 2842.
- [168] M. Hao, Y. Bai, S. Zeiske, L. Ren, J. Liu, Y. Yuan, N. Zarrabi, N. Cheng, M. Ghasemi, P. Chen, M. Lyu, D. He, J.-H. Yun, Y. Du, Y. Wang, S. Ding, A. Armin, P. Meredith, G. Liu, H.-M. Cheng, L. Wang, *Nat. Energy* **2020**, *5*, 79.
- [169] S. Panigrahi, S. Jana, T. Calmeiro, D. Nunes, R. Martins, E. Fortunato, *ACS Nano* **2017**, *11*, 10214.
- [170] F. Liu, Y. Zhang, C. Ding, T. Toyoda, Y. Ogomi, T. S. Ripolles, S. Hayase, T. Minemoto, K. Yoshino, S. Dai, Q. Shen, *J. Phys. Chem. Lett.* **2018**, *9*, 294.
- [171] F. Liu, C. Ding, Y. H. Zhang, T. S. Ripolles, T. Kamisaka, T. Toyoda, S. Hayase, T. Minemoto, K. Yoshino, S. Y. Dai, M. Yanagida, H. Noguchi, Q. Shen, *J. Am. Chem. Soc.* **2017**, *139*, 16708.
- [172] Y. X. Yao, P. J. Hang, P. Wang, L. B. Xu, C. Cui, J. S. Xie, K. Xiao, G. Li, P. Lin, S. Liu, D. Y. Xie, S. Y. Che, D. R. Yang, X. G. Yu, *Nanotechnology* **2020**, *31*, 085401.
- [173] X. Zhang, Z. Jin, J. Zhang, D. Bai, H. Bian, K. Wang, J. Sun, Q. Wang, S. F. Liu, *ACS Appl. Mater. Interfaces* **2018**, *10*, 7145.
- [174] R. Singh, S. R. Suranagi, S. J. Yang, K. Cho, *Nano Energy* **2018**, *51*, 192.
- [175] J. B. Hoffman, G. Zaiats, I. Wappes, P. V. Kamat, *Chem. Mater.* **2017**, *29*, 9767.
- [176] Q. Zeng, X. Zhang, X. Feng, S. Lu, Z. Chen, X. Yong, S. A. T. Redfern, H. Wei, H. Wang, H. Shen, W. Zhang, W. Zheng, H. Zhang, J. S. Tse, B. Yang, *Adv. Mater.* **2018**, *30*, 1705393.
- [177] M. Cha, P. Da, J. Wang, W. Wang, Z. Chen, F. Xiu, G. Zheng, Z.-S. Wang, *J. Am. Chem. Soc.* **2016**, *138*, 8581.
- [178] J. Zhang, D. Bai, Z. Jin, H. Bian, K. Wang, J. Sun, Q. Wang, S. Liu, *Adv. Energy Mater.* **2018**, *8*, 1703246.
- [179] J. Zhang, Z. Jin, L. Liang, H. Wang, D. Bai, H. Bian, K. Wang, Q. Wang, N. Yuan, J. Ding, S. Liu, *Adv. Sci.* **2018**, *5*, 1801123.
- [180] J. Yuan, X. Ling, D. Yang, F. Li, S. Zhou, J. Shi, Y. Qian, J. Hu, Y. Sun, Y. Yang, X. Gao, S. Duhm, Q. Zhang, W. Ma, *Joule* **2018**, *2*, 2450.
- [181] K. Chen, Q. Zhong, W. Chen, B. Sang, Y. Wang, T. Yang, Y. Liu, Y. Zhang, H. Zhang, *Adv. Funct. Mater.* **2019**, *29*, 1900991.

- [182] X. Ling, S. Zhou, J. Yuan, J. Shi, Y. Qian, B. W. Larson, Q. Zhao, C. Qin, F. Li, G. Shi, C. Stewart, J. Hu, X. Zhang, J. M. Luther, S. Duham, W. Ma, *Adv. Energy Mater.* **2019**, *9*, 1900721.
- [183] J. W. Shi, F. C. Li, J. Y. Yuan, X. F. Ling, S. J. Zhou, Y. L. Qian, W. L. Ma, *J. Mater. Chem. A* **2019**, *7*, 20936.
- [184] F. Liu, C. Ding, Y. H. Zhang, T. Karnisaka, Q. Zhao, J. M. Luther, T. Toyoda, S. Hayase, T. Minemoto, K. Yoshino, B. Zhang, S. Dai, J. K. Jiang, S. X. Tao, Q. Shen, *Chem. Mater.* **2019**, *31*, 798.
- [185] Z. Zolfaghari, E. Hassanabadi, D. Pitarch-Tena, S. J. Yoon, Z. Shariatnia, J. van de Lagemaat, J. M. Luther, I. Mora-Sero, *ACS Energy Lett.* **2019**, *4*, 251.
- [186] J. Yuan, C. Bi, S. Wang, R. Guo, T. Shen, L. Zhang, J. Tian, *Adv. Funct. Mater.* **2019**, *29*, 1906615.
- [187] M. M. Tavakoli, M. Nasilowski, J. Zhao, M. G. Bawendi, J. Kong, *Small Methods* **2019**, *3*, 1900449.
- [188] J. Kim, B. Koo, W. H. Kim, J. Choi, C. Choi, S. J. Lim, J.-S. Lee, D.-H. Kim, M. J. Ko, Y. Kim, *Nano Energy* **2019**, *66*, 104130.
- [189] K. Q. Chen, W. Jin, Y. P. Zhang, T. Q. Yang, P. Reiss, Q. H. Zhong, U. Bach, Q. T. Li, Y. W. Wang, H. Zhang, Q. L. Bao, Y. L. Liu, *J. Am. Chem. Soc.* **2020**, *142*, 3775.
- [190] S. B. Shivarudraiah, M. Ng, C. H. A. Li, J. E. Halpert, *ACS Appl. Energy Mater.* **2020**, *3*, 5620.
- [191] C. M. Liu, Q. S. Zeng, Y. Zhao, Y. Yu, M. X. Yang, H. Gao, H. T. Wei, B. Yang, *Solar Rrl* **2020**, *4*, 2000102.
- [192] Q. A. Akkerman, M. Gandini, F. Di Stasio, P. Rastogi, F. Palazon, G. Bertoni, J. M. Ball, M. Prato, A. Petrozza, L. Manna, *Nat. Energy* **2016**, *2*, 16194.
- [193] D. Ghosh, M. Y. Ali, D. K. Chaudhary, S. Bhattacharyya, *Sol. Energy Mater. Sol. Cells* **2018**, *185*, 28.
- [194] F. C. Li, S. J. Zhou, J. Y. Yuan, C. C. Qin, Y. G. Yang, J. W. Shi, X. F. Ling, Y. Y. Li, W. L. Ma, *ACS Energy Lett.* **2019**, *4*, 2571.
- [195] Y. Shirasaki, G. J. Supran, M. G. Bawendi, V. Bulovic, *Nat. Photonics* **2013**, *7*, 13.
- [196] M. Era, S. Morimoto, T. Tsutsui, S. Saito, *Appl. Phys. Lett.* **1994**, *65*, 676.
- [197] T. Hattori, T. Taira, M. Era, T. Tsutsui, S. Saito, *Chem. Phys. Lett* **1996**, *254*, 103.
- [198] J. Song, J. Li, X. Li, L. Xu, Y. Dong, H. Zeng, *Adv. Mater.* **2015**, *27*, 7162.
- [199] J. Pan, L. N. Quan, Y. Zhao, W. Peng, B. Murali, S. P. Sarmah, M. Yuan, L. Sinatra, N. M. Alyami, J. Liu, E. Yassitepe, Z. Yang, O. Voznyy, R. Comin, M. N. Hedhili, O. F. Mohammed, Z. H. Lu, D. H. Kim, E. H. Sargent, O. M. Bakr, *Adv. Mater.* **2016**, *28*, 8718.
- [200] J. Li, L. Xu, T. Wang, J. Song, J. Chen, J. Xue, Y. Dong, B. Cai, Q. Shan, B. Han, H. Zeng, *Adv. Mater.* **2017**, *29*, 1603885.
- [201] M. F. Aygüler, M. D. Weber, B. M. D. Puscher, D. D. Medina, P. Docampo, R. D. Costa, *J. Phys. Chem. C* **2015**, *119*, 12047.
- [202] H. Cho, S.-H. Jeong, M.-H. Park, Y.-H. Kim, C. Wolf, C.-L. Lee, J. H. Heo, A. Sadhanala, N. Myoung, S. Yoo, S. H. Im, R. H. Friend, T.-W. Lee, *Science* **2015**, *350*, 1222.
- [203] A. B. Wong, M. Lai, S. W. Eaton, Y. Yu, E. Lin, L. Dou, A. Fu, P. Yang, *Nano Lett.* **2015**, *15*, 5519.

- [204] S. Kumar, J. Jagielski, S. Yakunin, P. Rice, Y.-C. Chiu, M. Wang, G. Nedelcu, Y. Kim, S. Lin, E. J. G. Santos, M. V. Kovalenko, C.-J. Shih, *ACS Nano* **2016**, *10*, 9720.
- [205] W. Deng, X. Xu, X. Zhang, Y. Zhang, X. Jin, L. Wang, S.-T. Lee, J. Jie, *Adv. Funct. Mater.* **2016**, *26*, 4797.
- [206] X. Zhang, H. Lin, H. Huang, C. Reckmeier, Y. Zhang, W. C. H. Choy, A. L. Rogach, *Nano Lett.* **2016**, *16*, 1415.
- [207] X. Zhang, B. Xu, J. Zhang, Y. Gao, Y. Zheng, K. Wang, X. W. Sun, *Adv. Funct. Mater.* **2016**, *26*, 4595.
- [208] X. Zhang, C. Sun, Y. Zhang, H. Wu, C. Ji, Y. Chuai, P. Wang, S. Wen, C. Zhang, W. W. Yu, *J. Phys. Chem. Lett.* **2016**, *7*, 4602.
- [209] G. Li, F. W. R. Rivarola, N. J. L. K. Davis, S. Bai, T. C. Jellicoe, F. de la Peña, S. Hou, C. Ducati, F. Gao, R. H. Friend, N. C. Greenham, Z.-K. Tan, *Adv. Mater.* **2016**, *28*, 3528.
- [210] X. Zhang, W. Cao, W. Wang, B. Xu, S. Liu, H. Dai, S. Chen, K. Wang, X. W. Sun, *Nano Energy* **2016**, *30*, 511.
- [211] E. Yassitepe, Z. Yang, O. Voznyy, Y. Kim, G. Walters, J. A. Castañeda, P. Kanjanaboos, M. Yuan, X. Gong, F. Fan, J. Pan, S. Hoogland, R. Comin, O. M. Bakr, L. A. Padilha, A. F. Nogueira, E. H. Sargent, *Adv. Funct. Mater.* **2016**, *26*, 8757.
- [212] Q. Van Le, M. Park, W. Sohn, H. W. Jang, S. Y. Kim, *Adv. Electron. Mater.* **2017**, *3*, 1600448.
- [213] X. Zhang, B. Xu, W. Wang, S. Liu, Y. Zheng, S. Chen, K. Wang, X. W. Sun, *ACS Appl. Mater. Interfaces* **2017**, *9*, 4926.
- [214] X. Du, G. Wu, J. Cheng, H. Dang, K. Ma, Y.-W. Zhang, P.-F. Tan, S. Chen, *RSC Adv.* **2017**, *7*, 10391.
- [215] Q. Shan, J. Li, J. Song, Y. Zou, L. Xu, J. Xue, Y. Dong, C. Huo, J. Chen, B. Han, H. Zeng, *J. Mater. Chem. C* **2017**, *5*, 4565.
- [216] J. C. Yu, A.-Y. Lee, D. B. Kim, E. D. Jung, D. W. Kim, M. H. Song, *Advanced Materials Technologies* **2017**, *2*, 1700003.
- [217] T. Chiba, K. Hoshi, Y.-J. Pu, Y. Takeda, Y. Hayashi, S. Ohisa, S. Kawata, J. Kido, *ACS Appl. Mater. Interfaces* **2017**, *9*, 18054.
- [218] P. Liu, W. Chen, W. Wang, B. Xu, D. Wu, J. Hao, W. Cao, F. Fang, Y. Li, Y. Zeng, R. Pan, S. Chen, W. Cao, X. W. Sun, K. Wang, *Chem. Mater.* **2017**, *29*, 5168.
- [219] S. Zou, Y. Liu, J. Li, C. Liu, R. Feng, F. Jiang, Y. Li, J. Song, H. Zeng, M. Hong, X. Chen, *J. Am. Chem. Soc.* **2017**, *139*, 11443.
- [220] H. Wu, Y. Zhang, X. Zhang, M. Lu, C. Sun, T. Zhang, W. W. Yu, *Adv. Opt. Mater.* **2017**, *5*, 1700377.
- [221] J. Shamsi, P. Rastogi, V. Caligiuri, A. L. Abdelhady, D. Spirito, L. Manna, R. Krahn, *ACS Nano* **2017**, *11*, 10206.
- [222] H. C. Wang, W. G. Wang, A. C. Tang, H. Y. Tsai, Z. Bao, T. Ihara, N. Yarita, H. Tahara, Y. Kanemitsu, S. M. Chen, R. S. Liu, *Angew. Chem. Int. Ed.* **2017**, *56*, 13650.
- [223] S. Q. Lou, T. T. Xuan, C. Y. Yu, M. M. Cao, C. Xia, J. Wang, H. L. Li, *J. Mater. Chem. C* **2017**, *5*, 7431.
- [224] C. Zou, C. Y. Huang, E. M. Sanehira, J. M. Luther, L. Y. Lin, *Nanotechnology* **2017**, *28*, 455201.

- [225] C. Qin, T. Matsushima, A. S. D. Sandanayaka, Y. Tsuchiya, C. Adachi, *J. Phys. Chem. Lett.* **2017**, *8*, 5415.
- [226] J. Pan, Y. Shang, J. Yin, M. De Bastiani, W. Peng, I. Dursun, L. Sinatra, A. M. El-Zohry, M. N. Hedhili, A.-H. Emwas, O. F. Mohammed, Z. Ning, O. M. Bakr, *J. Am. Chem. Soc.* **2018**, *140*, 562.
- [227] Y. Tan, Y. Zou, L. Wu, Q. Huang, D. Yang, M. Chen, M. Ban, C. Wu, T. Wu, S. Bai, T. Song, Q. Zhang, B. Sun, *ACS Appl. Mater. Interfaces* **2018**, *10*, 3784.
- [228] Z. Shi, S. Li, Y. Li, H. Ji, X. Li, D. Wu, T. Xu, Y. Chen, Y. Tian, Y. Zhang, C. Shan, G. Du, *ACS Nano* **2018**, *12*, 1462.
- [229] J.-S. Yao, J. Ge, B.-N. Han, K.-H. Wang, H.-B. Yao, H.-L. Yu, J.-H. Li, B.-S. Zhu, J.-Z. Song, C. Chen, Q. Zhang, H.-B. Zeng, Y. Luo, S.-H. Yu, *J. Am. Chem. Soc.* **2018**, *140*, 3626.
- [230] X. Zhang, X. Bai, H. Wu, X. Zhang, C. Sun, Y. Zhang, W. Zhang, W. Zheng, W. W. Yu, A. L. Rogach, *Angew. Chem. Int. Ed.* **2018**, *57*, 3337.
- [231] S. Yuan, Z.-K. Wang, M.-P. Zhuo, Q.-S. Tian, Y. Jin, L.-S. Liao, *ACS Nano* **2018**, *12*, 9541.
- [232] A. Subramanian, Z. Pan, Z. Zhang, I. Ahmad, J. Chen, M. Liu, S. Cheng, Y. Xu, J. Wu, W. Lei, Q. Khan, Y. Zhang, *ACS Appl. Mater. Interfaces* **2018**, *10*, 13236.
- [233] J. Song, J. Li, L. Xu, J. Li, F. Zhang, B. Han, Q. Shan, H. Zeng, *Adv. Mater.* **2018**, *30*, 1800764.
- [234] X. Y. Chin, A. Perumal, A. Bruno, N. Yantara, S. A. Veldhuis, L. Martínez-Sarti, B. Chandran, V. Chirvony, A. S.-Z. Lo, J. So, C. Soci, M. Grätzel, H. J. Bolink, N. Mathews, S. G. Mhaisalkar, *Energy Environ. Sci.* **2018**, *11*, 1770.
- [235] T. Chiba, Y. Hayashi, H. Ebe, K. Hoshi, J. Sato, S. Sato, Y.-J. Pu, S. Ohisa, J. Kido, *Nat. Photonics* **2018**, *12*, 681.
- [236] Y. Liu, J. Cui, K. Du, H. Tian, Z. He, Q. Zhou, Z. Yang, Y. Deng, D. Chen, X. Zuo, Y. Ren, L. Wang, H. Zhu, B. Zhao, D. Di, J. Wang, R. H. Friend, Y. Jin, *Nat. Photonics* **2019**, *13*, 760.
- [237] W. Deng, X. Jin, Y. Lv, X. Zhang, X. Zhang, J. Jie, *Adv. Funct. Mater.* **2019**, *29*, 1903861.
- [238] F. H. Ye, H. J. Zhang, P. Wang, J. L. Cai, L. Wang, D. Liu, T. Wang, *Chem. Mater.* **2020**, *32*, 3211.
- [239] X. Z. Xu, X. J. Zhang, W. Deng, J. S. Jie, X. H. Zhang, *Small Methods* **2018**, *2*, 1700340.
- [240] D. Yang, M. Cao, Q. Zhong, P. Li, X. Zhang, Q. Zhang, *J. Mater. Chem. C* **2019**, *7*, 757.
- [241] S. Cai, X. Xu, W. Yang, J. Chen, X. Fang, *Adv. Mater.* **2019**, *31*, 1808138.
- [242] D. Q. Chen, X. Chen, *J. Mater. Chem. C* **2019**, *7*, 1413.
- [243] X. Zhang, S. Chen, X. Wang, A. Pan, *Small Methods* **2019**, *3*, 1800294.
- [244] L. Gao, K. Zeng, J. Guo, C. Ge, J. Du, Y. Zhao, C. Chen, H. Deng, Y. He, H. Song, G. Niu, J. Tang, *Nano Lett.* **2016**, *16*, 7446.
- [245] P. Ramasamy, D.-H. Lim, B. Kim, S.-H. Lee, M.-S. Lee, J.-S. Lee, *Chem. Commun.* **2016**, *52*, 2067.
- [246] J. Song, L. Xu, J. Li, J. Xue, Y. Dong, X. Li, H. Zeng, *Adv. Mater.* **2016**, *28*, 4861.
- [247] L. Niu, Q. Zeng, J. Shi, C. Cong, C. Wu, F. Liu, J. Zhou, W. Fu, Q. Fu, C. Jin, T. Yu, X. Liu, Z. Liu, *Adv. Funct. Mater.* **2016**, *26*, 5263.
- [248] X. Li, D. Yu, F. Cao, Y. Gu, Y. Wei, Y. Wu, J. Song, H. Zeng, *Adv. Funct. Mater.* **2016**, *26*, 5903.

- [249] J. Liu, Y. Xue, Z. Wang, Z.-Q. Xu, C. Zheng, B. Weber, J. Song, Y. Wang, Y. Lu, Y. Zhang, Q. Bao, *ACS Nano* **2016**, *10*, 3536.
- [250] P. Zhu, S. Gu, X. Shen, N. Xu, Y. Tan, S. Zhuang, Y. Deng, Z. Lu, Z. Wang, J. Zhu, *Nano Lett.* **2016**, *16*, 871.
- [251] X. S. Tang, Z. Q. Zu, H. B. Shao, W. Hu, M. Zhou, M. Deng, W. W. Chen, Z. G. Zang, T. Zhu, J. M. Xue, *Nanoscale* **2016**, *8*, 15158.
- [252] X. Li, D. Yu, J. Chen, Y. Wang, F. Cao, Y. Wei, Y. Wu, L. Wang, Y. Zhu, Z. Sun, J. Ji, Y. Shen, H. Sun, H. Zeng, *ACS Nano* **2017**, *11*, 2015.
- [253] X. Xu, X. Zhang, W. Deng, L. Huang, W. Wang, J. Jie, X. Zhang, *ACS Appl. Mater. Interfaces* **2018**, *10*, 10287.
- [254] H. Wu, H. Si, Z. Zhang, Z. Kang, P. Wu, L. Zhou, S. Zhang, Z. Zhang, Q. Liao, Y. Zhang, *Adv. Sci.* **2018**, *5*, 1801219.
- [255] X.-G. Zhao, J.-H. Yang, Y. Fu, D. Yang, Q. Xu, L. Yu, S.-H. Wei, L. Zhang, *J. Am. Chem. Soc.* **2017**, *139*, 2630.

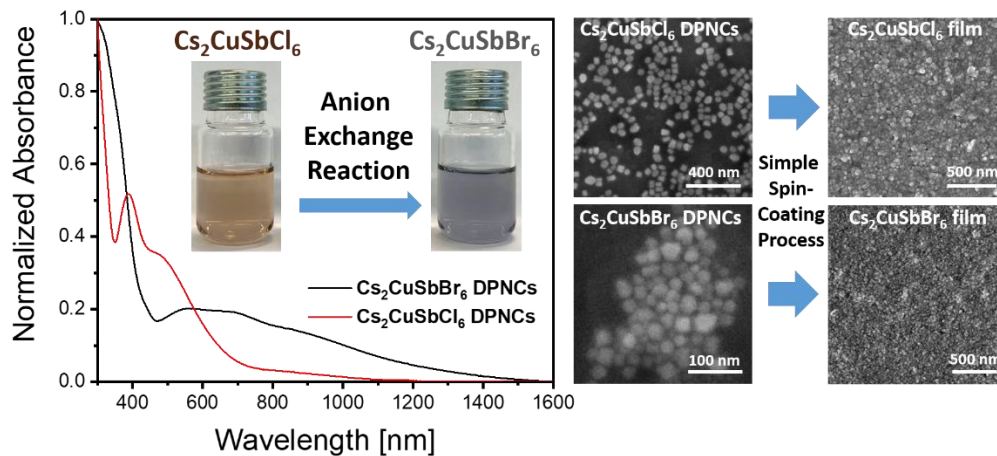
4 Room-Temperature Synthesis of Lead-Free Copper(I)-Antimony(III)-Based Double Perovskite Nanocrystals

This chapter is based on the following publication:

Shizhe Wang, Dan Han*, Clément Maheu, Zehua Xu, Alexander Biewald, Hannah Illner, Rik Hooijer, Thomas Mayer, Achim Hartschuh, Hubert Ebert, and Thomas Bein*, *APL Mater.* **2023**, 11, 041110.

Reprinted from *APL Mater.* **2023**, 11, 041110, with the permission of AIP Publishing.

Link to the published article: <https://aip.scitation.org/doi/full/10.1063/5.0144708>



The work was conceived by S.W.. S.W. contributed to the synthesis of double perovskite nanocrystals and the characterization of the nanocrystals and their thin films. The coordination work for X-ray photoelectron spectroscopy measurement, ultraviolet photoelectron spectroscopy measurement, photoluminescence measurement and theoretical study were conducted by S.W.. S.W. wrote the initial draft of the manuscript and edited until the final version.

Keywords: Lead-free halide perovskites, double perovskite nanocrystals, cesium copper antimony halides, room-temperature ligand-assisted reprecipitation, anion exchange

4.1 Abstract

In the field of perovskite solar cells, explorations of new lead-free all-inorganic perovskite materials are of great interest to address the instability and toxicity issues of lead-based hybrid perovskites. Recently, copper-antimony-based double perovskite materials have been reported with ideal band gaps, which possess great potential as absorbers for photovoltaic applications. Here, we synthesize $\text{Cs}_2\text{CuSbCl}_6$ double perovskite nanocrystals (DPNCs) at ambient conditions by a facile and fast synthesis method, namely, a modified ligand-assisted reprecipitation (LARP) method. We choose methanol as solvent for precursor salts as it is less toxic and easily removed in contrast to widely-used dimethylformamide. Our computational structure search shows that the $\text{Cs}_2\text{CuSbCl}_6$ structure containing alternating $[\text{CuCl}_6]^{5-}$ and $[\text{SbCl}_6]^{3-}$ octahedral units is a metastable phase that is 30 meV/atom higher in energy compared to the ground state structure with $[\text{CuCl}_3]^{2-}$ and $[\text{SbCl}_6]^{3-}$ polyhedra. However, this metastable $\text{Cs}_2\text{CuSbCl}_6$ double perovskite structure can be stabilized through the solution-based nanocrystal synthesis. Using an anion-exchange method, $\text{Cs}_2\text{CuSbBr}_6$ DPNCs are obtained for the first time, featuring a narrow band gap of 0.9 eV. Finally, taking advantage of the solution processability of DPNCs, smooth and dense $\text{Cs}_2\text{CuSbCl}_6$ and $\text{Cs}_2\text{CuSbBr}_6$ DPNC films are successfully fabricated.

4.2 Introduction

Halide double perovskites (HDPs) have been proposed as potential alternatives to lead halide perovskites in the field of photovoltaics and photoluminescence (PL). Using the strategy of cation-transmutation, *viz.* substituting two Pb^{2+} with monovalent (I) and trivalent (III) cations, three-dimensional (3D) double perovskite structure with the formula $\text{A}_2\text{B(I)B(III)X}_6$ (A is a small organic/inorganic cation, B is a metal cation, X is a halide anion) are formed.¹⁻³ As photoluminescent materials, the performance of HDPs is on par with that of lead halide perovskites, for example, bismuth-doped $\text{Cs}_2(\text{Ag}_{0.6}\text{Na}_{0.4})\text{InCl}_6$ emitted efficient warm-white light with $86 \pm 5\%$ quantum efficiency and showed outstanding stability for over 1,000 hours.⁴ However, the photovoltaic performance of HDPs is still much inferior compared to lead halide perovskites. One representative HDP is $\text{Cs}_2\text{AgBiBr}_6$, which possesses an indirect band gap of 1.95 eV.⁵ Such a large indirect band gap greatly limits the efficient optical absorption of $\text{Cs}_2\text{AgBiBr}_6$, and thus leads to much lower power conversion efficiency (PCE) ($\sim 6\%$) than that of lead-based halide perovskites (PCE $\sim 26\%$).⁶⁻⁹

Besides Ag-based HDPs, $\text{MA}_2\text{KBiCl}_6$ (MA= methylammonium)¹⁰ and $\text{Cs}_2\text{NaBiX}_6$ (X = Br, Cl)¹¹ were successfully synthesized but show even larger band gaps than $\text{Cs}_2\text{AgBiBr}_6$. Notably, the iodine-containing double perovskite $\text{Cs}_2\text{NaBiI}_6$ has also been synthesized. It showed a smaller indirect band gap (1.66 eV) than $\text{Cs}_2\text{AgBiBr}_6$, and to date achieved a PCE of 0.42%.¹²⁻¹³ Developing novel HDPs with narrow band gaps is highly desired for better photovoltaic performance. Compared to $\text{A}_2\text{B(I)B(III)X}_6$ HDPs (B(I) = K, Na and Ag), Cu(I)-based HDPs are predicted to have narrower band gaps.¹⁴ Moreover, in contrast to the noble metal Ag(I), the high abundance and low price of Cu provides great potential for commercial production. However, Cu(I)-based 3D HDPs bulk crystals have been rarely reported experimentally. To the best of our knowledge, only $\text{Cs}_2\text{CuSbCl}_6$ double perovskite nanocrystals (DPNCs) have been successfully synthesized via a modified hot-injection method.¹⁵ $\text{Cs}_2\text{CuSbCl}_6$ exhibits an indirect band gap of 1.66 eV, which is comparable to that of $\text{Cs}_2\text{NaBiI}_6$ and much smaller than that of $\text{Cs}_2\text{AgBiBr}_6$. Furthermore, substituting Cl with Br or I in $\text{Cs}_2\text{CuSbCl}_6$ can potentially further reduce the band gap, and enhance the optical absorption for photovoltaic applications.

The ground-state structure of Cu(I) halides favors three- or four- rather than six-fold coordination, which is suggested by theoretical calculations.¹⁶ However, Cu(I)-based perovskite structures containing $[\text{CuX}_6]^{5-}$ octahedra can be obtained via non-equilibrium methods. Besides the aforementioned example of $\text{Cs}_2\text{CuSbCl}_6$ nanocrystals, the double perovskite structure with six-fold coordination of Cu(I) can also be stabilized through dimensional reduction to layered perovskites.

Recently, some Cu(I)-based layered double perovskites have been successfully synthesized where Cu(I) displays an extremely distorted six-fold coordination but the perovskite structure is maintained, for instance, $(C_6H_{16}N_2)_2CuBiI_8$ ¹⁷, $(PPDA)_2CuRuCl_8$ ¹⁸, $(PEA)_4CuInCl_8$ ¹⁹⁻²⁰, $(BA)_4CuInCl_8$ ²⁰ (PPDA = para-phenylenediammonium, PEA = phenethylammonium, BA = butylammonium). It is evident that both the large organic cations and long-chain organic ligands can stabilize the Cu(I)-based double perovskite structure, offering an opportunity to investigate their optoelectronic properties. Therefore, developing new Cu(I)-based 3D HDPs at the nanoscale is a promising route to overcome the issues of kinetic instability and high formation energy of these materials.¹⁵

The synthesis of halide perovskite nanocrystals (PNCs) has greatly developed since the first successful synthesis of $CsPbX_3$ (X = Cl, Br, and I) PNCs via a hot-injection method.²¹ The two most-developed colloidal syntheses are hot-injection and room-temperature ligand-assisted reprecipitation (LARP) methods. Although the hot-injection method can give the best control over size and morphology of PNCs, it is not easily scalable due to the required high temperatures and protective inert gas environments, leading to high energy consumption and complex operation during the production.²²⁻²⁴ Due to the inherent ionic nature of halide perovskites, it is also possible to synthesize high-quality PNCs by the LARP method under ambient conditions. This relatively simple, energy-efficient and easily scalable approach relies on the spontaneous crystallization of substances upon reaching a supersaturated state, which can be achieved by lowering the temperature, evaporating solvents, or adding anti-solvents in which the solubility of the substance is low. However, the typical LARP method requires coordinating polar solvents with high precursor solubilities, such as N,N-dimethylformamide (DMF), which is not favored for large-scale production due to its toxicity.²⁵⁻²⁶ In addition, they are technically difficult to remove during the purification process, leading to a defective surface and poor stability.²³ Searching for less toxic and easily-removable solvents is a major objective for the synthesis of PNCs. Furthermore, the development of the LARP method is far behind that of the hot-injection method regarding control over size and morphology of the PNCs, especially for DPNCs.

Various post-treatments for PNCs can assist to transform their morphology, composition, and structure.²⁷ The soft lattice of PNCs allows for tuning their chemical composition via anion-exchange by introducing halide salts to a solution of PNCs, which offers a facile route to access novel materials with different optoelectronic properties.²⁸⁻³⁰ For DPNCs, we note that Cs_2AgBiI_6 is impossible to synthesize through direct synthesis, however, its DPNCs have been obtained by the post-treatment of

$\text{Cs}_2\text{AgBiBr}_6$ DPNCs via anion exchange.³⁰ Notably, although $\text{Cs}_2\text{CuSbCl}_6$ DPNCs have been obtained via hot-injection¹⁵, the bromide and iodide congeners have not yet been synthesized. Given that the anion-exchange reactivity of nanocrystals can provide access to metastable phases that may be difficult or impossible to synthesize directly,³⁰⁻³² we hypothesized that $\text{Cs}_2\text{CuSbBr}_6$ and $\text{Cs}_2\text{CuSbI}_6$ DPNCs may be obtained by using this method. Furthermore, the poor solubility of precursors inhibits the fabrication of high-quality HDP films via a solution-processed method.³³ In contrast, DPNCs show favorable solution processability, offering a facile and effective way to obtain high-quality DPNC films.

In our work, we demonstrate for the first time a facile and fast synthesis method for $\text{Cs}_2\text{CuSbCl}_6$ DPNCs via a modified LARP method under ambient conditions. We choose methanol as a solvent for precursor salts as it is less toxic and easily removed, and systematically study the effects of types of anti-solvents and the concentration of ligands on the size and morphology of $\text{Cs}_2\text{CuSbCl}_6$ DPNCs. Our computational structure search shows that the double perovskite $\text{Cs}_2\text{CuSbCl}_6$, containing $[\text{CuCl}_6]$ and $[\text{SbCl}_6]$ moieties, is metastable (30 meV/atom) compared to the ground state with $[\text{CuCl}_3]$ and $[\text{SbCl}_6]$ polyhedra, but that it can be stabilized through the solution-based nanocrystal synthesis. Using the anion-exchange method, $\text{Cs}_2\text{CuSbBr}_6$ DPNCs are obtained for the first time, featuring a narrow band gap of 0.9 eV. Finally, taking advantage of the solution processability of DPNCs, smooth and dense $\text{Cs}_2\text{CuSbCl}_6$ and $\text{Cs}_2\text{CuSbBr}_6$ DPNC films are successfully fabricated.

4.3 Experimental Methods

Materials. Cesium acetate (CsAc, 99.9%), copper chloride (99.999%), antimony trichloride ($\geq 99.95\%$), methanol (anhydrous, 99.8%), isopropanol (anhydrous, 99.5%), chloroform (anhydrous, $\geq 99\%$), *o*-xylene (anhydrous, 97%), toluene (anhydrous, 99.8%), *m*-xylene (anhydrous, 99%), benzene (anhydrous, 99.8%), hexane (anhydrous, 95%), octane (anhydrous, $\geq 99\%$), ethyl acetate (anhydrous, 99.8%), methyl acetate (anhydrous, 99.5%), oleic acid (90%), oleyamine (70%), bromotrimethylsilane ($>97\%$), iodotrimethylsilane (97%) were used as purchased (from Sigma Aldrich) without further purification.

Methods. *Synthesis of $\text{Cs}_2\text{CuSbCl}_6$ DPNCs.* The $\text{Cs}_2\text{CuSbCl}_6$ DPNCs were synthesized by a modified LARP method under ambient conditions. In a typical synthesis, 383.8 mg (2 mmol) cesium acetate (CsAc) was dissolved in 1 mL methanol as the source of Cs. To prepare the copper/antimony source, 268.9 mg (2 mmol) copper(II) chloride (CuCl_2) and 912.5 mg (4 mmol) of antimony trichloride (SbCl_3) were dissolved in 1 mL methanol. The CsAc precursor (150 μL) was added directly into the anti-solvent (9

mL) with different amounts of oleic acid (OA) and oleyamine (OAm) to form a transparent solution, termed the host solution. The solution of CuCl_2 and SbCl_3 (150 μL), termed the guest solution, was added into the host solution dropwise under vigorous stirring. The color of the mixture changed from blue to green to brown, and finally to black as all the guest solution was mixed with the host solution. The reaction was terminated after 5 minutes. For purification of PNCs, the crude black DPNC solution was transferred to a 50 mL centrifuge tube with the addition of ethyl acetate (EA) at a volume ratio of 9:1 (crude DPNC solution to EA) to enhance precipitation. The mixture was centrifuged at 7830 revolutions per minute (rpm) (7197 relative centrifugal force (rcf)) for 10 minutes. In the case of hexane as the anti-solvent, no extra EA was required because the crude solution could be separated easily. The supernatant was then decanted, and the residual pellet was re-dispersed in hexane (5 mL). This was then centrifuged a second time at 4500 rpm (2377 rcf) for 5 minutes. The supernatant was collected for further characterization, post-treatments and film deposition.

Anion Exchange Reaction. $\text{Cs}_2\text{CuSbCl}_6$ DPNCs synthesized by using 9 mL of toluene with 400 μL of OA and 175 μL of OAm were chosen as the starting materials. In a typical anion exchange reaction, the $\text{Cs}_2\text{CuSbCl}_6$ DPNC solution obtained via the method described above was used directly with a concentration of ~ 0.02 M, which was determined by inductively coupled plasma optical emission spectrometry (ICP-OES). Meanwhile, a 0.1 M solution of bromotrimethylsilane (TMSBr) in hexane was prepared. The reaction was performed in a N_2 -filled glovebox. Different amounts of TMSBr solution (0.2, 0.4, 0.8, 1.5, 2, 3 mL) were added to 1 mL of $\text{Cs}_2\text{CuSbCl}_6$ DPNC solution (containing 0.02 mmol of $\text{Cs}_2\text{CuSbCl}_6$) to achieve different levels of conversion. After the addition of TMSBr solution, the mixture was stirred for 5 minutes and then dried under vacuum to remove excess reagent and by-products. The final samples were dissolved in hexane or octane for further characterization, post-treatments and film deposition. The attempt to exchange Br to I was performed analogously but with iodotrimethylsilane (TMSI) instead.

Post-Purification and Thin-Film Synthesis of DPNCs. To prepare the DPNC solution for film deposition, the DPNCs were further purified by washing with EA to remove excess ligands and then redispersed in octane at a concentration of 70 mg/mL. A two-step spin-coating process was used to fabricate films. Specifically, 30 μL of the as-prepared octane solution of DPNCs was spin-coated on the substrate at 1000 rpm for 20 s and 2000 rpm for 45 s. Then methyl acetate (MA, 150 μL) was dropped on the DPNC layers to remove the long-chain ligands during the second spin-coating step. Films with

different thickness were obtained by repeating this process. The films were annealed at different temperatures to remove the residual solvents for further characterization and application.

Materials Characterization. *X-ray Diffraction (XRD) Measurements.* DPNCs without purification and thin-film XRD data were recorded using a Bruker D8 Discover diffractometer with Ni-filtered Cu K α radiation and a LynxEye position-sensitive detector in Bragg–Brentano geometry. Powder XRD data of DPNCs resulting from the post-purification process were recorded using a STOE STADI P diffractometer with Ge-filtered Cu K α radiation and a DECTRIS solid-state strip detector MYTHEN 1K in Debye–Scherrer geometry. For the preparation of samples without post-purification, the DPNCs were dried under vacuum to remove the solvents and redispersed in a small amount of hexane. The corresponding solutions with a high mass concentration were dropped on glass and dried under vacuum to remove the residual hexane. To prepare the samples resulting from post-purification for powder XRD measurements, the pellets obtained after purification were dried under vacuum and then ground into fine powder, which was not sticky anymore due to the low ligand density.

Absorption Measurements. The optical absorption spectra of both DPNC solutions and films were recorded on a Perkin–Elmer Lambda 1050 spectrometer equipped with a 150 mm integrating sphere.

Steady-State Photoluminescence (PL) and Time-Correlated Single-Photon Counting (TCSPC). A home-built confocal laser scanning microscope (CLSM) setup was used for characterizing the photoluminescence of DPNCs. Confocal PL images were obtained by placing the Cs₂CuSbCl₆ DPNC film sample (synthesized in toluene with 400 μ L of OA and 175 μ L of OAm) on an x,y piezo scan stage at room temperature. A subpicosecond pulsed fiber laser with a repetition rate of 40 MHz (Toptica iChrome TVIS) with the central wavelength of 476 nm was employed as the illumination source. An air objective (Nikon Chrome-Free Infinity-Corrected (CFI) Plan Apochromat 60x) with a numerical aperture of 0.95 and 60x magnification was used for focusing the laser light and for collecting the sample PL. The fluence of the excitation light in the focus was set to 1.2 mJ·cm⁻². Residual scattered laser light was suppressed using a long-pass filter (LP) with an edge at 490 nm. For the measurement of the PL spectra, the emitted light was sent to a grating spectrometer (Andor Shamrock SR303i) equipped with a charge coupled device (CCD) camera (Andor Newton Du-920-OE). For time-resolved measurements the PL light was directed to an avalanche photodiode (APD, MPD PDM Series) combined with a TCSPC-Card (Becker & Hickl).

Scanning Electron Microscopy (SEM) and Energy Dispersive X-Ray Spectroscopy (EDX). The DPNC samples were prepared by dropping diluted DPNC solutions (in hexane) on aluminium foil and dried

under vacuum. The DPNC film samples were prepared on the ITO substrates following the method mentioned above. SEM and EDX measurements were performed on an FEI Helios G3 UC instrument equipped with an additional concentric backscattered electron detector.

High-resolution Transmission Electron Microscopy (HR-TEM). HR-TEM images were obtained on a Titan Themis instrument at 120 kV accelerating voltage. HR-TEM specimens were prepared by dropping 10 μL of dilute DPNC solutions (in hexane) on carbon-coated Cu grids.

The details of X-ray photoelectron spectroscopy (XPS) and ultraviolet photoelectron spectroscopy (UPS) measurements can be found in the Supporting Information.

Computational methods. Crystal structure prediction for $\text{Cs}_2\text{CuSbCl}_6$ was performed using the Ab Initio Random Structure Searching (AIRSS) method.³⁴⁻³⁵ The search was constrained with the number of atoms in the reduced formula of 10, and generated and relaxed 829 random structures. The plane wave density functional theory (DFT) code CASTEP with core-corrected ultrasoft pseudopotentials generated as defined in the built-in QC5 library was used for efficient structure sampling.³⁶ A plane wave cutoff energy was set to 400 eV. The reciprocal space sampling was performed by using Monkhorst–Pack grids with a spacing of $0.05 \times 2\pi \text{ \AA}^{-1}$. For further relaxations and property calculations for low-energy structures, the Vienna ab initio simulation package (VASP) was used.³⁷⁻³⁸ The projector augmented wave with exchange correction potential of Perdew–Burke–Ernzerhof (PBE) was used.³⁹ An energy cutoff of 400 eV and a k-point density of $0.03 \times 2\pi \text{ \AA}^{-1}$ were employed. The convergence criteria for the energy and force were set to 10^{-5} eV and 0.01 eV/\AA , respectively. For electronic structure calculations, a hybrid functional with a 25% nonlocal Fock exchange (HSE06) was employed.⁴⁰ The spin-orbit coupling (SOC) effect was included as well. The calculations of the energy above the convex hull (E_{hull}) were performed via pymatgen.⁴¹⁻⁴² The theoretical conversion efficiency (spectroscopic limited maximum efficiency (SLME)) of the solar cell absorbers was calculated based on the method proposed by Yu, L. et al. and a python code (SL3ME).⁴³⁻⁴⁴

4.4 Results and Discussion

4.4.1 Theoretical Study of $\text{Cs}_2\text{CuSbCl}_6$ HDP Structure

Theoretically, Cu(I)- and Ag(I)-based 3D HDPs have been predicted to be potential substitutions for lead-based halide perovskites as less-toxic photovoltaic absorbers.^{14, 45-46} Ag(I)-based 3D HDPs have been successfully synthesized, for example, $\text{Cs}_2\text{AgBiX}_6$ ($X = \text{Cl}, \text{Br}$)⁴⁷, $\text{Cs}_2\text{AgSbCl}_6$ ⁴⁸ and $\text{Cs}_2\text{AgInCl}_6$ ⁴⁸.

However, Cu(I)-based 3D HDPs have been rarely studied experimentally. The relative instability of Cu(I)-based 3D HDPs is attributed to the preference of Cu(I) for three- or four-fold coordination rather than six-fold coordination, based on the comparison of the DFT calculated total energy for simple binary halides CuCl in different crystal structures and unsuccessful experimental trials for synthesizing Cu(I)-based double perovskites ($\text{Cs}_2\text{CuInX}_6$ ($X = \text{Cl}, \text{Br}$)) via solid-state methods.⁴⁹ Notably, several Cu(I)-based layered double perovskites ($(\text{C}_6\text{H}_{16}\text{N}_2)_2\text{CuBiI}_8$ ¹⁷, $(\text{PPDA})_2\text{CuRuCl}_8$ ¹⁸, $(\text{PEA})_4\text{CuInCl}_8$ ¹⁹⁻²⁰, $(\text{BA})_4\text{CuInCl}_8$ ²⁰) have been successfully synthesized where the Cu(I) atoms have distorted six-fold coordination and the perovskite structure is maintained within a two-dimensional plane.⁴⁹

Here, a global crystal structure search of the quaternary compound $\text{Cs}_2\text{CuSbCl}_6$ was performed to identify the possible crystal structures of $\text{Cs}_2\text{CuSbCl}_6$. We found three structure types including 3-, 4- and 6-fold coordinated Cu(I) atoms, which demonstrates the diversity of the local environment of the Cu(I)-halogen moieties (Figure 4.1a). The calculated E_{hull} shows that the $R3$ symmetry of $\text{Cs}_2\text{CuSbCl}_6$ with planar $[\text{CuCl}_3]$ polyhedra is the most energetically favorable, followed by the Cm symmetry containing $[\text{CuCl}_4]$ tetrahedra, and $Fmm2$ and $Fm\bar{3}m$ symmetry with $[\text{CuCl}_6]$ octahedra. The metastable phase $Fm\bar{3}m$ is 30 meV/atom higher in energy, which is within the energy range of possible entropy stabilization. Indeed, $\text{Cs}_2\text{CuSbCl}_6$ DPNCs with alternating $[\text{CuX}_6]$ and $[\text{SbX}_6]$ octahedra were synthesized by Zhou et. al.¹⁵ In this study, we also demonstrate the successful formation of metastable $\text{Cs}_2\text{CuSbCl}_6$ in $Fm\bar{3}m$ symmetry with $[\text{CuX}_6]$ moieties utilizing the LARP method.

4.4.2 Synthesis of $\text{Cs}_2\text{CuSbCl}_6$ DPNCs

As illustrated in Figure 4.1b, $\text{Cs}_2\text{CuSbCl}_6$ DPNCs were synthesized by a modified LARP method under ambient conditions. For the conventional LARP method, all reagents are dissolved in a good solvent (e.g., DMF or dimethyl sulfoxide) and dropped into an anti-solvent (e.g., toluene or hexane) with the assist of organic ligands to form PNCs. However, the poor solubility of cesium chloride makes it difficult to prepare one solution with all the reagents. Thus, we modified this method by using CsAc instead of CsCl as the Cs precursor since the former has higher solubility than the latter. The Cs and Cu/Sb/Cl precursors were prepared separately. Methanol was chosen as the solvent for the perovskite precursors, which is less toxic comparing to the commonly-used DMF.²⁶ In addition, methanol has a low boiling point, making it readily removable, and thus avoiding issues such as

redissolving nanocrystals or creating crystallographic surface defects. For more details, see the Experimental Methods and Supporting Information Video.

4.4.2.1 Impact of anti-solvents on $\text{Cs}_2\text{CuSbCl}_6$ DPNCs

For LARP, the polarity of solvents plays an important role in the crystal formation of PNCs.⁵⁰⁻⁵² Dutta et al. reported that the rate of formation of CsPbBr_3 PNCs can be drastically altered with a small difference in solvent polarity of anti-solvents.⁵⁰ Here, seven hydrophobic solvents with different polarities were chosen as the media for host solutions. They were isopropanol, chloroform, *o*-xylene, toluene, *m*-xylene, benzene and hexane with the dielectric constants 19.92, 4.81, 2.57, 2.38, 2.37, 2.28 and 1.89, respectively. The experimental details can be found in Experimental Methods and Supporting Information. We carried out XRD measurements to confirm the structure and phase purity of the products obtained by using the aforementioned seven anti-solvents before (Figure 4.1c) and after post-purification (Figure 4.1d). As shown in Figure 4.1c, the XRD patterns of as-prepared DPNCs without post-treatment are confirmed as the cubic $\text{Cs}_2\text{CuSbCl}_6$ structure with $Fm\bar{3}m$ space group symmetry where corner-sharing octahedra of $[\text{CuCl}_6]$ and $[\text{SbCl}_6]$ alternate along three directions and Cs^+ ions occupy the cuboctahedral cavities. The post-purification of DPNCs can remove excess insulating ligands, potentially benefitting the charge-carrier mobility of the DPNCs in film morphology (see below). However, there is a trade-off between the targeted increase of charge-carrier mobility and the structural stability of the DPNCs, especially for $\text{Cs}_2\text{CuSbCl}_6$, which has not been reported in the form of bulk crystals. It is thus crucial to confirm the phase purity of $\text{Cs}_2\text{CuSbCl}_6$ DPNCs after post-purification. As shown in Figure 4.1d, the DPNCs display good phase purity after post-treatment, except for the products obtained by using chloroform and isopropanol as anti-solvents. The additional reflections at $2\theta = 21.6^\circ$ and 30.7° from the sample synthesized in chloroform correspond to the (201) and (311) crystal planes of Cs_2CuCl_4 (PDF no. 01-071-0901), respectively. The impurity in the sample synthesized in isopropanol is confirmed as Cs_2CuCl_4 . This phenomenon, where residual chloroform and isopropanol, with relatively higher polarities, can affect the phase purity of $\text{Cs}_2\text{CuSbCl}_6$ DPNCs during the post-purification process has also been observed in lead-based PNCs.⁵²

As mentioned in the Experimental Methods, CuCl_2 was chosen as the Cu-providing precursor. Interestingly, the formal oxidation state of Cu in CuCl_2 is +2, while that in the desired HDP structure $\text{Cs}_2\text{CuSbCl}_6$ it is +1. To confirm the structure of the product, we compared the diffractograms to exclude the <111>-oriented layered double perovskite structure $\text{Cs}_4\text{CuSb}_2\text{Cl}_{12}$, where the oxidation of

Cu would be +2 (Figure 4.1c and 4.1d). To further distinguish the oxidation state of Cu, X-ray photoelectron spectroscopy (XPS) measurements were carried out (Figure S4.1). The Cu core-level spectrum consists of a 2p doublet exhibiting binding energies of 931.6 eV and 951.7 eV corresponding to Cu 2p_{3/2} and Cu 2p_{1/2}, respectively. This is consistent with the Cu(I) state.¹⁵ The characteristic core level for Cu(II) is expected at about 3 eV higher binding energy (935 eV and 955 eV) and is not observed. A similar phenomenon was also observed in the synthesis of Cs₂CuSbCl₆ DPNCs with the hot-injection method.¹⁵ The other elements were also found in their anticipated oxidation states, that is, Cs(I), Sb(III) and Cl(I), respectively.

In order to examine the effects of anti-solvents on the size and morphology of DPNCs, the as-prepared Cs₂CuSbCl₆ DPNCs were characterized by SEM (Figure 4.2). The DPNCs for SEM measurements were prepared without post-purification. Interestingly, different morphologies can be achieved by using anti-solvents with diverse dielectric constants (summarized in Figure 4.2h). As shown in Figure 4.2, Cs₂CuSbCl₆ DPNCs synthesized in hexane show irregular shapes with an average size of about 43 nm. In benzene, the as-synthesized samples show hexagonal plate morphology with an average length of 194 nm and width of 82 nm. By using *m*-xylene as anti-solvent, hexagonally-shaped nanocrystals can be obtained with smaller size (45 nm on average) but less regular in morphology, which is quite similar to nanocrystals synthesized in toluene (49 nm on average). However, when *o*-xylene is used as the anti-solvent, the morphology shows a significant change, forming nanorods with an average length of about 307 nm and width of 28 nm. Chloroform with relatively higher polarity can assist the formation of a mix of hexagonally-shaped nanocrystals and nanocuboids with an average size of 67 nm. Cs₂CuSbCl₆ nanocuboids (mean size 123 nm) and nanowires can be synthesized with isopropanol serving as anti-solvent. With the highest dielectric constant among these seven solvents, we hypothesize that isopropanol can not only act as a solvent, but also a nucleophile to partially remove OAm on the surface of DPNCs, which leads to the formation of relatively larger nanocrystals. The same phenomenon was also observed in the synthesis of CsPbBr₃ nanocrystals.⁵² Size distribution histograms of Cs₂CuSbCl₆ DPNCs synthesized with these seven different anti-solvents can be accessed in the Supporting Information (Figure S4.2). Based on our observations, it is clear that the type of anti-solvent has a strong impact on the kinetic pathways, which results in different anisotropically grown nanostructures.

4.4.2.2 Impact of the amount of OA and OAm ligands on $\text{Cs}_2\text{CuSbCl}_6$ DPNCs

In the synthesis of lead-based PNCs and other conventional quantum dots, organic acids and bases are commonly used ligands, with the ability to solvate the precursors effectively, affect the kinetic pathway to control the shape and size of nanomaterials and avoid the aggregation or agglomeration of the nanomaterials.^{23, 53-54} OA and OAm are a frequently used pair to synthesize PNCs. The impact of OA and OAm on lead-based PNCs synthesized by the hot-injection method has been already comprehensively studied, but their effect on DPNCs prepared via the LARP method remains poorly understood.⁵⁵⁻⁵⁶

Firstly, we studied the effect of different amounts of OA on the size and morphology of $\text{Cs}_2\text{CuSbCl}_6$ DPNCs synthesized by using three representative anti-solvents: chloroform, toluene and hexane, where three volumes of OA (300 μL , 400 μL , and 500 μL) were tested and the volume of OAm was fixed at 175 μL in the synthesis recipe. When chloroform was used as an anti-solvent, the smallest amount of OA (300 μL) leads to irregular morphologies, which are dumbbell-shaped nanocrystals with a length of about 120 nm, rhombus-shaped nanocrystals with a length of about 90 nm and other nanocrystals with irregular shapes (Figure 4.3a). Increasing the amount of OA to 400 μL , smaller nanospheres and nanocuboids can be obtained with an average size of 27 nm (Figure 4.3b). Further increasing the amount of OA to 500 μL , the size of nanocrystals increases, resulting in nanocuboids with an average length of 97 nm and width of 50 nm (Figure 4.3c). In the case of toluene as anti-solvent, a large range of uniform nanorods with an average width of 29 nm and length of 104 nm can be synthesized when the smallest amount of OA (300 μL) is used (Figure 4.3d). Increasing the amount of OA, the morphology can be changed to nanocuboids (Figure 4.3e, 400 μL of OA, mean size 42 nm) and to hexagonally-shaped nanocrystals (Figure 4.3f, 500 μL of OA, mean size 75 nm). The parameter window for a successful synthesis of $\text{Cs}_2\text{CuSbCl}_6$ DPNCs is relatively narrow when hexane is chosen as the anti-solvent. The DPNCs could not be obtained when 300 μL of OA was used in the reaction, leading to precipitation of the reagents with no uniform dispersion in hexane after the centrifugation, indicating that the size of particles was too big to be stable in the solution. Additionally, increasing the amount of OA to 500 μL , big particles with a size of hundreds of nanometers can be produced with irregular morphologies (Figure 4.3i). However, when 400 μL of OA was introduced to the reaction, irregular-shaped $\text{Cs}_2\text{CuSbCl}_6$ DPNCs with a relatively broad size distribution were obtained (Figure 4.3h). In short, toluene is demonstrated to be the best anti-solvent to synthesize $\text{Cs}_2\text{CuSbCl}_6$ DPNCs, resulting in well-defined sizes and morphologies.

To study the impact of the amount of OAm on the synthesis of $\text{Cs}_2\text{CuSbCl}_6$ DPNCs, toluene was used as the anti-solvent. Four different amounts of OAm in the synthesis recipe were tested, which were 150 μL , 175 μL , 200 μL , and 225 μL . The smallest amount of OAm leads to the formation of nanocuboids with an average length of 98 nm and width of 66 nm (Figure 4.4a). When further increasing the amount of OAm to 175 μL and 200 μL , the morphology changes to a mixture of nanocuboids and nanospheres with an average size of 32 nm (Figure 4.4b) and 43 nm (Figure 4.4c), respectively. When the amount of OAm reaches 225 μL (OA/OAm ratio of 1.78, Figure 4.4d), the morphology of nanorods with an average length of 116 nm and width of 30 nm is obtained, similar to the nanorods synthesized by using 300 μL OA and 175 μL OAm (OA/OAm volume ratio of 1.71, Figure 4.3d), which have a similar OA/OAm ratio. The same phenomenon can also be observed in the cases of OA/OAm volume ratio of 2.85 (500 μL of OA and 175 μL of OAm, Figure 4.3f) and 2.67 (400 μL of OA and 150 μL of OAm, Figure 4.4a), where bigger particles can be obtained. A smaller quantity of OAm provides faster growth kinetics and forms $\text{Cs}_2\text{CuSbCl}_6$ DPNCs, with relatively bigger size.⁵² The above observations indicate that the ratio of OA to OAm plays an important role in controlling the size and morphology of $\text{Cs}_2\text{CuSbCl}_6$ DPNCs.

4.4.3 Optical Properties of $\text{Cs}_2\text{CuSbCl}_6$ DPNCs

To evaluate the suitability of $\text{Cs}_2\text{CuSbCl}_6$ DPNCs as a potential absorber for photovoltaic applications, we characterized the optical absorption of the nanocrystals synthesized by using different anti-solvents (Figure 4.5a). The band gaps of these nanocrystals were calculated by using the Tauc plot method⁵⁷ (Figure S4.3), which reveals that the $\text{Cs}_2\text{CuSbCl}_6$ DPNCs synthesized with different anti-solvents show similar indirect band gaps with values between 1.67 eV and 1.78 eV. The $\text{Cs}_2\text{CuSbCl}_6$ DPNCs synthesized in chloroform have the smallest band gap of 1.67 eV, while the ones synthesized in isopropanol have the biggest band gap of 1.78 eV. $\text{Cs}_2\text{CuSbCl}_6$ DPNCs synthesized by using other anti-solvents showed similar band gaps around 1.72 eV (Figure S4.3). The reason for this observation is not clear, for example, different surface-ligand interactions and surface defect populations may lead to the differences in the value of the band gap.²⁷

The PL of $\text{Cs}_2\text{CuSbCl}_6$ DPNCs was observed after subpicosecond pulsed laser excitation at 476 nm (Figure 4.5b). The PL spectrum of $\text{Cs}_2\text{CuSbCl}_6$ DPNCs shows a broad emission band peaking at 1.8 eV (689 nm) with a full width at half maximum (FWHM) of 0.56 eV (215 nm). Surprisingly, a 10 times higher PL intensity was recorded after irradiation with 405 nm laser. Such “light soaking” (the PL of the sample increases after being exposed to UV light) also changes the PL spectrum of $\text{Cs}_2\text{CuSbCl}_6$

DPNCs. A significant spectral broadening to the blue side with the peak now centering at 1.85 eV (670 nm) and a FWHM of 0.65 eV (235 nm) was revealed when the sample was fully light-soaked, i.e. without further increase in PL intensity upon UV exposure. A TCSPC transient of light-soaked $\text{Cs}_2\text{CuSbCl}_6$ DPNCs recorded with 476 nm excitation is shown in Figure S4.4. The PL transients of $\text{Cs}_2\text{CuSbCl}_6$ DPNCs can be modelled by a bi-exponential decay function with a very short decay time below 10 ps (the temporal resolution of the experiment) and a slower decay time of 97 ps.

4.4.4 Synthesis of $\text{Cs}_2\text{CuSbBr}_6$ DPNCs by Anion-Exchange Reaction

We successfully obtained $\text{Cs}_2\text{CuSbBr}_6$ DPNCs via an anion-exchange reaction of $\text{Cs}_2\text{CuSbCl}_6$ DPNCs. Various anion-exchange agents can be used to drive the conversion, however, the agents should be chosen carefully as a wide range of reagents may cause the conversion of crystal phases or stoichiometries of the desired DPNC phase.⁵⁸ In addition, the degradation of PNCs can also occur during the purification after the anion-exchange reaction aimed at removing by-products and excess reagents. TMSI, TMSBr and TMSCl have been widely used for anion-exchange reactions of PNCs, as they can be easily removed due to their low boiling points of 107 °C, 79 °C, and 57 °C, respectively. They offer good miscibility with nonpolar alkane and arene solvents like hexane and toluene, which are commonly used for the dispersion of PNCs. The strength of the TMS-X bond (X = I, Br, Cl) increases significantly from the I to Br to Cl, and TMS-X (X = I, Br, Cl) have dissociation energies of 77, 96, and 113 (kcal/mol), respectively, which means that the substitution of TMS-Br bonds for TMS-I bonds or TMS-Cl bonds for TMS-Br is energetically favorable.⁵⁸ Here, TMSBr was adopted as the reagent for the conversion of $\text{Cs}_2\text{CuSbCl}_6$ DPNCs to $\text{Cs}_2\text{CuSbBr}_6$ DPNCs. To achieve different levels of conversion, $\text{Cs}_2\text{CuSbCl}_6$ DPNCs (0.02 mmol) were reacted with different amounts of TMSBr solution (0.1 M). The details of the reactions can be found in the Experimental Methods.

To identify the crystal structure of the products after the anion-exchange reaction, XRD measurements were carried out. An increasing amount of TMSBr leads to a shift to lower angles 2θ when compared to $\text{Cs}_2\text{CuSbCl}_6$ DPNCs, indicating the increase of lattice constants, as expected after the substitution of Cl with Br (Figure S4.5a). The XRD pattern of the completely converted product matches well with the simulated XRD pattern of $\text{Cs}_2\text{CuSbBr}_6$ DPNCs (Figure 4.6a) and the expansion of lattice constants can also be verified by HRTEM (Figure S4.6). The XPS results further confirm the complete removal of Cl in the final sample, as the characteristic peaks of Cl 2p (located at 198.5 eV and 200.1 eV) are not observed in the XPS spectrum (inset of Figure S4.7a). Additionally and importantly, the oxidation state of Cu is maintained as +1. The expected element ratio in the resulting

Cs₂CuSbBr₆ DPNCs is reasonably well confirmed as 2:0.7:0.8:6 (Cs:Cu:Sb:Br) by XPS, which is slightly off-stoichiometry. However, within the common uncertainties, the XPS data match the expected element ratios of the DPNCs quite well (which might also slightly differ due to the possible existence of surface defects). HRTEM and SEM characterization of the products obtained after anion-exchange reactions further illustrate that both the size and the morphology of the DPNCs are maintained (Figure S4.6b, S4.8).

The introduction of Br anions into Cs₂CuSbCl₆ DPNCs by the addition of TMSBr solutions results in a significant red-shift of the absorption edges (Figure 4.6b and S4.4b). The color of the DPNC solution changes from light brown to black after the complete conversion (inset of Figure 4.6b). The absorption spectra of DPNC solutions with different conversion levels are shown in Figure S4.5b. Figure 4.6b shows the absorption spectra of both Cs₂CuSbCl₆ and Cs₂CuSbBr₆ DPNC solutions (completely converted). The Cs₂CuSbBr₆ DPNCs exhibit a broad absorption with a strongly reduced indirect band gap of 0.9 eV, which is estimated with the Tauc plot method (Figure S4.9). This is, to the best of our knowledge, the narrowest band gap among the experimentally-reported HDP materials reported to date.

While the preparation of Cs₂CuSbBr₆ DPNCs by anion-exchange reaction was demonstrated to be successful, at this point attempts to access the conversion of Cs₂CuSbBr₆ to Cs₂CuSbI₆ DPNCs via the same method by using TMSI proved to be unsuccessful. A preceding theoretical study indicates that Cs₂CuSbI₆ is unstable with a negative decomposition enthalpy of -11 meV/atom.¹⁴ As a result, our attempts at synthesizing Cs₂CuSbI₆ DPNCs led to an orange mixture of products that were confirmed to be Cs₃Cu₂I₅, Cs₃Sb₂I₉ and CsI by XRD (Figure S4.10).

4.4.5 Electronic structure of Cs₂CuSbCl₆ and Cs₂CuSbBr₆ DPNCs

On the basis of DFT computations, the band structures and density of states (DOS) of Cs₂CuSbCl₆ and Cs₂CuSbBr₆ in *Fm* $\bar{3}$ *m* were calculated. As displayed in Figure 4.6c and 4.6d, Cs₂CuSbCl₆ and Cs₂CuSbBr₆ exhibit indirect band gaps of 1.68 eV and 1.18 eV with valence band maximum (VBM) and conduction band minimum (CBM) at X point and L point, respectively. Our HSE06+SOC calculated band gap for Cs₂CuSbCl₆ agrees well with the previous HSE06 calculated one (1.70 eV), indicating that the effect of spin-orbit coupling (SOC) on the electronic structure of Cs₂CuSbCl₆ is negligible. In addition, the calculated band gaps of Cs₂CuSbCl₆ and Cs₂CuSbBr₆ are in good agreement with our experimental data of these DPNCs. For Cs₂CuSbX₆ (X = Cl, Br), the valence band edges are dominantly derived from the Cu-3d states and the X-p (X = Cl, Br) orbitals while the conduction band edges are

mainly composed of Sb-5p and the X-p states (X = Cl, Br), as shown in Figure 4.6c and 4.6d. $\text{Cs}_2\text{CuSbBr}_6$ has a narrower band gap than $\text{Cs}_2\text{CuSbCl}_6$, which could be attributed to the VBM upshifting and CBM downshifting in bromides with respect to those in chlorides. The same trend of band gaps has been observed in comparing $\text{Cs}_2\text{AgBiBr}_6$ and $\text{Cs}_2\text{AgBiCl}_6$.⁵⁹⁻⁶⁰ The band dispersion around the band edges for $\text{Cs}_2\text{CuSbBr}_6$ and $\text{Cs}_2\text{CuSbCl}_6$ is similar, which is alike in the case of $\text{Cs}_2\text{AgBiX}_6$ (X = Cl, Br).⁶¹ The indirect and direct band gaps of $\text{Cs}_2\text{CuSbX}_6$ (X = Cl, Br) are greatly reduced compared to the $\text{Cs}_2\text{AgSbX}_6$ (X = Cl, Br) (See Table S4.1).

Furthermore, we computed the spectroscopic limited maximum efficiency (SLME) for $\text{Cs}_2\text{CuSbX}_6$ (X = Cl, Br) and $\text{Cs}_2\text{AgSbBr}_6$ as a function of thickness of the absorber layer. The SLME of $\text{Cs}_2\text{AgSbCl}_6$ was not calculated since the direct transition band gap is out of the range of the visible spectrum. As displayed in Figure S4.11, the predicted SLME of $\text{Cs}_2\text{CuSbX}_6$ (X = Cl, Br) and $\text{Cs}_2\text{AgSbBr}_6$ sharply increases to 4.1%, 5.6% and 5.1% for a film thickness reaching 0.3 μm . When the film thickness further increases, the predicted SLMEs of all compounds increase slowly and gradually saturate. Among the three compounds, $\text{Cs}_2\text{CuSbBr}_6$ exhibits the highest predicted SLME (8.5%) at a thickness of 3 μm . The SLME of $\text{Cs}_2\text{CuSbBr}_6$ is 1.3 times higher than that of $\text{Cs}_2\text{AgSbBr}_6$ at the same film thickness, illustrating that Cu(I)-based double perovskites have a higher conversion efficiency than Ag(I)-based ones.

4.4.6 Film Fabrication of $\text{Cs}_2\text{CuSbCl}_6$ and $\text{Cs}_2\text{CuSbBr}_6$ DPNCs

When aiming for optoelectronic applications of $\text{Cs}_2\text{CuSbCl}_6$ and $\text{Cs}_2\text{CuSbBr}_6$ DPNCs, high-quality films are a key requirement. Compared to organic-inorganic hybrid perovskite materials (such as MAPbI_3), it is more challenging to adopt the normally utilized solution-processing method to fabricate high-quality HDP films because of the lower solubility of the all-inorganic precursors and the higher formation temperatures.³³ In contrast, the solution processability of DPNCs offers a facile and effective process to obtain high-quality HDP films. Here, thin films of $\text{Cs}_2\text{CuSbCl}_6$ and $\text{Cs}_2\text{CuSbBr}_6$ were fabricated via a simple direct deposition of corresponding DPNC solutions by spin-coating (Figure 4.7a). The purified DPNCs were redispersed in octane at a concentration of about 70 mg/mL for the film deposition (details in Experimental Methods). MA and EA were used as washing solvents to initiate solid-state ligand exchange, which can avoid the re-dissolving issue as a second layer was deposited in parallel to enhance the electronic coupling between DPNCs. Thus, different film thicknesses could be obtained by a layer-by-layer deposition process. As shown in Figure 4.7b, the SEM image of a $\text{Cs}_2\text{CuSbCl}_6$ DPNC film without being exposed to a solid-state ligand exchange process

is quite indistinct due to the large amount of ligands left in the film. However, after washing the $\text{Cs}_2\text{CuSbCl}_6$ DPNC film with either MA or EA, distinct DPNC films can be observed, which are very smooth and dense (Figure 4.7c and 4.7d, Figure S4.12). A high-quality $\text{Cs}_2\text{CuSbBr}_6$ DPNC film can be obtained by the same process (Figure S4.13).

We carried out XPS and UPS measurements for both $\text{Cs}_2\text{CuSbCl}_6$ and $\text{Cs}_2\text{CuSbBr}_6$ DPNC films before and after the solid-state ligand exchange process. XPS spectra evidence the characteristic Cu(I) state at *ca.* 932 ($2p_{3/2}$) and *ca.* 952 eV ($2p_{1/2}$) binding energy (Figure S4.14). Relative concentrations of the different elements have also been calculated (See Table S4.2). We find that after ligand removal (*i.e.*, oleic acid and oleylamine), the C and O contents decrease, confirming the success of this procedure. Due to the large amounts of C, N, and O on the surfaces, a reliable derivation of the Cs:Cu:Sb:Cl or Br stoichiometry of the films from XPS data is difficult, but the off-stoichiometric compositions of the films might be due to different reasons, as already observed for the DPNCs (see above). Here, the measured element ratios of $\text{Cs}_2\text{CuSbCl}_6$ and $\text{Cs}_2\text{CuSbBr}_6$ films are, respectively: 1.5:0.4:0.9:6 and 1.9:0.5:0.7:6 (Cs:Cu:Sb:Cl or Br). The semi-quantitative analyses also show that these compositions remain basically unchanged after ligand removal (e.g., the Cs:Cl, Sb:Cl, Cu:Cl ratios remain relatively similar – see Table S4.2).

XPS and UPS data can also be combined to position the main energy levels of the semiconducting $\text{Cs}_2\text{CuSbCl}_6$ and $\text{Cs}_2\text{CuSbBr}_6$ films, that is, the Fermi level, the VBM, and the CBM. The energy cut-off ($E_{cut-off}$) has been deduced from UPS data (Figure S4.15). It leads to the work function of the sample, *i.e.*, the energy difference between the vacuum level and the Fermi level of the sample. Unfortunately, clear valence band edges of the sample cannot be distinguished by UPS, as a significant density of states is only observed above 2.0 eV. UPS is a highly surface sensitive technique, and the presence of organic ligands, even after partial removal, may hinder the analysis of the DPNC itself. To overcome this issue, the valence band edge has also been acquired by XPS. The kinetic energy of the valence band photoelectrons is higher in XPS than in UPS and results in a deeper depth of analysis. The valence band edge of $\text{Cs}_2\text{CuSbCl}_6$ was estimated at 1.2 eV below the 0.0 eV binding energy reference Fermi level. Similarly, this energy difference has been estimated to be 0.7 eV for the $\text{Cs}_2\text{CuSbBr}_6$, in agreement with a lower indirect band gap discussed above. This 0.5 eV offset can be explained by both the substitution of Cl 3p by Br 4p that have higher energy states and by a change of the doping. If the doping level of the sample is modified, by for instance anion-exchange, the Fermi level of the sample will shift, and if this reference level shifts all the spectra should shift accordingly. The Cs $3d_{5/2}$

and the Cu $2p_{3/2}$ states are shifted by 0.2 eV and 0.1 eV to lower energy after the ion exchange. This indicates that the Fermi level of $\text{Cs}_2\text{CuSbCl}_6$ has been shifted closer to the valence band by roughly 0.2 eV after its conversion to $\text{Cs}_2\text{CuSbBr}_6$. The remaining 0.3 eV (difference) is due to the substitution of the Cl 3p orbitals by Br 4p orbitals. Looking at a theoretical intrinsic position of the Fermi level ($E_{F,\text{in}}$), we find that the two materials are n-doped with an energy difference of 0.35 eV and 0.25 eV ($=E_F - E_{F,\text{in}}$) for $\text{Cs}_2\text{CuSbCl}_6$, and $\text{Cs}_2\text{CuSbBr}_6$, respectively. Using the valence band edge obtained by XPS, the work function obtained by UPS, and the optical band gap obtained by UV-Vis absorption, the resulting electronic structure diagram can be drawn (Figure S4.16). Interestingly, we note that the partial ligand removal has shifted the Fermi level of the DPNCs. For instance, the $E_F - E_{F,\text{in}}$ energy difference of $\text{Cs}_2\text{CuSbCl}_6$ is reduced from 0.35 eV to 0.05 with this procedure. Hence, the X-ion exchange from Cl to Br leads to more intrinsic materials.

In terms of ambient stability, $\text{Cs}_2\text{CuSbCl}_6$ DPNCs covered with a full ligand shell can be uniformly dispersed in hexane and octane as solutions after 520 days (Figure S4.17). However, the purified $\text{Cs}_2\text{CuSbCl}_6$ DPNCs (solid-state) started to decompose after 8 days in ambient conditions (Figure S4.18a). $\text{Cs}_2\text{CuSbCl}_6$ DPNC thin films washed with MA show better stability compared to the ones washed with isopropanol, which apparently has a better ligand-removing ability due to its higher dielectric constant (Figure S4.19). The $\text{Cs}_2\text{CuSbCl}_6$ DPNC films annealed at 140 °C for 5 minutes both in ambient conditions and in a N_2 -filled glovebox show evidence of decomposition (Figure S4.19). More stability test details can be found in the Supporting Information.

4.5 Conclusion

In summary, we report a facile and fast synthesis method for $\text{Cs}_2\text{CuSbCl}_6$ DPNCs by using a modified LARP method at ambient conditions. A less toxic and easily removable solvent, methanol, was chosen for solvating precursor salts. We demonstrate that the polarity of anti-solvents and the ratio of OA/OAm ligands have a strong effect on the size and morphology of the resulting DPNCs. $\text{Cs}_2\text{CuSbBr}_6$ DPNCs with a narrow band gap of 0.9 eV were successfully developed for the first time by employing an anion-exchange reaction in solution. Both $[\text{CuCl}_6]^{5-}$ and $[\text{CuBr}_6]^{5-}$ octahedra can be stabilized in these double perovskites at the nanoscale with the assist of organic ligands, which we expect to enable the development of other predicted-metastable (as bulk) Cu(I)-based double perovskite materials to enrich the double perovskite family and to benefit the screening of high performance lead-free HDPs materials for optoelectronic applications. Taking advantage of the solution processability of DPNCs, smooth and dense $\text{Cs}_2\text{CuSbCl}_6$ and $\text{Cs}_2\text{CuSbBr}_6$ DPNC films were successfully fabricated. Optimization

of the ligand density and developing new types of ligands, for example, conductive ligands, for these “unstable” DPNCs to balance the charge carrier mobility and phase stability need further effort and are expected to open new vistas in the development of optoelectronic applications of lead-free double perovskite materials.

4.6 Associated Content

Supporting Information

The Supporting Information is available free of charge at [Links: https://aip.scitation.org/doi/suppl/10.1063/5.0144708](https://aip.scitation.org/doi/suppl/10.1063/5.0144708)

4.7 Author Information

Corresponding Authors

Dan Han – Department of Chemistry, University of Munich (LMU), Munich D-81377, Germany; orcid.org/0000-0003-1890-4043; Email: Dan.Han@cup.uni-muenchen.de

Thomas Bein – Department of Chemistry and Center for NanoScience (CeNS), University of Munich (LMU), Munich D-81377, Germany; orcid.org/0000-0001-7248-5906; Email: bein@lmu.de

Authors

Shizhe Wang – Department of Chemistry and Center for NanoScience (CeNS), University of Munich (LMU), Munich D-81377, Germany; orcid.org/0000-0002-6771-5399

Clément Maheu – Surface Science Laboratory, Department of Materials and Earth Sciences, Technical University of Darmstadt, Darmstadt 64287, Germany; orcid.org/0000-0001-5417-5672

Zehua Xu – Department of Chemistry and Center for NanoScience (CeNS), University of Munich (LMU), Munich D-81377, Germany; orcid.org/0009-0006-7590-601X

Alexander Biewald – Department of Chemistry and Center for NanoScience (CeNS), University of Munich (LMU), Munich D-81377, Germany; orcid.org/0000-0003-0660-2072

Hannah Illner – Department of Chemistry, University of Munich (LMU), Munich D-81377, Germany; orcid.org/0000-0002-9559-1821

Rik Hooijer – Department of Chemistry and Center for NanoScience (CeNS), University of Munich (LMU), Munich D-81377, Germany; orcid.org/0000-0002-0038-2649

Thomas Mayer – Surface Science Laboratory, Department of Materials and Earth Sciences, Technical University of Darmstadt, Darmstadt 64287, Germany; orcid.org/0000-0001-6301-9196

Achim Hartschuh – Department of Chemistry and Center for NanoScience (CeNS), University of Munich (LMU), Munich D-81377, Germany; orcid.org/0000-0002-0518-6559

Hubert Ebert – Department of Chemistry, University of Munich (LMU), Munich D-81377, Germany

Notes

The authors declare no competing financial interest.

4.8 Acknowledgements

The authors thank Dr. Steffen Schmidt and Dr. Markus Döblinger for performing the SEM and TEM investigation, respectively. The authors acknowledge the Bavarian research network Solar Technologies go Hybrid (SolTech), the Deutsche Forschungsgemeinschaft (DFG, German Research Foundation) Excellence Cluster e-conversion (EXC 2089/1 – 390776260) and the DFG focus program SPP 2196 for funding of projects 423746744 (C.M., T.M.) and 424707803 (S.W., R.H., T.B.). D.H. and H.E. gratefully acknowledge the Gauss Centre for Supercomputing e.V. (www.gauss-centre.eu) for funding this project by providing computing time on the GCS Supercomputer SuperMUC-NG at Leibniz Supercomputing Centre (www.lrz.de). S.W. acknowledges support from the China Scholarship Council.

4.9 References

1. Slavney, A. H.; Hu, T.; Lindenberg, A. M.; Karunadasa, H. I., A bismuth-halide double perovskite with long carrier recombination lifetime for photovoltaic applications. *J. Am. Chem. Soc.* **2016**, *138* (7), 2138-2141.
2. Vargas, B.; Ramos, E.; Perez-Gutierrez, E.; Alonso, J. C.; Solis-Ibarra, D., A Direct Bandgap Copper-Antimony Halide Perovskite. *J. Am. Chem. Soc.* **2017**, *139* (27), 9116-9119.
3. Tewari, N.; Lam, D.; Li, C. H. A.; Halpert, J. E., Recent advancements in batteries and photo-batteries using metal halide perovskites. *APL Mater.* **2022**, *10* (4), 040905.
4. Luo, J.; Wang, X.; Li, S.; Liu, J.; Guo, Y.; Niu, G.; Yao, L.; Fu, Y.; Gao, L.; Dong, Q.; Zhao, C.; Leng, M.; Ma, F.; Liang, W.; Wang, L.; Jin, S.; Han, J.; Zhang, L.; Etheridge, J.; Wang, J.; Yan, Y.; Sargent, E. H.; Tang,

- J., Efficient and stable emission of warm-white light from lead-free halide double perovskites. *Nature* **2018**, *563* (7732), 541-545.
5. Tress, W.; Sirtl, M. T., Cs₂AgBiBr₆ Double Perovskites as Lead-Free Alternatives for Perovskite Solar Cells? *Solar RRL* **2022**, *6* (2), 2100770.
6. Zhang, Z.; Sun, Q.; Lu, Y.; Lu, F.; Mu, X.; Wei, S.-H.; Sui, M., Hydrogenated Cs₂AgBiBr₆ for significantly improved efficiency of lead-free inorganic double perovskite solar cell. *Nat. Commun.* **2022**, *13* (1), 3397.
7. Han, D.; Feng, C.; Du, M.-H.; Zhang, T.; Wang, S.; Tang, G.; Bein, T.; Ebert, H., Design of High-Performance Lead-Free Quaternary Antiperovskites for Photovoltaics via Ion Type Inversion and Anion Ordering. *J. Am. Chem. Soc.* **2021**, *143* (31), 12369-12379.
8. <https://www.nrel.gov/pv/cell-efficiency.html> **National Renewable Energy Laboratory, Best Research-Cell Efficiencies chart.**
9. Li, B.; Li, Z.; Wu, X.; Zhu, Z., Interface functionalization in inverted perovskite solar cells: from material perspective. *Nano Res. Energy* **2022**, *1* (1), e9120011.
10. Wei, F.; Deng, Z.; Sun, S.; Xie, F.; Kieslich, G.; Evans, D. M.; Carpenter, M. A.; Bristowe, P. D.; Cheetham, A. K., The synthesis, structure and electronic properties of a lead-free hybrid inorganic-organic double perovskite (MA)₂KBiCl₆ (MA = methylammonium). *Mater. Horiz.* **2016**, *3* (4), 328-332.
11. Lee, W.; Choi, D.; Kim, S., Colloidal Synthesis of Shape-Controlled Cs₂NaBiX₆ (X = Cl, Br) Double Perovskite Nanocrystals: Discrete Optical Transition by Non-Bonding Characters and Energy Transfer to Mn Dopants. *Chem. Mater.* **2020**, *32* (16), 6864-6874.
12. Zhang, C.; Gao, L.; Teo, S.; Guo, Z.; Xu, Z.; Zhao, S.; Ma, T., Design of a novel and highly stable lead-free Cs₂NaBiI₆ double perovskite for photovoltaic application. *Sustainable Energy & Fuels* **2018**, *2* (11), 2419-2428.
13. Dai, C.-M.; Zhang, T.; Wu, Y.-N.; Chen, S., Halide Double-Perovskite Light-Emitting Centers Embedded in Lattice-Matched and Coherent Crystalline Matrix. *Adv. Funct. Mater.* **2020**, *30* (17), 2000653.
14. Zhao, X.-G.; Yang, J.-H.; Fu, Y. H.; Yang, D. W.; Xu, Q. L.; Yu, L. P.; Wei, S.-H.; Zhang, L. J., Design of Lead-Free Inorganic Halide Perovskites for Solar Cells via Cation-Transmutation. *J. Am. Chem. Soc.* **2017**, *139* (7), 2630-2638.
15. Zhou, W.; Han, P.; Zhang, X.; Zheng, D.; Yang, S.; Yang, Y.; Luo, C.; Yang, B.; Hong, F.; Wei, D.; Lu, R.; Han, K., Lead-Free Small-Bandgap Cs₂CuSbCl₆ Double Perovskite Nanocrystals. *J. Phys. Chem. Lett.* **2020**, *11* (15), 6463-6467.
16. Wolf, N. R.; Connor, B. A.; Slavney, A. H.; Karunadasa, H., Doubling the Stakes: The Promise of Halide Double Perovskites. *Angew. Chem. Int. Ed.* **2021**, *133* (30), 16400-16414.
17. Bi, L.-Y.; Hu, Y.-Q.; Li, M.-Q.; Hu, T.-L.; Zhang, H.-L.; Yin, X.-T.; Que, W.-X.; Lassoued, M. S.; Zheng, Y.-Z., Two-dimensional lead-free iodide-based hybrid double perovskites: crystal growth, thin-film preparation and photocurrent responses. *J. Mater. Chem. A* **2019**, *7* (34), 19662-19667.
18. Vishnoi, P.; Zuo, J. L.; Li, X.; Binwal, D. C.; Wyckoff, K. E.; Mao, L.; Kautzsch, L.; Wu, G.; Wilson, S. D.; Kanatzidis, M. G.; Seshadri, R.; Cheetham, A. K., Hybrid Layered Double Perovskite Halides of Transition Metals. *J. Am. Chem. Soc.* **2022**, *144* (15), 6661-6666.

19. Aubrey, M. L.; Saldivar Valdes, A.; Filip, M. R.; Connor, B. A.; Lindquist, K. P.; Neaton, J. B.; Karunadasa, H. I., Directed assembly of layered perovskite heterostructures as single crystals. *Nature* **2021**, *597* (7876), 355-359.
20. Connor, B. A.; Smaha, R. W.; Li, J.; Gold-Parker, A.; Heyer, A. J.; Toney, M. F.; Lee, Y. S.; Karunadasa, H. I., Alloying a single and a double perovskite: a Cu^{+/2+} mixed-valence layered halide perovskite with strong optical absorption. *Chem. Sci.* **2021**, *12* (25), 8689-8697.
21. Protesescu, L.; Yakunin, S.; Bodnarchuk, M. I.; Krieg, F.; Caputo, R.; Hendon, C. H.; Yang, R. X.; Walsh, A.; Kovalenko, M. V., Nanocrystals of Cesium Lead Halide Perovskites (CsPbX₃, X = Cl, Br, and I): Novel Optoelectronic Materials Showing Bright Emission with Wide Color Gamut. *Nano Lett.* **2015**, *15* (6), 3692-3696.
22. Wang, S.; Yousefi Amin, A. A.; Wu, L.; Cao, M.; Zhang, Q.; Ameri, T., Perovskite Nanocrystals: Synthesis, Stability, and Optoelectronic Applications. *Small Struct.* **2021**, *2* (3), 2000124.
23. Bai, Y.; Hao, M.; Ding, S.; Chen, P.; Wang, L., Surface Chemistry Engineering of Perovskite Quantum Dots: Strategies, Applications, and Perspectives. *Adv. Mater.* **2022**, *34* (4), 2105958.
24. Yu, Y.; Li, C.; Li, C.; Zhou, W.; Han, P.; Zhao, K.; Li, H.; Lu, R., Conversion of the non-luminous lead-free inorganic halide perovskite variant CsNiCl₃ nanocrystals into photoluminescent materials by Cu⁺ and In³⁺ doping. *APL Mater.* **2022**, *10* (11), 111110.
25. Zhang, F.; Zhong, H.; Chen, C.; Wu, X.-g.; Hu, X.; Huang, H.; Han, J.; Zou, B.; Dong, Y., Brightly Luminescent and Color-Tunable Colloidal CH₃NH₃PbX₃ (X = Br, I, Cl) Quantum Dots: Potential Alternatives for Display Technology. *ACS Nano* **2015**, *9* (4), 4533-4542.
26. Greul, E.; Docampo, P.; Bein, T., Synthesis of Hybrid Tin Halide Perovskite Solar Cells with Less Hazardous Solvents: Methanol and 1,4-Dioxane. *Z. Anorg.Allg. Chem.* **2017**, *643* (21), 1704-1711.
27. Paul, S.; Acharya, S., Postsynthesis Transformation of Halide Perovskite Nanocrystals. *ACS Energy Lett.* **2022**, *7* (6), 2136-2155.
28. Scharf, E.; Krieg, F.; Elimelech, O.; Oded, M.; Levi, A.; Dirin, D. N.; Kovalenko, M. V.; Banin, U., Ligands Mediate Anion Exchange between Colloidal Lead-Halide Perovskite Nanocrystals. *Nano Lett.* **2022**, *22* (11), 4340-4346.
29. Jang, D. M.; Park, K.; Kim, D. H.; Park, J.; Shojaei, F.; Kang, H. S.; Ahn, J. P.; Lee, J. W.; Song, J. K., Reversible Halide Exchange Reaction of Organometal Trihalide Perovskite Colloidal Nanocrystals for Full-Range Band Gap Tuning. *Nano Lett.* **2015**, *15* (8), 5191-5199.
30. Creutz, S. E.; Crites, E. N.; De Siena, M. C.; Gamelin, D. R., Colloidal Nanocrystals of Lead-Free Double-Perovskite (Elpasolite) Semiconductors: Synthesis and Anion Exchange To Access New Materials. *Nano Lett.* **2018**, *18* (2), 1118-1123.
31. Gupta, S.; Kershaw, S. V.; Rogach, A. L., 25th Anniversary Article: Ion Exchange in Colloidal Nanocrystals. *Adv. Mater.* **2013**, *25* (48), 6923-6944.
32. Rivest, J. B.; Jain, P. K., Cation exchange on the nanoscale: an emerging technique for new material synthesis, device fabrication, and chemical sensing. *Chem. Soc. Rev.* **2013**, *42* (1), 89-96.
33. Tailor, N. K.; Listorti, A.; Colella, S.; Satapathi, S., Lead-Free Halide Double Perovskites: Fundamentals, Challenges, and Photovoltaics Applications. *Adv. Mater. Technol.* **2023**, *8*, 2200442.
34. Pickard, C. J.; Needs, R., High-pressure phases of silane. *Phys. Rev. Lett.* **2006**, *97* (4), 045504.

35. Pickard, C. J.; Needs, R., Ab initio random structure searching. *J. Phys.: Condens. Matter* **2011**, *23* (5), 053201.
36. Clark, S. J.; Segall, M. D.; Pickard, C. J.; Hasnip, P. J.; Probert, M. I.; Refson, K.; Payne, M. C., First principles methods using CASTEP. *Z. Kristallogr. - Cryst. Mater.* **2005**, *220* (5-6), 567-570.
37. Kresse, G.; Joubert, D., From ultrasoft pseudopotentials to the projector augmented-wave method. *Phys. Rev. B.* **1999**, *59* (3), 1758-1775.
38. Kresse, G.; Furthmüller, J., Efficient iterative schemes for ab initio total-energy calculations using a plane-wave basis set. *Phys. Rev. B.* **1996**, *54* (16), 11169-11186.
39. Perdew, J. P.; Burke, K.; Ernzerhof, M., Generalized gradient approximation made simple. *Phys. Rev. Lett.* **1996**, *77* (18), 3865.
40. Heyd, J.; Scuseria, G. E.; Ernzerhof, M., Hybrid functionals based on a screened coulomb potential. *J. Chem. Phys.* **2003**, *118* (18), 8207-8215.
41. Ong, S. P.; Wang, L.; Kang, B.; Ceder, G., Li-Fe-P-O₂ phase diagram from first principles calculations. *Chem. Mater.* **2008**, *20* (5), 1798-1807.
42. Ong, S. P.; Jain, A.; Hautier, G.; Kang, B.; Ceder, G., Thermal stabilities of delithiated olivine MPO₄ (M= Fe, Mn) cathodes investigated using first principles calculations. *Electrochem. Commun.* **2010**, *12* (3), 427-430.
43. Logan, W.; Michael, W. SL3ME. <https://github.com/ldwillia/SL3ME>.
44. Yu, L.; Zunger, A., Identification of potential photovoltaic absorbers based on first-principles spectroscopic screening of materials. *Phys. Rev. Lett.* **2012**, *108* (6), 068701.
45. Volonakis, G.; Filip, M. R.; Haghhighirad, A. A.; Sakai, N.; Wenger, B.; Snaith, H. J.; Giustino, F., Lead-Free Halide Double Perovskites via Heterovalent Substitution of Noble Metals. *J. Phys. Chem. Lett.* **2016**, *7* (7), 1254-1259.
46. Zhao, X.-G.; Yang, D.; Sun, Y.; Li, T.; Zhang, L.; Yu, L.; Zunger, A., Cu-In Halide Perovskite Solar Absorbers. *J. Am. Chem. Soc.* **2017**, *139* (19), 6718-6725.
47. Filip, M. R.; Hillman, S.; Haghhighirad, A. A.; Snaith, H. J.; Giustino, F., Band Gaps of the Lead-Free Halide Double Perovskites Cs₂BiAgCl₆ and Cs₂BiAgBr₆ from Theory and Experiment. *J. Phys. Chem. Lett.* **2016**, *7* (13), 2579-2585.
48. Tran, T. T.; Panella, J. R.; Chamorro, J. R.; Morey, J. R.; McQueen, T. M., Designing indirect-direct bandgap transitions in double perovskites. *Mater. Horiz.* **2017**, *4* (4), 688-693.
49. Xiao, Z.; Du, K.-Z.; Meng, W.; Mitzi, D. B.; Yan, Y., Chemical Origin of the Stability Difference between Copper(I)- and Silver(I)-Based Halide Double Perovskites. *Angew. Chem.* **2017**, *129* (40), 12275-12279.
50. Dutta, A.; Behera, R. K.; Pradhan, N., Solvent Polarity: How Does This Influence the Precursor Activation, Reaction Rate, Crystal Growth, and Doping in Perovskite Nanocrystals? *ACS Energy Lett.* **2019**, *4* (4), 926-932.
51. Fang, F.; Chen, W.; Li, Y.; Liu, H.; Mei, M.; Zhang, R.; Hao, J.; Mikita, M.; Cao, W.; Pan, R.; Wang, K.; Sun, X. W., Employing Polar Solvent Controlled Ionization in Precursors for Synthesis of High-Quality Inorganic Perovskite Nanocrystals at Room Temperature. *Adv. Funct. Mater.* **2018**, *28* (10), 1706000.

52. Seth, S.; Samanta, A., A Facile Methodology for Engineering the Morphology of CsPbX₃ Perovskite Nanocrystals under Ambient Condition. *Sci. Rep.* **2016**, *6* (1), 37693.
53. Zhang, Y.; Siegler, T. D.; Thomas, C. J.; Abney, M. K.; Shah, T.; De Gorostiza, A.; Greene, R. M.; Korgel, B. A., A “Tips and Tricks” Practical Guide to the Synthesis of Metal Halide Perovskite Nanocrystals. *Chem. Mater.* **2020**, *32* (13), 5410-5423.
54. Zhuang, Z.; Peng, Q.; Li, Y., Controlled synthesis of semiconductor nanostructures in the liquid phase. *Chem. Soc. Rev.* **2011**, *40* (11), 5492-5513.
55. Pan, A.; He, B.; Fan, X.; Liu, Z.; Urban, J. J.; Alivisatos, A. P.; He, L.; Liu, Y., Insight into the Ligand-Mediated Synthesis of Colloidal CsPbBr₃ Perovskite Nanocrystals: The Role of Organic Acid, Base, and Cesium Precursors. *ACS Nano* **2016**, *10* (8), 7943-7954.
56. Pradhan, N., Why Do Perovskite Nanocrystals Form Nanocubes and How Can Their Facets Be Tuned? A Perspective from Synthetic Prospects. *ACS Energy Lett.* **2021**, *6* (1), 92-99.
57. Tauc, J.; Grigorovici, R.; Vancu, A., Optical Properties and Electronic Structure of Amorphous Germanium. *Phys. Status Solidi (b)* **1966**, *15* (2), 627-637.
58. Creutz, S. E.; Crites, E. N.; De Siena, M. C.; Gamelin, D. R., Anion Exchange in Cesium Lead Halide Perovskite Nanocrystals and Thin Films Using Trimethylsilyl Halide Reagents. *Chem. Mater.* **2018**, *30* (15), 4887-4891.
59. Han, D.; Ogura, M.; Held, A.; Ebert, H., Unique Behavior of Halide Double Perovskites with Mixed Halogens. *ACS Appl. Mater. Interfaces* **2020**, *12* (33), 37100-37107.
60. Li, T.; Zhao, X.; Yang, D.; Du, M.-H.; Zhang, L., Intrinsic Defect Properties in Halide Double Perovskites for Optoelectronic Applications. *Phys. Rev. Applied* **2018**, *10* (4), 041001.
61. Han, D.; Zhang, T.; Huang, M.; Sun, D.; Du, M.-H.; Chen, S., Predicting the thermodynamic stability of double-perovskite halides from density functional theory. *APL Mater.* **2018**, *6* (8), 084902.

4.10 List of Figure Legends

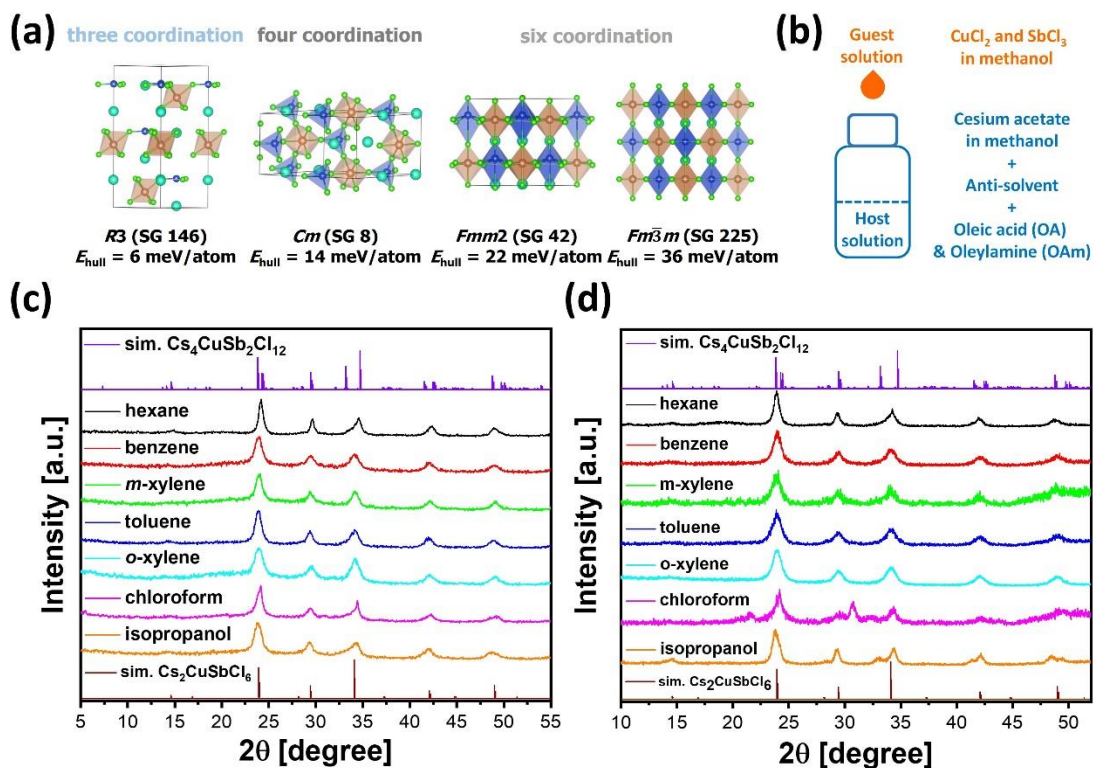


Figure 4.1: (a) Predicted crystal structures for $\text{Cs}_2\text{CuSbCl}_6$ with 3-, 4-, 6-fold coordinated Cu(I) atoms and $[\text{SbCl}_6]$ octahedra. Cyan, blue, orange, green balls represent Cs, Cu, Sb, Cl atoms, respectively. Unit cells are indicated with black lines. (b) Schematic illustration of the process for the modified LARP method and the starting materials in the guest solution and host solution. XRD patterns of $\text{Cs}_2\text{CuSbCl}_6$ DPNCs synthesized in different anti-solvents before (c) and after (d) post-purification process. The references are simulated XRD patterns of $\text{Cs}_2\text{CuSbCl}_6$ (bottom) and $\text{Cs}_4\text{CuSb}_2\text{Cl}_{12}$ (top), respectively.

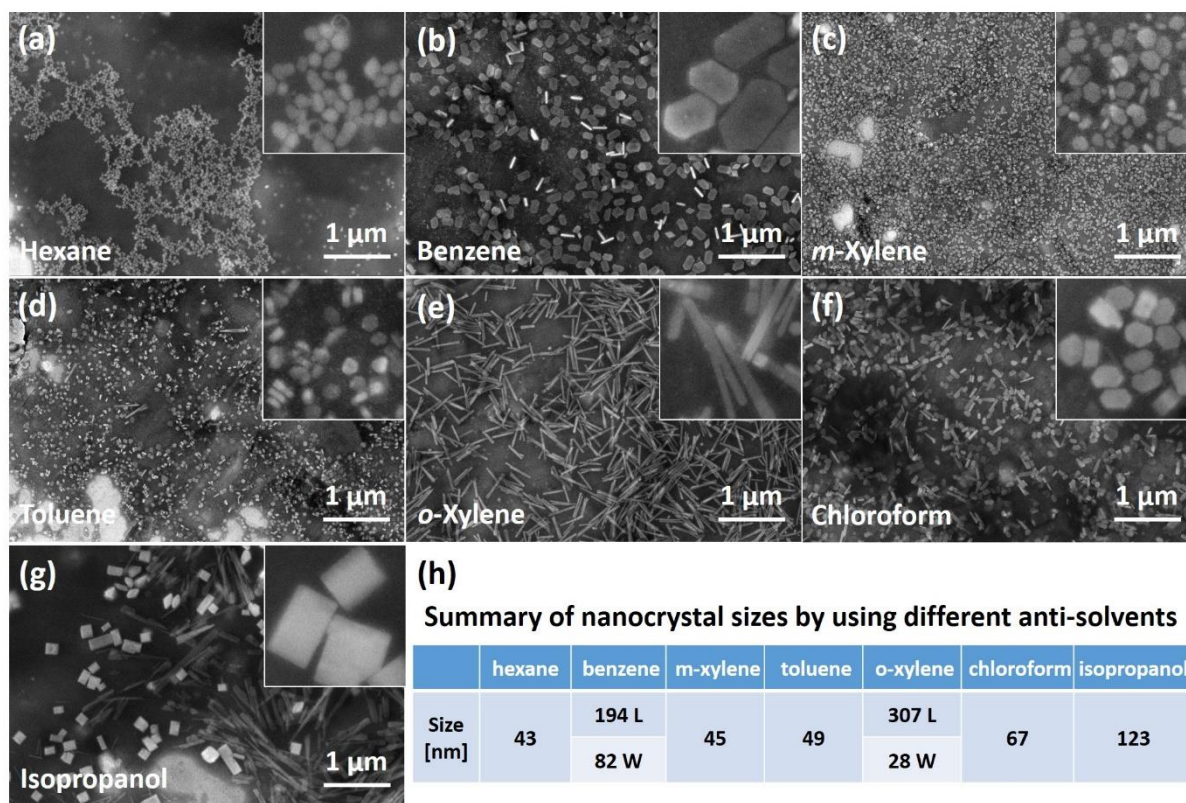


Figure 4.2: SEM images of $\text{Cs}_2\text{CuSbCl}_6$ DPNCs synthesized in hexane (a), benzene (b), m-xylene (c), toluene (d), o-xylene (e), chloroform (f), and isopropanol (g). The amounts of OA and OAm are fixed at 400 μL and 150 μL in the synthesis recipes, respectively. Insets: 400 nm \times 400 nm fields of view. (h) Summary of nanocrystal sizes by using different anti-solvents (L means length; W means width).

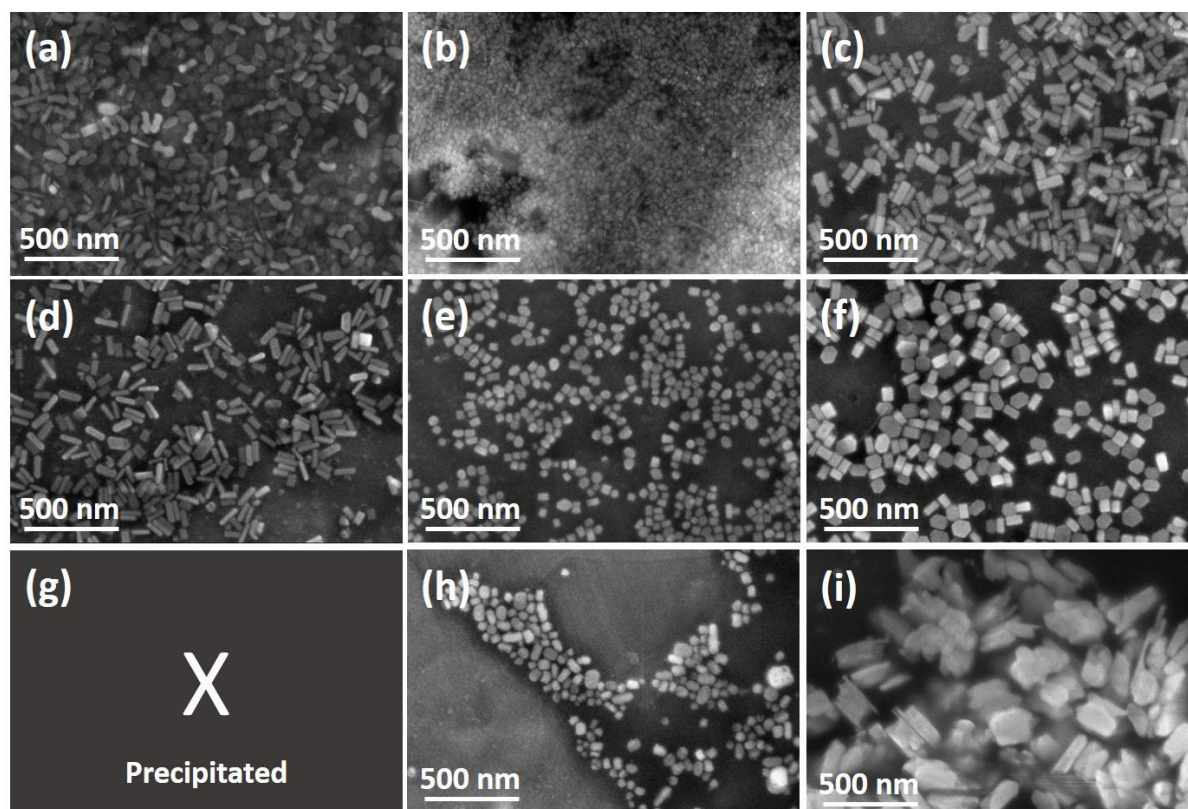


Figure 4.3: SEM images of $\text{Cs}_2\text{CuSbCl}_6$ DPNCs synthesized by using 300 μL (a, d, g), 400 μL (b, e, h) and 500 μL (c, f, i) of OA in chloroform (a-c), toluene (d-f) and hexane (g-i). (g) The products were all precipitated during the separation. The amount of OAm is fixed at 175 μL in the synthesis recipe.

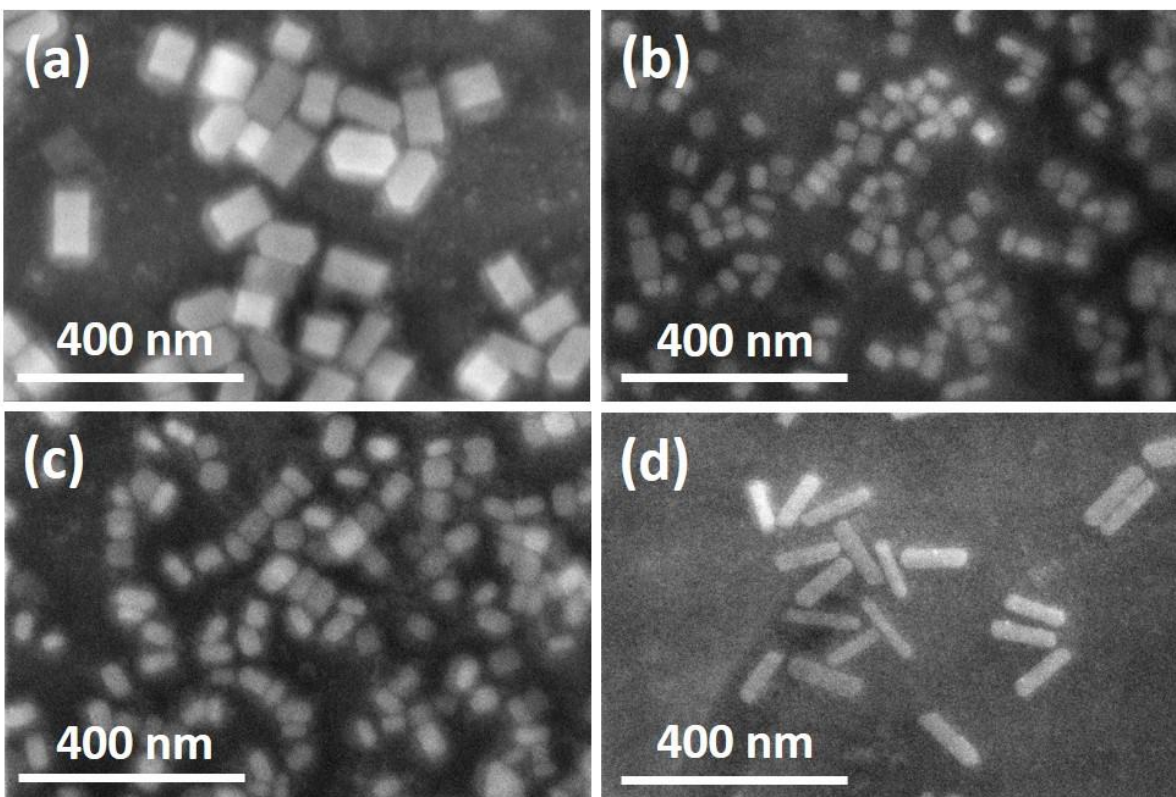


Figure 4.4: SEM images of $\text{Cs}_2\text{CuSbCl}_6$ DPNCs synthesized by using 150 μL (a), 175 μL (b), 200 μL (c), and 225 μL (d) of OAm. The anti-solvent is toluene, and the amount of OA is fixed at 400 μL in the synthesis recipe. The images are noisy due to the residues of ligands.

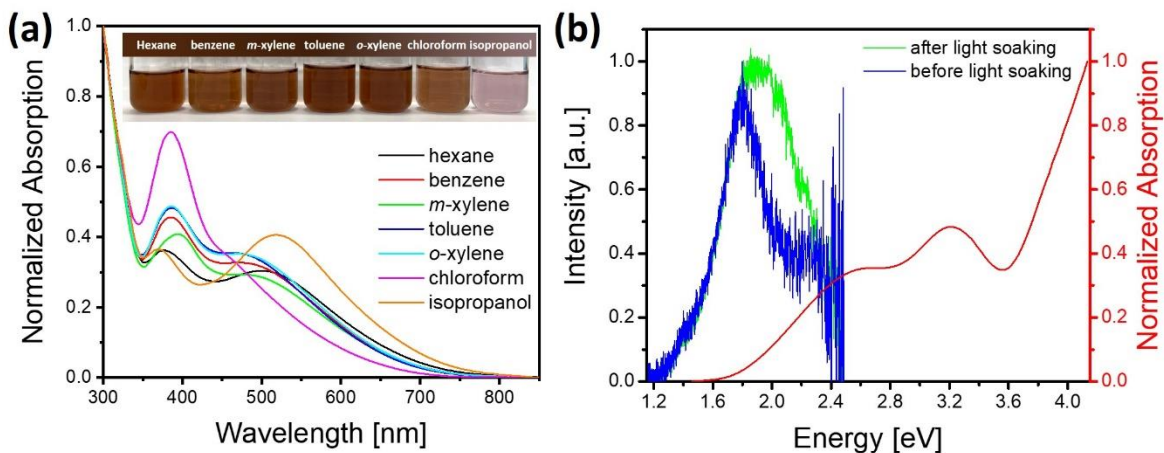


Figure 4.5: (a) Normalized absorption spectra of $\text{Cs}_2\text{CuSbCl}_6$ DPNCs synthesized in hexane, benzene, *m*-xylene, toluene, *o*-xylene, chloroform, and isopropanol. The amounts of OA and OAm are fixed at 400 μL and 150 μL in the synthesis recipe, respectively. Inset: photographs of $\text{Cs}_2\text{CuSbCl}_6$ DPNC solutions obtained by using the corresponding anti-solvents. (b) Absorption spectrum and photoluminescence (both normalized) of $\text{Cs}_2\text{CuSbCl}_6$ DPNCs. The noise at around 2.4 eV is due to the low PL intensity of the sample and low sensitivity of the detector in this region.

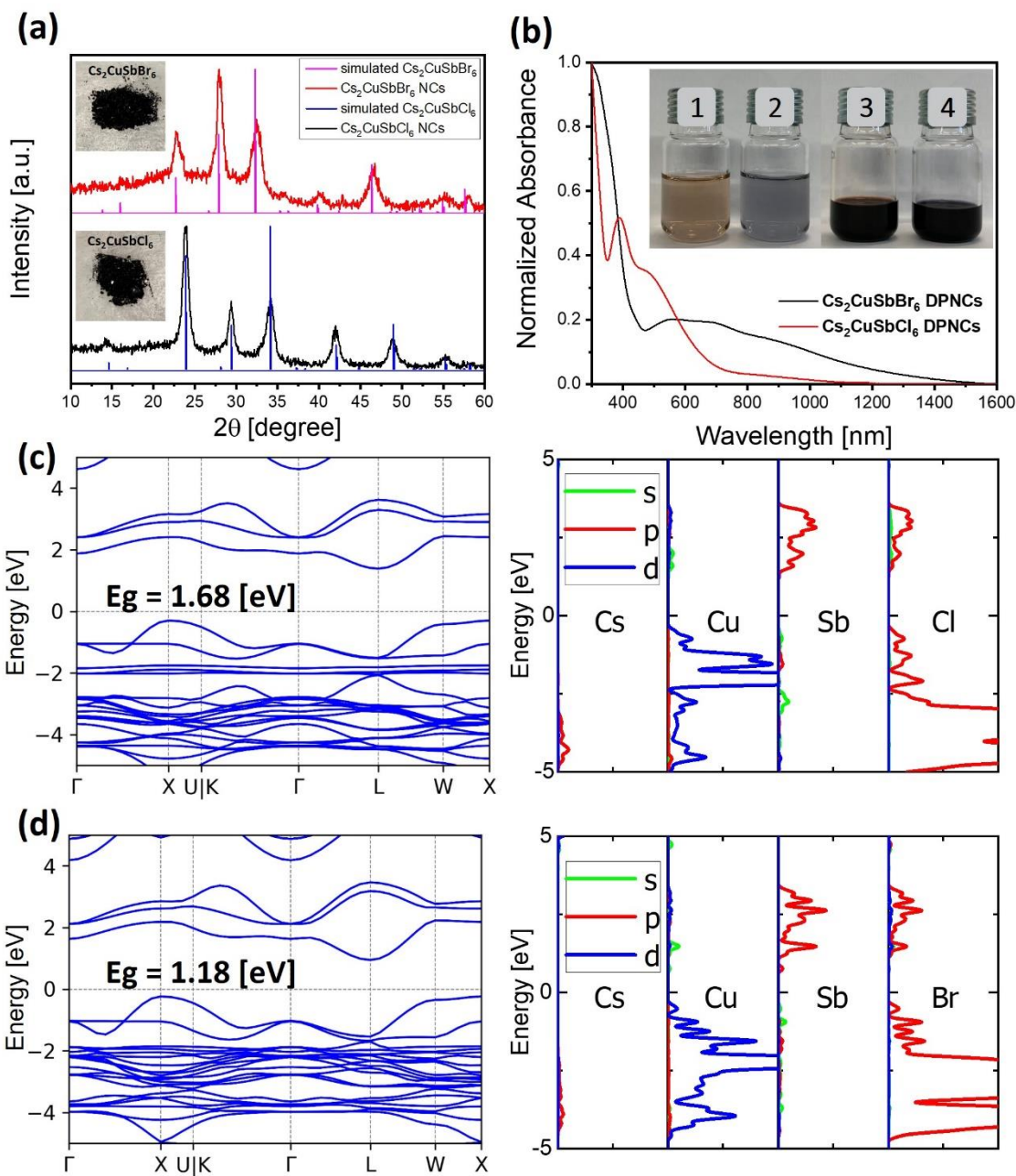


Figure 4.6: (a) XRD patterns illustrating the conversion of the $\text{Cs}_2\text{CuSbCl}_6$ DPNCs to $\text{Cs}_2\text{CuSbBr}_6$ DPNCs. The references are simulated XRD patterns of $\text{Cs}_2\text{CuSbCl}_6$ (bottom) and $\text{Cs}_2\text{CuSbBr}_6$ (top), respectively. Inset: photographs of $\text{Cs}_2\text{CuSbCl}_6$ converted to $\text{Cs}_2\text{CuSbBr}_6$ DPNC powders. (b) Absorption spectra illustrating the conversion of $\text{Cs}_2\text{CuSbCl}_6$ DPNCs to $\text{Cs}_2\text{CuSbBr}_6$ DPNC solutions. Inset: photographs of $\text{Cs}_2\text{CuSbCl}_6$ (1, 3) converted to $\text{Cs}_2\text{CuSbBr}_6$ (2, 4) DPNC solutions with low concentration (1, 2) and high concentration (3, 4). HSE+SOC calculated band structures and density of states (DOS) of (c) $\text{Cs}_2\text{CuSbCl}_6$ and (d) $\text{Cs}_2\text{CuSbBr}_6$ in space group $Fm\bar{3}m$.

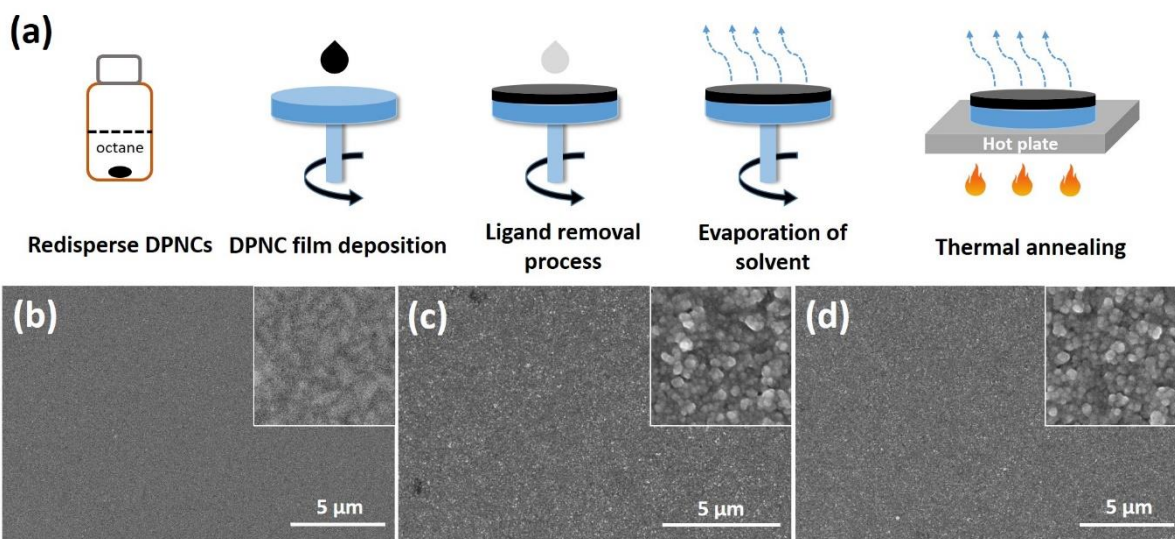


Figure 4.7: (a) Schematic illustration of the process of DPNC film fabrication. SEM images of $\text{Cs}_2\text{CuSbCl}_6$ DPNC films without washing (b), or washed with methyl acetate (c) or ethyl acetate (d). All films were spin-coated for 3 times on ITO. Insets: 500 nm \times 500 nm.

4.11 Supporting Information

4.11.1 Experimental Details

4.11.1.1 Synthesis of $\text{Cs}_2\text{CuSbCl}_6$ DPNCs with different anti-solvents.

The synthesis of $\text{Cs}_2\text{CuSbCl}_6$ DPNCs with different anti-solvents is described in the Experimental Methods. In the host solution, the amounts of OA and OAm were fixed as 400 μL and 150 μL , respectively, in 9 mL of the corresponding anti-solvents. The amount of CsAc methanol solution and $\text{CuCl}_2/\text{SbCl}_3$ methanol solution involved were both fixed at 150 μL . The $\text{Cs}_2\text{CuSbCl}_6$ DPNCs can be obtained by using these different anti-solvents. However, in the case of using hexane as the anti-solvent, it should be noted that the guest solution and the host solution can't form a homogeneous mixture immediately due to the immiscibility of hexane and methanol. The guest solution dropped down to the bottom of the vial and released CuCl_2 and SbCl_3 precursors slowly under vigorous stirring. The black crude DPNC solution could be obtained after ca. 20 minutes. This was not the case when the other six anti-solvents were used because the guest solution and host solution can be mixed homogeneously and the color of the mixture changed directly. Meanwhile, the yield of the DPNCs synthesized by using hexane is relatively low compared to using other anti-solvents.

4.11.1.2 Atomic force microscopy (AFM).

The AFM measurements were carried with the help of the Atomic Force Microscope mode in a NeaSNOM instrument from attocube systems AG. Silicon tips (Arrow-NCPT) were used in intermittent contact mode at a resonant frequency (R.F. = 250 kHz) and at a tapping amplitude of 80 nm. The images were later processed using Gwyddion and customized MATLAB code.

4.11.1.3 X-ray photoelectron spectroscopy (XPS) and Ultraviolet photoelectron spectroscopy (UPS) Measurements.

XPS measurements were carried out at both the University of Munich (LMU) and at the Technical University of Darmstadt (TU Darmstadt). At LMU, the XPS measurement was performed by using a VSW TA10 X-ray source providing non-monochromatized Al $K\alpha$ radiation ($h\nu = 1486.6$ eV) set at 15 mA and 12 kV and a VSW HA100 hemispherical analyzer. For calibration, the binding energies of the Au $4f_{4/2}$, Ag $3d_{5/2}$ and Cu $2p_{3/2}$ lines were used. The samples measured in Munich were transported via air to the analytical chamber which has a base pressure of 5×10^{-10} mbar. All spectra were recorded with a pass energy of 22 eV and a dwell time of 0.1 s per measurement point. While for a survey scan the step size was 1 eV and 10 scans were carried out, the number of scans was increased

up to 30 for detailed spectra and the step size was set to 0.1 eV. For the confirmation of the oxidation states of elements and the element ratios in the samples, the photoelectron peaks were fitted in Igor Pro 6.0.2.4 using a convolution of Doniach-Šunjić and Gaussian functions after a linear background subtraction. The peak intensities were normalized by the element and core level specific cross-sections¹ and the transmission function of the analyzer. The comparisons of the corrected peak areas give then approximate ratios of the elemental composition of the sample.

The samples shipped to Darmstadt were packed under nitrogen atmosphere, opened in the N₂-filled glovebox and transferred under vacuum to the cluster tool of the DAISY-SOL laboratory. XPS and UPS measurements were performed with a Thermo Fisher VG Escalab 250 spectrometer. XPS was carried out with a monochromatic Al K α X-ray source ($h\nu = 1486.6$ eV) set at 12 mA and 15 kV. The measurement mode was adjusted to get a lateral resolution of 650 μm in diameter and overcomes possible inhomogeneity at the sample surface. UPS was carried out with He I ($h\nu = 21.2$ eV) as a UV source. The pressure inside the analytical chamber was monitored below 3×10^{-9} mbar. Additional information on the calibration method can be found in our previous study.² Survey spectra were acquired with a pass energy of 50 eV, a step size of 0.1 eV, and a dwell time of 50 ms per measurement point. The high-resolution spectra were acquired with lower pass energy (10 eV) and smaller step size (0.05 eV); up to 50 scans were made to increase the signal-to-noise ratio. For the XPS quantitative chemical analysis and the binding energy (BE) shifts, spectra were analyzed with CasaXPS (version 2.3.19PR1.0). Spectra were fitted by first subtracting spectral background using a Shirley-type function, using a weighted least-squares method and model curves (Voigt functions of 70% Gaussian and 30% Lorentzian), and using *casaXPS-scofield.lib* for the relative sensitivity factors (R.S.F).³

4.11.1.4 Stability of Cs₂CuSbCl₆ and Cs₂CuSbBr₆ DPNCs.

The stability of purified Cs₂CuSbCl₆ and Cs₂CuSbBr₆ DPNCs in the solid state under ambient conditions was studied. On day 2, Cs₂CuSbBr₆ DPNCs started to decompose as confirmed by XRD results, where an obvious peak at ca. 53.7° appeared (Figure S4.18). Cs₂CuSbCl₆ DPNCs showed better stability than Cs₂CuSbBr₆ DPNCs, as that the peak at ca. 53.8° appeared only after 8 days. The degradation products in the samples were confirmed as CsCuCl₃ and CsCuBr₃ by XRD for Cs₂CuSbCl₆ and Cs₂CuSbBr₆ DPNCs, respectively. In case of Cs₂CuSbCl₆ DPNCs with full ligand shell covered in solution, it can be still uniformly dispersed in hexane and octane after 520 days (Figure S4.17).

Regarding DPNC thin films, a trade-off between removing insulating organic ligands for enhancing charge transport and keeping them for the stabilization of the double perovskite phase has to be

emphasized.⁴ Here, we compared two washing solvents, MA with the dielectric constant of 7.3 and isopropanol with the dielectric constant of 19.92. Isopropanol has a better ability to remove the ligands, as the film still looks transparent after 8 deposition cycles. Meanwhile, the film washed with MA looks relatively opaque, indicating that a large amount of ligand is left in the film (inset of Figure S4.19a). In Figure S4.18a, $\text{Cs}_2\text{CuSbCl}_6$ DPNCs without treatment as well as treated with MA and isopropanol exhibit a difference in absorption edges, which are 672 nm, 688 nm and 697 nm, respectively. The red-shift of the absorption edge suggests the decrease of the inter-NC distance and enhanced electronic coupling between NCs in the film.⁵ The slight decrease of the peak at ca. 388 nm for the film treated with isopropanol indicates the partial decomposition of the $\text{Cs}_2\text{CuSbCl}_6$ DPNCs, which was confirmed by XRD (Figure S4.19b). Small peaks appear at 20.5° and 21.7° in the XRD pattern of $\text{Cs}_2\text{CuSbCl}_6$ DPNCs treated with isopropanol, which can be indexed to (121) and (201) crystal planes of Cs_2CuCl_4 . However, the film treated with MA showed no decomposition.

The thermal stability of $\text{Cs}_2\text{CuSbCl}_6$ DPNC films treated with MA was also tested both in ambient air and in inert atmosphere. The $\text{Cs}_2\text{CuSbCl}_6$ DPNC film annealed at 60°C for 5 minutes showed good stability both in ambient air and in inert atmosphere as no big difference was observed in the absorption spectra and the XRD pattern (Figure S4.19c and S4.19d, respectively). The film annealed at 140°C for 5 minutes in ambient air turned yellow and decomposed to CsCuCl_3 and $\text{Cs}_3\text{Sb}_2\text{Cl}_9$, which was confirmed by XRD (Figure S4.19d). Meanwhile, the same annealing process performed in a N_2 -filled glovebox showed a smaller amount of impurities (CsCuCl_3 and $\text{Cs}_3\text{Sb}_2\text{Cl}_9$) forming in the film, where the color changed to purple (inset of Figure S4.19d). Figure S4.19c shows that the film annealed at 140°C in ambient condition features a significant decrease in absorption ranging from ca. 500 nm to 700 nm, and the film annealed at the same temperature in inert atmosphere shows less decomposition. Unfortunately, but as expected, $\text{Cs}_2\text{CuSbBr}_6$ films showed poorer stability than $\text{Cs}_2\text{CuSbCl}_6$ films, which requires more effort to find solutions towards stabilizing its double perovskite structure.

4.11.2 Supporting Figures

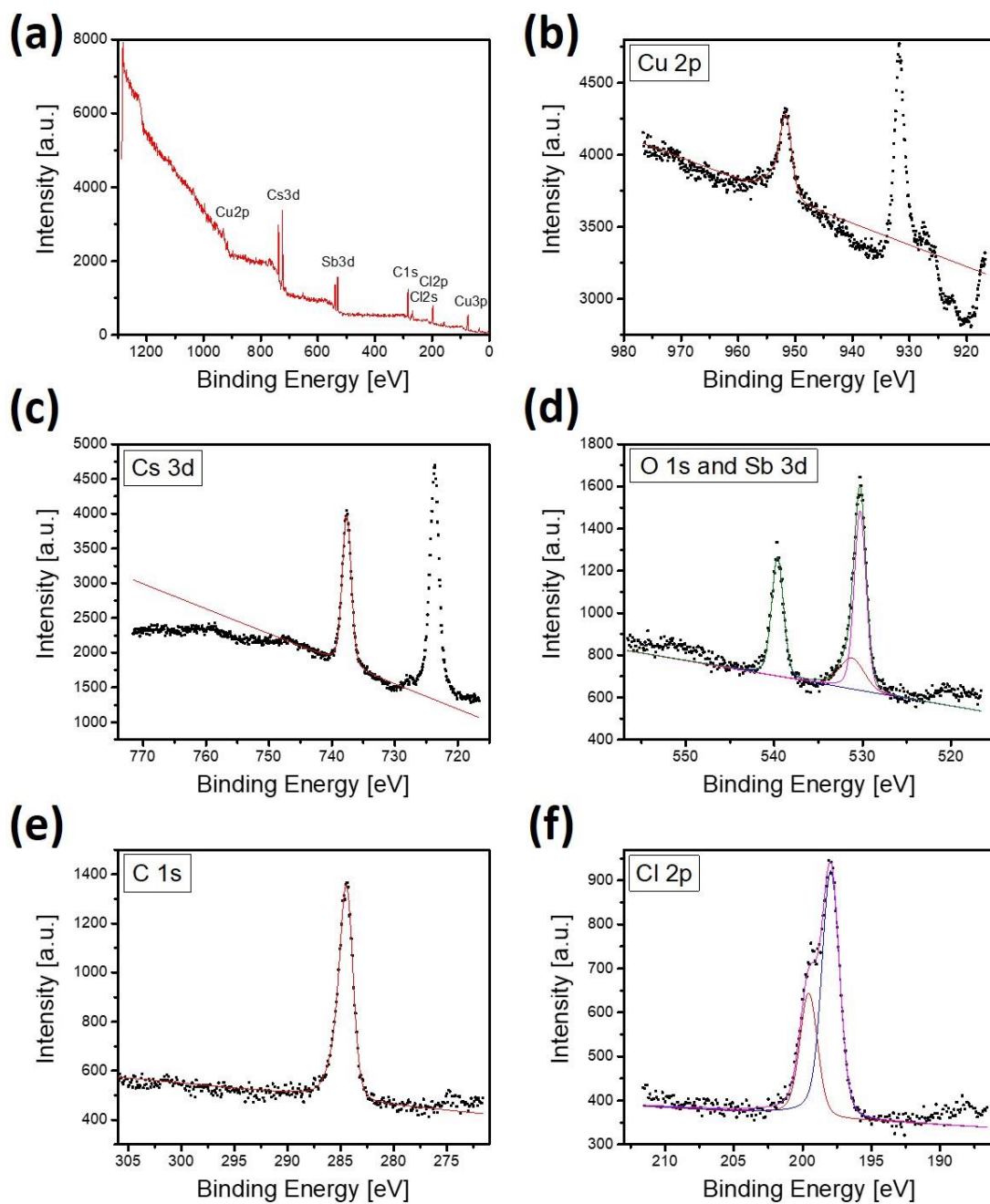


Figure S4.1: XPS survey spectrum of $\text{Cs}_2\text{CuSbCl}_6$ DPNC film (a) and core level spectra of Cu 2p (b), Cs 3d (c), Sb 3d (d), O 1s (d), C 1s (e) and Cl 2p (f). The measurements were performed at LMU.

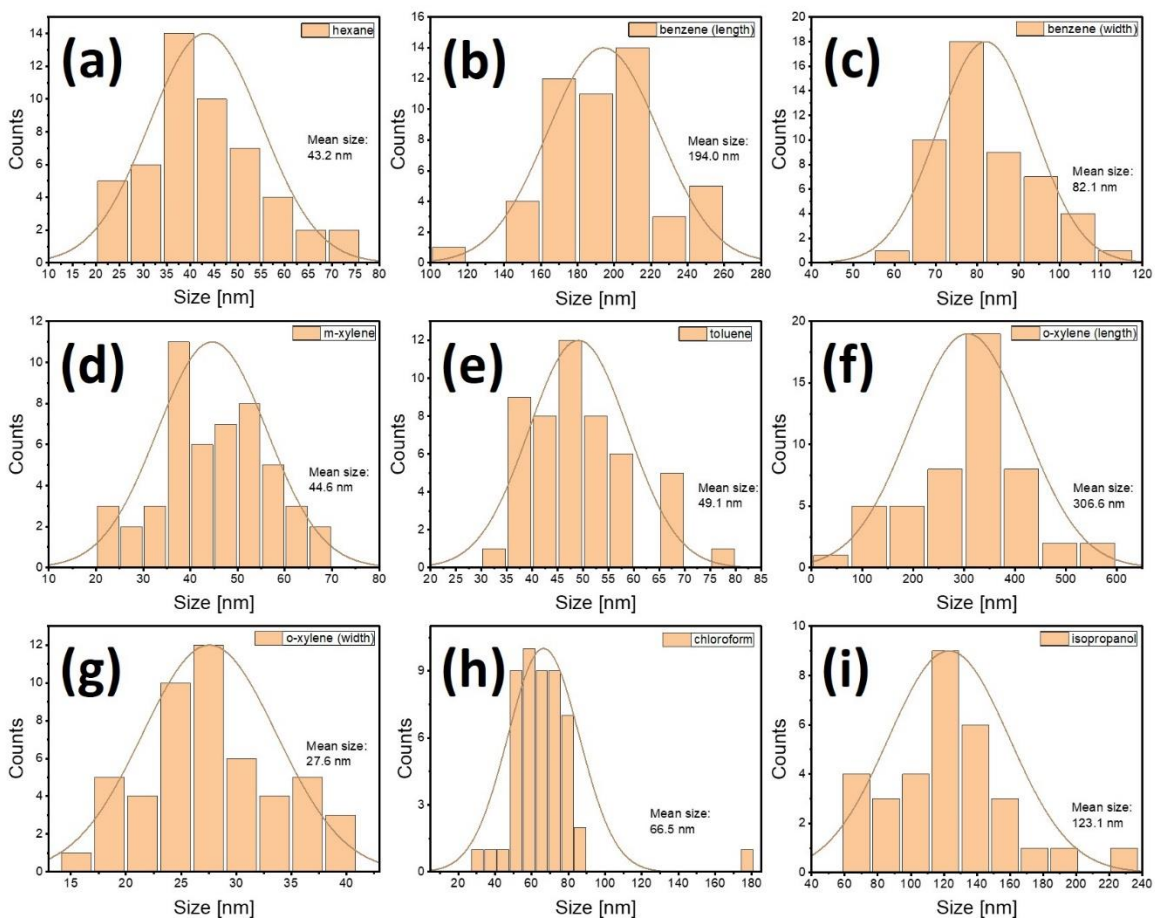


Figure S4.2: Size (length and width) distribution histograms of $Cs_2CuSbCl_6$ DPNCs synthesized in different anti-solvents. The size distribution of $Cs_2CuSbCl_6$ DPNCs was obtained by direct counting in SEM images.

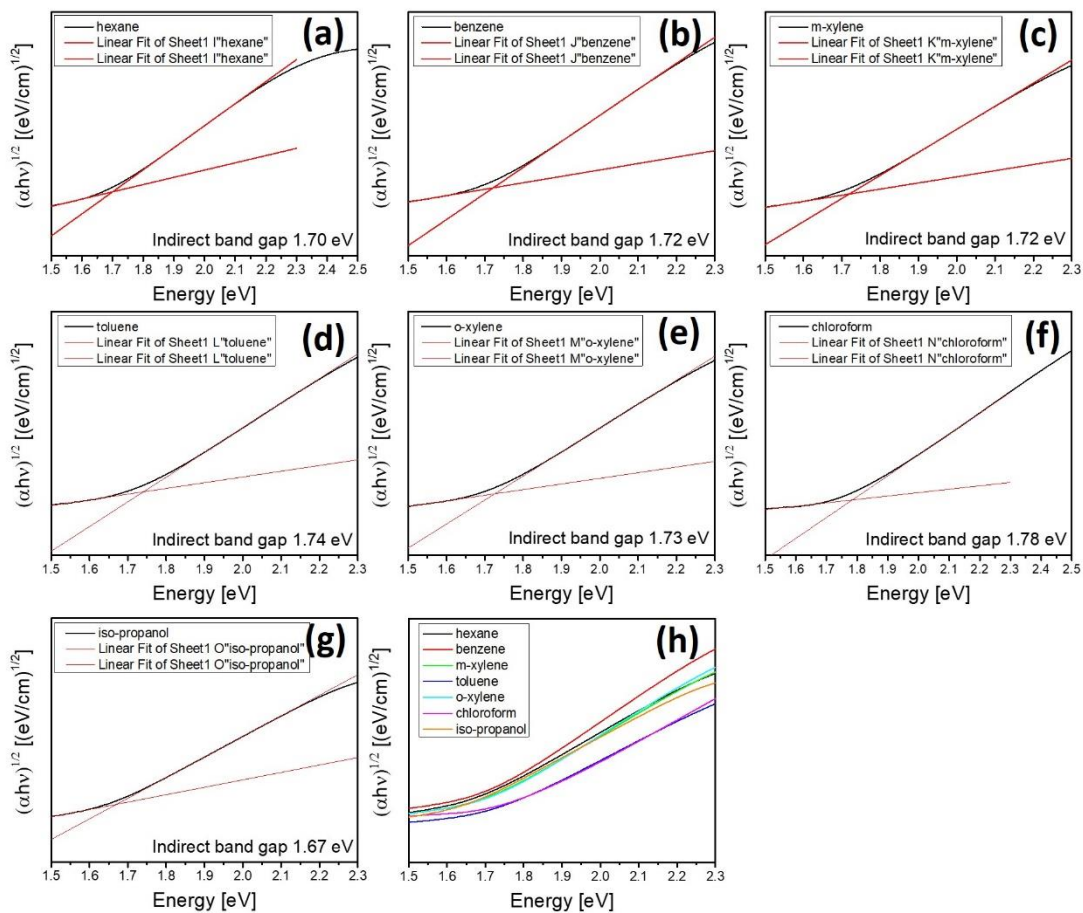


Figure S4.3: (a-g) Tauc plots of $\text{Cs}_2\text{CuSbCl}_6$ DPNCs synthesized in different anti-solvents. (h) Summary of all Tauc plots (a-g).

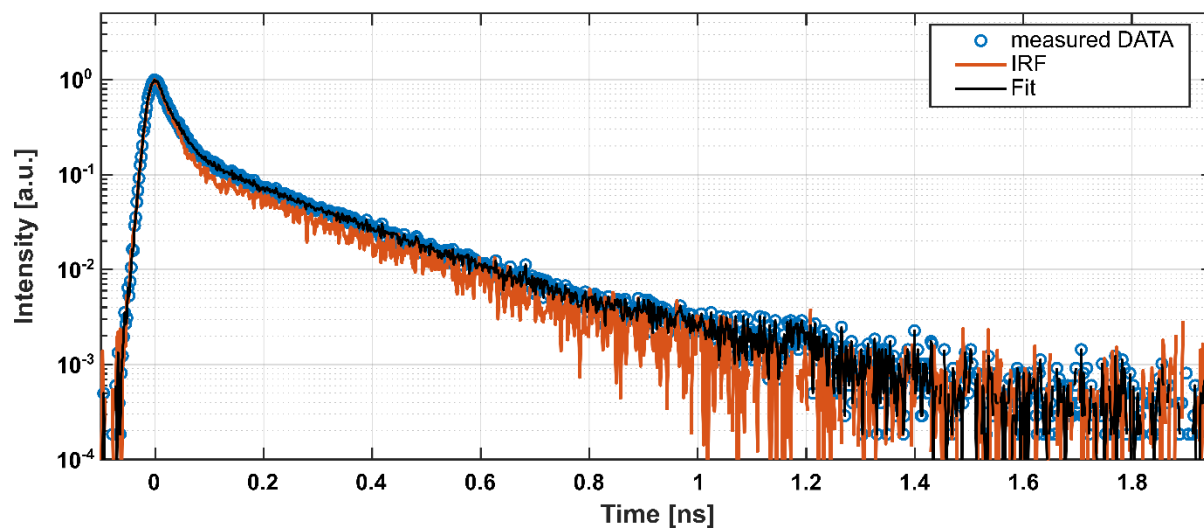


Figure S4.4: PL transient at room temperature (blue circle) of Cs₂CuSbCl₆ DPNCs. The lifetimes $\tau_1 < 10$ ps and $\tau_2 = 97$ ps were obtained from a bi-exponential fit (black curve). The fitted bi-exponential model function was convoluted with the instrument response function (IRF) of the setup (red curve).

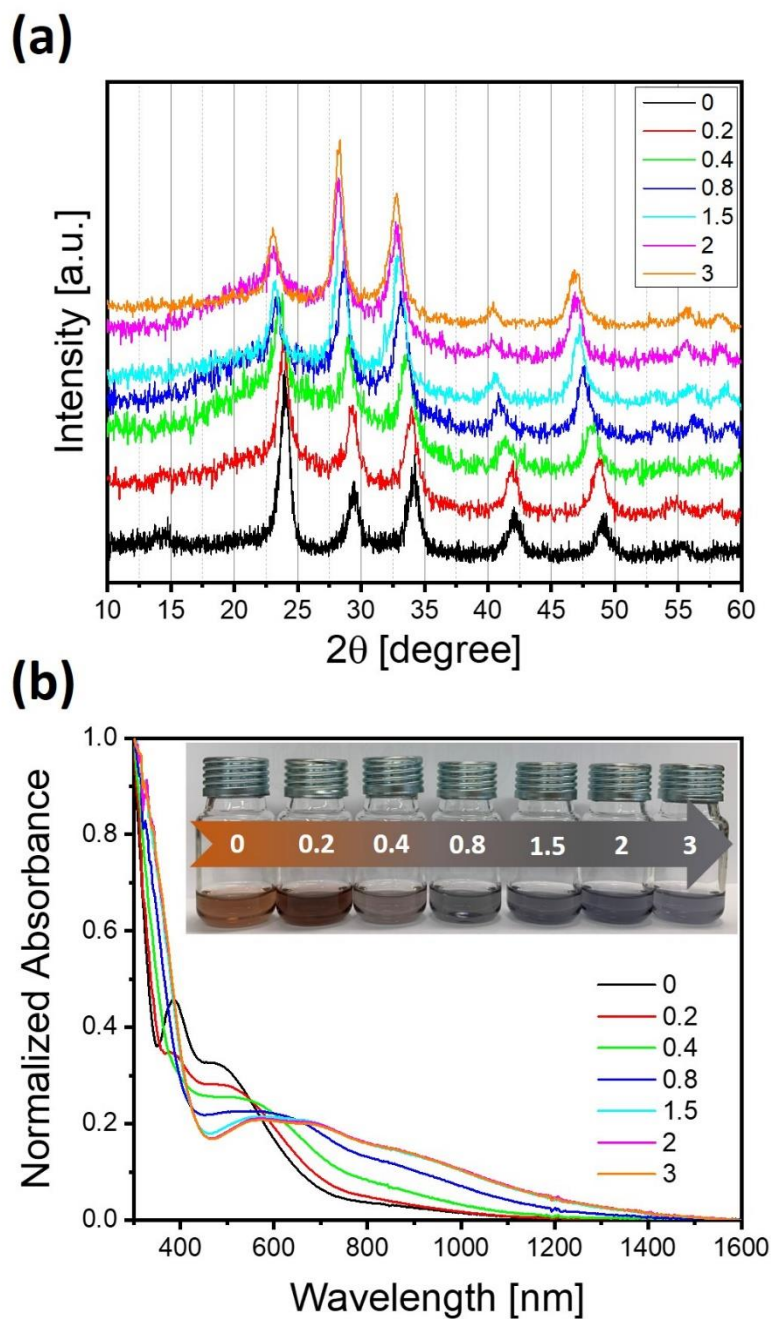


Figure S4.5: XRD patterns (a) and absorption spectra (b) of DPNCs with different levels of anion exchange conversion, which is achieved by the addition of different amounts of TMSBr solutions (from 0 to 3 mL, concentration of 0.1 M) in the starting $Cs_2CuSbCl_6$ DPNC solutions. When more than 2 mL of TMSBr solution was added into $Cs_2CuSbCl_6$ DPNCs, the conversion was completed as the XRD patterns showed the same peak positions. The absorption spectra of the products with the addition of 2 and 3 mL of TMSBr solution show no difference, indicating the end point of the reaction, which is in agreement with the XRD results.

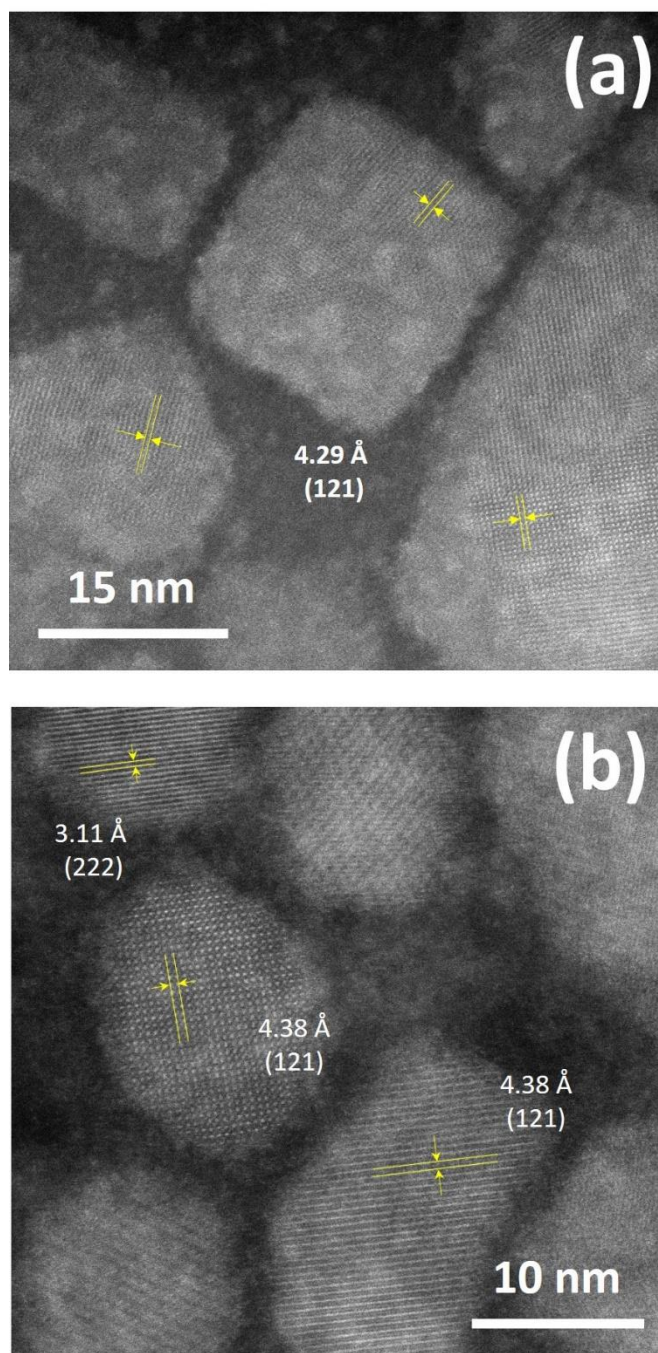


Figure S4.6: HRTEM images of $Cs_2CuSbCl_6$ (a) and $Cs_2CuSbBr_6$ (b) DPNCs. Well-defined lattice fringes with 4.29 Å distance are indexed to (121) lattice planes of $Cs_2CuSbCl_6$. Lattice fringes with 3.11 Å and 4.38 Å are indexed to (222) and (121) lattice planes of $Cs_2CuSbBr_6$ DPNCs, respectively. The distances were determined via Fourier transformation.

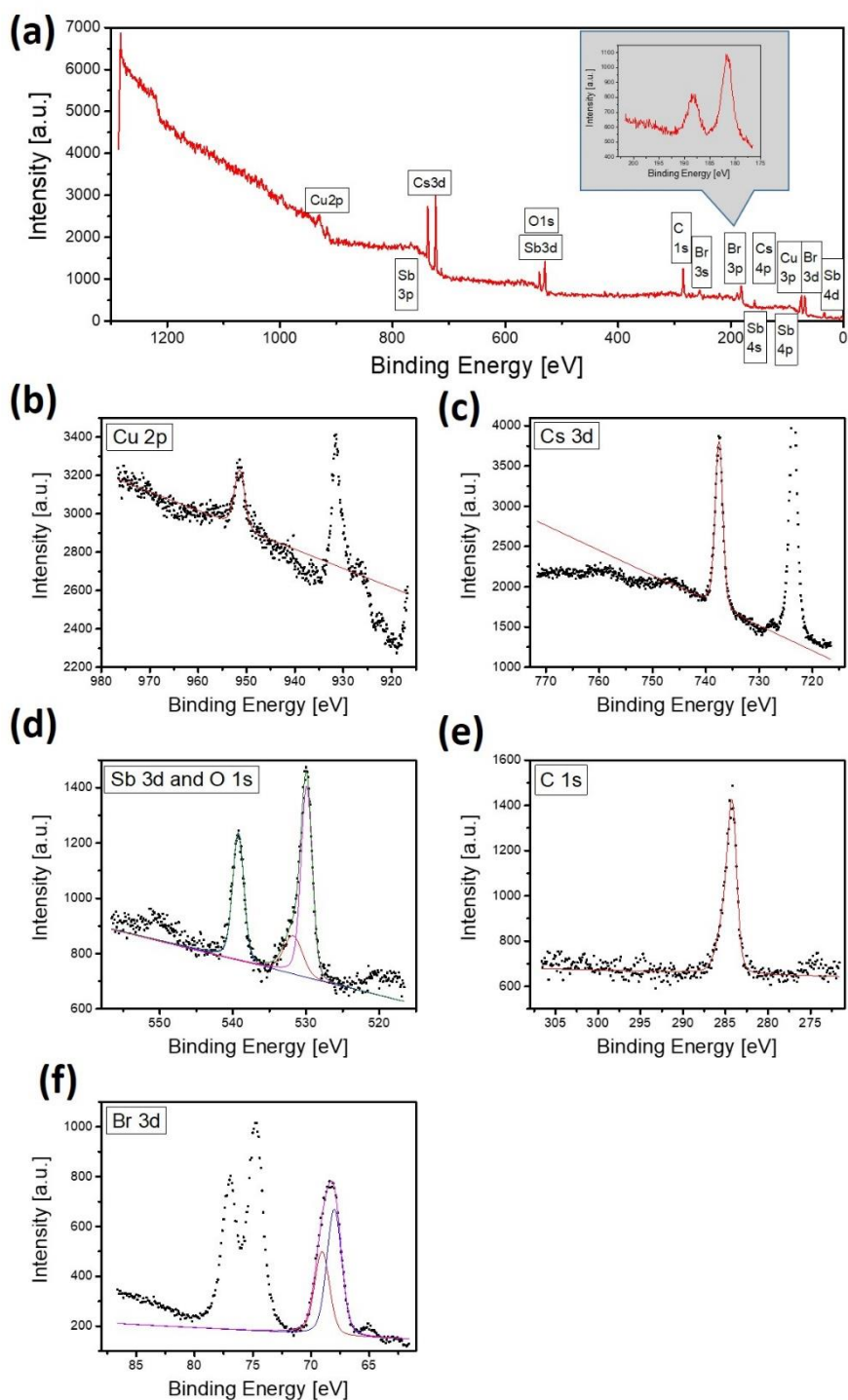


Figure S4.7: (a) XPS survey spectrum of a $\text{Cs}_2\text{CuSbBr}_6$ DPNC film. Inset: Zoom-in area of Cl 2p from the XPS spectrum of $\text{Cs}_2\text{CuSbBr}_6$ DPNC film. XPS core level spectra of Cu 2p (b), Cs 3d (c), Sb 3d (d), O 1s (d), C 1s (e), and Br 3d (e). The measurements were performed at LMU.

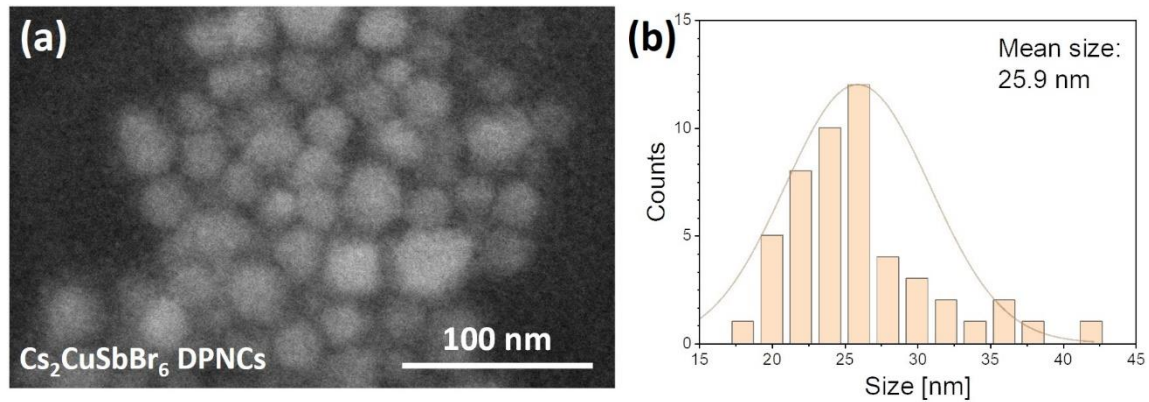


Figure S4.8: (a) SEM image of Cs₂CuSbBr₆ DPNCs. (b) Size distribution histogram of Cs₂CuSbBr₆ DPNCs. The size distribution of Cs₂CuSbBr₆ DPNCs was obtained from SEM measurements.

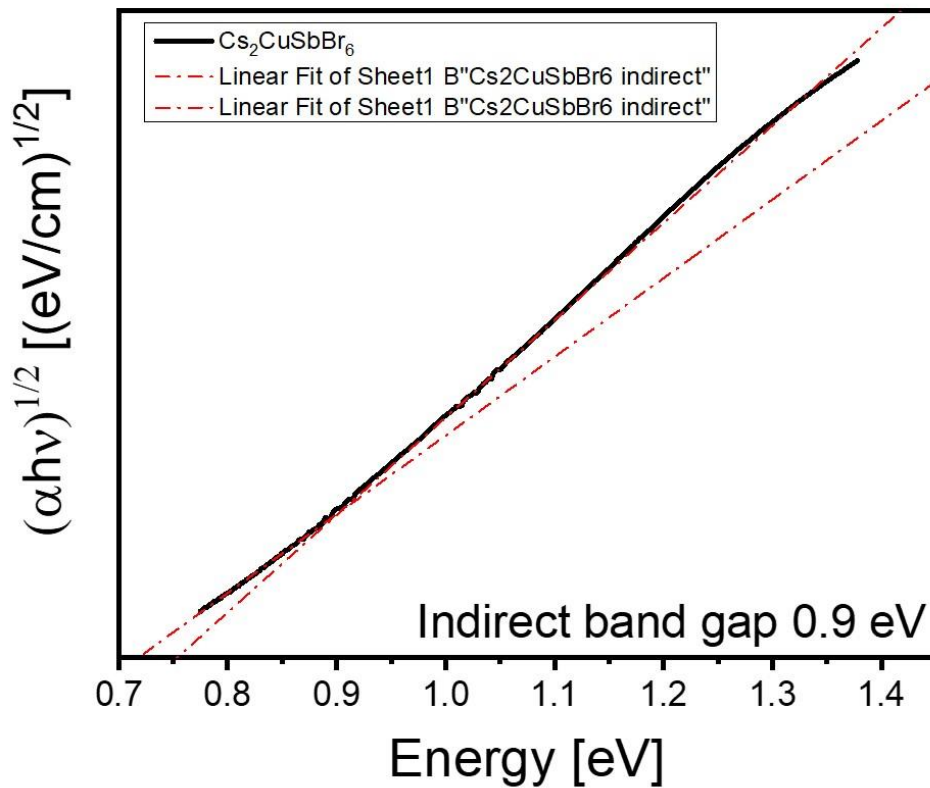


Figure S4.9: Tauc plots of Cs₂CuSbBr₆ DPNCs.

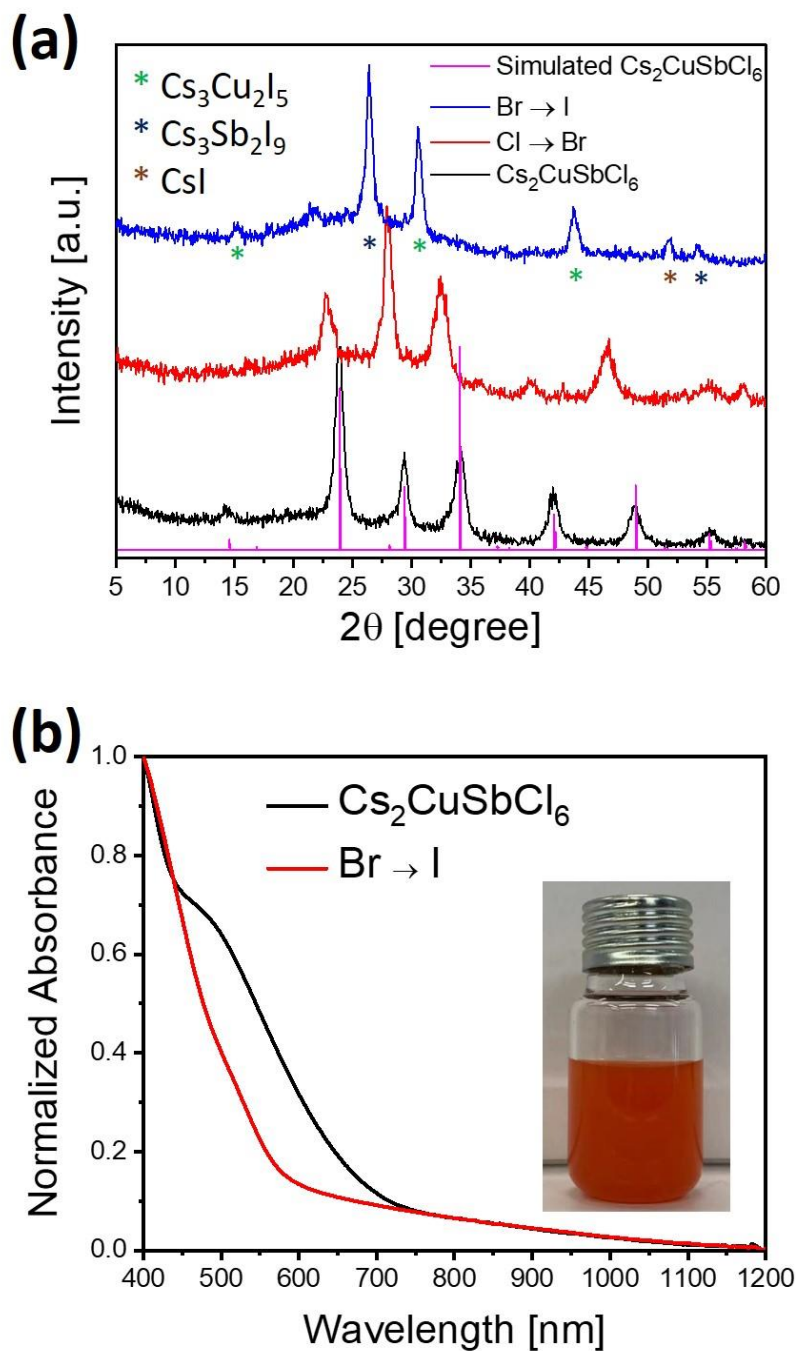


Figure S4.10: (a) XRD patterns of $\text{Cs}_2\text{CuSbCl}_6$, $\text{Cs}_2\text{CuSbBr}_6$ DPNCs and the products obtained after the addition of TMSI solution. The diffraction peaks marked in different color are from the undesired products $\text{Cs}_3\text{Cu}_2\text{I}_5$ (green), $\text{Cs}_3\text{Sb}_2\text{I}_9$ (navy) and CsI (brown). (b) Absorption spectra of $\text{Cs}_2\text{CuSbCl}_6$ DPNCs and the products obtained after the addition of TMSI solution. Inset: photograph of the products obtained after the addition of TMSI solution.

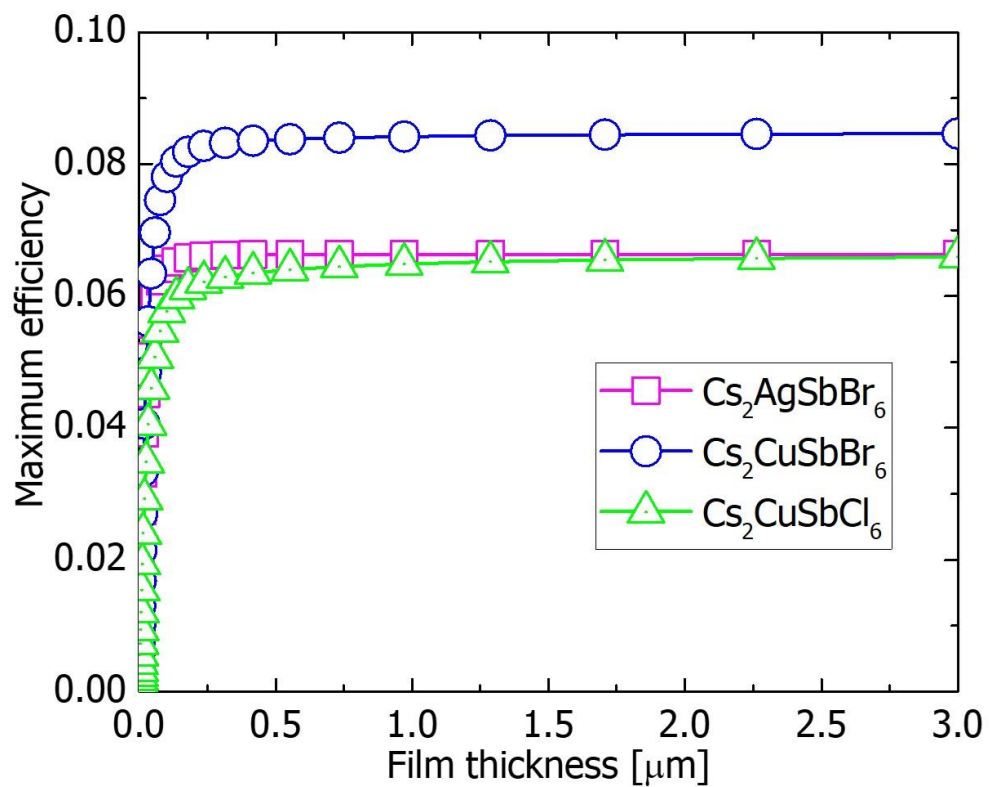


Figure S4.11: Spectroscopic limited maximum efficiency of solar cells with the absorbers Cs_2CuSbX_6 ($X = Cl, Br$) and $Cs_2AgSbBr_6$.

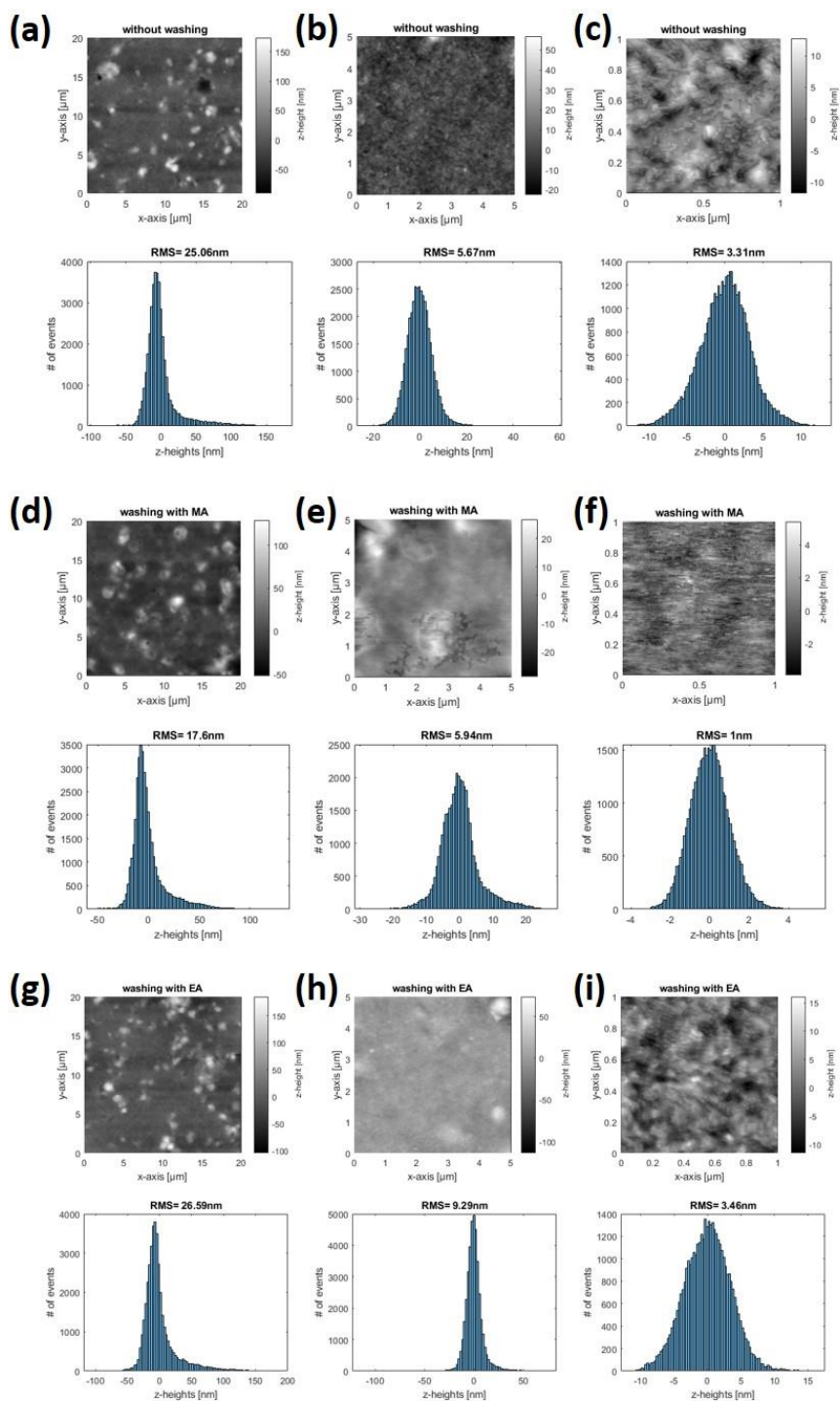


Figure S4.12: AFM images of $\text{Cs}_2\text{CuSbCl}_6$ DPNC films without washing (a, b, c), or washed with methyl acetate (MA) (d, e, f) or ethyl acetate (g, h, i). The scanning areas are $20 \times 20 \mu\text{m}^2$ (a, d, g), $5 \times 5 \mu\text{m}^2$ (b, e, h) and $1 \times 1 \mu\text{m}^2$ (c, f, i). Histograms of the z-height distributions are presented below the AFM images.

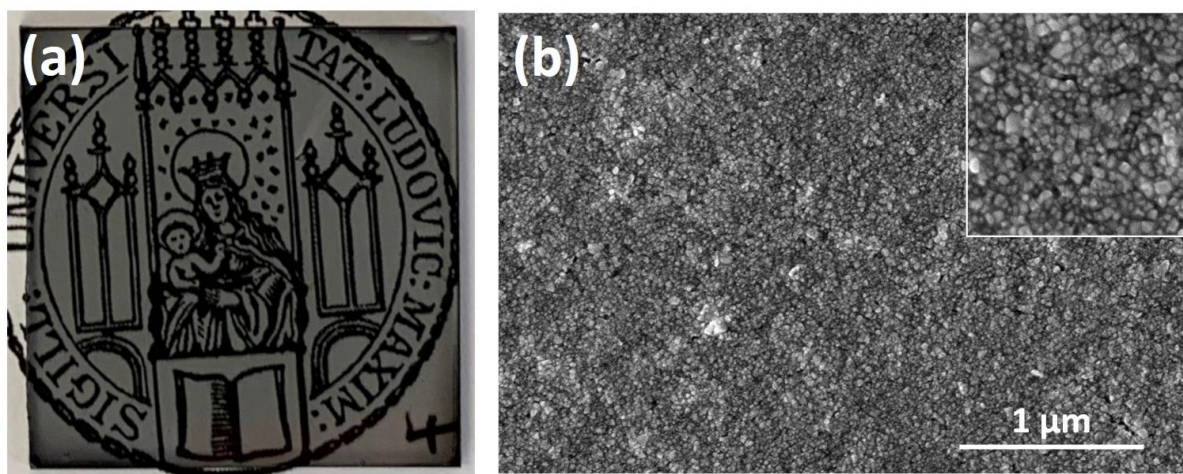


Figure S4.13: (a) Photograph of a $\text{Cs}_2\text{CuSbBr}_6$ DPNC film. (b) SEM image of $\text{Cs}_2\text{CuSbBr}_6$ DPNC film. Inset: 500 nm \times 500 nm.

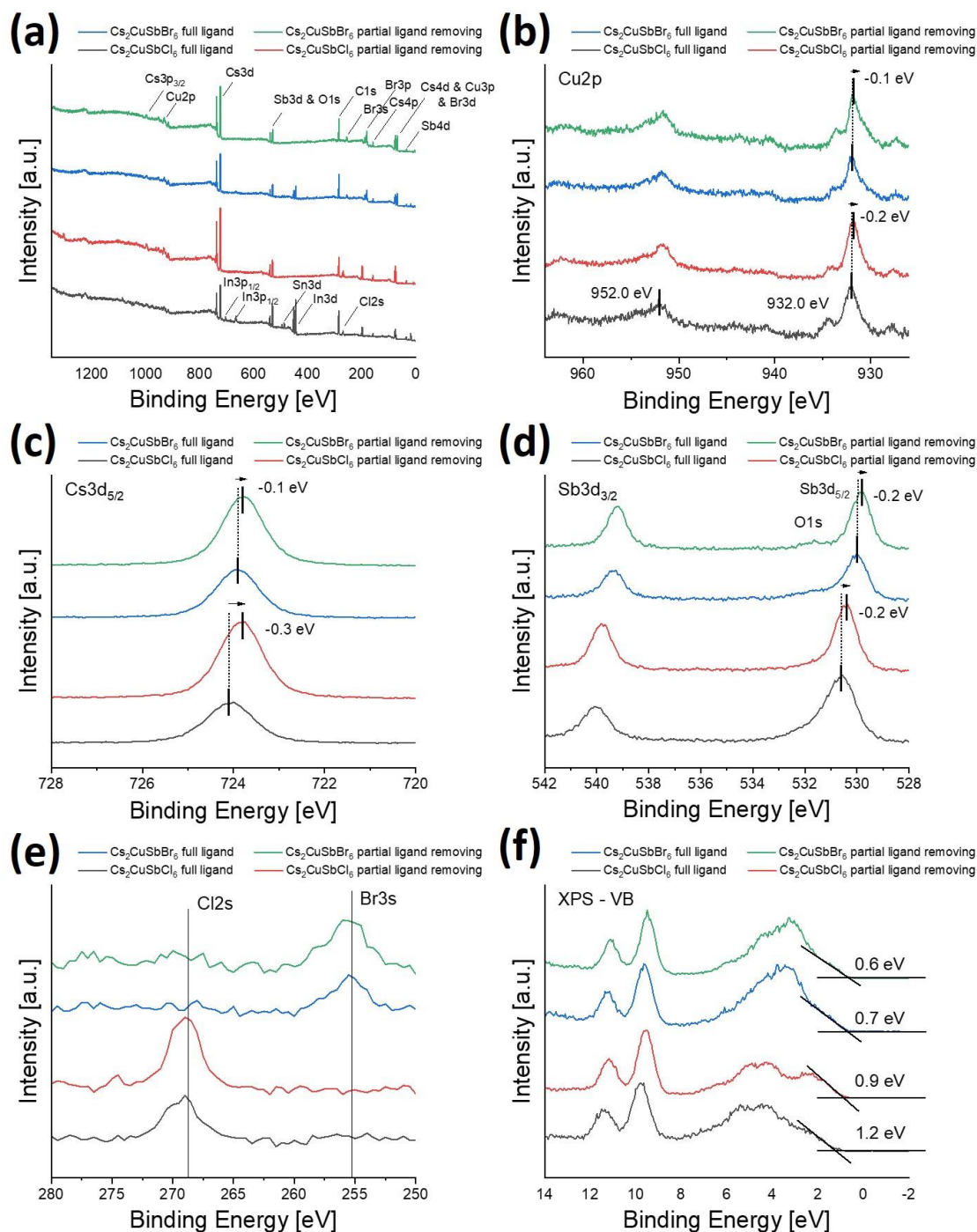


Figure S4.14: XPS survey spectra (a) and core level spectra of $\text{Cu}2p$ (b), $\text{Cs}3d_{5/2}$ (c), $\text{Sb}3d$ (d), $\text{O}1s$ (d), $\text{Cl}2s$ (e), $\text{Br}3s$ (e), and VB edge (f) for $\text{Cs}_2\text{CuSbCl}_6$ and $\text{Cs}_2\text{CuSbBr}_6$ DPNC films with full ligand and partial ligand removing. The measurements were performed at TU Darmstadt.

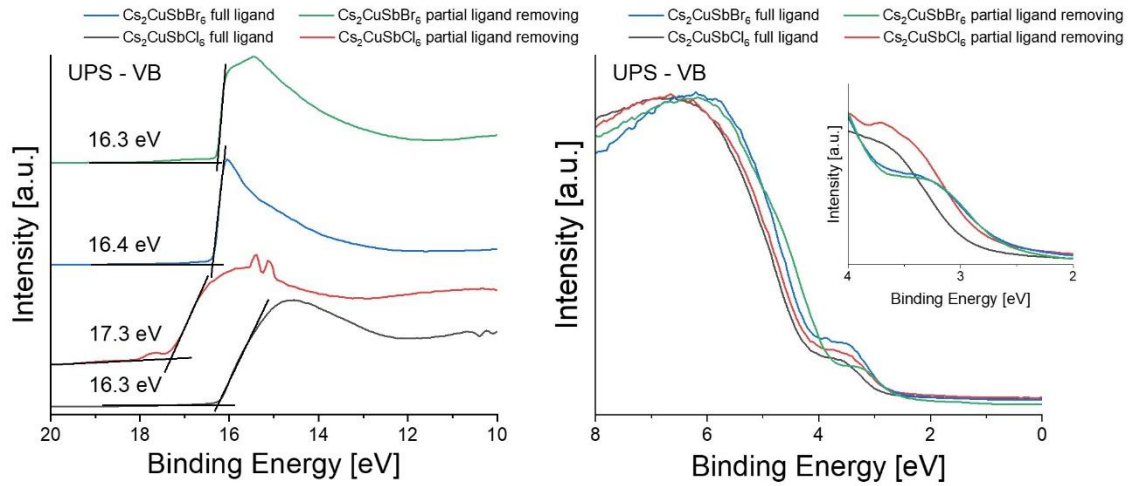


Figure S4.15: UPS spectra of the four samples ($\text{Cs}_2\text{CuSbCl}_6$ and $\text{Cs}_2\text{CuSbBr}_6$ DPNC films with full ligand and partial ligand removing) with (left) the energy cut-off ($E_{\text{cut-off}}$) area obtained by applying a 6V bias, the $E_{\text{cut-off}}$ has been deduced by linear extrapolation. (right) the valence band edge area.

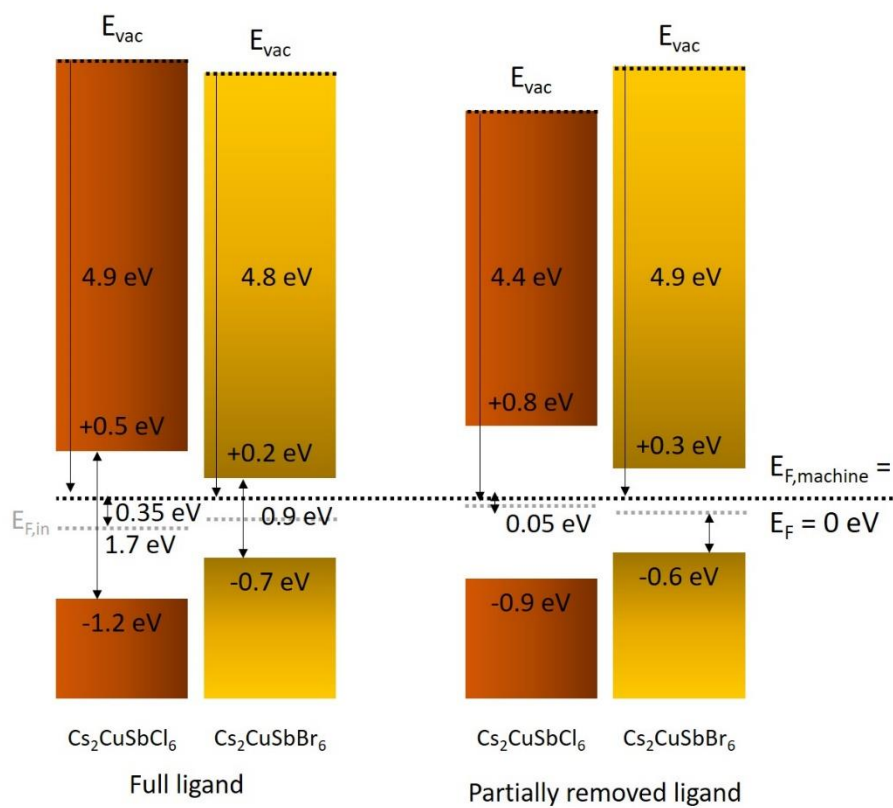


Figure S4.16: Electronic structure diagram of $\text{Cs}_2\text{CuSbCl}_6$ and $\text{Cs}_2\text{CuSbBr}_6$ DPNC films before (left) and after partial ligand removal (right). Everything has been plotted relatively to the Fermi levels of the samples. In grey, $E_{F,\text{in}}$ is a guide to the eye indicating the midgap position, i.e. the Fermi level if the semiconductor was intrinsic.

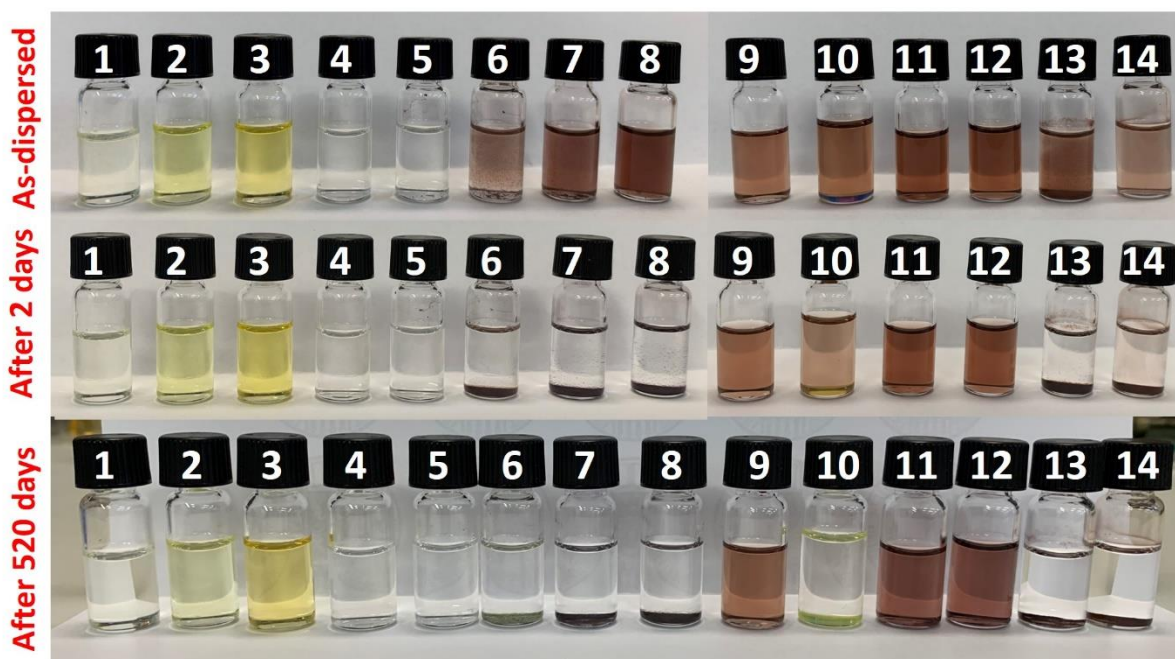


Figure S4.17: Solution stability measurements: photographs of $Cs_2CuSbCl_6$ DPNCs redispersed in different solvents. 1) dimethyl sulfoxide, 2) dimethylformamide, 3) *N*-methyl-2-pyrrolidone, 4) methanol, 5) ethanol, 6) isopropanol, 7) 1-butanol, 8) 1-pentanol, 9) chloroform, 10) toluene, 11) hexane, 12) octane, 13) methyl acetate, 14) ethyl acetate. $Cs_2CuSbCl_6$ DPNCs were dissolved immediately when dispersed in dimethyl sulfoxide, dimethylformamide, *N*-methyl-2-pyrrolidone, methanol and ethanol. In isopropanol, 1-butanol and 1-pentanol, $Cs_2CuSbCl_6$ DPNCs can't be dissolved totally as one can see some dark brown particles agglomerated and precipitated after a few hours. The same phenomenon can also be observed in case of methyl acetate and ethyl acetate. $Cs_2CuSbCl_6$ DPNCs showed excellent stability when dispersed in hexane and octane as there is no precipitation even when stored in ambient conditions after 520 days. In contrast, after stored in ambient conditions after 520 days, $Cs_2CuSbCl_6$ DPNCs dispersed in toluene decomposed.

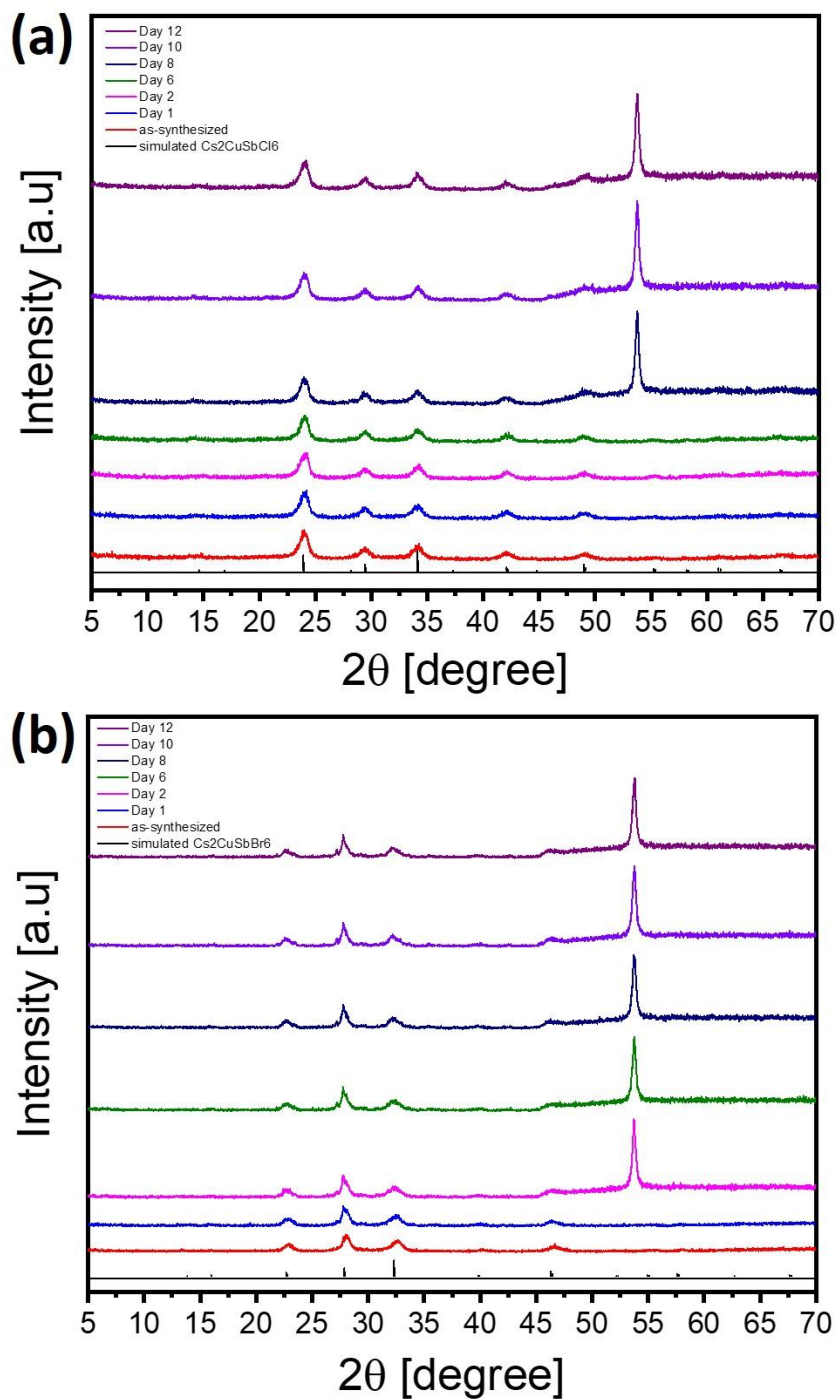


Figure S4.18: Air stability measurements of $\text{Cs}_2\text{CuSbCl}_6$ and $\text{Cs}_2\text{CuSbBr}_6$ DPNCs after post-purification: XRD patterns of as-synthesized $\text{Cs}_2\text{CuSbCl}_6$ (a) and $\text{Cs}_2\text{CuSbBr}_6$ (b) DPNCs, which were stored in air under natural light for 12 days. Exposure times are given in the figure.

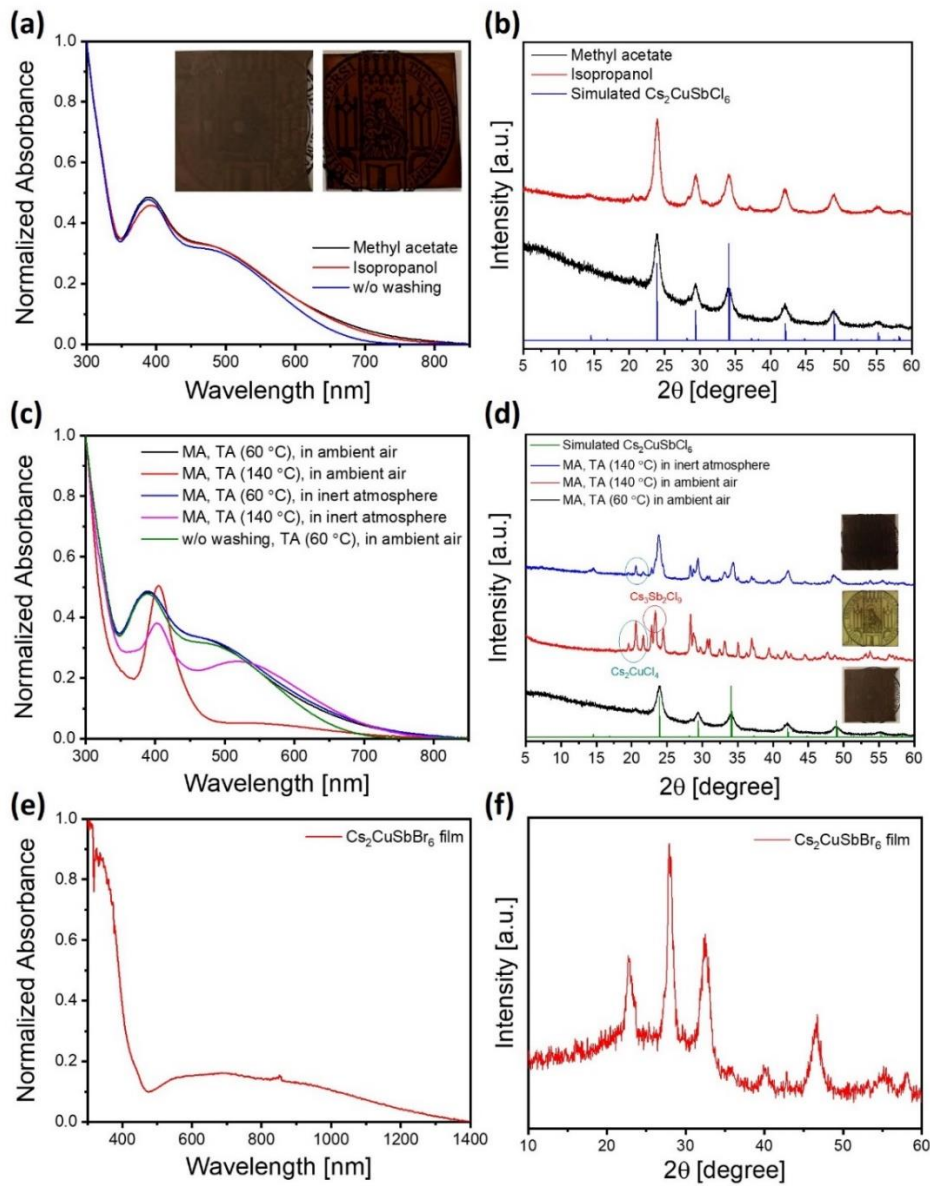


Figure S4.19: (a) Absorption spectra of $\text{Cs}_2\text{CuSbCl}_6$ DPNC films without washing and washed with methyl acetate (MA) and isopropanol. Inset: photographs of $\text{Cs}_2\text{CuSbCl}_6$ DPNC films washed with methyl acetate (left) and isopropanol (right). A Layer-by-layer deposition process was repeated for 8 times for each film. (b) XRD patterns of $\text{Cs}_2\text{CuSbCl}_6$ DPNC films washed with methyl acetate and isopropanol. (c) Absorption spectra of $\text{Cs}_2\text{CuSbCl}_6$ DPNC films without washing and washed with methyl acetate. The films were thermally annealed (TA) at 60 °C or 140 °C for 5 minutes in ambient air or in inert atmosphere. (d) XRD patterns of $\text{Cs}_2\text{CuSbCl}_6$ DPNC films annealed at 60 °C in ambient air, at 140 °C in ambient air and in inert atmosphere. Inset: photographs of the films treated with the corresponding thermal stability tests. The absorption spectrum (e) and XRD pattern (f) of $\text{Cs}_2\text{CuSbBr}_6$ DPNC film.

Table S4.1: The calculated indirect (E^i) and direct (E^d) band gaps of $\text{Cs}_2\text{CuSbX}_6$ ($X = \text{Cl}, \text{Br}$) and $\text{Cs}_2\text{AgSbX}_6$ ($X = \text{Cl}, \text{Br}$).

	$\text{Cs}_2\text{CuSbCl}_6$	$\text{Cs}_2\text{CuSbBr}_6$	$\text{Cs}_2\text{AgSbCl}_6$	$\text{Cs}_2\text{AgSbBr}_6$
E^i	1.68	1.18	2.24	1.59
E^d	2.70	2.41	3.33	2.70

Table S4.2: C, N, O, Cs, Cu, Sb, and X (= Br, Cl) contents of the four samples deduced from XPS measurements, performed in Darmstadt. Spectra were fitted by first subtracting the spectral background using a Shirley-type function, using a weighted least-squares method and model curves (Voigt functions of 70% Gaussian and 30% Lorentzian), and using *casaXPS-scofield.lib* for the relative sensitivity factors (R.S.F).³

Structure	Ligand state	C (%)	N (%)	O (%)	Cs (%)	Cu (%)	Sb (%)	X (%)	Cs/X	Sb/X	Cu/X
$\text{Cs}_2\text{CuSbCl}_6$	Full amount	61	2	12	4	1	3	18	0,25	0,15	0,07
$\text{Cs}_2\text{CuSbCl}_6$	Partial removing	54	3	2	7	2	3	29	0,26	0,10	0,08
$\text{Cs}_2\text{CuSbBr}_6$	Full amount	68	4	5	5	1	2	16	0,31	0,12	0,09
$\text{Cs}_2\text{CuSbBr}_6$	Partial removing	66	3	3	7	2	2	18	0,37	0,13	0,10

^a The expected Cs/X, Sb/X, and Cu/X stoichiometries are, respectively, 0.33, 0.17, and 0.17.

4.11.3 References

1. Yeh, J. J.; Lindau, I., Atomic subshell photoionization cross sections and asymmetry parameters: $1 \leq Z \leq 103$. *At. Data Nucl. Data Tables* **1985**, 32 (1), 1-155.
2. Sirtl, M. T.; Hooijer, R.; Armer, M.; Ebadi, F. G.; Mohammadi, M.; Maheu, C.; Weis, A.; van Gorkom, B. T.; Häringer, S.; Janssen, R. A. J.; Mayer, T.; Dyakonov, V.; Tress, W.; Bein, T., 2D/3D Hybrid Cs₂AgBiBr₆ Double Perovskite Solar Cells: Improved Energy Level Alignment for Higher Contact-Selectivity and Large Open Circuit Voltage. *Adv. Energy Mater.* **2022**, 12 (7), 2103215.
3. Fairley, N.; Fernandez, V.; Richard-Plouet, M.; Guillot-Deudon, C.; Walton, J.; Smith, E.; Flahaut, D.; Greiner, M.; Biesinger, M.; Tougaard, S.; Morgan, D.; Baltrusaitis, J., Systematic and collaborative approach to problem solving using X-ray photoelectron spectroscopy. *Appl. Surf. Sci. Adv.* **2021**, 5, 100112.
4. Liu, L.; Najar, A.; Wang, K.; Du, M. Y.; Liu, S. Z., Perovskite Quantum Dots in Solar Cells. *Adv. Sci.* **2022**, 9 (7), 2104577.
5. Han, R.; Zhao, Q.; Su, J.; Zhou, X.; Ye, X.; Liang, X.; Li, J.; Cai, H.; Ni, J.; Zhang, J., Role of Methyl Acetate in Highly Reproducible Efficient CsPbI₃ Perovskite Quantum Dot Solar Cells. *J. Phys. Chem. C* **2021**, 125 (16), 8469-8478.

5 Overcoming Intrinsic Quantum Confinement and Ultrafast Self-Trapping in Ag-Bi-I and Cu-Bi-I Based 2D Double Perovskites through Electroactive Cations

Rik Hooijer^{†,1}, Shizhe Wang^{†,1}, Alexander Biewald¹, Christian Eckel², Marcello Righetto³, Meizhu Chen¹, Zehua Xu¹, Dominic Blätte¹, Dan Han^{1,4}, Hubert Ebert¹, Laura M. Herz^{3,5}, R. Thomas Weitz², Achim Hartschuh¹, Thomas Bein^{*,1}

¹ Department of Chemistry and Center for NanoScience (CeNS), University of Munich (LMU), Butenandtstraße 5-13, 81377 Munich, Germany

² First Institute of Physics, Faculty of Physics, Georg-August-University, 37073 Göttingen, Germany

³ Department of Physics, University of Oxford, Clarendon Laboratory, Parks Road, Oxford, OX1 3PU, United Kingdom

⁴ School of Materials Science and Engineering, Jilin University, Changchun, 130012, China

⁵ Institute for Advanced Study, Technical University of Munich, Lichtenbergstrasse 2a, D-85748 Garching, Germany

R.H. and S.W. contributed equally to this work. The work was conceived by R.H. and S.W.. S.W. synthesized the organic cations. R.H. and S.W. contributed to the synthesis of single crystals, thin-film fabrication and characterization, as well as optoelectronic device fabrication and characterization. R.H. contributed to thin-film crystal structure analysis by grazing-incidence wide angle X-ray scattering (GIWAXS) measurement. The coordination work for photoluminescence measurement, out-of-plane conductivity measurement and optical-pump terahertz-probe spectroscopy measurement were conducted by R.H. The coordination work for the theoretical study was conducted by S.W.. R.H. wrote the initial draft of the manuscript and R.H. and S.W. edited until the final version.

Keywords: 2D double perovskite, solar cell, aromatic spacer cation, quantum confinement, silver, copper, bismuth, iodide, out-of-plane conductivity

5.1 Abstract

The possibility to combine organic semiconducting materials with inorganic halide perovskites opens exciting pathways towards tuning optoelectronic properties. Exploring stable and non-toxic, double perovskites as a host for electroactive organic cations to form two-dimensional hybrid materials is an emerging opportunity to create both functional and lead-free materials for optoelectronic applications. By introducing naphthalene and pyrene moieties into Ag-Bi-I and Cu-Bi-I double perovskite lattices, intrinsic electronic challenges of double perovskites are addressed and the electronic anisotropy of two-dimensional perovskites can be modulated. $(\text{POE})_4\text{AgBiI}_8$ containing pyrene moieties in the 2D layers was selected from a total of eight new 2D double perovskites, exhibiting a favorable electronic band structure with a type IIb multiple quantum well system based on a layer architecture suitable for out-of-plane conductivity, and leading to a photocurrent response ratio of almost three orders of magnitude under AM1.5G illumination. Finally, an exclusively parallel oriented thin film of $(\text{POE})_4\text{AgBiI}_8$ was integrated into a device to construct the first pure $n = 1$ Ruddlesden-Popper 2D double perovskite solar cell.

5.2 Introduction

Two-dimensional (2D) organic-inorganic metal halide perovskites are emerging as a promising class of semiconductors, not only owing to their superior intrinsic and extrinsic stability but also to their vast compositional and structural space.^[1] Especially the organic component offers unique opportunities to tune the physical properties and to control key features relevant for applications.^[2] In the quest for more stable and less toxic alternatives to Pb-based perovskites, double perovskites (DP) based on Ag, Cu, Bi and Sb are at the focus of recent research efforts.^[3,4] The flag-bearing DP $\text{Cs}_2\text{AgBiBr}_6$ has emerged as a stable alternative to Pb-based perovskites for applications in solar cells, photocatalysts or X-ray detectors.^[5-8] The introduction of the corresponding 2D counterparts – referred to as 2D DPs – has further broadened their compositional space owing to their superior thermodynamic stability, thus giving access to iodide DPs and smaller band gaps. This, combined with the tunability of the organic intragallery phase makes them prototypical to study underlying physical properties such as electronic structure, charge-carrier dynamics, electrical conductivity and photoresponse.^[9-12]

Generally, 2D Ruddlesden-Popper (RP) DPs have the chemical formula $A'_4A_{2n-2}B(\text{I})_nB(\text{III})_nX_{6n+2}$, where A' is a large monovalent organic cation, A is a small monovalent organic or inorganic cation, $B(\text{I})$ is a

monovalent metal ion, B(III) is a trivalent metal ion, X is a halide anion and n is the number of corner-sharing metal halide $[B(I)X_6]^{5-}$ and $[B(III)X_6]^{3-}$ octahedral layers (Figure 5.1a). Due to the spatial separation of the inorganic and organic layers in the crystal structure, the resulting electronic band structure can be described as a multiple quantum well (QW) system.^[13] The band alignment in QW systems is determined by the frontier orbital contributions of the large organic cation - i.e. its highest occupied molecular orbital (HOMO) and lowest unoccupied molecular orbital (LUMO) - and the inorganic layer band edges, namely its valence band maximum (VBM) and conduction band minimum (CBM). As shown in Figure 5.1b, the energetic alignment between the organic and inorganic bands yields an organic-inorganic heterojunction and four cases are possible, classified as Ia, Ib, IIa and IIb. In 2D perovskites, the most commonly formed heterojunction is the type Ib, where charge carriers or excitons are confined into the inorganic layer, thus yielding large exciton binding energies and charge transport anisotropy.^[14] Since several optoelectronic device applications require directional charge transport (e.g. between contacts in solar cells) this anisotropy must be considered and adapted accordingly. However, attempts to control the crystallization direction of 2D perovskite thin films and understanding the relevant mechanisms to date have shown only limited success.^[15,16] An alternative promising strategy is to overcome the quantum confinement intrinsically, by modulating the frontier band energy levels through the use of electroactive, functional cations.^[17-19] While this strategy has been recently employed for lead-based 2D perovskites, it remains mostly uncharted for 2D DPs.^[20-24]

In this work, we present the synthesis of eight new $n = 1$ RP DPs based on naphthalene/pyrene containing cations in Ag-Bi-I and Cu-Bi-I inorganic frameworks. We investigate their structural and optoelectronic properties, with special regard to the electrical conductivity and the charge-carrier dynamics to finally construct the first solar cell based on this materials class.

5.3 Results and Discussion

5.3.1 Structural Characterization

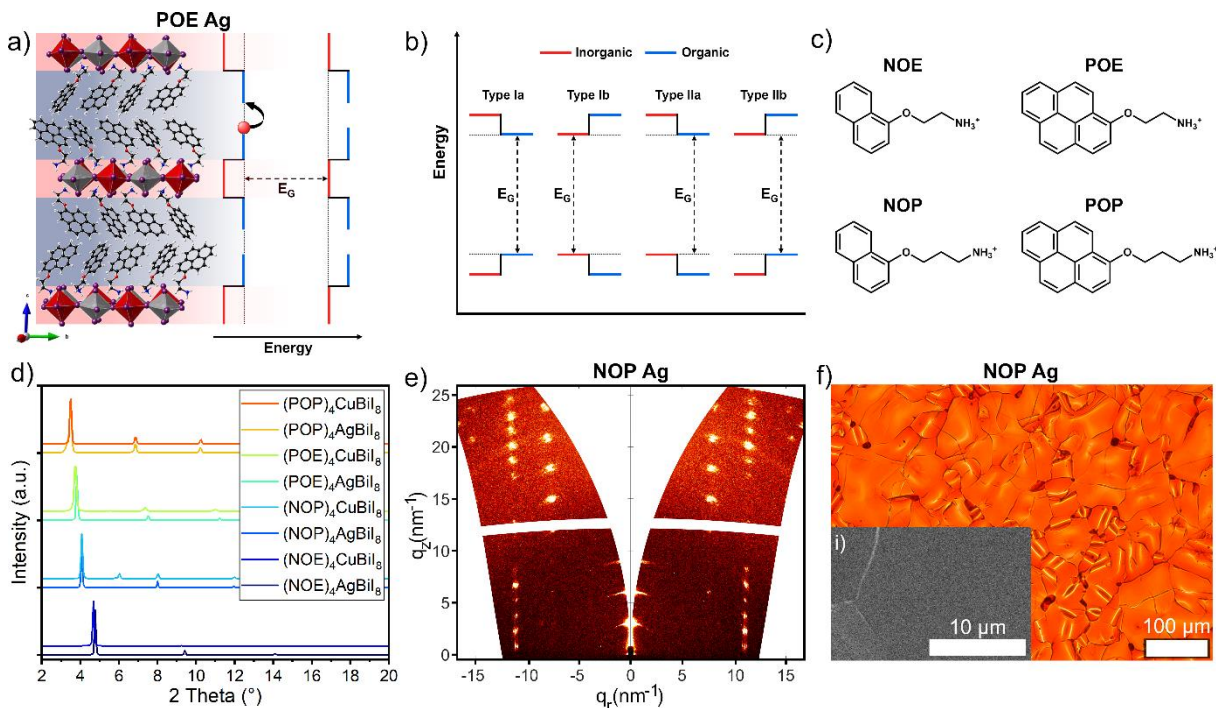


Figure 5.1: a) Exemplary crystal structure of the $n = 1$ RP DP phase POE-Ag with illustration of the electronic quantum well structure in context of the layered structure. A type IIb QW is shown, as determined by means of DFT calculations. In POE-Ag, the schematic hole (red sphere) is able to traverse the gap in the organic bilayer, as confirmed through conductivity data. b) Different possible types of electronic QWs in 2D perovskites. c) Structural formulas of the organic cations used in this work. d) Thin film diffractograms of all eight materials displaying the characteristic, low 2θ reflections for parallel crystal orientation. Y-axis offset was added for visibility. e) GIWAXS data of a NOP-Ag thin film on ITO measured with a sample-detector distance (SDD) of 121 mm and incident angle $\alpha_i = 0.3^\circ$. f) Optical micrograph and scanning electron micrograph (inset i) of NOP-Ag thin film on ITO.

The $n = 1$ RP structures are based on the inorganic framework containing either $[\text{AgI}_6]^{5-} + [\text{BiI}_6]^{3-}$ or $[\text{CuI}_6]^{5-} + [\text{BiI}_6]^{3-}$ octahedra, with organic cations based on the polycyclic aromatic systems naphthalene or pyrene (Figure 5.1a), fused by an ether linkage to an ethyl- or propylammonium chain: naphthalene-O-ethylammonium (NOE), naphthalene-O-propylammonium (NOP), pyrene-O-ethylammonium (POE), pyrene-O-propylammonium (POP) (Figure 5.1c), yielding $(\text{NOE})_4\text{AgBiI}_8$

(NOE-Ag), (NOP)₄AgBiI₈ (NOP-Ag), (POE)₄AgBiI₈ (POE-Ag), (POP)₄AgBiI₈ (POP-Ag), (NOE)₄CuBiI₈ (NOE-Cu), (NOP)₄CuBiI₈ (NOP-Cu), (POE)₄CuBiI₈ (POE-Cu) and (POP)₄CuBiI₈ (POP-Cu).

The structures and high crystallinity of the thin films are confirmed by XRD (Figure 5.1d). The visible reflections in the low 2θ region correspond to the crystallographic planes orthogonal to their unit cells long axis, which in context of the layered structure is the out-of-plane direction. The length of this directly correlates with the size of the organic cations, as the organic layers consist of a double-layer of adjacent organic cations. The reflections shift downwards to smaller angles 2θ for increasing size of the cations along NOE < NOP < POE < POP (SI Table S5.2).

Additionally, single crystals of NOP-Ag, POE-Ag and POP-Ag were obtained through a vapor diffusion method, enabling us to obtain their structure solutions (SI Tables S5.9-5.10), with the exemplary 2D RP crystal structure of POE-Ag shown in Figure 5.1a. Due to the insufficient quality of the POE-Ag single crystals, we optimized the structure through DFT calculations for further discussion and for the band structure calculations (Section 5.3.2). Although suitable single crystals for the other materials could not be grown for reasons discussed in more detail in Figure S5.4-Figure S5.5, their 2D RP structure in thin film form was confirmed through GIWAXS, as well as room temperature Raman measurements (Figure S5.7). Furthermore, the crystalline orientation indicated earlier by the thin film XRD measurements was also confirmed through GIWAXS. The strong preferential orientation with the organic and inorganic layers parallel to the substrate surface is indicated in the GIWAXS data by the reflections of the set of planes along (00ℓ) being located in the middle at $q_r = 0 \text{ nm}^{-1}$, along the azimuthal angle $\chi = 0^\circ$ (Figure 5.1e). The other observable reflections originate from the set of planes of (10ℓ) and (01ℓ) , at $q_r \approx 8 \text{ nm}^{-1}$ and from (11ℓ) at $q_r \approx 11 \text{ nm}^{-1}$.

All materials show very similar patterns, confirming the 2D RP structure, as they could either be indexed directly to their single crystal structural models (NOP-Ag, POE-Ag and POP-Ag) or to refined lattice parameters, originating from the other single crystal structures (full set of GIWAXS data and index parameters shown in Figure S5.2-Figure S5.3). The most notable difference in these patterns is seen in the pattern of NOE-Cu, where indexing revealed larger changes of the lattice parameters, most notably the different lengths of the a and b axes ($a = 12.1 \text{ \AA}$ and $b = 8.6 \text{ \AA}$) and the strong deviation from 90° of the α and β angles compared to the other seven materials.

We further evaluated the morphology of thin film samples with visible light microscopy and scanning electron microscopy. The thin films, spincoated from DMF or DMSO solutions, form homogeneously at both the macroscopic and microscopic scale, showing complete coverage with large crystallites and

domain sizes (Figure 5.1f shows NOP-Ag, with the remaining materials shown in Figure S5.6). The crystal structure of low n value 2D perovskites typically leads to the formation of large, oriented crystalline domains with lateral sizes ranging in the tens of microns. This phenomenon can be observed in many other thin films or the plate-like crystal habit of single crystals of these materials.^[11]

Overall, the 2D RP structure is confirmed for all materials, as well as their exclusively parallel orientation when grown as thin films on substrates. This offers an attractive platform to investigate and understand the limitations of electronic anisotropy in the $n = 1$ 2D RP DPs and to evaluate the influence of the organic cations.

5.3.2 Electronic Structure and Band Alignment

The optimized crystal structure parameters of NOP-Ag, POE-Ag and POP-Ag, based on the single crystal structure solutions agree well as shown in Table S5.3-5.4. The PBE+SOC calculated band gaps of NOP-Ag, POE-Ag and POP-Ag are smaller compared to the experimentally measured band gaps. Nevertheless, PBE+SOC gives a reasonable qualitative description of band dispersion and band edge components.^[25] For all the materials, the VBM and CBM are located at the Γ point, as shown in Figure 5.2a for POE-Ag and in Figure S5.8a and Figure S5.9a for NOP-Ag and POP-Ag, leading to their direct band gaps.^[10]

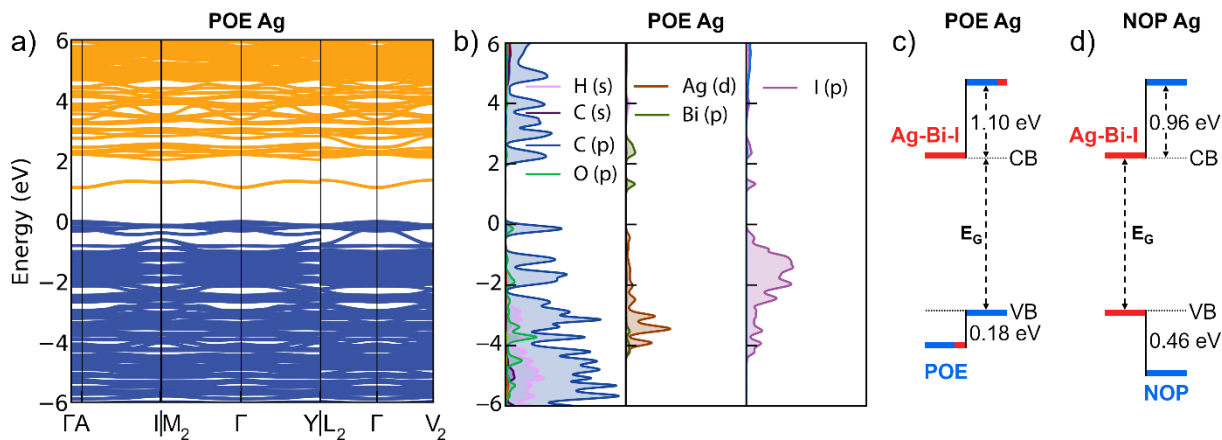


Figure 5.2: a) PBE+SOC calculated band structure with b) the partial density of states and c) the band alignment for POE-Ag. d) Band alignment for NOP-Ag (Band structure in Fig. S5.8).

Moreover, the projected densities of states (DOS) are used to understand the atomic character of the frontier orbitals and the role of the different organic cations (NOP, POE and POP) on the transport

properties. For NOP-Ag, as shown in Figure S5.8b, the VBM is composed of Ag-d orbitals and I-p orbitals, and the CBM is dominated by Bi-p and I-p orbitals, analogous to its 3D prototype $\text{Cs}_2\text{AgBiX}_6$ ($X = \text{Cl}/\text{Br}$).^[26,27] Due to the dominant contribution of inorganic parts to the band edges, the VB and CB of NOP-Ag are dispersive. For POE-Ag and POP-Ag, the compositions of the VBM change. As shown in Figure 5.2b and Figure S5.9b, they are predominantly made up of the organic cations C-p and O-p orbitals instead of the inorganic orbitals, and therefore the band dispersions of the VB become smaller with respect to NOP-Ag. The components of the CBM for POE-Ag and POP-Ag are the same as that of NOP-Ag, namely the Bi-p and I-p orbitals. Besides the electronic structure, Figure 5.2c-d and S5.9c display the band alignment of POE-Ag, NOP-Ag and POP-Ag, respectively. NOP-Ag forms a type Ib heterojunction between the inorganic and organic parts, whilst POP-Ag forms a type IIb heterojunction. Notably, POE-Ag shows a unique band alignment. As shown in Figure 5.2c, in POE-Ag, there are overlapping states which are composed dominantly of the POE organic cations and a small portion of the inorganic component. The overlapping state around the VB is almost isoenergetic to the HOMO (VBM), and the state above the CBM shows a separation of around 1 eV with the CBM. Their partial charge density is displayed in Figure S5.10. Such mixed states would support the transport of charge carriers in POE-Ag, providing joint transport channels.

In addition to the overlapping states, there are different molecular stacking types within the organic layers for NOP-Ag, POE-Ag and POP-Ag (See Figure S5.11-Figure S5.13). In crystalline pyrene the stacking distance between the parallel oriented pyrene molecules is around 3.54 Å, which is within the range of typical distance range of the π - π interaction, namely, 3.40 – 3.70 Å.^{[28][29]} This benefits the charge separation and transfer among molecules.^[30] In POE-Ag, the pyrene moieties in the POE molecules are arranged in a similar manner, indicating a π - π interaction (Figure S5.11). In contrast, POP molecules in POP-Ag do not show this type of arrangement. Furthermore, POE molecules display an edge-face arrangement of the organic intralayer, i.e. along the out-of-plane direction, contrary to the edge-edge arrangement observed in POP-Ag and NOP-Ag (Figure S5.12). As demonstrated by Passarelli et al., edge-to-face interactions across the van der Waals gap yield better orbital overlap and enhanced out-of-plane conductivity as compared to edge-to-edge interactions.^[22] These two factors combined, i.e. the electronic characters of the quantum wells and the structural arrangement of the organic cations enable better charge transport and photoresponse in POE-Ag compared to all other materials, as shown later in section 5.3.4.

5.3.3 Optical Properties

5.3.3.1 Absorption

All materials based on the Ag-Bi inorganic framework show similar absorbance spectra with absorption edges and corresponding band gap energies between 2.15 - 2.19 eV, shown in Figure 5.3a, followed by two peaks, that are characteristic for 2D iodide double perovskites. [11,24] One would tentatively assign these peaks to excitonic contributions, akin to their 2D lead perovskite counterparts, given that the systems here are also quantum confined systems, where Wannier-type excitonic species could be confined to the inorganic octahedral network. Contrarily, theoretical absorption spectra that exclude excitonic effects also result in the characteristic shape with one lower and one higher energy maximum.[11,24] Additionally, the emission for 2D DPs is not as typically narrow at cryogenic temperatures as one would expect for a purely excitonic origin, although as we showed for $(4\text{FPEA})_4\text{AgBiI}_8$, a moderate narrowing can still be observed.[11] The complete picture for DPs and 2D DPs is not as clear as for other well-known semiconductors, since many effects and charge carrier species exist simultaneously. Firstly, since the heavy p-electron Bi atom introduces strong spin-orbit coupling, leading to a largely separated band in the CBM (Figure 5.2a, S5.8a and S5.9a), the first absorbance maximum should be related to the associated transitions, as was also shown for $\text{Cs}_2\text{AgBiBr}_6$. [31] Secondly, one can still expect the formation of indirect or self-trapped excitonic species from these states, as well as electron-phonon coupling which is known to be very strong in 3D DPs and even stronger in 2D DPs.[32-36] The observed double peak in 2D DPs could thus be a combination of the above effects but is not trivial to model without further spectroscopic and theoretical insights.

The materials NOP-Cu, POE-Cu and POP-Cu, based on the Cu-Bi inorganic framework show slightly smaller band gap energies, between 2.01 - 2.07 eV and do not exhibit the two peaks as clearly as seen in the Ag-Bi materials. The smaller band gaps of NOP-Cu, POE-Cu and POP-Cu should be related to the different electronic contributions to the band structure, since the inorganic VBM contributions are based on Ag/Cu-d and I-p orbitals and Cu 3d electrons have higher relative energy than Ag 4d electrons.[37] For Ag and Cu based materials, POE-Ag and POE-Cu both exhibit the respectively smallest band gap based on calculated and experimental values (Figure 5.3 and Table S5.4), as we showed due to the dominant contribution of POE to the VBM. NOE-Cu deviates from the other materials, in that its absorbance exhibits a blueshift with a band gap energy of 2.46 eV but again with a strong peak at 2.6 eV. Since Bi will still introduce spin-orbit coupling effects to the electronic structure of Cu-Bi based materials, the same reasoning for the maxima, mentioned before applies,

with similar absorbance responses shown in other works on Cu-Bi 2D DPs and 3D Cu-Bi DPs.^[37,38] The less distinct peaks were also observed in Cu-Bi thin films elsewhere,^[16] but still without a clear reason established. For the inorganic contributions to the electronic structure, the octahedral distortions, tilts and bond lengths play the major role, as this dictates the orbital overlap.^[10,39] The formation of octahedra in double perovskites requires Cu or Ag to reside in a 6-fold coordination by halogen atoms. In fact, Cu(I) halides prefer to form 3- or 4-fold coordination as $[\text{CuX}_3]$ polyhedra or $[\text{CuX}_4]$ tetrahedra. Instead, Ag(I) can be 3-, 4- but also more easily 6-fold coordinated with halogen atoms. Especially for larger halogen atoms such as Br and I, based on Pauling's first rule, the smaller radius of Cu(I) ions may lead to more distortions with 6-fold coordination compared to Ag(I) ions.^[40,41] Therefore there is so far also no report of Cu-Bi based 3-dimensional DPs, as far as we know. Next, one must also consider the modulating effect of the organic cations on the inorganic lattice. For NOE, the shorter ethyl-linkage leads to less freedom and possibly a shorter penetration depth of the anchoring ammonium moiety into the cuboctahedral cavities. This, combined with the reduced π - π interactions compared with POE and POP cations, NOE cations may have an inferior ability to modulate the inorganic framework. NOE-Cu does indeed show a very different GIWAXS pattern and lattice parameters compared to NOE-Ag as mentioned in section 5.3.1 and shown in Figure S5.3, possibly leading to the different absorption profile compared to the other materials. The other three Cu-Bi based materials (NOP-Cu, POE-Cu and POP-Cu) display very similar GIWAXS patterns compared to their Ag-Bi based counterparts, in agreement with their similar absorbance profiles (Figure S5.3 and Figure 5.3b). Finally yet importantly, the pyrene-based 2D DPs POE-Ag, POP-Ag, POE-Cu and POP-Cu, show increased absorbance in the UV region beyond 3.1 eV, compared to NOE and NOP based materials, with a strong peak at 3.21 eV. This fits the molecular absorption of pyrene, which has a strong absorption peak at 3.28 eV (378 nm) in its crystalline form, originating from its monomeric $^1\text{L}_b$ transition.^[22,42-44]

Overcoming Intrinsic Quantum Confinement and Ultrafast Self-Trapping in Ag-Bi-I and Cu-Bi-I Based 2D Double Perovskites through Electroactive Cations

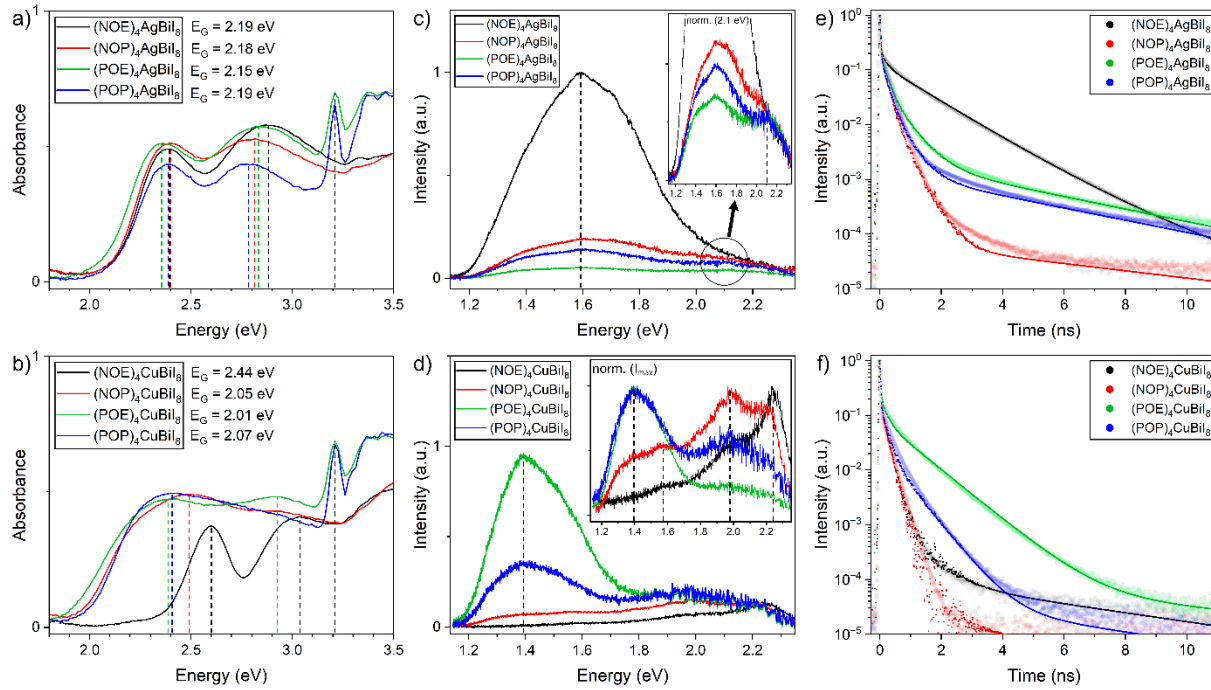


Figure 5.3: Thin film UV-Vis absorbance spectra of a) Ag-Bi and b) Cu-Bi based materials with an inset detailing the estimated band gap energies obtained with the Tauc method. The characteristic two maxima as well as the pyrene absorption are marked with droplines, in their respective color. c) and d) Steady-state photoluminescence spectra of Ag-Bi and Cu-Bi based materials with insets of spectra normalized to the second peak at 2.1 eV for Ag-Bi based materials and to the highest intensity peaks for Cu-Bi based materials ($E_{exc} = 3.1$ eV). Time-resolved photoluminescence spectra of e) Ag-Bi and f) Cu-Bi based materials, with the experimental data in semi-transparent points and the fitted transients overlaid as full points.

5.3.3.2 Charge-Carrier Dynamics and Photoluminescence

Photoluminescence (PL) emission of thin films was recorded following excitation by a laser with an energy of 3.1 eV. As shown in Figure 5.3c-f, the steady state and time resolved spectra exhibit characteristics similar to other 2D DPs, namely i) a broad emission spectrum, ii) weak emission intensity and iii) charge-carrier lifetimes on the order of nanoseconds. The Ag-Bi materials all show similar emission profiles, with an emission maximum centered at ≈ 1.6 eV and full-width half-maximum values of ≈ 500 meV at room temperature (RT). Furthermore, they show a second, weak feature centered around 2.1 eV. Normalized spectra reveal these emission bands to be identical for all four Ag-Bi materials (Inset of Figure 5.3c). The FWHM is very broad also in context of similar structures such as $(4FPEA)_4AgBiI_8$ showing a FWHM of 320 meV at RT.^[11] As shown in previous

publications, the origin of this broad emission does not exclusively lie in the excitonic band-to-band emission, but rather in the prevalence of various kinds of structural and electronic defects in these 2D double perovskites.^[11,45,46] The broad emission can generally be observed in 3D double perovskites as well as in single-crystals of 2D double perovskites, which excludes lowered structural dimensionality or thin film crystal quality being a primary reason for the broad PL.^[47,48] Structural defects such as iodine vacancies, molecular cation interactions with excitons or charge-carriers at defect sites, self-trapping and disorder between Ag and Bi metal octahedral sites have all been proposed as possible origins for this emission.^[46,49] We note that the absolute intensities of this first feature decreases along NOE-Ag > NOP-Ag > POP-Ag > POE-Ag, with NOE-Ag showing a much larger intensity than the other materials (Figure 5.3c). As shown earlier, NOP-Ag forms a type Ib QW which should promote radiative band-to-band recombination from CBM to VBM, given the dominant contribution to the band edges of the inorganic sublattice. Due to the even stronger PL intensity of NOE-Ag, we can also assume a type Ib QW, since both cations are based on naphthalene and its electronic contribution is quite far below the VBM for NOP-Ag (around 0.46 eV lower, Figure 5.2d). Since the features at 1.6 eV are the energetically lowest, they could predominantly originate from excited states of the first absorption feature, i.e. transitions into the separated CBM of the inorganic layers. The intensity trend supports this, since NOP-Ag, POE-Ag and POP-Ag have direct band gaps and for NOE-Ag it can be assumed to also be direct. The dispersive VBM in NOP-Ag and possibly also NOE-Ag, both dominantly inorganic, promotes radiative recombination from the dominantly inorganic CBM (for all materials) compared to the flat VBM in POE-Ag and POP-Ag, both dominantly organic. The broadness centered around this feature at 1.6 eV would then also support the earlier mentioned origins, since almost all structural defects, such as various Schottky and Frenkel defects, especially the known influence of vacancies and disorder of equatorial iodines, self-trapping, octahedral disorder and color-centers, would be located in the inorganic sublattice.^[6,26,46]

Besides the first main feature centered at 1.6 eV, there is a second feature centered at 2.1 eV (Figure 5.3c), with much lower intensity but the same profile for all four Ag-Bi materials (Figure 5.3c inset). The ratio between the emissions at 2.1 eV and 1.6 eV decreases along POE-Ag > POP-Ag ≥ NOP-Ag >>> NOE-Ag (Figure S5.14). Since for all four materials, there is a large energetic gap between the lowered inorganic band forming the CBM and the higher lying bands, made up of firstly organic contributions and growingly mixed inorganic-organic contributions (Figure 5.2, Figure S5.8-Figure S5.9), radiative recombination at 2.1 eV would be favored for POE-Ag and POP-Ag, since their VBM is predominantly based on orbitals from the organic sublattice.

Next, we discuss steady-state spectra of Cu-Bi materials, where the first emission is centered at ≈ 1.4 eV for NOP-Cu, POE-Cu and POP-Cu. This redshift is consistent with the ≈ 0.2 eV smaller E_G of the Cu-Bi materials compared to the Ag-Bi materials. The absolute intensity decreases along POE-Cu > POP-Cu > NOP-Cu, inverted to Ag-Bi materials (Figure 5.3d). This emission is only distinguishable for POE-Cu and POP-Cu with a FWHM ≈ 300 meV, being narrower than the Ag-Bi emission at 1.6 eV. NOE-Cu does not show this emission, which could be due to its larger E_G of 2.44 eV, i.e. the excitation energy being much closer than for the other materials, or due to different decay pathways in the structurally slightly different material. If this energetically lowest emission is related to similar origins as discussed for Ag-Bi materials, the observed inverted intensities could be due to the different contribution of the organic cations to the band structure for Cu-Bi materials, since the relative energy of Cu 3d electrons is larger, as mentioned earlier, which will result in relative changes of the organic cation energy levels. Looking at the absorbance data and the less pronounced maxima, the energetic separation of the CBM could also be smaller compared to Ag-Bi materials. The next emission peak, observable for NOE-Cu and NOP-Cu, lies at 1.58 eV (Figure 5.3d inset), which could be overshadowed by the larger emission at 1.4 eV for POE-Cu and POP-Cu. Furthermore, a third and fourth emission peak can be observed at 1.98 eV and 2.24 eV, where the former is visible for all materials but the latter is predominantly seen in NOE-Cu and NOP-Cu (Figure S5.14). Due to the lack of crystal and band structure for Cu-Bi materials, we do not wish to speculate about the origins of the different emission spectra, with the exception, that the different spectrum observed for NOE-Cu is clearly due to its blueshifted absorption profile.

Next, we discuss the time resolved PL transients for all eight materials. They were fitted with a triexponential decay function (Tables S5.5-5.6). The transients show an initial, fast component on the order of less than 10 ps, followed by a second, longer-lived component in the range of ns and a third component up to 10 ns (Fig. 3e-f), integrating over the whole spectral range. While the third component is evident in for example POE-Ag and POP-Ag, its intensity is on the low end of the signal (see amplitudes in Tables S5.5-5.6). We thus used the triexponential fit for all materials, although it most likely is just a very weakly emissive state caused by the slowest, possibly defect-related recombination process. The signal around 2.1 eV contains only the fast component, supporting an emissive state from a higher energy level, due to the band splitting and the intensity ratio between high and lower energy emissions, as discussed earlier (Figure S5.15). Accordingly, the slower component is most pronounced in NOE-Ag and POE-Cu, with both showing the strongest intensities for the low energy emissions at 1.6 eV and 1.4 eV, respectively (Figure 5.3c-f). These ultrafast decay

Overcoming Intrinsic Quantum Confinement and Ultrafast Self-Trapping in Ag-Bi-I and Cu-Bi-I Based 2D Double Perovskites through Electroactive Cations

times are in line with previous reports on 2D double perovskites and are most likely linked to a similar mechanism. Before the initial observed PL component, an ultrafast localization or self-trapping process of an excitonic polaronic state takes place, whose emission appears <10 ps.^[6,11] This state is possibly further mediated through defect-state recombination, which appear on the two following timescales in the range of ns.^[11] This interpretation should be considered in addition to the previously discussed electronic band characteristics and QW structures. To determine the diffusion coefficients of the emissive species, we recorded time resolved PL across the confocal spot leaving the excitation beam stationary in a confocal microscope (Figure 5.4a-b).

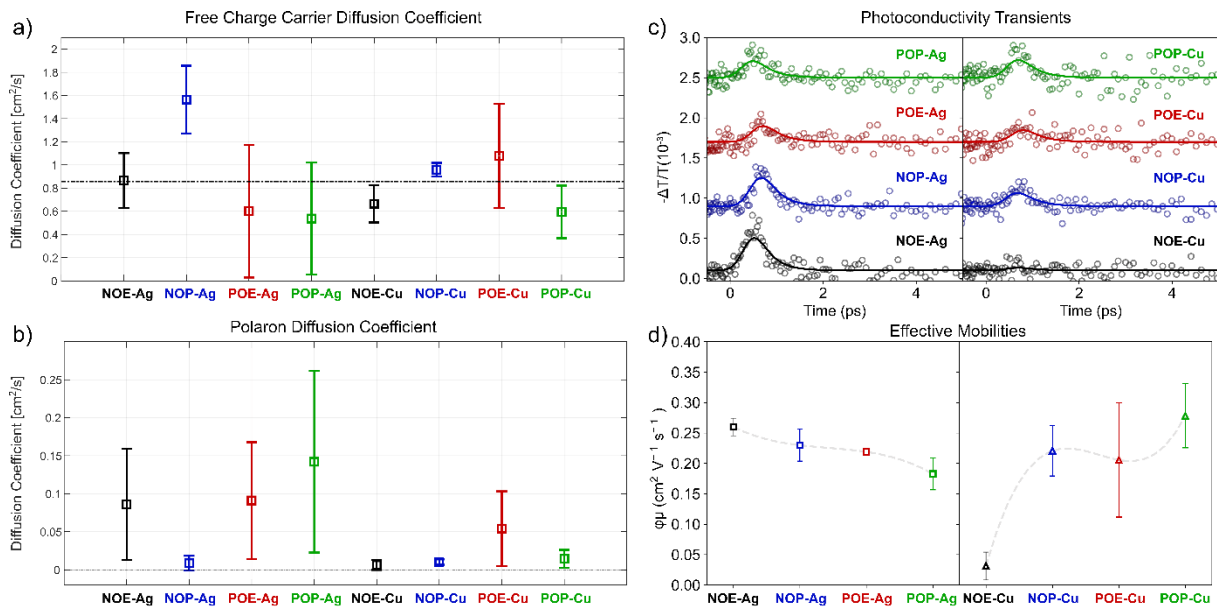


Figure 5.4: Diffusion coefficients extracted from fluorescence-lifetime imaging for a) the initial ultrafast component, attributed to free charge carriers and for b) the second, longer lived component, attributed to the polarons. c) Photoconductivity transients from optical-pump terahertz-probe spectroscopy and d) the extracted effective mobilities.

From fitting the broadening of the gaussian-shaped confocal PL emission, we extracted the diffusion coefficients for two individual time scales (Figure S5.16). The first component appears on the ps timescale as an initial broadening in the rising signal. We attribute this to the ambipolar charge carrier diffusion (Figure 5.4a) from free charge-carriers generated upon nonresonant photoexcitation, as further shown through optical-pump terahertz-probe (OPTP) spectroscopy measurements later on. The second component appears on the ns timescale, which we attribute to the excitonic polaron

diffusion (Figure 5.4b) as a result of charge-carrier localization processes already reported for different 2D and 3D DPs.^[6,11,50] As further support for this attribution, we note that the diffusion coefficients for the initial free charge carriers are around one to two orders of magnitude larger than for the following polaron diffusion. Therefore, we propose the following mechanism: upon nonresonant photoexcitation mobile free ambipolar charge carriers are generated. These charge carriers rapidly localize and form an excitonic state, coupled to a phonon deforming the surrounding lattice (forming a polaron) which reduces their mobility, yet preserving a remnant mobility. For all materials, the diffusion coefficients of the fast component scatter around $0.8 \text{ cm}^2/\text{s}$ (dotted line in Figure 5.4a), which is a combination of excitons and free charge carriers. It is not possible to separate both signals. Observing the fast diffusion coefficient in the first picoseconds is in good agreement with the OPTP measurements having an ultrafast localization of the excited state. This is in agreement with the aforementioned strong electron- and exciton-phonon coupling in DPs.^[33,35,50,51] In the soft, ionic lattice of DP crystals, lattice charge shielding effects or electron-phonon-coupling will occur, reducing the mobility of all charge carriers. Since this PL diffusion signal appears at the noise free signal rise (Figure S5.16), these values are an estimation for an upper boundary of the free ambipolar charge-carrier diffusion coefficient. The diffusion coefficients of the polaronic, excitonic state, on the longer time scale of up to 2 ns, vary for the different materials (Figure 5.4b). Hereby, the materials with POE and POP show the highest values up to $0.14 \text{ cm}^2/\text{s}$. The Cu-Bi based ones with NOE and NOP have the slowest mobile excited state at $0.01 \text{ cm}^2/\text{s}$. Comparing the measured polaron lifetime with the diffusion coefficients, it seems that the materials with higher mobility are connected to longer excited state lifetimes. One interpretation is that the organic molecules have an influence on quenching the excited states, which are not contributing anymore to further energy conversion of charge separation processes.

To further confirm the proposed mechanism, we investigate the early-time dynamics of free charge carriers by OPTP spectroscopy measurements. The THz photoconductivity following photoexcitation with the same energy (3.1 eV) shows a consistent ultrafast decay with a time constant of around 300 fs (Figure 5.4c) for all the studied thin films. The observed THz photoconductivity decay confirms the presence of an ultrafast transition between an initially photogenerated mobile state and an immobile state. A similar behavior has been reported for different 2D DPs and has been attributed to a phonon-mediated self-trapping process, which is a hallmark of Ag-Bi halide semiconductors.^[6,11,52,53] It is worth noting that, given the high exciton binding energy in 2D DPs (generally in the range of $\approx 250 \text{ meV}$ or higher for 2D DPs)^[36,54], we expect the presence of strong excitonic interaction and the

formation of a stable exciton population at room temperature, as predicted by the Saha equation.^[55] Given this high exciton binding energy, which shifts intraexcitonic transition into the mid-IR range, the observed THz photoconductivity in the measured THz range (between 0.5 to 2.5 THz) can be safely attributed to free charge-carrier conductivity similarly to that reported for 3D DPs.^[56] The estimated effective mobilities are very similar for all the studied materials and lie between $\varphi\mu \approx 0.2 - 0.3 \text{ cm}^2 \text{ V}^{-1} \text{ s}^{-1}$. Slightly higher mobility values are observed for NOE and NOP-based materials than for POE- and POP-based materials, except for NOE-Cu due to its larger E_G and for POP-Cu, which shows the highest mobility of all materials. We stress that, also considering the high exciton binding energies in these materials, charge-carrier mobilities reported here are effective mobilities, depending on the ratio between free charge carriers and excitons generated. Hence, the near absence of signal observed for NOE-Cu, could possibly be caused by the higher E_G (Figure 5.3b). Furthermore, we note that small variation in the estimated $\varphi\mu$ can reflect either changes in the exciton binding energies or changes in the mobilities. Interestingly, observed charge-carrier mobility values are slightly lower than our previously reported mobility of $\approx 0.6 \text{ cm}^2 \text{ V}^{-1} \text{ s}^{-1}$ for $(4\text{FPEA})_4\text{AgBiI}_8$ (possibly due to different octahedral distortions) and an order of magnitude lower compared to mobilities for $\text{Cs}_2\text{AgBiBr}_6$ of $\approx 1.3 \text{ cm}^2 \text{ V}^{-1} \text{ s}^{-1}$ (localized state) and $\approx 3 \text{ cm}^2 \text{ V}^{-1} \text{ s}^{-1}$ (delocalized state).^[6,11] These ultrafast charge carrier dynamics are consistent with all results on 2D DPs and can either be attributed to exciton formation or ultrafast charge-carrier localization.^[57] Finally, we note that the PL diffusion and the OTP mobility measurements are both probing in-plane charge transport of thin film samples and thus cannot give information about the out-of-plane transport and mobilities of these anisotropic 2D structures.

5.3.4 Photoconductivity and Photovoltaic Performance

To assess the suitability of the investigated 2D DPs for photoactive applications, we initially conducted simple in-plane photoconductivity measurements with top-evaporated contacts on thin films (Figure S5.17-Figure S5.18). Under dark conditions, only POE-Ag, POE-Cu and POP-Ag showed conductivity values above the instrument sensitivity of $1 \times 10^{-10} \text{ A}$. At maximum bias voltage of 5 V, POE-Ag showed a current of around $1 \times 10^{-9} \text{ A}$, while POE-Cu showed a higher current of around $1 \times 10^{-7} \text{ A}$. Under illuminated conditions, different responses were observed. Materials based on NOE and NOP showed only slightly increased conductivities (Figure 5.5a-b). Materials based on POE and POP showed much larger photoresponses, with POE-Ag and POP-Ag having the highest on/off ratios with factors between one and three orders of magnitude. While POE-Cu did not feature a large on/off ratio,

Overcoming Intrinsic Quantum Confinement and Ultrafast Self-Trapping in Ag-Bi-I and Cu-Bi-I Based 2D Double Perovskites through Electroactive Cations

due to its higher conductivity under dark conditions its absolute conductivity under illuminated conditions was still the highest among the samples (Figure 5.6b). The photoresponse of POP-Cu was comparable to the small values of the materials based on NOE and NOP and was thus excluded from further investigation. Since POE-Ag showed the most promising photoresponse, we further investigated the influence of thin film synthesis conditions to optimize performance (Figure S5.19 and Table S5.7), resulting in the values shown in Figure 5.5a and Figure 5.5b.

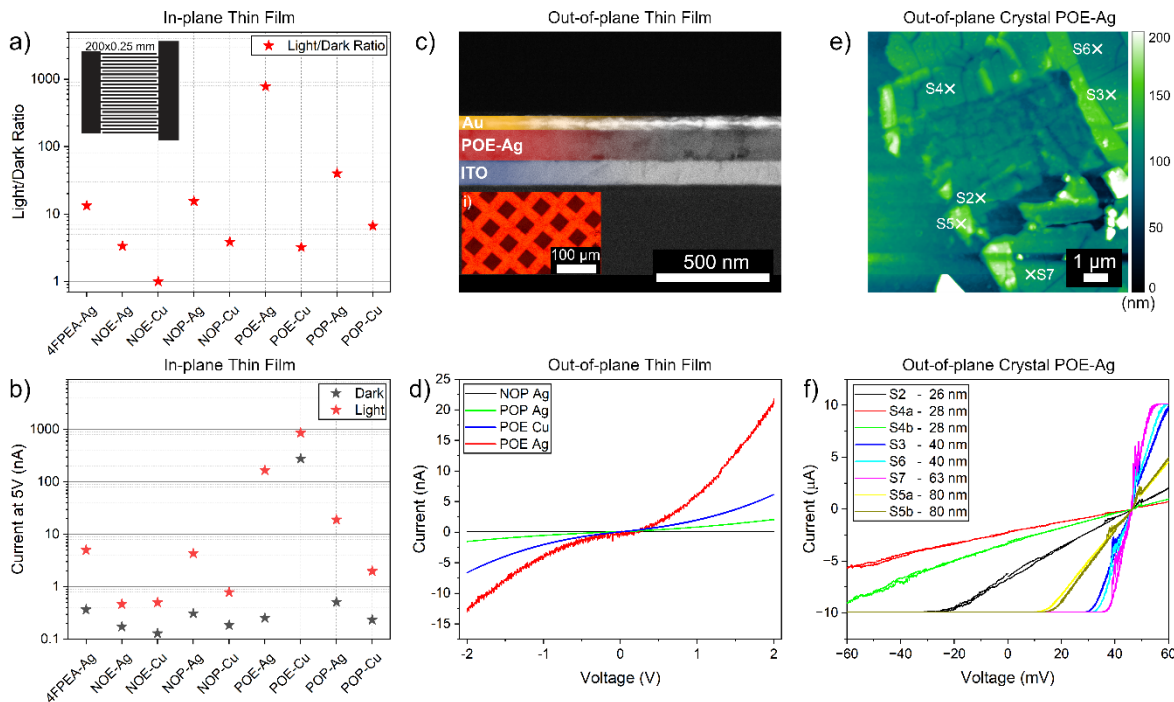


Figure 5.5: a) Light/dark in-plane conductivity ratios with an inset showing the top contact evaporation mask with channel length and width 200 x 0.25 mm. b) Current values at 5 V bias of thin film samples on ITO for all eight materials and 4FPEA-Ag as a reference material. c) SEM cross section of the cAFM thin film sample of POE-Ag on ITO, with top evaporated Au contacts, shown in an inset as an optical light microscopy top view. d) Out-of-plane cAFM IV curves of NOP-Ag, POE-Ag, POP-Ag and POE-Cu thin film samples. The increased signal/noise in the POE-Ag curve is due to a decreased sensitivity setting, due to the higher current flow in the sample. e) Height profile AFM image of exfoliated POE-Ag single crystal fragments on ITO with measured spots indicated as white crosses. f) The respective cAFM IV curves of different spots shown in e).

To compare the impact of the aromatic system in the organic cations, we also prepared $(4FPEA)_4AgBiI_8$ as a reference material, under the exact same preconditions. The current under dark and light conditions as well as the on/off ratio is far below the values of POE-Ag, and is more similar

to the values of NOE-Ag, NOE-Cu, NOP-Ag, NOP-Cu and POP-Cu. We note that a clear differentiation between in- and out-of-plane contributions is not possible due to the device architecture featuring top-evaporated electrodes. Nonetheless, we assume that it is unlikely that all current is exclusively flowing through only the surface layer of the thin films, i.e. one or several atomic layers. Since all materials are exclusively oriented with the organic and inorganic layers parallel to the substrate surface, an improved in- and out-of-plane photoconductivity for POE-Ag, POE-Cu and POP-Ag can thus be assumed. Some materials exhibit a hysteresis in the photoconductivity scans, where the zero current points have an offset, namely at positive bias for the forward scan (-5 V to 5 V) and at negative bias for the backward scan (5 V to -5 V)(Figure S5.17). This points to a built-in potential or polarizability for some of the materials. Metal halide perovskites are ionic crystals and ionic mobility is a well-known phenomenon.^[58] Moreover, crystal lattices of 2D perovskites are known to be polarizable due to non-centrosymmetric space groups (which our results demonstrate for POE-Ag = Cc and POP-Ag = C2) or due to reorganization of the organic cations under voltage bias.^[59] Another possible explanation for this phenomenon could be a charge buildup under bias, resembling simple capacitive behavior, i.e. an insufficient conductivity for charge carriers to move through the lattice under applied voltage. In the case of POE-Ag this could be an explanation for the hysteresis under dark conditions, while the conductivity is greatly increased and no hysteresis is observable under light conditions (Figure S5.17 and Figure S5.19).

To assess the out-of-plane conductivity of the most conducting materials POE-Ag, POP-Ag and POE-Cu compared to the moderately conducting NOP-Ag, we performed out-of-plane conductivity measurements on illuminated thin films with top electrodes and bottom indium doped tin oxide (ITO) substrates (Figure 5.5c-d). Top electrodes were contacted via a conductive atomic force microscopy (AFM) tip to ensure the mechanical integrity of the functional film. The *IV* curves in Figure 5.5d show the largest current for POE-Ag and lower currents for POE-Cu and POP-Ag, while NOP-Ag shows no current response at all. This agrees well with the measured photoconductivity responses of macroscopic in-plane measurements (Figure S5.17).

Furthermore, an exfoliated single crystal sample of POE-Ag made through adhesive tape exfoliation of POE-Ag crystals onto an ITO substrate (Figure 5.6g) clearly confirms the significant out-of-plane conductivity, measured on multiple different spots at different crystal thickness with an AFM tip as top electrode in contact mode (Figure 5.5e-f). Apparently, there is no clear thickness dependence of the measured currents, which could be caused by different contact resistances due to different crystal

surfaces resulting from exfoliation or the different contact quality due to the volatility of the AFM tip in contact mode. Interestingly, a different type of hysteresis than previously mentioned, namely an increased current signal in the positive bias direction can be observed for out-of-plane thin film measurements of POE-Ag, POP-Ag and POE-Cu. Their *IV*-curves exhibit a non-linear behaviour (Figure 5.5d), in contrast to the linear ohmic behavior of the out-of-plane crystal samples (Figure 5.5f) and the in-plane thin film samples (Figure S5.17). The S-shape observed is typically caused by large contact interface resistance, which is plausible since out-of-plane thin film samples are contacted through a 30 μm^2 evaporated Au pad compared to the out-of-plane crystal sample, where the contact is directly the AFM tip with a tip radius > 25 nm. In contrast, in-plane thin film measurements do not exhibit this S-shape (Figure S5.17 and Figure S5.20), although they are contacted through an evaporated Ag electrode with surface contact on the order of mm^2 (Figure 5.5a inset). The difference could either be caused by the different work functions of Ag ($\varphi = 4.0$ eV – 4.6 eV) and Au ($\varphi = 5.2$ eV – 5.4 eV),^[60,61] or by the different measurement geometry at the same anisotropic, crystal orientation. More detailed views of the *IV* curves are shown in Figure S5.20-Figure S5.23 which show a clear Schottky barrier type behavior (Figure S5.21b) only for POE-Ag while POE-Cu and POP-Ag show the S-shaped *IV* curve. This could be caused by the larger out-of-plane photoconductivity of POE-Ag compared to the other materials. Since 2D perovskites are known to suppress ion migration, especially in the out-of-plane direction we attribute the S-shape in the out-of-plane thin film measurements to the different Schottky barrier heights at the Au contact and the different work functions of Ag and Au. Nonetheless, a small hysteresis upon multiple cycle measurement for out-of-plane thin film POP-Ag is observable, pointing towards small ionic movements and the build-up of an electric field (Figure S5.23).

Consistent with the above observations, it makes sense why the free charge carrier diffusion coefficients (Figure 5.4a) and effective mobilities (Figure 5.4d) are slightly higher for NOE-Ag and NOP-Ag compared to POE-Ag and POP-Ag. As shown earlier through DFT calculations, NOP-Ag has a type Ib QW structure and shows no significant out-of-plane conductivity. Thus the charge carriers are confined to the inorganic layers. POE-Ag and POP-Ag behave vice versa, showing smaller free charge carrier diffusion coefficients and mobilities (Figure 5.4a and Figure 5.4d), while showing larger polaron diffusion coefficients (Figure 5.4b), compared to NOP-Ag. Since the polaron diffusion is the component with the much longer lifetime, it could be connected with the increased photoconductivities for POE and POP materials. With NOE-Ag lying between the values of the two cases, we hypothesize that it should also have a type Ib QW structure due to the similar energy levels

Overcoming Intrinsic Quantum Confinement and Ultrafast Self-Trapping in Ag-Bi-I and Cu-Bi-I Based 2D Double Perovskites through Electroactive Cations

of its constituents like NOP-Ag. As discussed earlier, the organic intralayer arrangement also plays an important role in out-of-plane charge transport, which was shown to be favorable with the ethyl linkage compared to the propyl linkage (POE>POP), as is the case here with NOE compared to NOP.

Overall, the results establish the proof-of-concept for the enhancement of out-of-plane conductivity in samples featuring functional, organic cations with fused aromatic π -systems such as POE and POP, exhibiting favorable QW band alignment as well as favorable intra-organic layer alignment compared to other 2D DP materials.

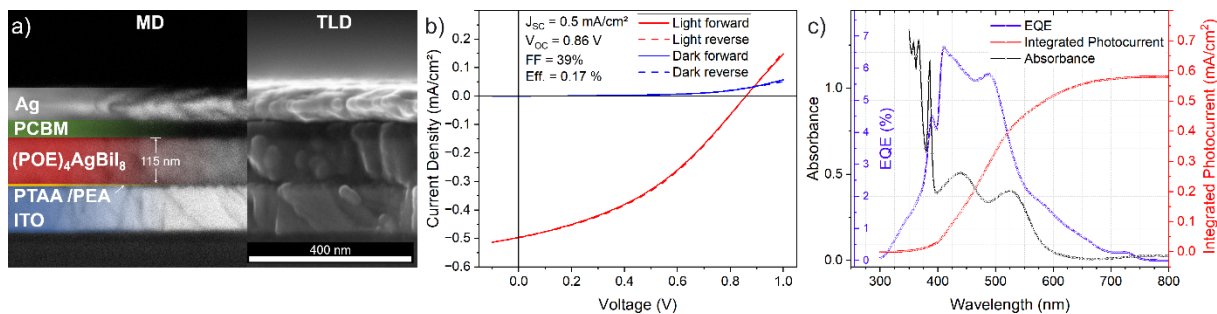


Figure 5.6: a) SEM cross section of the constructed solar cell with inverted *p-i-n* architecture ITO/PTAA/PEA/POE-Ag/PCBM/Ag for back-scattered electrons (MD = mirror detector) and secondary electrons (TLD = through lense detector). b) Corresponding *JV* curve and c) EQE and absorbance spectrum of the solar cell.

Having identified POE-Ag as the most promising candidate of the eight materials for photoactive application, we constructed solar cells to assess the viability of 2D DPs in this context. We chose a planar architecture to ensure the parallel orientation of the POE-Ag active layer, consisting of ITO as the cathode substrate, a 2 nm thick poly[bis(4-phenyl)(2,4,6-trimethylphenyl)amine] (PTAA) layer as the hole-transport-material (HTM), a phenethylammonium (PEA) interface passivation treatment (1 mg/ml) for increased wettability and better connection of the perovskite layer, POE-Ag as the active perovskite layer, [6,6]-Phenyl-C61-butyrac methyl ester (PCBM) as the electron-transport-material (ETL) and Ag as the anode electrode (Figure 5.6a). To confirm the crystalline quality and the orientation of the POE-Ag layer, we measured GIWAXS on a functioning pixel of a full device (Figure S5.24). The non-optimized champion device produced a $J_{sc} = 0.5 \text{ mA/cm}^2$, $V_{oc} = 0.86 \text{ V}$, fill factor (FF) = 39 % and power conversion efficiency (PCE) = 0.17 % and the *JV* curve of the solar cell showed no hysteresis in the forward and reverse scan (Figure 5.6b). Statistical box plots are shown in Figure S5.26. As an evaluation criterion for working pixels, a V_{oc} above 0.4 V was chosen, as it confirms a complete active layer and no short circuit in the diode structure. The solar cells were constructed

from different POE-Ag solution concentrations (0.075 M, 0.0375 M and 0.01875 M) to achieve different thicknesses, since the results discussed above establish a strong impact of thickness on out-of-plane conductivity. For thicker layers, i.e. cells 1-4, almost no J_{sc} could be measured, due to the perovskite layer being too thick for significant charge being extracted, as the mobility of free charge carriers is too small. For thinner active layers, i.e. cells 5-12, J_{sc} values above 0.15 mA/cm² could be measured, indicating that the optimal thickness for charges to be extracted ranges from 100-200 nm. While a thinner layer should be able to produce higher J_{sc} values, with a decreased thickness the continuity and complete coverage of the active layer becomes increasingly challenging with the fabrication of the solar cell, and the light capturing becomes less efficient. The champion device with a POE-Ag thickness of 115 nm (Figure 5.6a) consistently had all pixels producing an average J_{sc} of 0.47 mA/cm², with average V_{oc} values of 0.83 V. While this represents already a promising initial V_{oc} , the difference to the band gap of the material at 2.15 eV still indicates a significant voltage loss in the full device. Reasons could include defect states in the active material (trapping sites and sub bandgap states), as well as non-optimized energy alignment with the HTL and ETL materials. As most commercially available HTL and ETL materials are optimized for lead based perovskites and small band gap active materials, we envision that future transport layer optimisation will improve V_{oc} values by a significant margin. The energy levels of POE-Ag have to be determined through ultraviolet photoelectron spectroscopy (UPS) to select and synthesize suitable transport materials. Furthermore, the low FFs between 30-40 % indicate a large series resistance in POE-Ag solar cells, which is expected due to the low out-of-plane conductivity of 2D perovskites in general, as well as possibly high interfacial resistances. This is also evident in the S-shape of the out-of-plane IV curve shown in Figure 5.5d, due to contact resistances. Finally, to confirm the origin of the J_{sc} from the POE-Ag active layer, we performed external quantum efficiency (EQE) measurements (Figure 5.6c). With the absorbance of POE-Ag overlaid, it is clear that the generated current originates from the generation of charge carriers in the POE-Ag layer, as the spectral UV-vis absorption profile matches the EQE profile in good agreement. Furthermore, the predicted integrated photocurrent of 0.58 mA/cm² is in good agreement with the solar cell's J_{sc} of 0.5 mA/cm². Interestingly, the absorbance peak at 390 nm, originating from the pyrene moiety, also contributes to the photocurrent as observed in the EQE peak at the same position. This is another key indication that (i) the organic layer contributes to the generation of mobile charge carriers and (ii) that these charge carriers can get extracted from the organic layer, providing further evidence of the out-of-plane charge carrier transport.

5.4 Conclusion

We synthesized eight new two-dimensional $n = 1$ RP double perovskites (DPs) based on Ag-Bi-I and Cu-Bi-I inorganic networks with large, organic cations NOE, NOP, POE and POP containing fused aromatic moieties. Thin films of these materials crystallize in the typical manner with their 2D layers oriented parallel to the substrate, allowing us to determine their anisotropic charge carrier and electrical conductivity properties. Through DFT calculations, we confirmed the formation of different quantum well structures of the type Ib for NOP-Ag and type IIb for POE-Ag and POP-Ag. All materials show similar optical properties for Bi-based DPs, with band gap energies around 2.2 eV for Ag-Bi materials and 2.0 eV for Cu-Bi materials, with the exception of NOE-Cu at 2.4 eV. The emissive and charge carrier properties were found to be similar to other reported 2D DPs, further confirming their intrinsic mechanism of ultrafast conversion of free charge carriers to less mobile states due to exciton formation, phonon-mediated self-trapping (i.e. small polaron formation) or other defect states. The diffusion coefficients of the free charge carriers average at around $0.8 \text{ cm}^2 \text{ s}^{-1}$ with associated picosecond lifetimes for all materials ($1.6 \text{ cm}^2 \text{ s}^{-1}$ for NOP-Ag), while the polaron diffusion coefficients (with associated lifetimes of nanoseconds) reach larger values between $0.09 - 0.14 \text{ cm}^2 \text{ s}^{-1}$ only for NOE-Ag, POE-Ag, POE-Cu and POP-Ag. Accordingly, the electrical conductivity is greatest for these materials and POE-Ag showed a photoconductivity on/off ratio of 779. Due to the different QW types and the different intraorganic layer arrangement, POP-Ag, POE-Ag and POE-Cu showed out-of-plane conductivity with a 10x greater out-of-plane current for POE-Ag compared to POP-Ag. Finally, POE-Ag was employed as the active material for the construction of a solar cell with a $J_{sc} = 0.5 \text{ mA/cm}^2$, $V_{oc} = 0.86 \text{ V}$, $FF = 39 \%$ and $PCE = 0.17 \%$. To the best of our knowledge, this is the first report of a functioning lead-free, $n = 1$, 2D DP solar cell in a planar architecture with exclusively parallel oriented layers. We envision that with further research aiming to achieve higher n value iodide 2D DPs i.e. lowering their E_G towards optimum for reaching the Shockley-Queisser limit and by purposeful integration of functional organic cations to tune the charge carrier and transport properties, this material class can be a stable and lead-free alternative for constructing single-junction solar cells. Beyond the use in photovoltaics, the nanoscale integration of organic semiconducting materials and 2D lead-free perovskites offers numerous opportunities for designing novel heterostructures with widely tunable optoelectronic properties.

5.5 Acknowledgment

The authors gratefully thank Dr. Steffen Schmidt for the SEM measurements and Dr. Peter Mayer for the SC-XRD measurements and structure solutions. Furthermore, the authors thank the Bavarian research network Solar Technologies go Hybrid, the Deutsche Forschungsgemeinschaft (DFG) Excellence Cluster e-conversion (EXC 2089/1 – 390776260) and the DFG focus program SPP 2196 for funding. L.M.H. acknowledges support through a Hans Fischer Senior Fellowship from the Technical University of Munich's Institute for Advanced Study, funded by the German Excellence Strategy. L.M.H. and M.R. acknowledge funding from the UK Engineering and Physical Sciences Research Council (EPSRC).

5.6 References

- [1] X. Li, J. M. Hoffman, M. G. Kanatzidis, *Chem. Rev.* **2021**, *121*, 2230.
- [2] J. Sun, K. Wang, K. Ma, J. Y. Park, Z.-Y. Lin, B. M. Savoie, L. Dou, *J. Am. Chem. Soc.* **2023**, *145*, 20694.
- [3] Y. Wei, W. Wang, Z. Wang, H. Yang, X. You, Y. Zhao, P. Dang, H. Lian, J. Hao, G. Li, J. Lin, *Adv. Funct. Mater.* **2023**, *33*, 2205829.
- [4] X. Chen, M. Jia, W. Xu, G. Pan, J. Zhu, Y. Tian, Di Wu, X. Li, Z. Shi, *Adv. Optical Mater.* **2023**, *11*, 2202153.
- [5] M. T. Sirtl, R. Hooijer, M. Armer, F. G. Ebadi, M. Mohammadi, C. Maheu, A. Weis, B. T. van Gorkom, S. Häringer, R. A. J. Janssen, T. Mayer, V. Dyakonov, W. Tress, T. Bein, *Adv. Energy Mater.* **2022**, *12*, 2103215.
- [6] A. D. Wright, L. R. V. Buizza, K. J. Savill, G. Longo, H. J. Snaith, M. B. Johnston, L. M. Herz, *J. Phys. Chem. Lett.* **2021**, *12*, 3352.
- [7] Z. Zhang, Y. Liang, H. Huang, X. Liu, Q. Li, L. Chen, D. Xu, *Angew. Chem.* **2019**, *58*, 7263.
- [8] W. Pan, H. Wu, J. Luo, Z. Deng, C. Ge, C. Chen, X. Jiang, W.-J. Yin, G. Niu, L. Zhu, L. Yin, Y. Zhou, Q. Xie, X. Ke, M. Sui, J. Tang, *Nat. Photonics* **2017**, *11*, 726.
- [9] P. Vishnoi, R. Seshadri, A. K. Cheetham, *J. Phys. Chem. C* **2021**, *125*, 11756.
- [10] B. A. Connor, A. C. Su, A. H. Slavney, L. Leppert, H. I. Karunadasa, *Chem. Sci.* **2023**, *14*, 11858.
- [11] R. Hooijer, A. Weis, A. Biewald, M. T. Sirtl, J. Malburg, R. Holfeuer, S. Thamm, A. A. Y. Amin, M. Righetto, A. Hartschuh, L. M. Herz, T. Bein, *Adv. Optical Mater.* **2022**, *10*, 220035.
- [12] B. Chen, R. Yu, G. Xing, Y. Wang, W. Wang, Y. Chen, X. Xu, Q. Zhao, *ACS Energy Lett.* **2024**, *9*, 226.
- [13] Y. Gao, E. Shi, S. Deng, S. B. Shiring, J. M. Snaider, C. Liang, B. Yuan, R. Song, S. M. Janke, A. Liebman-Peláez, P. Yoo, M. Zeller, B. W. Boudouris, P. Liao, C. Zhu, V. Blum, Y. Yu, B. M. Savoie, L. Huang, L. Dou, *Nature chemistry* **2019**, *11*, 1151.
- [14] C. Liu, W. Huhn, K.-Z. Du, A. Vazquez-Mayagoitia, D. Dirkes, W. You, Y. Kanai, D. B. Mitzi, V. Blum, *Phys. Rev. Lett.* **2018**, *121*, 146401.

- [15] Y. Xu, M. Wang, Y. Lei, Z. Ci, Z. Jin, *Adv. Energy Mater.* **2020**, *10*, 2002558.
- [16] L.-Y. Bi, T.-L. Hu, M.-Q. Li, B.-K. Ling, M. S. Lassoued, Y.-Q. Hu, Z. Wu, G. Zhou, Y.-Z. Zheng, *J. Mater. Chem. A* **2020**, *8*, 7288.
- [17] J. V. Passarelli, C. M. Mauck, S. W. Winslow, C. F. Perkinson, J. C. Bard, H. Sai, K. W. Williams, A. Narayanan, D. J. Fairfield, M. P. Hendricks, W. A. Tisdale, S. I. Stupp, *Nature chemistry* **2020**, *12*, 672.
- [18] D. B. Mitzi, K. Chondroudis, C. R. Kagan, *Inorganic chemistry* **1999**, *38*, 6246.
- [19] Y. Boeije, W. T. M. van Gompel, Y. Zhang, P. Ghosh, S. J. Zelewski, A. Maufort, B. Roose, Z. Y. Ooi, R. Chowdhury, I. Devroey, S. Lenaers, A. Tew, L. Dai, K. Dey, H. Salway, R. H. Friend, H. Sirringhaus, L. Lutsen, D. Vanderzande, A. Rao, S. D. Stranks, *J. Am. Chem. Soc.* **2023**, *145*, 21330.
- [20] M. Braun, W. Tuffentsammer, H. Wachtel, H. C. Wolf, *Chemical Physics Letters* **1999**, *303*, 157.
- [21] M. Braun, W. Tuffentsammer, H. Wachtel, H. C. Wolf, *Chemical Physics Letters* **1999**, *307*, 373.
- [22] J. V. Passarelli, D. J. Fairfield, N. A. Sather, M. P. Hendricks, H. Sai, C. L. Stern, S. I. Stupp, *J. Am. Chem. Soc.* **2018**, *140*, 7313.
- [23] D. Han, S. Chen, M.-H. Du, *J. Phys. Chem. Lett.* **2021**, *12*, 9754.
- [24] M. K. Jana, S. M. Janke, D. J. Dirkes, S. Dovletgeldi, C. Liu, X. Qin, K. Gundogdu, W. You, V. Blum, D. B. Mitzi, *J. Am. Chem. Soc.* **2019**, *141*, 7955.
- [25] M.-H. Du, *The journal of physical chemistry letters* **2015**, *6*, 1461.
- [26] Z. Xiao, W. Meng, J. Wang, Y. Yan, *ChemSusChem* **2016**, *9*, 2628.
- [27] D. Han, M. Ogura, A. Held, H. Ebert, *ACS applied materials & interfaces* **2020**, *12*, 37100.
- [28] A. Camerman, J. Trotter, *Acta Cryst* **1965**, *18*, 636.
- [29] Z. Zhao, S. Chen, J. W. Y. Lam, Z. Wang, P. Lu, F. Mahtab, H. H. Y. Sung, I. D. Williams, Y. Ma, H. S. Kwok, B. Z. Tang, *J. Mater. Chem.* **2011**, *21*, 7210.
- [30] Y. Ge, Y. Wen, H. Liu, T. Lu, Y. Yu, X. Zhang, B. Li, S.-T. Zhang, W. Li, B. Yang, *J. Mater. Chem. C* **2020**, *8*, 11830.
- [31] Alexander Schmitz, L. Leander Schaberg, Svetlana Sirovinskaya, Martina Pantaler, Doru C. Lupascu, Niels Benson, and Gerd Bacher, *ACS energy letters*, **2020**, *5*, 559.
- [32] S. J. Zelewski, J. M. Urban, A. Surrente, D. K. Maude, A. Kuc, L. Schade, R. D. Johnson, M. Dollmann, P. K. Nayak, H. J. Snaith, P. Radaelli, R. Kudrawiec, R. J. Nicholas, P. Plochocka, M. Baranowski, *J. Mater. Chem. C* **2019**, *7*, 8350.
- [33] J. A. Steele, P. Puech, M. Keshavarz, R. Yang, S. Banerjee, E. Debroye, C. W. Kim, H. Yuan, N. H. Heo, J. Vanacken, A. Walsh, J. Hofkens, M. B. J. Roeloffs, *ACS Nano* **2018**, *12*, 8081.
- [34] L. Zhang, S. Li, H. Sun, Q. Jiang, Y. Wang, Y. Fang, Y. Shi, D. Duan, K. Wang, H. Jiang, L. Sui, G. Wu, K. Yuan, B. Zou, *Angew. Chem. Int. Ed.* **2023**, *62*, e202301573.
- [35] R. Kentsch, M. Scholz, J. Horn, D. Schlettwein, K. Oum, T. Lenzer, *J. Phys. Chem. C* **2018**, *122*, 25940.
- [36] M. Palummo, S. Postorino, C. Borghesi, G. Giorgi, *Appl. Phys. Lett.* **2021**, *119*, 51103.
- [37] A. Bala, V. Kumar, *Phys. Rev. Materials* **2021**, *5*, 095401.

- [38] M. Chen, X. Dong, Z. Shan, Z. Xu, S. F. Liu, *J. Phys. Chem. C* **2022**, *126*, 14824.
- [39] J. T. Race, T. Liu, P. M. Woodward, *Crystal Growth & Design* **2024**, *24*, 1367.
- [40] S. Wang, D. Han, C. Maheu, Z. Xu, A. Biewald, H. Illner, R. Hooijer, T. Mayer, A. Hartschuh, H. Ebert, T. Bein, *APL Materials* **2023**, *11*, 041110.
- [41] Z. Xiao, K.-Z. Du, W. Meng, D. B. Mitzi, Y. Yan, *Angew. Chem.* **2017**, *129*, 12275.
- [42] J. Ferguson, *The Journal of Chemical Physics* **1958**, *28*, 765.
- [43] B. Stevens, *Spectrochimica Acta* **1962**, *18*, 439.
- [44] R. D. Pensack, R. J. Ashmore, A. L. Paoletta, G. D. Scholes, *J. Phys. Chem. C* **2018**, *122*, 21004.
- [45] S. Kahmann, D. Meggiolaro, L. Gregori, E. K. Tekelenburg, M. Pitaro, S. D. Stranks, F. D. Angelis, M. A. Loi, *ACS Energy Lett.* **2022**, *7*, 4232.
- [46] A. S. Rury, A. M. Sanni, D. Konadu, T. Danielson, *The Journal of Chemical Physics* **2023**, *158*, 11101.
- [47] X. Zhang, T. Zhu, C. Ji, Y. Yao, J. Luo, *J. Am. Chem. Soc.* **2021**, *143*, 20802.
- [48] J. Y. Park, R. Song, J. Liang, L. Jin, K. Wang, S. Li, E. Shi, Y. Gao, M. Zeller, S. J. Teat, P. Guo, L. Huang, Y. S. Zhao, V. Blum, L. Dou, *Nature chemistry* **2023**, *15*, 1745.
- [49] M. D. Smith, H. I. Karunadasa, *Accounts of chemical research* **2018**, *51*, 619.
- [50] J. G. Mann, F. He, Q. A. Akkerman, T. Debnath, J. Feldmann, *J. Phys. Chem. Lett.* **2024**, *15*, 2169.
- [51] B. Martín-García, D. Spirito, M.-L. Lin, Y.-C. Leng, S. Artyukhin, P.-H. Tan, R. Krahne, *Adv. Optical Mater.* **2022**, *10*, 2200240.
- [52] M. Righetto, Y. Wang, K. A. Elmostekawy, C. Q. Xia, M. B. Johnston, G. Konstantatos, L. M. Herz, *Adv. Mater.* **2023**, *35*, e2305009.
- [53] S. Lal, M. Righetto, A. M. Ulatowski, S. G. Motti, Z. Sun, J. L. MacManus-Driscoll, R. L. Z. Hoye, L. M. Herz, *J. Phys. Chem. Lett.* **2023**, *14*, 6620.
- [54] M. Pantaler, V. Diez-Cabanes, V. I. E. Queloz, A. Sutanto, P. A. Schouwink, M. Pastore, I. García-Benito, M. K. Nazeeruddin, D. Beljonne, D. C. Lupascu, C. Quarti, G. Grancini, *JACS Au* **2022**, *2*, 136.
- [55] M.N. Saha, *Proc. R. Soc. Lond. A* **1921**, *99*, 135.
- [56] M. Righetto, S. Caicedo-Dávila, M. T. Sirtl, V. J.-Y. Lim, J. B. Patel, D. A. Egger, T. Bein, L. M. Herz, *J. Phys. Chem. Lett.* **2023**, *14*, 10340.
- [57] S. G. Motti, M. Kober-Czerny, M. Righetto, P. Holzhey, J. Smith, H. Kraus, H. J. Snaith, M. B. Johnston, L. M. Herz, *Adv Funct Materials* **2023**, *33*, 2300363.
- [58] T. P. Schneider, J. Glaser, J. Horn, F. Schmitz, T. Gatti, D. Schlettwein, *ACS Appl. Electron. Mater.* **2024**, *6*, 987.
- [59] Y. Liu, W. Guo, L. Hua, X. Zeng, T. Yang, Q. Fan, Y. Ma, C. Gao, Z. Sun, J. Luo, *J. Am. Chem. Soc.* **2023**, *145*, 16193.
- [60] N. D. Lang, W. Kohn, *Phys. Rev. B* **1971**, *3*, 1215.
- [61] H. L. Skriver, N. M. Rosengaard, *Physical review. B, Condensed matter* **1992**, *46*, 7157.

5.7 Supporting Information

Thin Film Synthesis

All substrates were cleaned by ultrasonication for 15 min in a solution of acetone, isopropanol, and ethanol (1:1:1). Afterward, the substrates were cleaned for 10 min under nitrogen plasma. Stoichiometric amounts of 1 eq. AgI (Sigma-Aldrich, 99%), 1 eq. CuI (Sigma-Aldrich, 99.995% trace metal basis), 1 eq. BiI₃ (TCI, anhydrous >98%) and 4 eq. NOEI, NOPI, POEI, POPI (prepared according to Ref.^[1]) were weighed in and dissolved in DMF (Sigma-Aldrich, anhydrous 99.8%), DMSO (Sigma-Aldrich, anhydrous >99.9%), GBL (Sigma-Aldrich >99%) or NMP (Sigma-Aldrich, anhydrous, 99.5%) in different ratios depending on the material and substrate, to receive the desired concentrations. The optimized solvent mixture and annealing temperatures for all materials are given in Table S5.1. If not specified elsewhere, thin films were prepared according to these conditions. All thin films were spin-coated in a glove box with N₂ atmosphere. The spin-coating program consists of an initial step of 10 s at 3000 rpm, followed by a second step of 40 s at 5000 rpm. Spin-coating solutions were preheated at 70 °C and substrates were preheated at 100 °C.

Table S5.1: Optimized solvent and annealing parameters for the synthesis of all eight materials.

	Material	Solvent	Annealing 1 (1 min)	Annealing 2 (5 min)
1	(NOE) ₄ AgBiI ₈	1:1 (DMSO:DMF)	140 °C	100 °C
2	(NOP) ₄ AgBiI ₈	1:1 (DMSO:DMF)	140 °C	100 °C
3	(POE) ₄ AgBiI ₈	4:1 (DMSO:DMF)	140 °C	100 °C
4	(POP) ₄ AgBiI ₈	4:1 (DMSO:DMF)	140 °C	100 °C
5	(NOE) ₄ CuBiI ₈	1:1 (DMSO:DMF)	140 °C	100 °C
6	(NOP) ₄ CuBiI ₈	4:1 (DMSO:DMF)	100 °C	140 °C
7	(POE) ₄ CuBiI ₈	4:1 (DMSO:DMF)	140 °C	100 °C
8	(POP) ₄ CuBiI ₈	4:1 (DMSO:DMF)	140 °C	100 °C

Thin Film X-Ray Diffraction (TF-XRD)

TF-XRD measurements were carried out on a Bruker D8 Discover diffractometer in Bragg–Brentano geometry, with Ni-filtered Cu-K α 1 radiation ($\lambda = 1.5406 \text{ \AA}$) and a position sensitive LynxEye detector.

Single-Crystal X-Ray Diffraction (SC-XRD)

SC-XRD measurements were carried out on a Bruker D8 Venture Txs system equipped with a multilayer mirror monochromator and a Mo-K α rotating anode X-ray tube ($\lambda = 0.71073 \text{ \AA}$). The frames were integrated with the Bruker SAINT software package. Data were corrected for absorption effects using the Multi-Scan method (SADABS). The structure was solved and refined using the Bruker Shelxtl Software Package.

Grazing-Incidence Wide Angle X-Ray Scattering (GIWAXS)

GIWAXS measurements were carried out on an Anton-Paar SAXSpoint 2.0 with a Primux 100 microfocus source with Cu-K α 1 radiation ($\lambda = 1.5406 \text{ \AA}$) and a Dectris Eiger R 1M 2D Detector.

Scanning Electron Microscopy (SEM)

SEM measurements were carried out on an FEI Helios NanoLab G3 UC Dual Beam microscope.

Optical Visible Light Microscopy

Optical microscopy measurements were carried out on a Leica – DM4 M light microscope equipped with a digital camera. Images were acquired in incident or transmission lighting settings and for single-crystals a polarization filter was used.

Computational Methods

The calculations of electronic structure were carried out within the framework of density functional theory (DFT),^[2,3] which was performed with the Vienna Ab initio Simulation Package (VASP).^[4,5] The projector augmented-wave (PAW) method was employed to describe the interactions between core and valence electrons.^[6] The plane wave cutoff energy was set to 520 eV, and a Γ -centered Monkhorst-Pack k-point mesh with a grid spacing of $2\pi \times 0.030 \text{ \AA}^{-1}$ was used for Brillouin zone integration. The geometry optimization was performed until the energy and force reached less than 10^{-6} eV and 0.001 eV/ \AA , respectively. The Perdew-Burke-Ernzerhof (PBE) exchange-correlation functional with Tkatchenko-Scheffler (TS) van der Waals (vdW) corrections was employed to describe the long-range interaction.^[7-9] The reliability of TS for low dimensional perovskite halides has been validated.^[10,11]

The optimized lattice parameters agree with experimental ones, which are listed in Table S5.1. It is noteworthy that unreasonable geometry optimization, viz. large difference, leads to the artificial Rashba splitting.^[10-12] As the spin-orbit coupling (SOC) effect strongly influences the electronic structure of compounds containing heavy p-electron elements like Bi,^[13,14] it was included here. In the meantime, hybrid functional with SOC was not currently affordable for these large systems, as the computational resources are demanding and was thus not included. The post-processing of band structure and density of states were carried out by sumo.^[15]

UV-Vis Absorption (UV-Vis)

UV-Vis spectra were taken on a Perkin- Elmer Lambda 1050 spectrometer equipped with a 150 mm integrating sphere. Thin films were measured in transmittance mode.

Raman Spectroscopy

FT-Raman measurements were performed on film samples with a RAM II extension of the Bruker Vertex 70 with a N₂ cooled germanium detector at an excitation wavelength of 1064 nm and a laser power of 300 mW. Spectra were recorded with a resolution of 4 cm⁻¹ and averaged over 10000 scans.

Confocal Photoluminescence (PL)

For PL measurements, hyperspectral images and time resolved PL images, a home-built confocal laser scanning microscope was used. It is based on a microscope body (NIKON) which is combined with an xyz-piezo-scanning stage (PHYSIK INSTRUMENTE). The samples were measured upside down in epi-direction with an air objective (0.85 NA, NIKON). A beamsplitter (MELLES GRIOT 03BTL005) and a spectral, 490 nm long pass filter was used to separate the laser from the PL-light. A sub picosecond laser (ichrome TOPTICA) which is tunable from 476 nm to 645 nm was used for excitation. Here, the laser wavelength was set to 476 nm which was additionally filtered by a 473/10 nm band pass (CHROMA) in the excitation arm. The detection side consists of two parts, which are separated by a collapsible mirror. Additionally, a scannable mirror in the back focal plane was installed for the diffusion measurements scanning around the confocal spot. One arm in the detection has an avalanche photo diode (APD, type: MPD PDM, detector size 50 x 50 μm), which can be combined with Time Correlated Single Photon Counting (TCSPC) electronics (BECKER UND HICKEL) measuring time resolved PL- transients. The second part consists of a spectrometer (ANDOR SHAMROCK SRi303) combined with an open electrode CCD camera (ANDOR NEWTON DU920) recording spectra. The data were recorded using a customized LABVIEW (NATIONAL INSTRUMENTS) program that combines the

manufacturers' software to our desired measurements. Further processing and analysis were carried out using MATLAB (MATHWORKS) to obtain the PL spectra, TCSPC transients and the images.

Optical-Pump Terahertz-Probe Spectroscopy

Optical pump terahertz probe (OPTP) measurements were performed using a setup described in full detail elsewhere.^[16] Briefly, an amplified Ti:sapphire laser system (Spitfire ACE, Spectra-Physics) provides 800-nm pulses with 5-kHz repetition rate and 35-fs pulse duration. This fundamental output is used to generate single-cycle THz radiation pulses in a spintronic emitter (W/Co₄₀Fe₄₀B₂₀/Pt multilayer film on quartz) through the inverse spin Hall effect.^[17] Furthermore, 400-nm pulses used for photoexciting the thin film samples are generated in a beta-barium-borate (BBO) crystal by second-harmonic generation. In the measurements, fractional changes in the THz transmission (0.5-2.5 THz range of interest) following the 400-nm photoexcitation are monitored by using free-space electro-optic sampling (EOS) in a 1-mm-thick (110)-ZnTe crystal. We measured 2D double perovskites thin films deposited onto 2 mm thick z-cut quartz. During OPTP measurements, the THz emission and detection optics and samples are kept under vacuum at pressures below 0.1 mbar.

External Quantum Efficiency (EQE)

EQE Measurements were performed on a homemade system with a halogen lamp, a monochromator and a silicon reference diode. The light was chopped at 330 Hz and the signal was detected through a lock-in amplifier.

In-Plane-Conductivity

Electrical in-plane conductivity was measured by constructing thin films on isolating glass substrates. For contacts, Ag was evaporated on top of the thin films, through a shadow mask with interdigitated electrode pattern (Figure 5.5a inset). Measurements were taken with a standard white light LED spectrum, calibrated to the intensity of 1 sun, and under dark conditions through a voltage sweep between -5 V and 5 V using a Keithley 2401 source meter.

Out-of-Plane-Conductivity

The electrical measurements for out-of-plane conductivity on thin films and flakes (Figure 5.5 in the main manuscript) were performed with an atomic force microscope (Jupiter Oxford) under ambient atmosphere. A conductive AFM tip (SCM-PIT-W from NanoWorlds, Width: 28 μm ; Length: 225 μm ; resonance frequency: 75kHz; force constant: 2.8 N/m) was used to contact the top side of the sample. The conducting substrate ITO was grounded with Ag paste. For the thin film samples additional top electrodes (100 nm Au, 30 μm x 30 μm) were thermally evaporated with shadow masks to increase the area of charge injection. The *IV*-curves were recorded completely by the AFM program without additional measurement equipment. Mention should be made of the quantitative values of such measurement. Many factors are preventing to read out exact values for the out-of-plane conductivity. For instance, tip degeneracy, tip pressure, surface roughness. To minimize the influence of these and other factors we performed multiple *IV*-curves at different spots while using the same tip. This enables a qualitative comparison between the materials.

Solar Cell Characterization

Current density–voltage (*JV*) characteristics were measured using a Newport OriolSol 2A solar simulator with a Keithley 2401 source meter. The devices were illuminated through a shadow mask, yielding an active area of 0.0831 cm^2 . The *JV* curves were recorded under standard AM 1.5G illumination from a xenon lamp, and calibrated to a light intensity of 100 mW cm^{-2} with a Fraunhofer ISE certified silicon diode.

Mechanical Exfoliation of the (POE)₄AgBiI₈ Crystals

The POE-Ag crystal was carefully picked up by tweezers and placed on a low adhesion tape (ELP BT-150P-LC from Nitto). A new piece of low adhesion tape was slightly pressed on the attached crystal on the tape and quickly removed. Two mirrored crystal areas on the tapes were thus created. The tapes were then pressed together and removed for 4-5 times, where each time the two tapes are slightly misplaced in order to avoid crystal areas overlapping. Then tape with exfoliated crystal was firmly pressed on a plasma cleaned ITO glass substrate. The substrate was placed on a hot plate and heated to 70 $^{\circ}\text{C}$ for 10 minutes. At the end, the tape was gently removed and the POE-Ag thin sheets remained on the substrate.

Table S5.2: Angle 2 Theta ($^{\circ}$) of the first characteristic reflection of the thin film diffractograms and its corresponding lattice spacing distance d (nm), for all eight materials. Visualization in Figure S5.1 below.

Material	First reflection 2 Theta ($^{\circ}$)	d (nm)
(NOE) ₄ AgBiI ₈	4.76	1.857
(NOP) ₄ AgBiI ₈	4.02	2.200
(POE) ₄ AgBiI ₈	3.80	2.323
(POP) ₄ AgBiI ₈	3.43	2.574
(NOE) ₄ CuBiI ₈	4.65	1.899
(NOP) ₄ CuBiI ₈	4.07	2.172
(POE) ₄ CuBiI ₈	3.86	2.291
(POP) ₄ CuBiI ₈	3.49	2.535

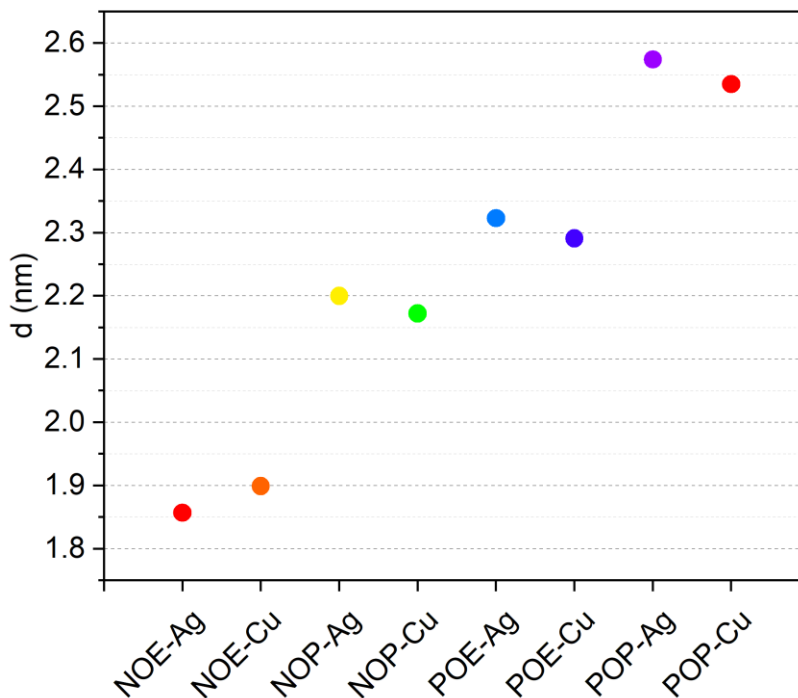
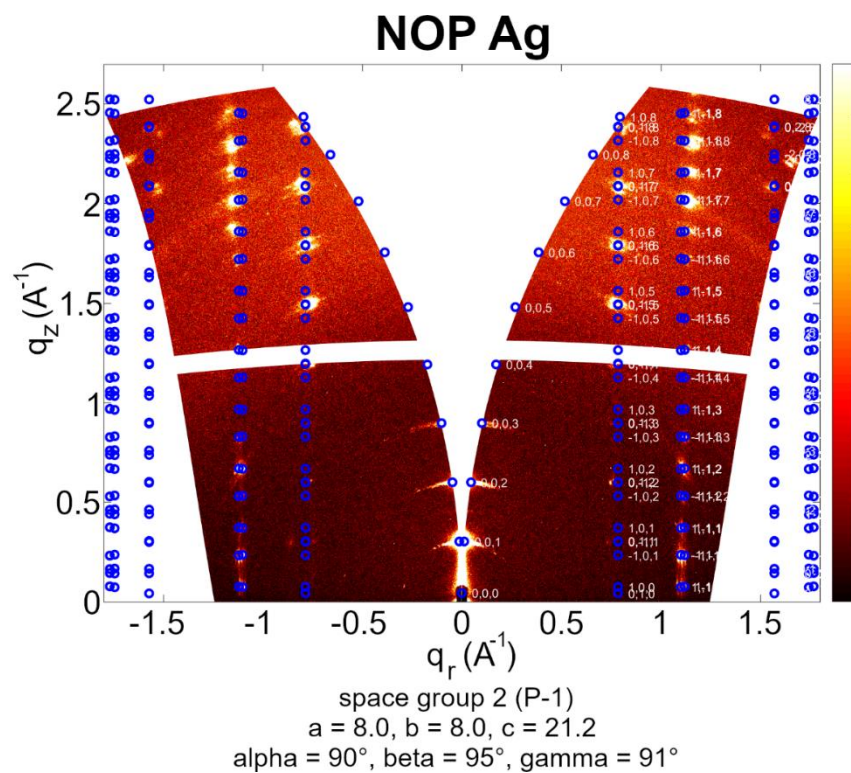
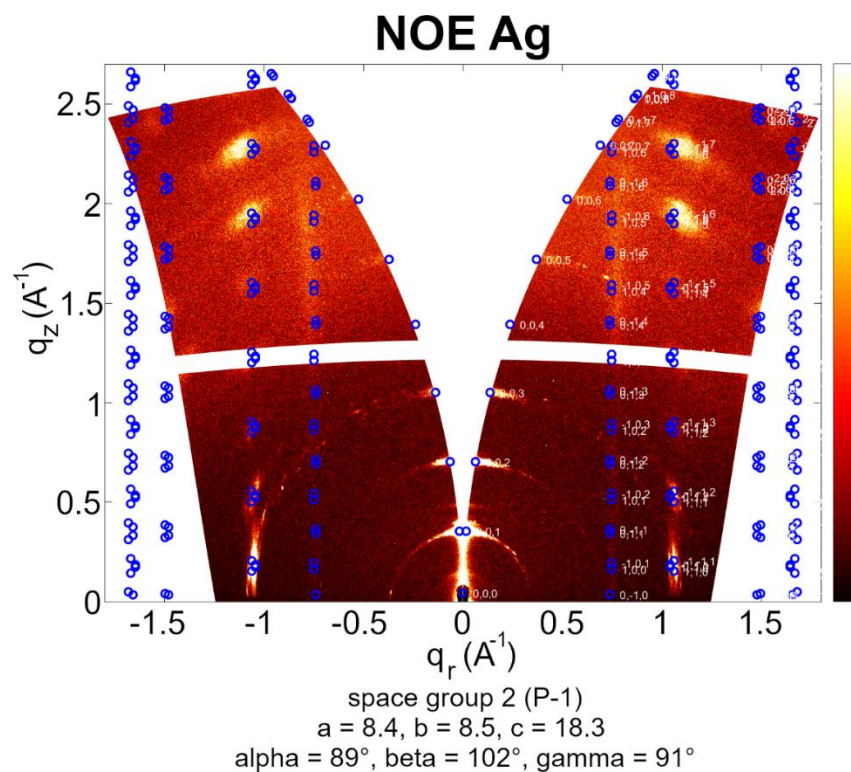


Figure S5.1: Visualization of the data in Table S5.2, the lattice spacing d (nm) of the first characteristic reflections of the thin film diffractograms of all eight materials.

The observed trend in Table S5.1 and Figure S5.1 corresponds to the increasing size of the organic bilayer due to the increasing size of NOE < NOP < POE < POP. Between two materials with the same organic cation a small difference is observable between the Ag and Cu material. While NOE-Ag < NOE-Cu, the remaining materials are the opposite, i.e. NOP-Ag > NOP-Cu, POE-Ag > POE-Cu, POP-Ag > POP-Cu. Reasons for the small differences could include different axial bond lengths in $[\text{Ag}/\text{CuI}_6]^{5-}$ octahedra, as for Ag-I they tend to be larger than for Cu-I, due to the different electronic configuration and ionic size, as well as due to the stronger Jahn-Teller distortion in Cu over Ag complexes/coordination. Furthermore, the distortion of the octahedral layers of the materials can be different. Thirdly, the organic cations have some degree of freedom regarding their orientation within the organic layer itself, which also strongly affects the lattice spacing distance.



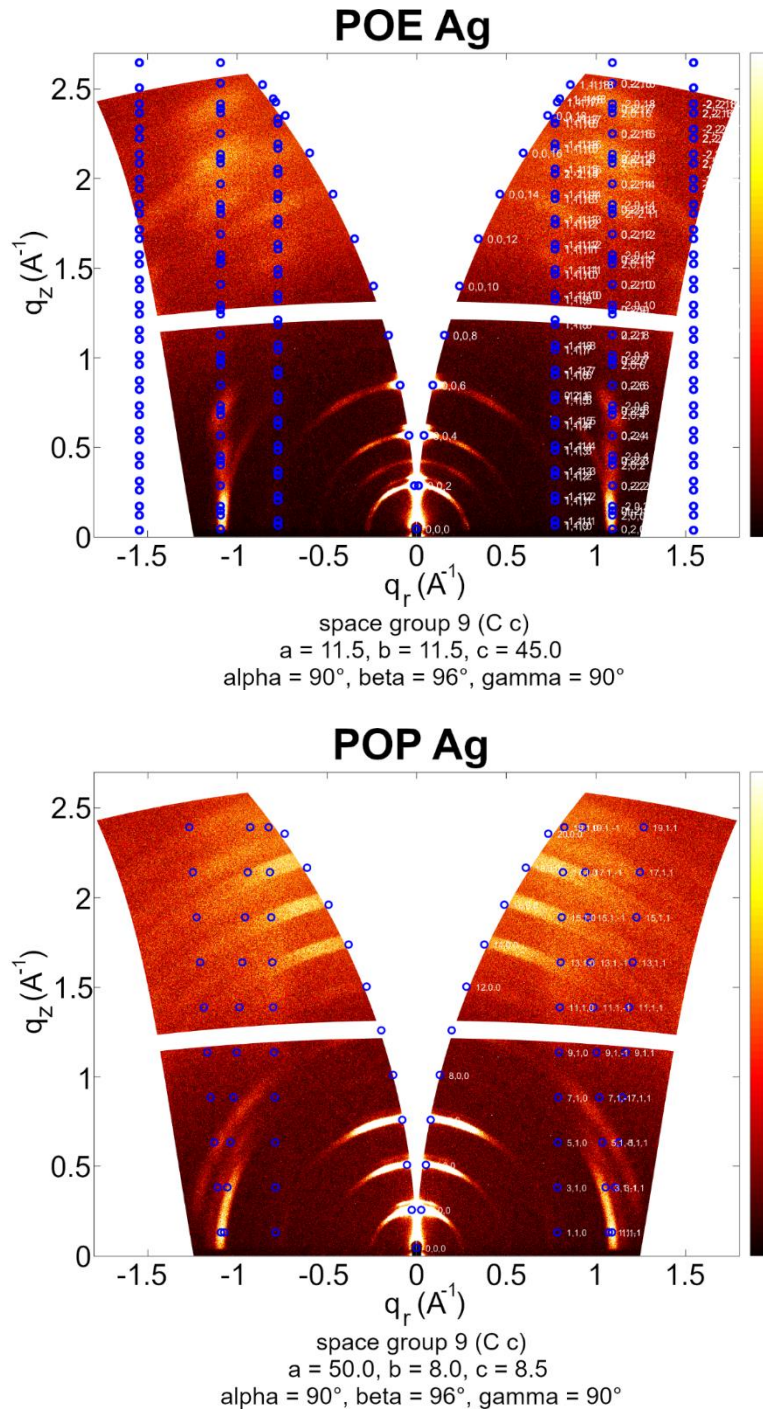
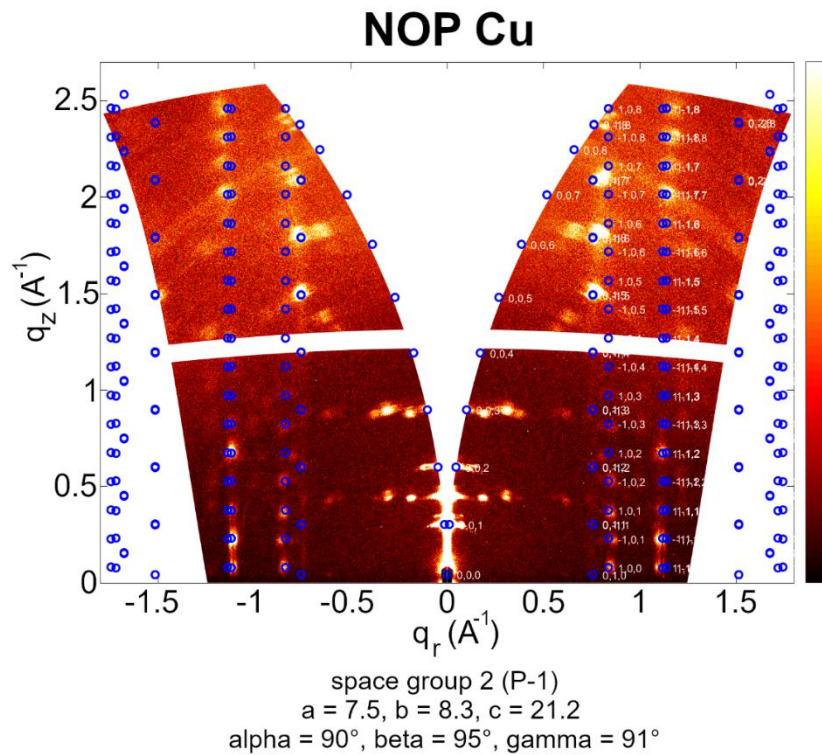
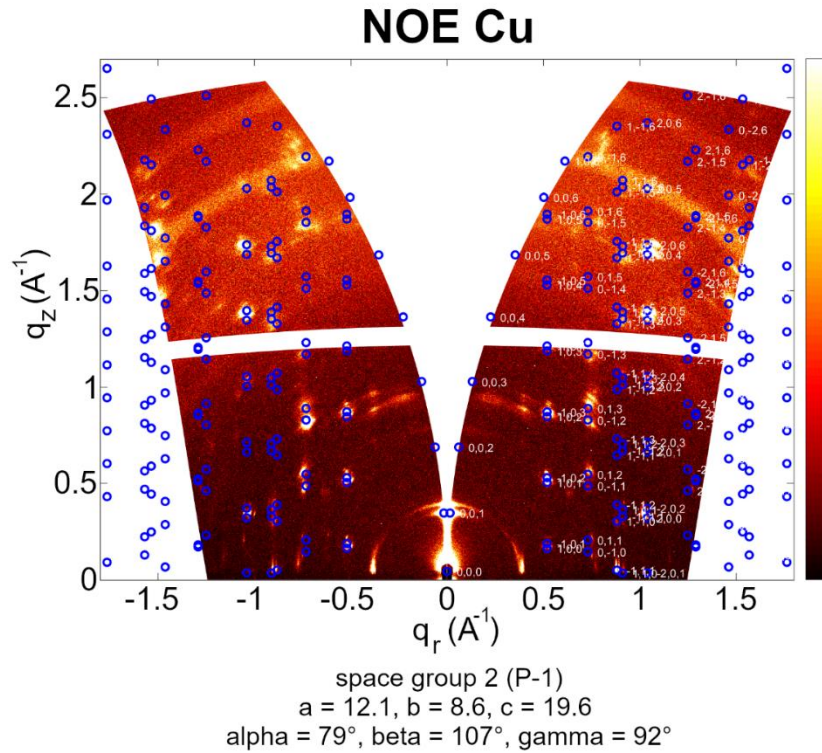


Figure S5.2: Indexed GIWAXS images for Ag-Bi materials on ITO substrates. Measurement time was 30 minutes with an incident angle $\alpha_i = 0.3^\circ$ and a sample detector distance (SDD) = 121 mm. The unit cell length parameters are given in \AA .



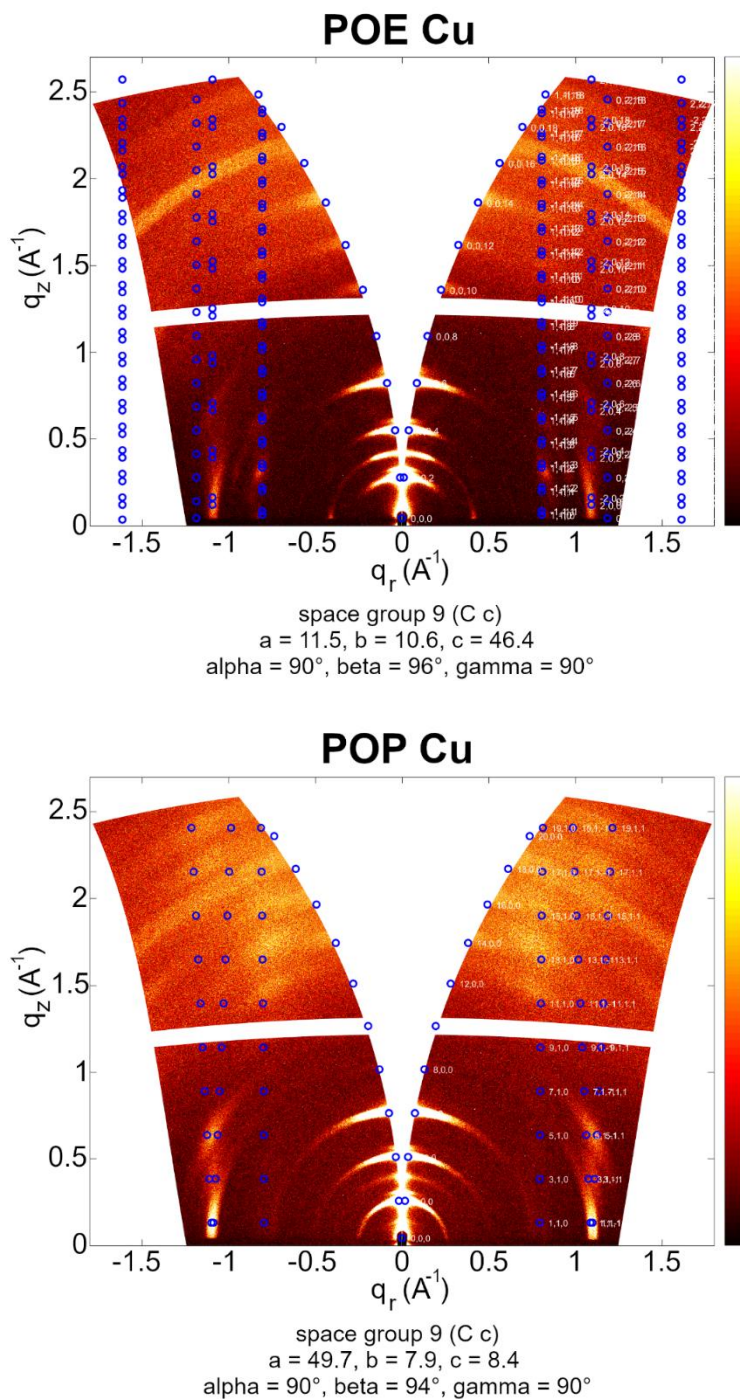


Figure S5.3: Indexed GIWAXS images for Cu-Bi materials on ITO substrates. Measurement time was 30 minutes with an incident angle $\alpha_i = 0.3^\circ$ and a sample detector distance (SDD) = 121 mm. The unit cell length parameters are given in Å.

To confirm the 2D Ruddlesden-Popper double perovskite structures, all thin films were measured and indexed according to our single crystal structure solutions from NOP-Ag, POE-Ag and POP-Ag (see CIF files or Tables S7-S8). GIWAXS signals are generally somewhat broadened, on the one hand due to the polycrystalline nature of macroscopically probed thin films and on the other hand due to the different scattering events in thin film GIWAXS under the distorted wave Born-approximation, as a result of combinations of refraction at the film surface, reflection at film/substrate interface and diffraction of the film material. This, combined with broadened reflections due to thin film quality and thermal stress exerted on thin film structures during annealing, gives an approximation of lattice parameters through indexing, but is not directly comparable to single crystal solutions and DFT optimization results. Nonetheless, the 2D RP DP structure and the well-defined thin film orientation can be confirmed for all eight materials in this work.

All resulting lattice parameters and space groups are listed below the respective GIWAXS image (Figure S5.2 and Figure S5.3). For the calculation of the diffraction positions, the lattice planes corresponding to the out-of-plane 2D orientation were chosen to be parallel to the substrate surface plane, i.e. (001) for NOE-Ag, NOP-Ag, POE-Ag, NOE-Cu, NOP-Cu and POE-Cu and (100) for POP-Ag and POP-Cu. For NOE-Ag and NOP-Ag, the calculated positions agree well with the observed signals, since the diffraction signals are well defined. For POE-Ag the orientational distribution is not as well defined as for example for NOP-Ag, but still dominantly parallel to the substrate (observable for the (002), (004) and (006) signals). This distribution can vary depending on the sample and substrate, but as shown in Figure S5.16 for the POE-Ag solar cell, it is exclusively parallel to the substrate surface. The weaker signals observable slightly above the (002), (004) and (006) diffractions are due to the scattering events that include reflection at the film/substrate surface, i.e. intrinsic to the GIWAXS measurement setup. An additional signal is observable in the middle of the (002) and (004) signals. In space group #9 Cc, the reflections where $h + l$ is odd should be extinct, here this would be the (003) reflection. This could arise due to a deviation from the ideal Cc symmetry through for example twinning or stacking faults, which in fact are very likely for these 2D RP materials, as we observed often in the growth of single crystals (Figure S5.4 and Figure S5.5). The terrace like growth along the c or out-of-plane direction can be observed in Figure S5.4a and Figure S5.5, demonstrating the proneness to stacking faults, while the twinning growth of four crystals can be observed in the polarized light microscopy image in Figure S5.4b. For POP-Ag films, less distinct oriented diffraction is observed, similar to POE-Ag, but still dominantly parallel to the substrate, indicating a mixed orientation of crystal domains in the polycrystalline film. For POE-Cu the lattice parameters show the

strongest deviations from the other materials, most notably a larger difference between parameters a and b , as well as the angle α and β . As mentioned in the main article, the absorption data and band gap value extracted for this sample being very different to the other materials, point to a different structural arrangement or octahedral bond lengths and distortions, which could explain the different lattice parameters. Single crystal analysis would be needed to further confirm this, but attempts towards growing single crystals have not been successful so far. The indexed parameters for NOE-Cu agree well with the observed diffraction pattern with a dominant orientation of the (001) direction parallel to the substrate surface, although a partial orientation vertical to the substrate can be observed for signals close to the (001) diffraction, at $q_r = -0.4 \text{ \AA}^{-1}$ and 0.4 \AA^{-1} . For NOP-Cu the indexed parameters also agree well with orientation parallel to the substrate, with the exception of some additional signals most notably between the (001) and (002) diffractions, and next to the (003) reflection, at $q_z = 0.4 \text{ \AA}^{-1}$ and 0.9 \AA^{-1} , respectively. For POE-Cu and POP-Cu the observed pattern again agrees well with the indexed parameters and the calculated positions, with a dominant parallel orientation but again less defined, similar to POE-Ag and POP-Ag. Both show an additional signal between the (002) and (004) reflection for POE-Cu and between (200) and (400) for POP-Cu, as also observed for POE-Ag and NOP-Cu, probably due to crystal twinning, as discussed before and shown in Figure S5.4.

Overall, the 2D RP DP structures and the (predominantly) parallel orientations of the 2D perovskite sheets on the substrates can be confirmed, as required for the study addressing the anisotropic electrical conductivity.

Single Crystal Growth

Single crystals of NOP-Ag, POE-Ag and POP-Ag were obtained through a vapor diffusion method of dichloromethane (DCM) into γ -butyrolactone (GBL) solutions of the 2D DPs. Similar methods were attempted for the other five materials, but were unsuccessful for different reasons. Due to the different alkyl linkage chain length, NOE and POE are more soluble compared to NOP and POP, because of which we could not recrystallize NOE-Ag-solutions successfully. Furthermore, Cu-Bi based material organic solutions showed signs of degradation, i.e. a color change to dark red, possibly linked to the oxidation of Cu^+ . Crystallization attempts from concentrated aqueous hydroiodic acid were also unsuccessful, due to the strong hydrophobicity of all organic cations.

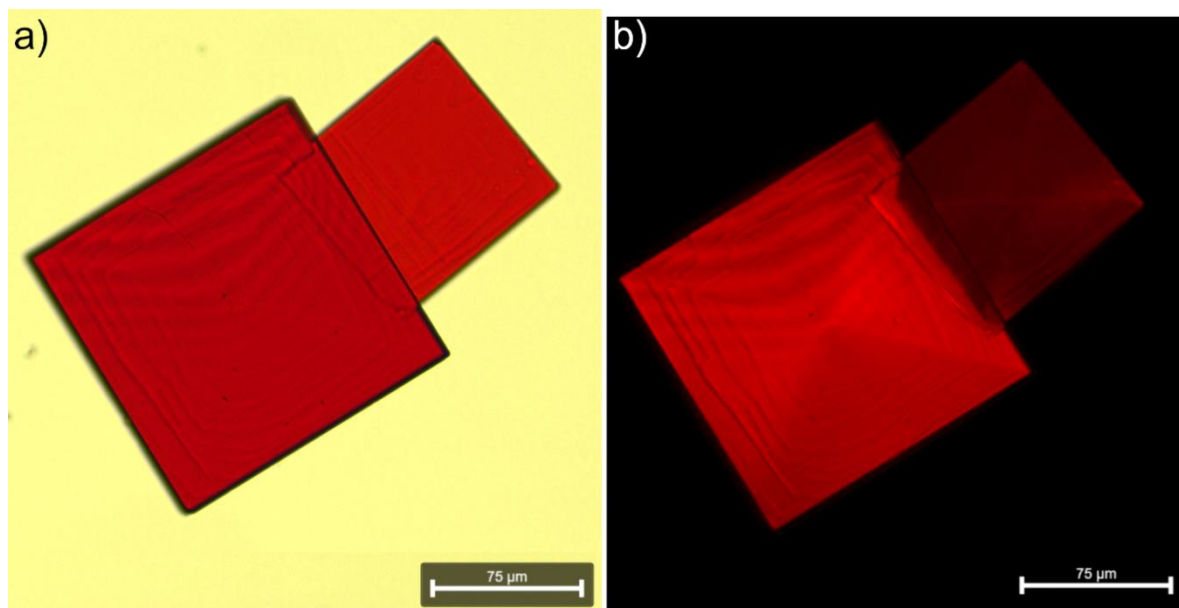


Figure S5.4: Optical light microscopy images of POE-Ag single crystals with transmission lighting a) without and b) with polarization filter. In b) the twinning of four crystals can be observed with a fourfold rotational axis originating in the center of the crystal.

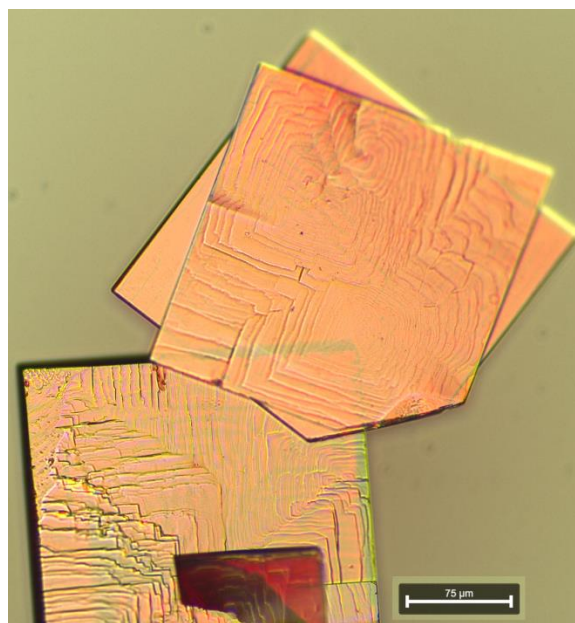


Figure S5.5: Optical light microscopy image of POE-Ag single crystals with transmission lighting, showing the terrace like growth in the c or out-of-plane direction.

The micrographs in Figure S5.4 and Figure S5.5 show the issue with the quality of the single crystal structure solution for POE-Ag. The proneness to twinning (Figure S5.4b) and stacking faults (Figure S5.5) result in broadened diffraction signals. The crystal structure was hence refined by theoretical calculations as shown in Table S5.3 and the appended CIF-file for the optimized POE-Ag structure.

Overcoming Intrinsic Quantum Confinement and Ultrafast Self-Trapping in Ag-Bi-I and Cu-Bi-I Based 2D Double Perovskites through Electroactive Cations

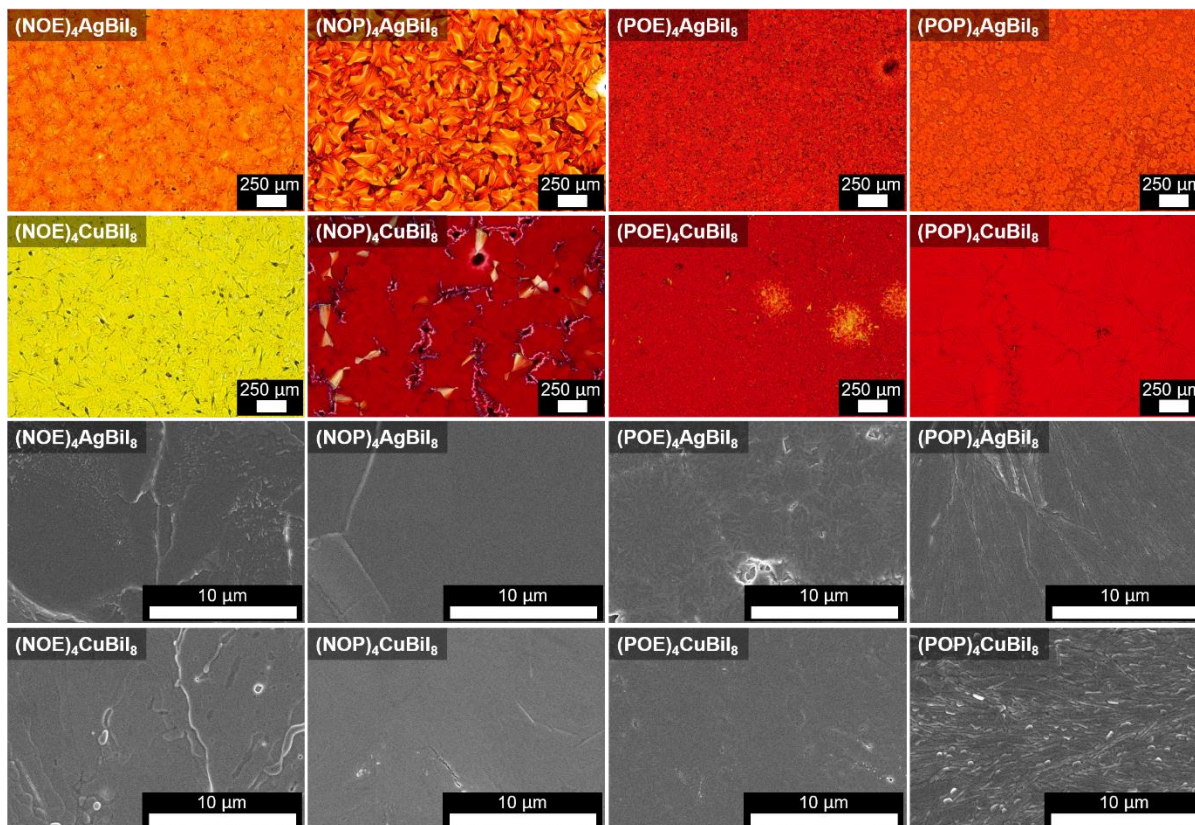


Figure S5.6: Optical visible light (top) and scanning electron (bottom) micrographs of all eight materials synthesized as thin films on ITO substrates.

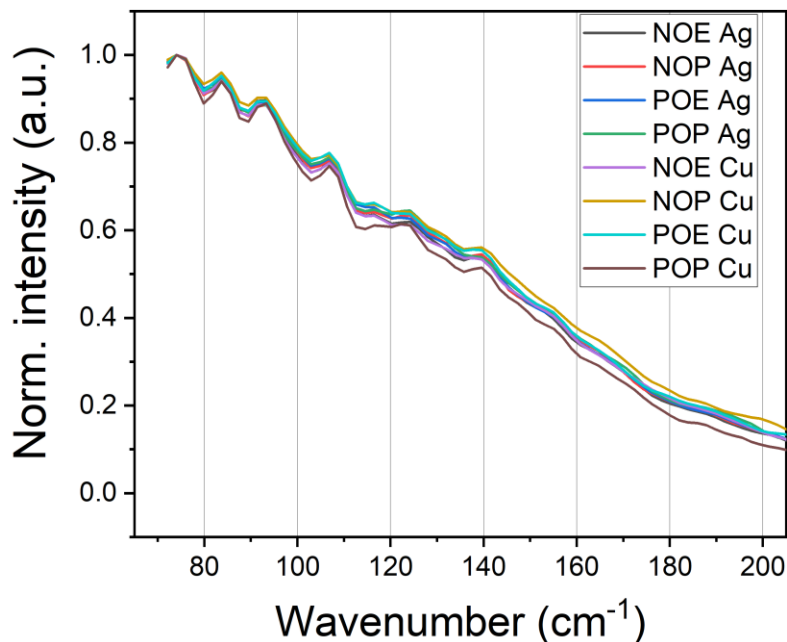


Figure S5.7: Raman spectra for all eight materials indicating the similar phonon modes and inorganic framework structures being present.

Recently, first detailed Raman studies of 2D double perovskites have been published with special focus on the electron-phonon coupling to gain insight into the crystal structure and possible phase transitions.^[18,19] Although we cannot provide such detailed investigations, our room temperature Raman measurements in the 70-200 cm⁻¹ region, where information about the lattice modes would be visible, feature the same peak positions and similar relative intensities for all 8 materials. Thus, indicating similar phonon bands of the inorganic lattice.

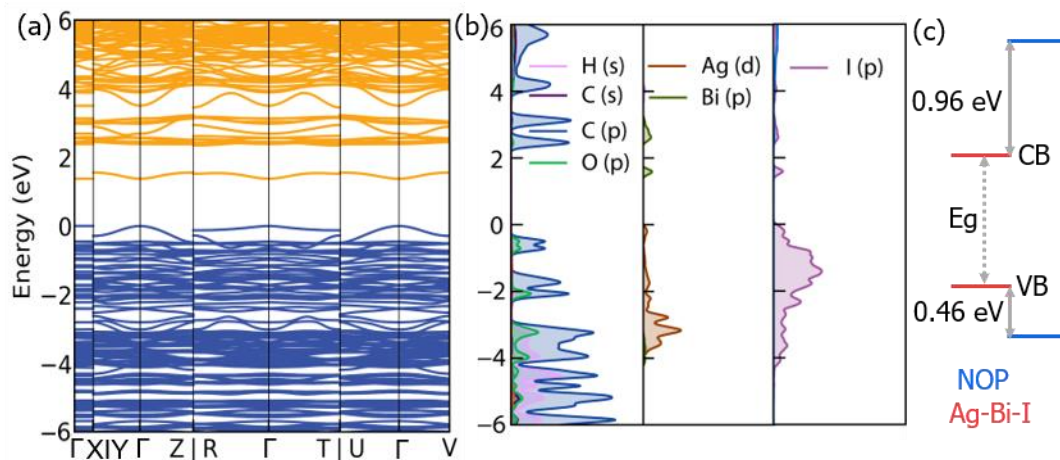


Figure S5.8: a) PBE+SOC calculated band structure with b) the partial density of states and c) the band alignment for NOP-Ag.

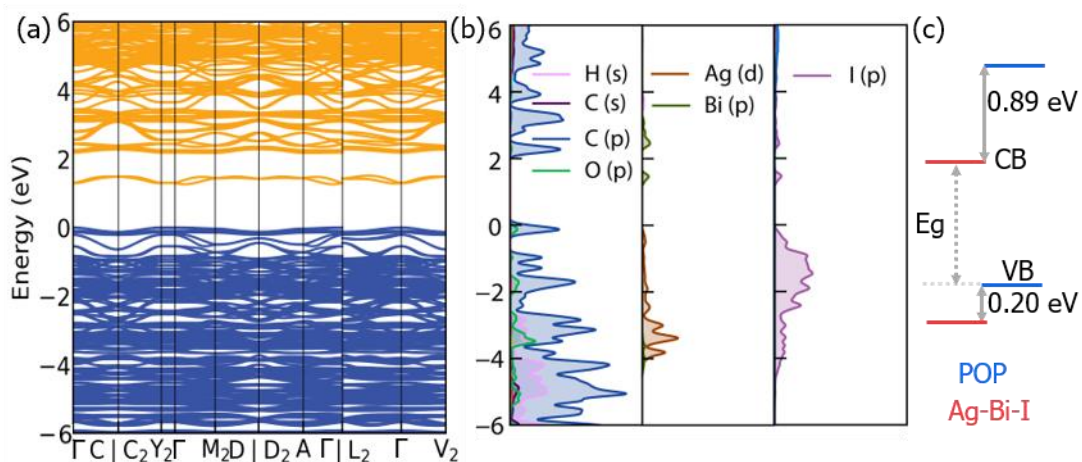


Figure S5.9: a) PBE+SOC calculated band structure with b) the partial density of states and c) the band alignment for POP-Ag.

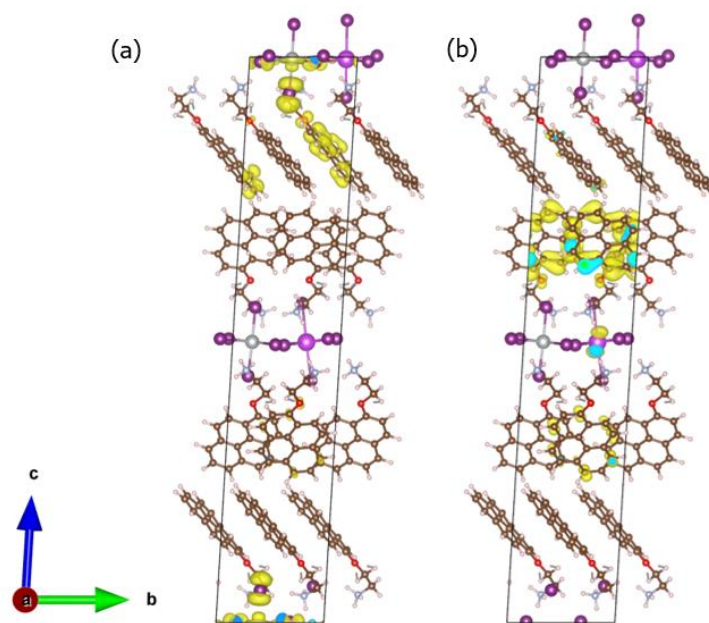


Figure S5.10: The partial charge density for the (a) overlapping states below the VB and (b) overlapping states above the CB in POE-Ag. The yellow contours show the isosurface of the norm squared wave-function with the isovalue at 0.0005.

Table S5.3: Lattice parameters of NOP-Ag, POE-Ag, POP-Ag from theoretical optimization (ISIF 3) and experimental single crystal solutions.

	Theo.	Expt.
	a, b, c (Å); α , β , γ ($^\circ$); space group (#)	a, b, c (Å); α , β , γ ($^\circ$); space group (#)
NOP-Ag	22.556, 8.913, 7.908; 89.828, 98.333, 90.632; P-1 (#2)	22.526, 8.931, 8.163 90.220, 95.284, 90.415; P-1 (#2)
POE-Ag	8.707, 8.707, 46.665; 86.309, 93.691, 89.701; Cc (#9)	8.786, 8.786, 47.097; 85.491, 94.509, 90.138; Cc (#9)
POP-Ag	51.964, 8.033, 9.129 90.000, 94.523, 90.000; C2 (#5)	52.957, 8.162, 9.117 90.000, 94.641, 90.000; C2 (#5)

Overcoming Intrinsic Quantum Confinement and Ultrafast Self-Trapping in Ag-Bi-I and Cu-Bi-I Based 2D Double Perovskites through Electroactive Cations

Table S5.4: PBE and PBE+SOC calculated and experimental band gaps of NOP-Ag, POE-Ag, POP-Ag.

	PBE (eV)	PBE+SOC (eV)	Expt.(eV)
NOP-Ag	1.9920	1.3791	2.18
POE-Ag	1.7688	1.0938	2.15
POP-Ag	1.8161	1.2620	2.19

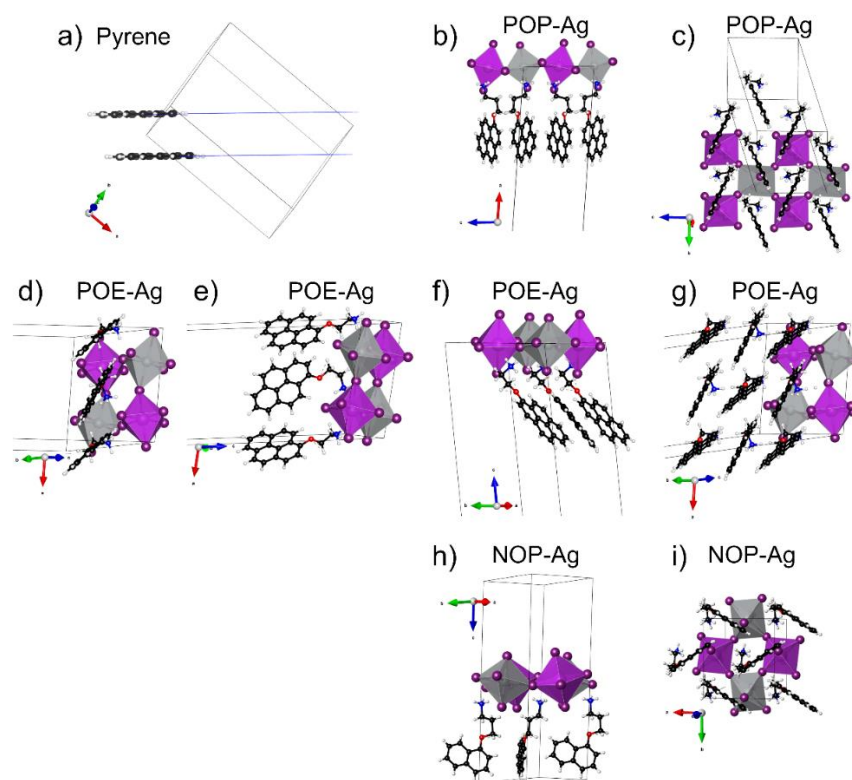


Figure S5.11: Comparison of the molecular alignment of a) crystalline pyrene to the organic cation alignment in b) and c) of POP-Ag; d-g) of POE-Ag and h) and i) of NOP-Ag. b) f) and h) highlight a similar point of view for the organic half-layer arrangement from the side for POP-Ag, POE-Ag and NOP-Ag. c), g) and i) highlight a similar point of view for the organic half-layer arrangement from below for POP-Ag, POE-Ag and NOP-Ag. d) and e) highlight the face-face arrangement of POE-Ag cations in one column of the organic half-layer, most closely resembling that of pyrene in a), potentially giving rise to π - π interactions, compared to POP-Ag and NOP-Ag where the arrangement show angles which make π - π interaction unlikely, i.e. POP-Ag showing a herringbone arrangement (c) and NOP-Ag showing almost 90° angles between naphthalene moieties (h and i).

Overcoming Intrinsic Quantum Confinement and Ultrafast Self-Trapping in Ag-Bi-I and Cu-Bi-I Based 2D Double Perovskites through Electroactive Cations

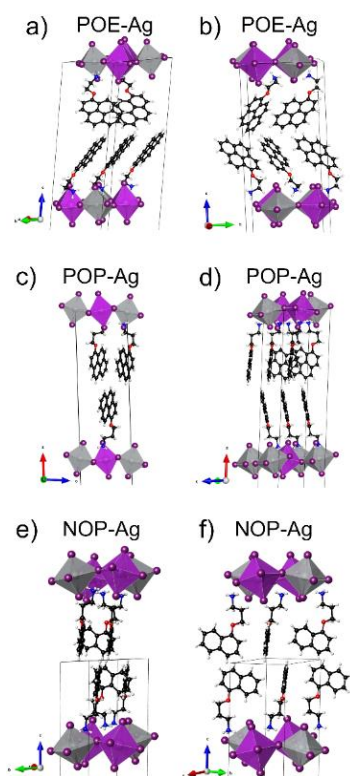


Figure S5.12: Comparison of the organic bilayer and intralayer arrangement for POE-Ag in a) and b), for POP-Ag in c) and d) and for NOP-Ag in e) and f). While POE-Ag displays an edge-face arrangement within the organic bilayer, shown to be favorable for orbital coupling and charge transport, POP-Ag and NOP-Ag display an edge-edge arrangement, shown to be unfavorable for orbital coupling and charge transport.^[1]

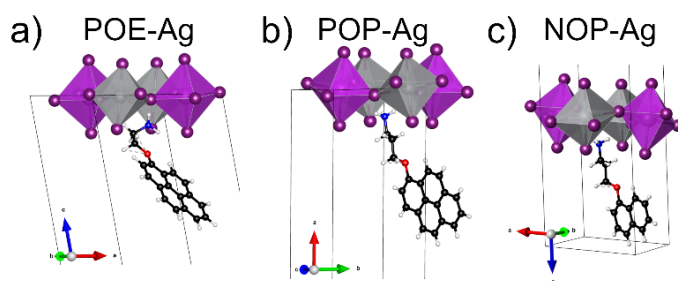


Figure S5.13: Comparison of the proximity of the pyrene and naphthalene moieties in a) POE-Ag, b) POP-Ag and c) NOP-Ag, to the inorganic octahedral lattice, highlighting the different angle, being almost 45° for POE-Ag and almost 90° for POP-Ag and NOP-Ag, which should further lead to an increased orbital overlap for POE-Ag. Moreover, this depiction highlights the different conformation of the ethyl- vs. the propyl-linkage moieties.

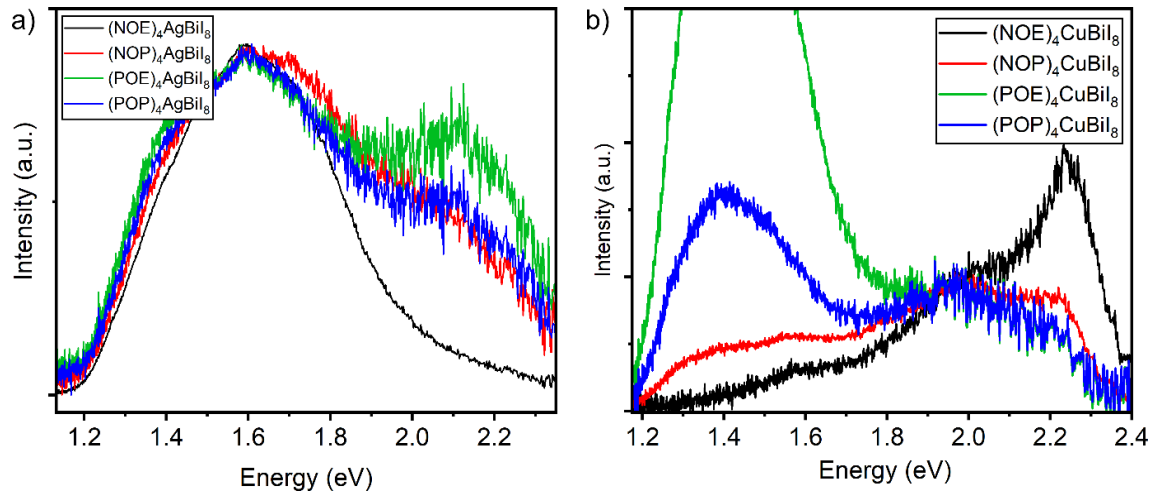


Figure S5.14: a) PL steady state spectra normalized at 1.6 eV for the Ag-Bi materials, highlighting the similar emission shape of the first feature at 1.6 eV and the different ratios of the first to the second feature at 2.1 eV. b) PL steady state spectra normalized at 1.97 eV for the Cu-Bi materials, for better comparison of the emissive features, as discussed in the main text.

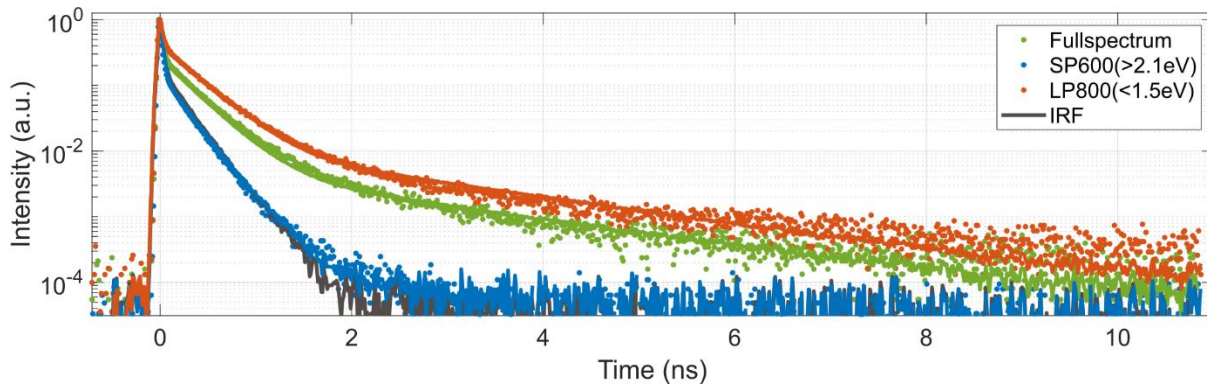


Figure S5.15: PL transients of POE-Ag at room temperature with full spectrum (green), short-pass filter 600 nm (blue) and long-pass filter 800 nm (red). Solid lines represent tri-exponential function fits to the data with lifetime parameters $\tau_1 < 10$ ps, $\tau_2 = 280$ ps, and $\tau_3 = 2$ ns. The fitted tri-exponential model function was convoluted with the instrument response function (IRF) of the setup (grey curve). Note that the lifetime parameters are slightly different to the values reported in table S5, but still on the same order of magnitude. This is due to the fact that here (S5.15) an exfoliated crystal flake of POE-Ag was measured compared to the thin film samples on glass measured in tables S5.5 and S5.6.

Overcoming Intrinsic Quantum Confinement and Ultrafast Self-Trapping in Ag-Bi-I and Cu-Bi-I
Based 2D Double Perovskites through Electroactive Cations

The transient PL spectra were fitted according to a triexponential decay function shown below:

$$f(t) = A_1 e^{-\frac{t}{\tau_1}} + A_2 e^{-\frac{t}{\tau_2}} + A_3 e^{-\frac{t}{\tau_3}}$$

Table S5.5: Transient PL fit parameters for Ag-Bi materials. Due to the IRF being 28 ps, the first, ultrafast component has a large standard deviation. Nonetheless, the fast process happens on timescales ≤ 20 ps.

	NOE-Ag	NOP-Ag	POE-Ag	POP-Ag
$A_1/\text{sum}(A_1)$	0.97	0.99	0.99	0.99
$A_2/\text{sum}(A_2)$	0.03	0.006	0.01	0.01
$A_3/\text{sum}(A_3)$	0.001	2E-5	6E-4	3E-4
τ_1 (ns)	0.01 \pm 0.01	0.02 \pm 0.01	0.01 \pm 0.01	0.01 \pm 0.01
τ_2 (ns)	1.241 \pm 0.06	0.419 \pm 0.06	0.538 \pm 0.06	0.442 \pm 0.06
τ_3 (ns)	2.44 \pm 0.5	6.51 \pm 0.5	3.80 \pm 0.5	3.89 \pm 0.5

Table S5.6: Transient PL fit parameters for Cu-Bi materials. Due to the IRF being 28 ps, the first, ultrafast component has a large standard deviation. Nonetheless, the fast process happens on timescales ≤ 20 ps.

	NOE-Cu	NOP-Cu	POE-Cu	POP-Cu
$A_1/\text{sum}(A_1)$	1	1	0.98	0.99
$A_2/\text{sum}(A_2)$	4E-4	4E-5	0.02	0.01
$A_3/\text{sum}(A_3)$	2E-5	5E-6	3E-5	1E-5
τ_1 (ns)	0.01 \pm 0.01	0.01 \pm 0.01	0.01 \pm 0.01	0.01 \pm 0.01
τ_2 (ns)	0.681 \pm 0.06	0.819 \pm 0.06	0.952 \pm 0.06	0.620 \pm 0.06
τ_3 (ns)	5.36 \pm 0.5	5.45 \pm 0.5	8.33 \pm 0.5	5.28 \pm 0.5

Analysis of the Remote Detected Time Resolved Emission Data

From remote detected time resolved PL, the diffusion coefficient is extracted via a 2 Gaussian fit for every step. One Gaussian with a fixed width is representing a nonmoving species which stays constant in width according to the resolution limit. The second Gaussian curve represents the diffusive excited states. Since we assumed that this is 2D diffusive transport, the change in width has the following relation:

$$\sigma^2(t) = 2Dt$$

Two time scales can be observed, one in the signal rise, the second on longer time scales, which we assign to two different species, the free ambipolar charge carriers and the polaronic excitons.

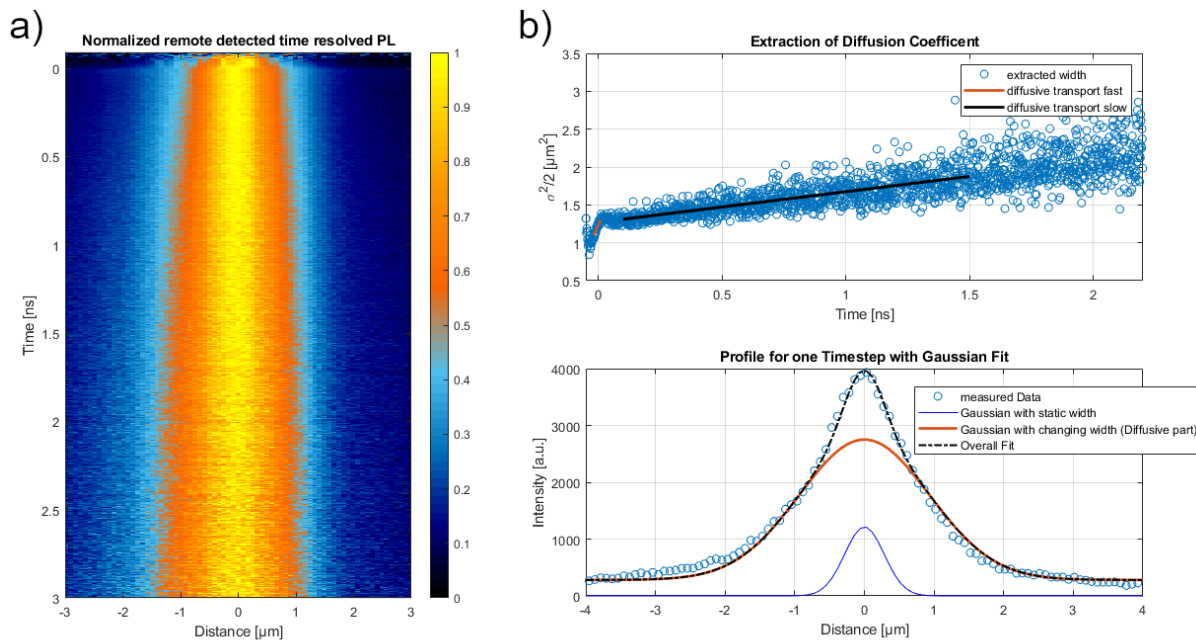


Figure S5.16: a) Normalized remote detected time resolved PL. b) Extraction of diffusion coefficient and the Gaussian fit used for the extraction as described above.

Extraction of Charge-Carrier Mobility from OPTP Measurements

We extracted effective charge-carrier mobility from OPTP measurement following the procedure developed by Wright et al. and Buizza et al.^[16,20] The method is based on the approach developed by Wehrenfennig et al.^[21] to estimate charge-carrier mobilities in semiconductor thin films. Briefly, for semiconducting materials with thicknesses smaller than the wavelength of the incident THz radiation, we can retrieve the sheet photoconductivity from the fractional change in the transmitted THz electric field $\Delta T/T$, and we can express it as

$$\Delta S = -\epsilon_0 c (n_1 + n_3) \left(\frac{\Delta T}{T} \right) \quad (\text{S1})$$

where $n_3 = 2.13$ and $n_1 = 1$ are the refractive indexes of quartz and vacuum, respectively.^[22] Here, in order to derive the effective charge-carrier mobility from the sheet photoconductivity, we need to estimate the number of initially photogenerated carriers, defined as:

$$N = \phi \frac{E\lambda}{hc} (1 - R_{pump} - T_{pump}) \quad (\text{S2})$$

where ϕ is the photon-to-charge branching ratio (i.e., the fraction of generated charges per absorbed photon absorbed), E is the pump pulse energy, λ is the excitation wavelength, and R_{pump} and T_{pump} are the reflectance and transmittance of the sample at the excitation wavelength (400 nm, 3.1 eV). Here, Equation S1 and Equation S2 can be used to extract the charge-carrier mobility μ as

$$\mu = \frac{\Delta S A_{eff}}{Ne} \quad (\text{S3})$$

where A_{eff} is the effective overlap area between THz and pump beam and e is the elementary charge. By substituting Equation S1 and Equation S2 into Equation S3, we obtain the effective (i.e., multiplied by the photon-to-charge branching ratio) charge-carrier mobility as:

$$\phi\mu = -\epsilon_0 c (n_q + n_v) \frac{A_{eff} hc}{eE\lambda(1 - R_{pump} - T_{pump})} \left(\frac{\Delta T}{T} \right) \quad (\text{S4})$$

We note that the sheet photoconductivity signal measured by OPTP arises from the contributions of both photogenerated free electrons and holes. Therefore, the extracted charge-carrier mobility is the effective electron-hole sum mobility.

To better capture the effect of charge carrier localization processes on charge-carrier mobilities in emerging metal halides, Wright and Buizza developed a two-level mobility model.^[16,20] In this model, described in detail in References ^[20] and ^[16], the photoconductivity of the material is defined as the sum of photoconductivity for two different states: a delocalized state and a localized state with population and mobility (n_{del}, μ_{del}) and (n_{loc}, μ_{loc}) , respectively. Assuming a predominantly monomolecular recombination from the localised state, the carrier population is defined by the following set of coupled rate equations:

$$\begin{cases} \frac{dn_{del}}{dt} = -k_{loc}n_{del}(t) \\ \frac{dn_{loc}}{dt} = k_{loc}n_{del}(t) - k_1n_{loc}(t) \end{cases} \quad (S5)$$

Here, k_{loc} and k_1 are the localization and monomolecular recombination rates, respectively. As described in details in Refs.^[20] and ^[16], the resulting $\Delta T/T$ signal can be described as:

$$\frac{\Delta T}{T} = -\frac{Ne}{\epsilon_0 c(n_1 + n_3)A_{eff}} \left(\left(\mu_{del} - \frac{\mu_{loc}k_{loc}}{k_{loc} - k_1} \right) e^{-k_{loc}t} + \frac{\mu_{loc}k_{loc}}{k_{loc} - k_1} e^{-k_1t} \right) \quad (S6)$$

Furthermore, to fit the experimental data reported in Figure 4c and Figure S5, we convoluted Equation S6 with a Gaussian function with broadening $\sigma = 200$ fs to account for the instrumental response function, as described in Reference ^[16]

Photoconductivity Measurements

We fabricated thin films on isolating glass substrates with top evaporated, interdigitated 100 nm Ag electrodes. The conductivity was measured through a voltage sweep from -5 V to 5 V in dark and light conditions. The illumination source was a standard white light spectrum LED, calibrated to the intensity of 1 sun. To exclude the influence of thin film morphologies, we evaluated the thin film quality in terms of homogeneity, thickness and continuity regarding large grain boundaries through optical microscopy, ensuring similar conditions. Cross section SEM images are shown in Figure S5.18, displaying continuous and homogeneous thin films. The noise or fine structure, observable for current signals below 10^{-9} A are due to the signal resolution limit of the Keithley source meter and most likely correspond to a minimal charge buildup. The fine structure is connected to the step-size of the measurement.

Overcoming Intrinsic Quantum Confinement and Ultrafast Self-Trapping in Ag-Bi-I and Cu-Bi-I Based 2D Double Perovskites through Electroactive Cations

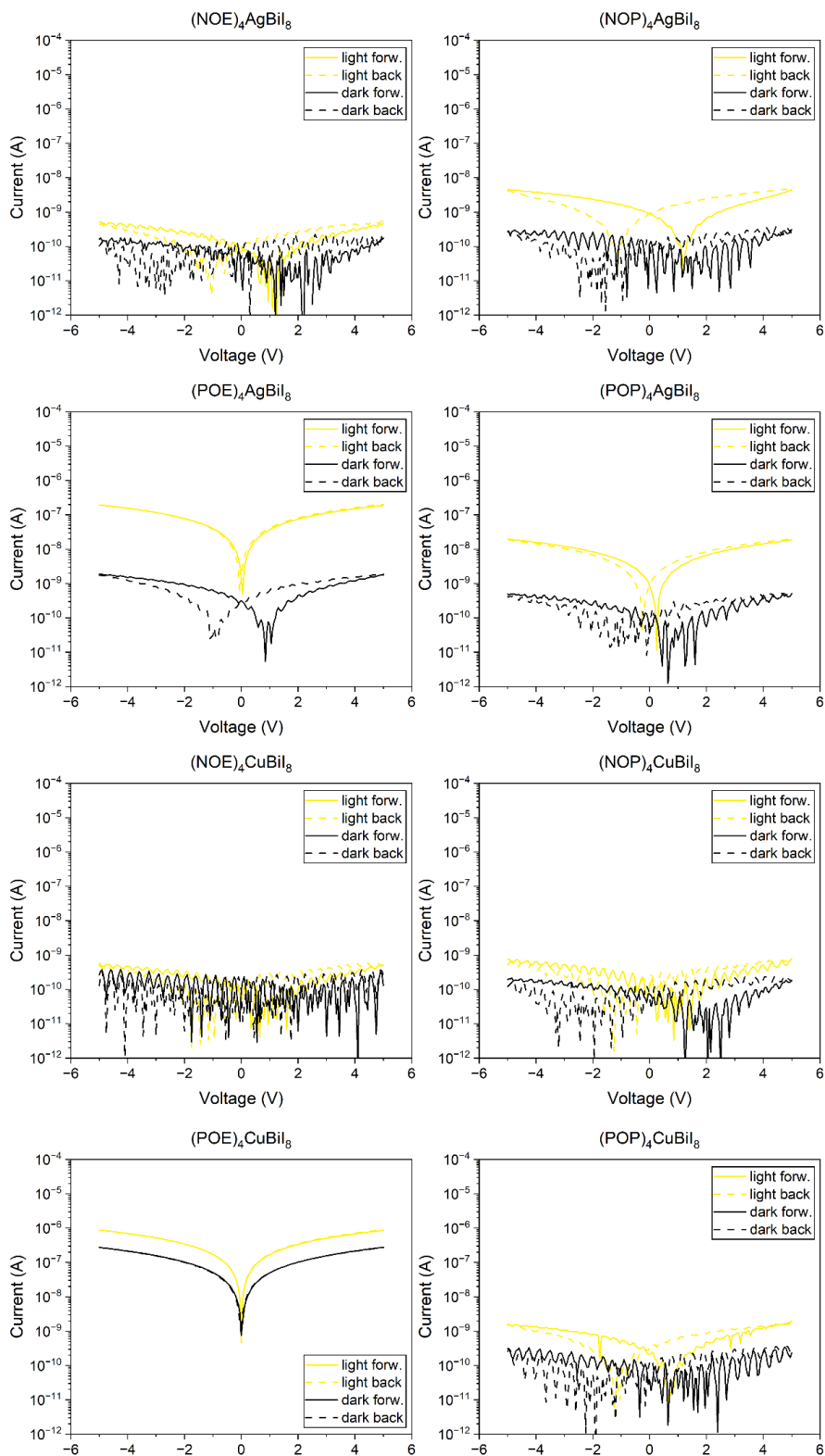


Figure S5.17: Photoconductivity IV curves for all eight materials under dark and light conditions.

Overcoming Intrinsic Quantum Confinement and Ultrafast Self-Trapping in Ag-Bi-I and Cu-Bi-I Based 2D Double Perovskites through Electroactive Cations

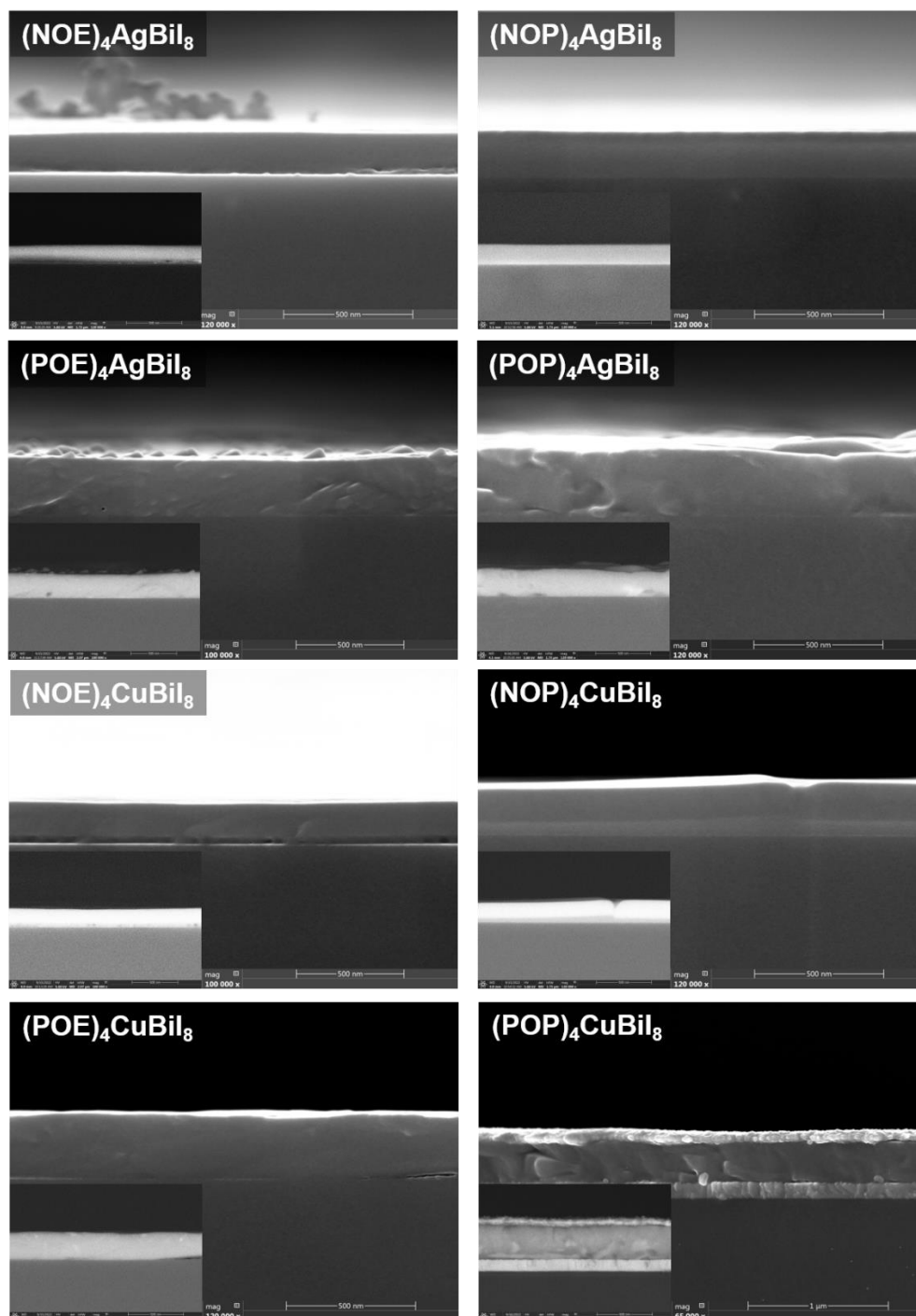


Figure S5.18: SEM cross section images for all eight materials using secondary electrons; the inset shows images obtained with back-scattered electrons. All samples show dense, continuous and homogeneous morphology, confirming the comparability for the conductivity measurements shown in Figure S5.16 for top evaporated Ag electrodes (Ag electrodes are visible in the micrograph of POP-Cu).

Overcoming Intrinsic Quantum Confinement and Ultrafast Self-Trapping in Ag-Bi-I and Cu-Bi-I Based 2D Double Perovskites through Electroactive Cations

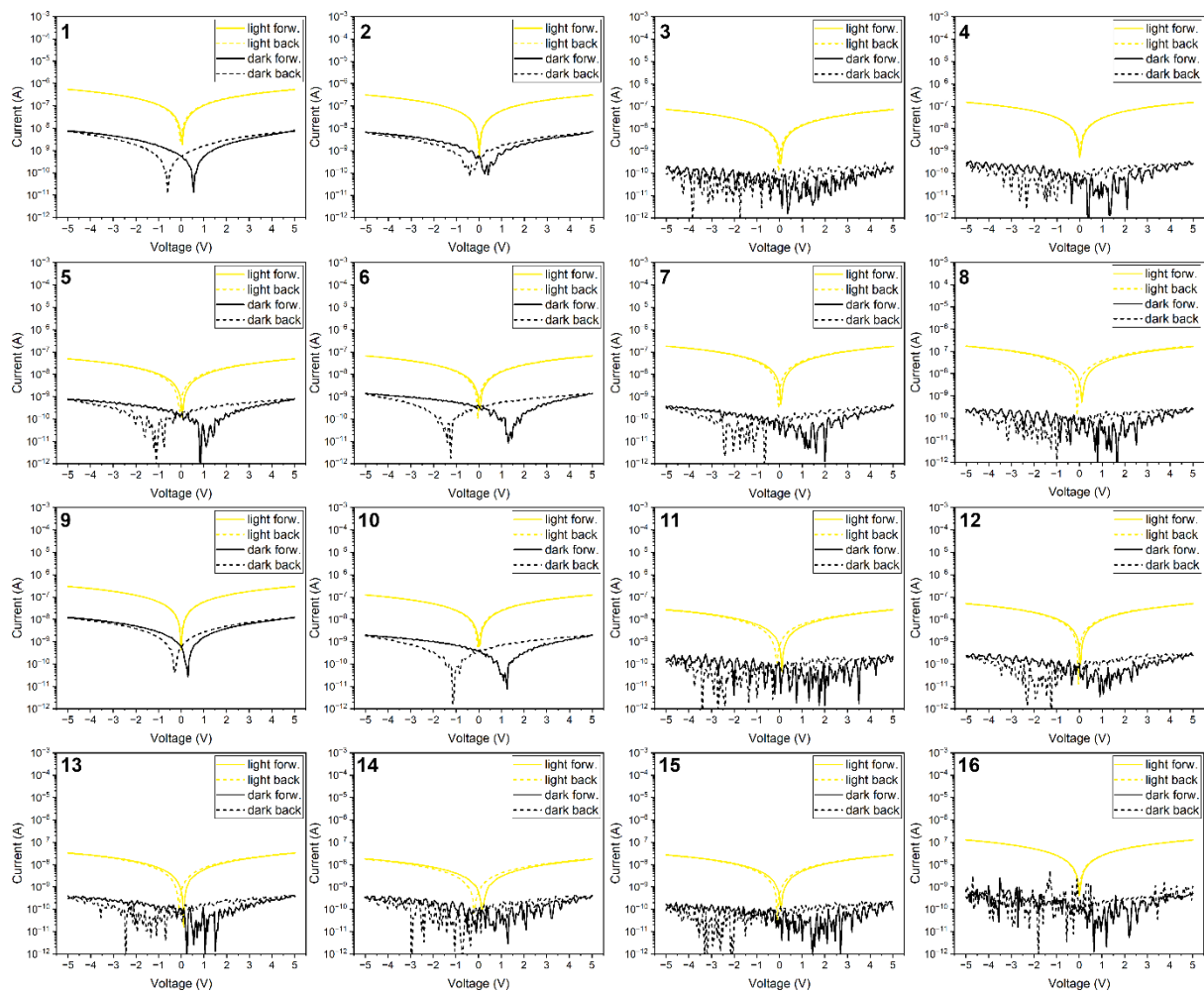


Figure S5.19: Optimization row for POE-Ag thin films for top-evaporated in-plane conductivity measurements based on different synthesis conditions shown below in Table S5.6. As evident, different synthesis parameters result in different light and dark current responses and ratios. We selected sample 7 to be the best performing sample in terms of light/dark ratio ($\times 779$), while sample 1 showed the highest absolute current response (5.04×10^{-7} A at 5V).

Overcoming Intrinsic Quantum Confinement and Ultrafast Self-Trapping in Ag-Bi-I and Cu-Bi-I Based 2D Double Perovskites through Electroactive Cations

Table S5.7: Synthesis conditions for POE-Ag thin film samples for top-evaporated in-plane conductivity measurements shown in Figure S5.19. Solvents were varied to test the different crystallization behavior. Concentrations were varied to test the influence of different thin film thicknesses. Antisolvent chlorobenzene (CB) was tested to potentially improve crystallinity and surface smoothness. Annealing temperatures and times were kept constant, to ensure the formation of the desired phase.

	Material	Solvent	c (mol/L)	AS	Annealing 1 (1 min)	Annealing 2 (5 min)
1	(POE) ₄ AgBiI ₈	DMF	0.3	-	140 °C	100 °C
2	(POE) ₄ AgBiI ₈	DMF	0.3	CB 500 μL	140 °C	100 °C
3	(POE) ₄ AgBiI ₈	DMSO DMF 1:1	0.3	-	140 °C	100 °C
4	(POE) ₄ AgBiI ₈	DMSO DMF 1:1	0.3	CB 500 μL	140 °C	100 °C
5	(POE) ₄ AgBiI ₈	GBL DMF 1:1	0.3	-	140 °C	100 °C
6	(POE) ₄ AgBiI ₈	GBL DMF 1:1	0.3	CB 500 μL	140 °C	100 °C
7	(POE) ₄ AgBiI ₈	NMP DMF 1:1	0.3	-	140 °C	100 °C
8	(POE) ₄ AgBiI ₈	NMP DMF 1:1	0.3	CB 500 μL	140 °C	100 °C
9	(POE) ₄ AgBiI ₈	DMF	0.15	-	140 °C	100 °C
10	(POE) ₄ AgBiI ₈	DMF	0.15	CB 500 μL	140 °C	100 °C
11	(POE) ₄ AgBiI ₈	DMSO DMF 1:1	0.15	-	140 °C	100 °C
12	(POE) ₄ AgBiI ₈	DMSO DMF 1:1	0.15	CB 500 μL	140 °C	100 °C
13	(POE) ₄ AgBiI ₈	GBL DMF 1:1	0.15	-	140 °C	100 °C
14	(POE) ₄ AgBiI ₈	GBL DMF 1:1	0.15	CB 500 μL	140 °C	100 °C
15	(POE) ₄ AgBiI ₈	NMP DMF 1:1	0.15	-	140 °C	100 °C
16	(POE) ₄ AgBiI ₈	NMP DMF 1:1	0.15	CB 500 μL	140 °C	100 °C

The influence of CB as antisolvent on the conductivity was negligible. The influence of the precursors concentration, i.e. the resulting thickness of the thin films, shows a decreased absolute current for thinner samples obtained from $c = 0.15$ mol/L, compared to their counterparts from $c = 0.3$ mol/L. This is another indication that POE-Ag does indeed have an out-of-plane component in its conductivity, since otherwise the film thickness should not have a large influence, as charge transport would be limited to the topmost atomic layers of the 2D DP thin films. The dark currents are very low, at the detection minimum for the employed setup, for solutions based on DMSO:DMF 1:1, and NMP:DMF 1:1 (i.e. samples 3, 4, 7, 8, 11, 12, 15, 16). Samples based on pure DMF or GBL:DMF 1:1 show increased responses, which should be based on better crystallization of the thin film. This can result in a number of factors improving the conductivity, such as improved homogeneity, fewer defects, larger crystallites or better intergrown crystallite/domain boundaries, or even slightly different orientations.

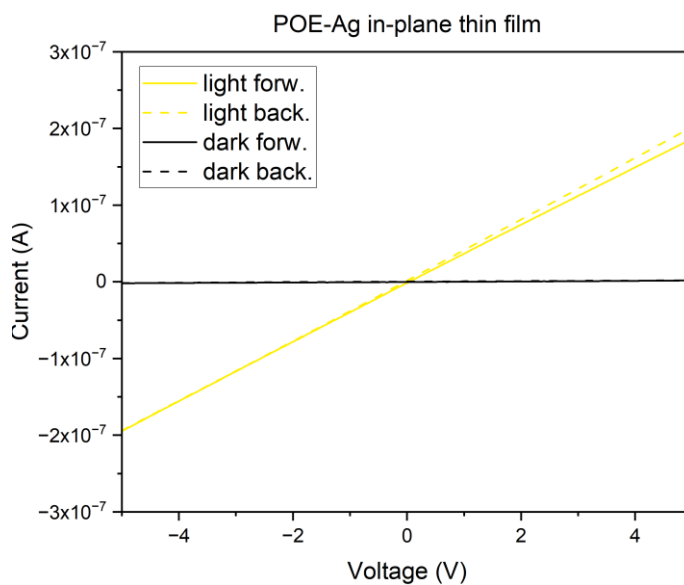


Figure S5.20: Linear IV curve plot for POE-Ag in-plane thin film samples with evaporated top Ag contacts, displaying a linear, ohmic behavior.

Out-of-Plane Conductivity

In the following figures a detailed view of the thin film out-of-plane IV curves is shown to display the characteristics.

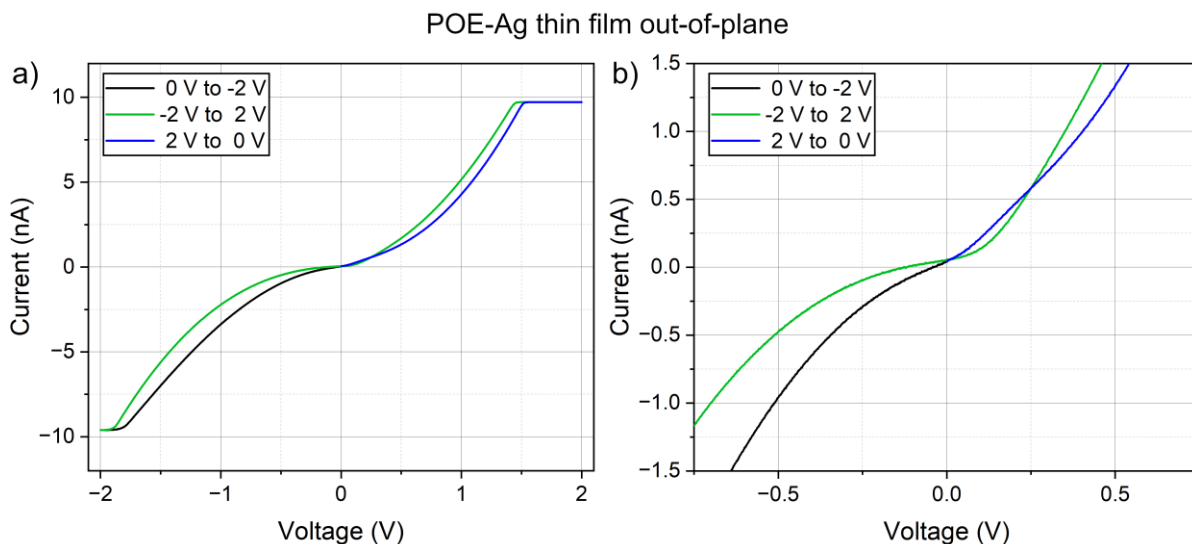


Figure S5.21: a) IV curves of POE-Ag thin film out-of-plane measurement and b) zoom-in around the axes origin, revealing the Schottky barrier type behavior.

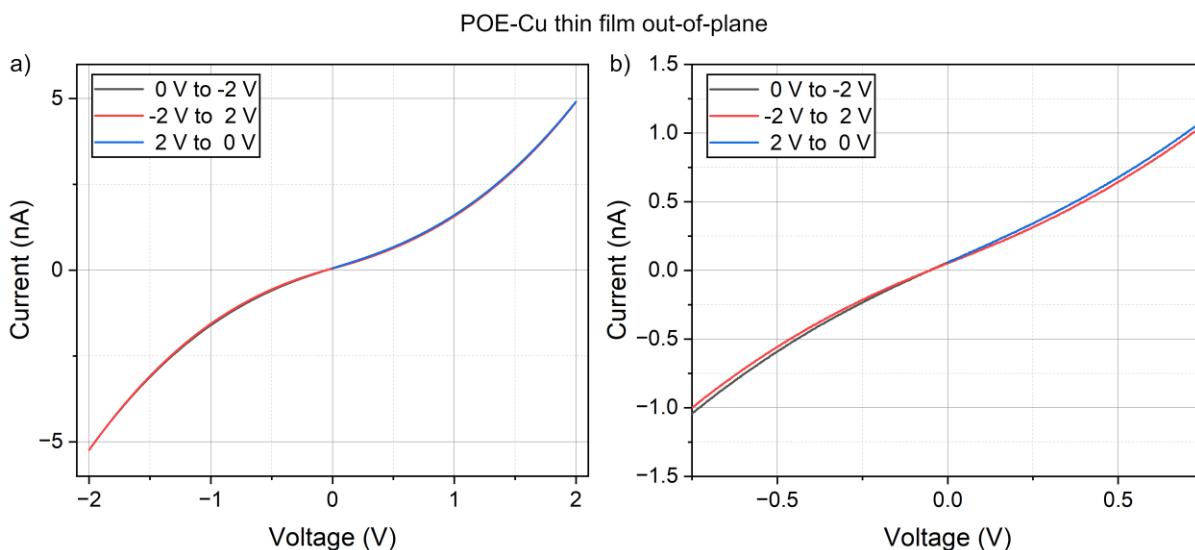


Figure S5.22: a) IV curves of POE-Cu thin film out-of-plane measurement and b) zoom-in around the axes origin. The S-shape is observable but no distinct Schottky barrier type behavior is exhibited compared to POE-Ag in Figure S5.20.

Overcoming Intrinsic Quantum Confinement and Ultrafast Self-Trapping in Ag-Bi-I and Cu-Bi-I Based 2D Double Perovskites through Electroactive Cations

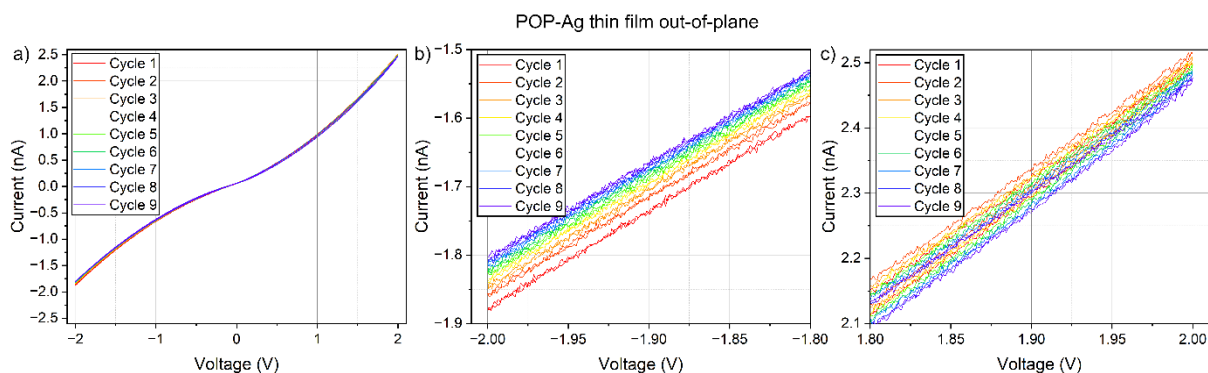


Figure S5.23: a) IV curves of POP-Ag thin film out-of-plane measurement measured for 9 cycles with zoom-in at the negative voltage maximum bias in b) and positive voltage maximum bias in c). The S-shape is observable but no distinct Schottky barrier type behavior is exhibited compared to POE-Ag in Figure S5.20. The cycling shows a very small hysteresis, observable in b) and c), where upon multiple cycles the maximum currents shift towards lower values.

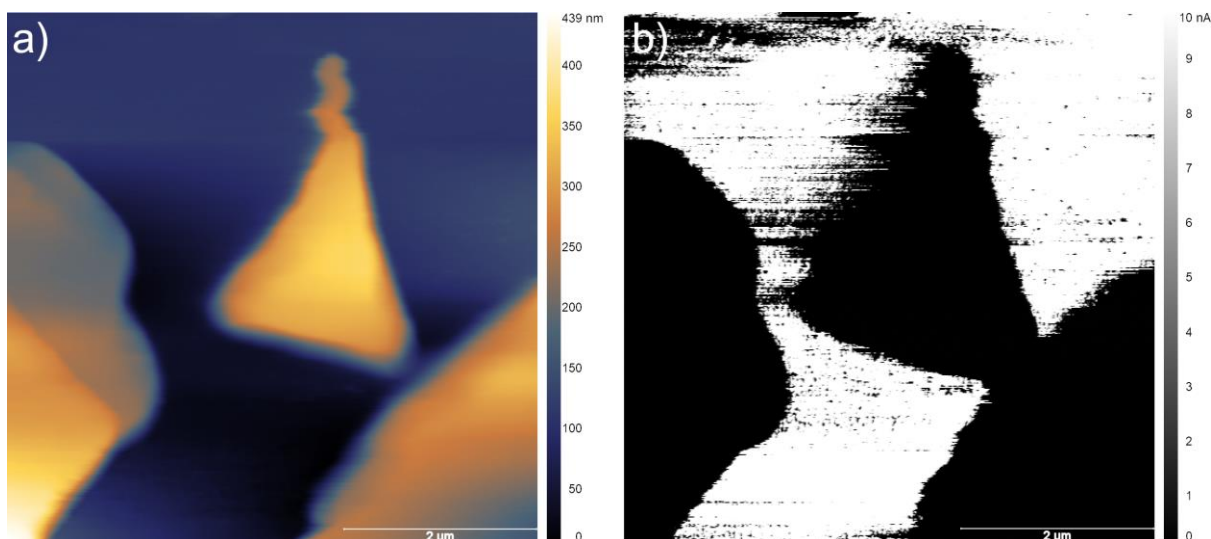


Figure S5.24: a) AFM height profile image and b) cAFM image of exfoliated 4FPEA-Ag crystals on ITO substrate. 4FPEA-Ag does not show any out-of-plane conductivity.

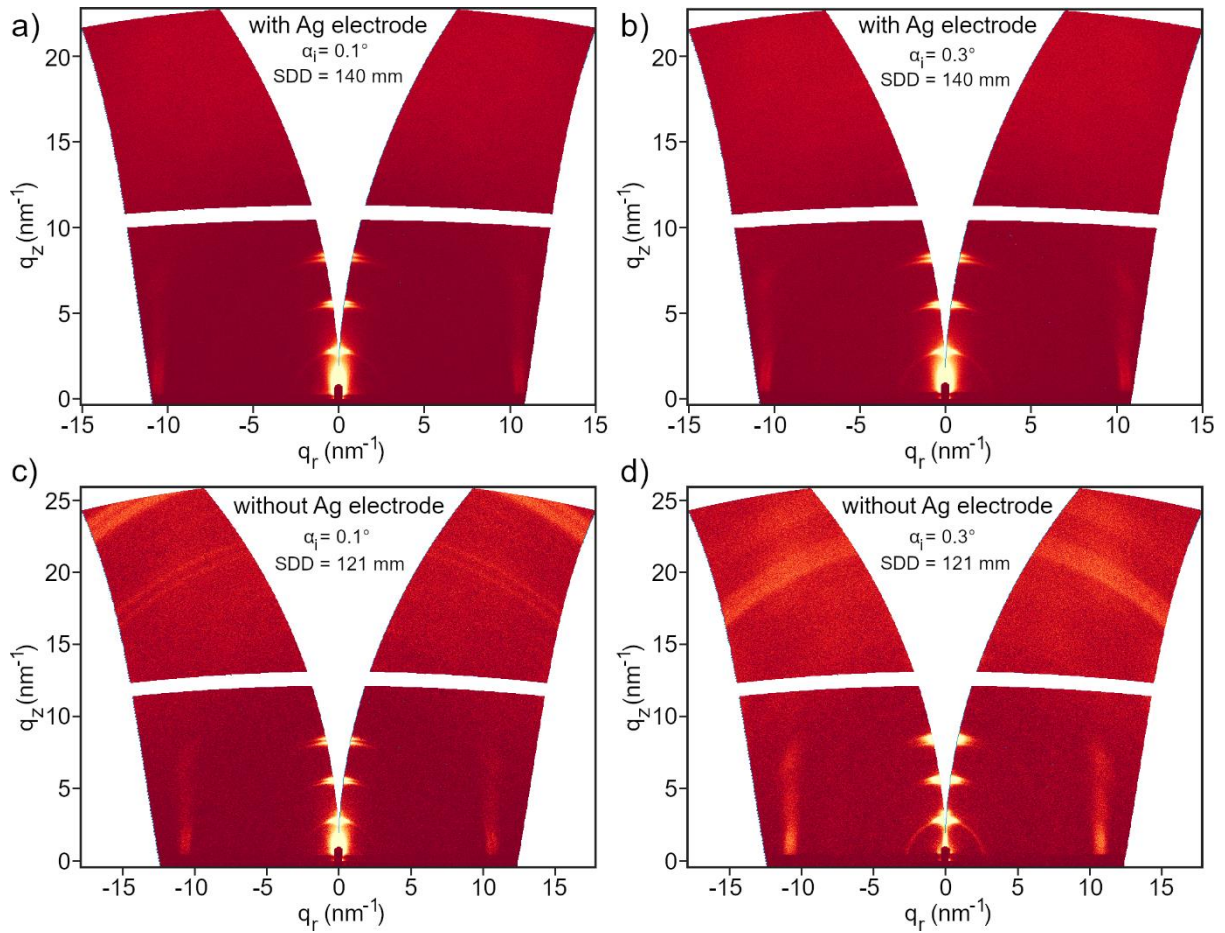


Figure S5.25: GIWAXS data of a pixel of the champion solar cell constructed with POE-Ag. Measurements were taken with at sample detector distances 121 mm and 140 mm, an incident angle of 0.3° to probe deep into the device, as well as at 0.1° to probe predominantly the surface, on two different spots with a) and b) a PCBM/silver electrode terminated surface and c) and d) only a PCBM terminated surface. As shown in Figure S5.2, independent of the depth, the 2D perovskite layer is exclusively oriented parallel to the substrate surface. Note, that for measurements taken with a silver terminated surface, the reflections split up due to the additional reflectance and scattering as the X-ray beam travels through the silver layer and an additional interface.

Overcoming Intrinsic Quantum Confinement and Ultrafast Self-Trapping in Ag-Bi-I and Cu-Bi-I Based 2D Double Perovskites through Electroactive Cations

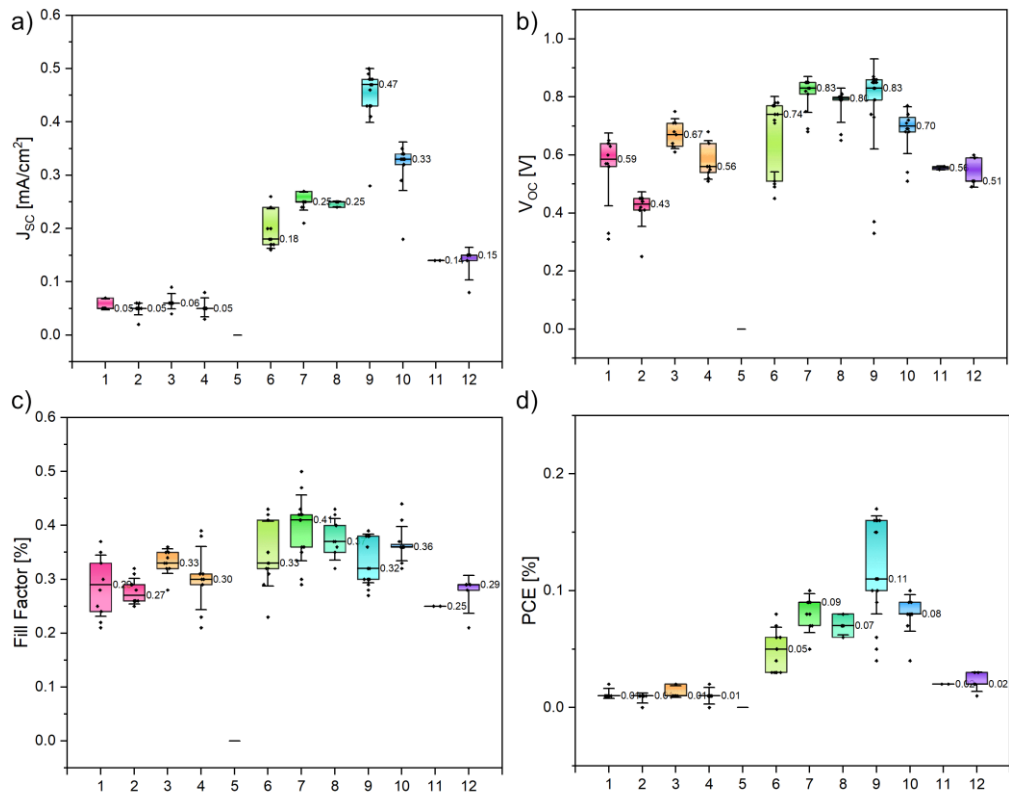


Figure S5.26: Statistical box plots of the solar cell characteristics with POE-Ag as the active layer with a) the J_{sc} , b) the V_{oc} , c) the Fill Factor and d) the power conversion efficiency. The sample numbers on the x-axis correspond to the sample synthesis conditions listed in table S5.8, primarily resulting in different thicknesses.

Solar cells were prepared on glass/ITO substrates, which were patterned by etching with zinc-powder and 3 M HCl, cleaned with a detergent followed by washing with acetone and ethanol and dried under an air stream. Before applying the hole transport layer (HTL), substrates were nitrogen plasma cleaned for 10 minutes. The HTL PTAA (Sigma-Aldrich, 2 mg/mL in 1:1 chlorobenzene/toluene, doped with 2 μ L/mL of a 1 mg/mL F4TCNQ solution in DMF) was spincoated with 60 μ L at 6000 rpm for 35 seconds and annealed at 100 $^{\circ}$ C for 5 minutes. Then PEAI (1 mg/mL DMF) was spincoated on the PTAA layer with 100 μ L at 3000 rpm for 30 seconds and annealed at 100 $^{\circ}$ C for 5 minutes. Subsequently the active layer POE-Ag was spincoated as specified in Table S5.8. The electron transport layer (ETL) PCBM (20 mg/mL in 1:1 chlorobenzene/toluene, 60 μ L) was spincoated at 2000 rpm for 30 seconds and annealed at 100 $^{\circ}$ C for 5 minutes. Finally, 100 nm Ag electrodes were evaporated through thermal evaporation.

Overcoming Intrinsic Quantum Confinement and Ultrafast Self-Trapping in Ag-Bi-I and Cu-Bi-I
Based 2D Double Perovskites through Electroactive Cations

Table S5.8: Synthesis conditions for the active layer POE-Ag in the solar cells shown in Figure S5.26 and discussed in the main text (cell number 9). Spin-coating volume is 70 μ L. Solutions were preheated to 60 °C and substrates were preheated to 80 °C.

	cation	metal	solvent	M	Annealing 1	Annealing 2
1	POE	Ag	DMF	0.075	60 °C 4 min	100 °C 5 min
2	POE	Ag	DMF	0.075	60 °C 4 min	140 °C 2 min
3	POE	Ag	DMF	0.075	60 °C 8 min	100 °C 5 min
4	POE	Ag	DMF	0.075	60 °C 8 min	140 °C 2 min

5	POE	Ag	DMF	0.0375	60 °C 4 min	100 °C 5 min
6	POE	Ag	DMF	0.0375	60 °C 4 min	140 °C 2 min
7	POE	Ag	DMF	0.0375	60 °C 8 min	100 °C 5 min
8	POE	Ag	DMF	0.0375	60 °C 8 min	140 °C 2 min

9	POE	Ag	DMF	0.01875	60 °C 4 min	100 °C 5 min
10	POE	Ag	DMF	0.01875	60 °C 4 min	140 °C 2 min
11	POE	Ag	DMF	0.01875	60 °C 8 min	100 °C 5 min
12	POE	Ag	DMF	0.01875	60 °C 8 min	140 °C 2 min

Crystallographic Data

1. Crystallographic data. (NOP-Ag) AgBiI₈C₁₃H₁₆N₄O

Experimental details

The X-ray intensity data of bv211 were measured on a Bruker D8 Venture TXS system equipped with a multilayer mirror monochromator and a Mo K α rotating anode X-ray tube ($\lambda = 0.71073 \text{ \AA}$). The frames were integrated with the Bruker SAINT software package. Data were corrected for absorption effects using the Multi-Scan method (SADABS). The structure was solved and refined using the Bruker SHELXTL Software Package. All hydrogen atoms have been calculated in ideal geometry riding on their parent atoms. The figures have been drawn at the 25% ellipsoid probability level.

Table S5.9: Crystallographic data for NOP-Ag

	1
net formula	C ₅₂ H ₆₄ AgBiI ₈ N ₄ O ₄
$M_r/\text{g mol}^{-1}$	2141.12
crystal size/mm	0.120 \times 0.080 \times 0.030
T/K	298.(2)
radiation	MoK α
diffractometer	'Bruker D8 Venture TXS'
crystal system	triclinic
space group	'P -1'
$a/\text{\AA}$	8.1626(3)
$b/\text{\AA}$	8.9305(3)
$c/\text{\AA}$	22.5258(7)
$\alpha/^\circ$	90.4150(10)
$\beta/^\circ$	95.2840(10)
$\gamma/^\circ$	90.2200(10)
$V/\text{\AA}^3$	1635.01(10)
Z	1

Overcoming Intrinsic Quantum Confinement and Ultrafast Self-Trapping in Ag-Bi-I and Cu-Bi-I
Based 2D Double Perovskites through Electroactive Cations

calc. density/g cm ⁻³	2.175
μ/mm^{-1}	6.804
absorption correction	Multi-Scan
transmission factor range	0.49–0.82
refls. measured	28790
R_{int}	0.0385
mean $\sigma(I)/I$	0.0388
θ range	2.905–27.484
observed refls.	6098
x, y (weighting scheme)	0.0300, 2.6508
hydrogen refinement	constr
Flack parameter	?
refls in refinement	7498
parameters	321
restraints	0
$R(F_{\text{obs}})$	0.0329
$R_w(F^2)$	0.0805
S	1.046
shift/error _{max}	0.001
max electron density/e Å ⁻³	0.828
min electron density/e Å ⁻³	-1.421

2. Crystallographic data. (POP-Ag) AgBiI₈C₁₉H₁₈N₄O

Experimental details

The X-ray intensity data of bv197 were measured on a Bruker D8 Venture TXS system equipped with a multilayer mirror monochromator and a Mo K α rotating anode X-ray tube ($\lambda = 0.71073 \text{ \AA}$). The frames were integrated with the Bruker SAINT software package. Data were corrected for absorption effects using the Multi-Scan method (SADABS). The structure was solved and refined using the Bruker SHELXTL Software Package. All hydrogen atoms have been calculated in ideal geometry riding on their parent atoms. The structure has been refined as a 2-component inversion twin. The twin domain volume ratio refined to 0.88/0.12. The figure has been drawn at the 25% ellipsoid probability level.

Table S5.10: Crystallographic data for POP-Ag

	2
net formula	C ₇₆ H ₇₂ AgBi ₈ N ₄ O ₄
$M_r/g \text{ mol}^{-1}$	2437.42
crystal size/mm	0.150 × 0.090 × 0.020
T/K	298.(2)
radiation	MoK α
diffractometer	'Bruker D8 Venture TXS'
crystal system	monoclinic
space group	'C 1 2 1'
$a/\text{\AA}$	52.957(3)
$b/\text{\AA}$	8.1623(5)
$c/\text{\AA}$	9.1169(6)
$\alpha/^\circ$	90
$\beta/^\circ$	94.641(2)
$\gamma/^\circ$	90
$V/\text{\AA}^3$	3927.9(4)
Z	2
calc. density/g cm ⁻³	2.061

Overcoming Intrinsic Quantum Confinement and Ultrafast Self-Trapping in Ag-Bi-I and Cu-Bi-I
Based 2D Double Perovskites through Electroactive Cations

μ/mm^{-1}	5.679
absorption correction	Multi-Scan
transmission factor range	0.73–0.90
refls. measured	30285
R_{int}	0.0219
mean $\sigma(I)/I$	0.0286
θ range	2.751–27.485
observed refls.	8208
x, y (weighting scheme)	0.0067, 42.7984
hydrogen refinement	constr
Flack parameter	0.125(13)
refls in refinement	8906
parameters	428
restraints	1
$R(F_{\text{obs}})$	0.0405
$R_w(F^2)$	0.0893
S	1.215
shift/error $_{\text{max}}$	0.001
max electron density/ $e \text{ \AA}^{-3}$	2.287
min electron density/ $e \text{ \AA}^{-3}$	-1.572

References

- [1] J. V. Passarelli, D. J. Fairfield, N. A. Sather, M. P. Hendricks, H. Sai, C. L. Stern, S. I. Stupp, *J. Am. Chem. Soc.* **2018**, *140*, 7313.
- [2] P. Hohenberg, W. Kohn, *Phys. Rev.* **1964**, *136*, B864-B871.
- [3] W. Kohn, L. J. Sham, *Phys. Rev.* **1965**, *140*, A1133-A1138.
- [4] G. Kresse, J. Furthmüller, *Physical review. B, Condensed matter* **1996**, *54*, 11169.
- [5] G. Kresse, D. Joubert, *Physical review. B, Condensed matter* **1999**, *59*, 1758.
- [6] P. E. Blöchl, *Physical review. B, Condensed matter* **1994**, *50*, 17953.
- [7] J. P. Perdew, K. Burke, M. Ernzerhof, *Physical review letters* **1996**, *77*, 3865.
- [8] A. Tkatchenko, R. A. DiStasio, R. Car, M. Scheffler, *Physical review letters* **2012**, *108*, 236402.
- [9] T. Bučko, S. Lebègue, J. Hafner, J. G. Ángyán, *Phys. Rev. B* **2013**, *87*.
- [10] M. K. Jana, R. Song, H. Liu, D. R. Khanal, S. M. Janke, R. Zhao, C. Liu, Z. Valy Vardeny, V. Blum, D. B. Mitzi, *Nature communications* **2020**, *11*, 4699.
- [11] D. Han, S. Chen, M.-H. Du, *J. Phys. Chem. Lett.* **2021**, *12*, 9754.
- [12] S. Yu, G. Na, S. Luo, O. Rubel, L. Zhang, *Journal of Applied Physics* **2020**, *128*.
- [13] D. Han, C. Feng, M.-H. Du, T. Zhang, S. Wang, G. Tang, T. Bein, H. Ebert, *J. Am. Chem. Soc.* **2021**, *143*, 12369.
- [14] M.-H. Du, *The journal of physical chemistry letters* **2015**, *6*, 1461.
- [15] A. M Ganose, A. J Jackson, D. O Scanlon, *JOSS* **2018**, *3*, 717.
- [16] L. R. V. Buizza, A. D. Wright, G. Longo, H. C. Sansom, C. Q. Xia, M. J. Rosseinsky, M. B. Johnston, H. J. Snaith, L. M. Herz, *ACS energy letters* **2021**, *6*, 1729.
- [17] T. Seifert, S. Jaiswal, U. Martens, J. Hannegan, L. Braun, P. Maldonado, F. Freimuth, A. Kronenberg, J. Henrizi, I. Radu, E. Beaurepaire, Y. Mokrousov, P. M. Oppeneer, M. Jourdan, G. Jakob, D. Turchinovich, L. M. Hayden, M. Wolf, M. Münzenberg, M. Kläui, T. Kampfrath, *Nat. Photonics* **2016**, *10*, 483.
- [18] B. Martín-García, D. Spirito, M.-L. Lin, Y.-C. Leng, S. Artyukhin, P.-H. Tan, R. Krahne, *Adv. Optical Mater.* **2022**, *10*, 2200240.
- [19] B. Martín-García, D. Spirito, G. Biffi, S. Artyukhin, B. Francesco, R. Krahne, *J. Phys. Chem. Lett.* **2021**, *12*, 280.
- [20] A. D. Wright, L. R. V. Buizza, K. J. Savill, G. Longo, H. J. Snaith, M. B. Johnston, L. M. Herz, *J. Phys. Chem. Lett.* **2021**, *12*, 3352.
- [21] C. Wehrenfennig, G. E. Eperon, M. B. Johnston, H. J. Snaith, L. M. Herz, *Advanced materials (Deerfield Beach, Fla.)* **2014**, *26*, 1584.
- [22] H. J. Joyce, J. L. Boland, C. L. Davies, S. A. Baig, M. B. Johnston, *Semicond. Sci. Technol.* **2016**, *31*, 103003.

6 Conclusions and Outlook

In summary, this thesis focused on the development of novel lead-free double perovskite materials with superior optoelectronic properties. According to theoretical studies, some candidates with promising optoelectronic properties comprise metastable octahedral arrangements, and have not been synthesized as bulk crystals. In this thesis, we proved that these metastable octahedral arrangements can be stabilized by morphological and molecular level dimensional reduction, namely in the form of double perovskite nanocrystals and layered two-dimensional double perovskite materials, respectively. We believe that these strategies can enrich the double perovskite family and benefit the screening of high-performance lead-free halide double perovskite materials for optoelectronic applications.

In the first section of the thesis, we reviewed the strategy of morphological level dimensional reduction. We summarized the latest advances of the synthesis methods for both lead-based and lead-free perovskite nanocrystals. Regarding the stability of perovskite nanocrystals, we reviewed the crystal structural stability, interface-induced stability and environmental stability, such as oxygen, moisture, light and thermal stability. Moreover, strategies for encapsulation to protect perovskite nanocrystals were discussed. Importantly, various applications of the PNCs in optoelectronics, like solar cells, light-emitting diodes and photodetectors were briefly presented. Finally, the challenges remaining for improving the stability of PNCs and an outlook towards possible directions in developing PNC-based devices with high performance and great operational durability were addressed.

The second section presented an example of stabilizing metastable double perovskites through morphological level dimensional reduction. We reported a facile and fast synthesis method for $\text{Cs}_2\text{CuSbCl}_6$ double perovskite nanocrystals by using a modified LARP method at ambient conditions. A less toxic and easily removable solvent, methanol, was chosen for solvating precursor salts. We demonstrated that the polarity of anti-solvents and the ratio of oleic acid/oleylamine (OA/OAm) ligands have a strong effect on the size and morphology of the resulting double perovskite

nanocrystals. $\text{Cs}_2\text{CuSbBr}_6$ double perovskite nanocrystals with a narrow band gap of 0.9 eV were successfully developed for the first time by employing an anion-exchange reaction in solution. Both $[\text{CuCl}_6]^{5-}$ and $[\text{CuBr}_6]^{5-}$ octahedra can be stabilized in these double perovskites at the nanoscale with the assistance of organic ligands, which we expect to enable the development of other predicted-metastable (as bulk) Cu(I)-based double perovskite materials to enrich the double perovskite family and to benefit the screening of high performance lead-free halide double perovskite materials for optoelectronic applications. Taking advantage of the solution processability of double perovskite nanocrystals, smooth and dense $\text{Cs}_2\text{CuSbCl}_6$ and $\text{Cs}_2\text{CuSbBr}_6$ double perovskite nanocrystals films were successfully fabricated.

The third section presented an example of stabilizing metastable double perovskites through molecular level dimensional reduction. Inorganic frameworks containing either $[\text{AgI}_6]^{5-} + [\text{BiI}_6]^{3-}$ or $[\text{CuI}_6]^{5-} + [\text{BiI}_6]^{3-}$ octahedra were successfully stabilized by introducing large functional organic cations into double perovskite structures and “cutting” the 3D structures along a certain plane to form 2D perovskites. We report that both Ag-Bi-I and Cu-Bi-I systems are thermodynamically stable with the structures of (aromatic-*O*-linker- NH_3) $_4\text{AgBiI}_8$ and (aromatic-*O*-linker- NH_3) $_4\text{CuBiI}_8$, respectively, where the aromatic moiety is naphthalene or pyrene and the linker is ethyl or propyl. We investigated their structural and optoelectronic properties, with special regard to the electrical conductivity and the charge carrier dynamics. With extended conjugated systems, (pyrene-*O*-ethyl- NH_3) $_4\text{AgBiI}_8$ shows a higher photocurrent response ratio and an enhanced out-of-plane conductivity among eight new 2D double perovskites due to a better energy level matching between organic and inorganic layers (type IIb quantum well system) and a favorable intra-organic layer arrangement. Based on superior out-of-plane conductivity, the first functional $n = 1$ Ruddlesden-Popper phase 2D double perovskite solar cell with parallel-oriented (pyrene-*O*-ethyl- NH_3) $_4\text{AgBiI}_8$ film as an active layer was successfully fabricated with a power conversion efficiency of 0.17% and a V_{OC} of 0.86 V.

Although our concept of stabilizing metastable double perovskites through morphological and molecular level strategies has been confirmed, more comprehensive research efforts are needed to achieve high performance optoelectronic devices based on double perovskite materials. On the one hand, more effort is required for screening high-performance double perovskite materials both theoretically and experimentally. Especially, for inorganic-organic hybrid layered double perovskites, theoretical studies lag behind those of their 3D counterparts. On the other hand, in-depth investigations are needed regarding the crystallization mechanism of these materials and the design

strategies for functional organic compounds for stabilizing the inorganic moieties and enhancing the electronic coupling of adjacent inorganic moieties in both double perovskite nanocrystals and layered double perovskites.

Various processes for the synthesis of perovskite nanocrystals have been reported, among which the ligands are typically necessary to form nanoscale structures. Comparing to conventional nanoscale semiconductors, achieving precise control of the size and shape of double perovskite nanocrystals needs further effort. In addition, the mechanisms of how ligands control the size and shape of the double perovskite nanocrystals need to be elaborated. Optimization of the ligand density and developing new types of ligands, for example, conductive ligands, for these “unstable” double perovskite nanocrystals to balance the charge carrier mobility and phase stability need further effort. A systematic exploration of novel ligands for the sake of stable surface termination in double perovskite nanocrystals and a deep understanding of their functionality are of key importance. Besides, it is also of great interest to study the impact of ligands on the electronic band structure of double perovskite nanocrystals. We believe that the research of functional ligands will open new vistas in the development of optoelectronic applications of lead-free double perovskite materials.

Inorganic-organic hybrid layered double perovskites with bulky organic spacers can effectively stabilize the inorganic slabs, leading to excellent environmental stability. However, the performance of photovoltaic devices based on these materials is still inferior to their 3D counterparts, mostly due to insufficient exciton dissociation and poor charge transport ability. Intrinsically, the small dielectric constants and insulating nature of traditional organic spacers account for the poor resulting device performance. Additionally, multiple types of quantum wells (different n -value phases in single films) and random orientation of crystals are commonly seen in thin films, resulting in unsatisfactory charge conductivity. To achieve layered double perovskite based solar cells with both high efficiency and good stability, three key points need to be further studied.

Firstly, precise control over the phase purity and vertical orientation of high n -value layered double perovskites is required, for example, through synthetic approaches like hot casting, additive and/or solvent engineering, solvent vapor annealing and so on. Furthermore, a deep understanding of the growth mechanism and crystallization kinetics is required in view of the diversity of organic spacers, which is believed to be able to guide the design strategy towards functional organic spacers.

Secondly, to address the insulating nature of traditional organic spacers, designing suitable functional organic spacers and establishing structure-property relationships for these novel layered double

perovskites are crucial for the sake of 'breaking' the quantum well and mobilizing the self-trapped excitons and charge carriers. A large effort has recently been dedicated to this challenge. We believe that more and more "star organic spacers" will be designed and synthesized soon with the benefit of effective selecting methods such as machine learning.

Thirdly, in view of commercialization, the large-scale fabrication of layered double perovskites as well as related devices lags behind their 3D counterparts, and should be enhanced in the future.

The advancement of functional organic ligands or spacers for double perovskites invokes the flourishing development of organometallic chemistry dating back to the 19th century, which bridges inorganic chemistry and organic chemistry and benefits commercially important reactions such as homogenous catalysts or stoichiometric reagents. The study of functional organic ligands and spacers for perovskite nanocrystals and layered perovskites, respectively, is expected to elevate the research of perovskite materials to a new level, at which stability issues can be addressed while excellent optoelectronic properties are maintained.

7 Publications and Conference Contributions

7.1 Publications

1. Shizhe Wang^{*}, AmirAbbas YousefiAmin, Linzhong Wu, Muhan Cao, Qiao Zhang^{*}, and Tayebbeh Ameri^{*}, **Perovskite Nanocrystals: Synthesis, Stability and Optoelectronic Applications**, *Small Struct.* **2021**, 2, 2000124. (back cover image: *Small Struct.* **2021**, 2, 2170009.)
2. Dan Han^{*}, Chunbao Feng, Mao-Hua Du, Tao Zhang, Shizhe Wang, Gang Tang^{*}, Thomas Bein, and Hubert Ebert, **Design of High-Performance Lead-Free Quaternary Antiperovskites for Photovoltaics via Ion Type Inversion and Anion Ordering**, *J. Am. Chem. Soc.* **2021**, 143, 12369-12379
3. Dan Han^{*}, Mao-Hua Du, Menglin Huang, Shizhe Wang, Gang Tang^{*}, Thomas Bein, and Hubert Ebert, **Ground-state structures, electronic structure, transport properties and optical properties of Ca-based anti-Ruddlesden-Popper phase oxide perovskites**, *Phys. Rev. Mater.* **2022**, 6, 114601.
4. Shizhe Wang, Dan Han^{*}, Clément Maheu, Zehua Xu, Alexander Biewald, Hannah Illner, Rik Hooijer, Thomas Mayer, Achim Hartschuh, Hubert Ebert, and Thomas Bein^{*}, **Room-Temperature Synthesis of Lead-Free Copper(I)-Antimony(III)-Based Double Perovskite Nanocrystals**, *APL Mater.* **2023**, 11, 041110.
5. Rik Hooijer[†], Shizhe Wang[†], Alexander Biewald, Christian Eckel, Marcello Righetto, Meizhu Chen, Zehua Xu, Dominic Blätte, Dan Han, Hubert Ebert, Laura M. Herz, R. Thomas Weitz, Achim Hartschuh, Thomas Bein^{*}, **Overcoming Intrinsic Quantum Confinement and Ultrafast Self-Trapping in Ag-Bi-I and Cu-Bi-I Based 2D Double Perovskites through Electroactive Cations** (submitted).

^{*} Corresponding authors.

[†] Author contributed equally.

7.2 Contribution to Conferences

7.2.1 Oral Presentations

1. “Stabilizing Metastable Lead-Free Double Perovskite Structures by Morphological and Molecular Level Dimension Reduction”

Shizhe Wang, Dan Han, Clément Maheu, Zehua Xu, Alexander Biewald, Hannah Illner, Rik Hooijer, Thomas Mayer, Achim Hartschuh, Hubert Ebert, and Thomas Bein.

PC/TC Colloquium (LMU), Großhadern, Germany, December 2023.

2. “Room-Temperature Synthesis of Lead-Free Copper(I)-Antimony(III)-Based Double Perovskite Nanocrystals”

Shizhe Wang, Dan Han, Clément Maheu, Zehua Xu, Alexander Biewald, Hannah Illner, Rik Hooijer, Thomas Mayer, Achim Hartschuh, Hubert Ebert, and Thomas Bein.

The Materials for Sustainable Development Conference (MATSUS24), Barcelona, Spain, March 2024.

7.2.2 Poster Presentations

1. “Room-Temperature Synthesis of Lead-Free Copper-Antimony-Based Double Perovskite Nanocrystals for Photovoltaic Application”

Shizhe Wang, Dan Han, Rik Hooijer, Andreas Weis, Florian Wolf, Hubert Ebert, and Thomas Bein.

2022 International Conference on Hybrid and Organic Photovoltaics (HOPV22), Valencia, Spain, May 2022.

2. “Room-Temperature Synthesis of Lead-Free Copper(I)-Antimony(III)-Based Double Perovskite Nanocrystals”

Shizhe Wang, Dan Han, Clément Maheu, Zehua Xu, Alexander Biewald, Hannah Illner, Rik Hooijer, Thomas Mayer, Achim Hartschuh, Hubert Ebert, and Thomas Bein.

2023 International Conference on Hybrid and Organic Photovoltaics (HOPV23), London, England, June 2023.

3. “Lead-Free Antimony-Based Materials for Photovoltaic Applications”

Shizhe Wang, Andreas Weis, Rik Hooijer, Dan Han, Waldemar Kaiser, Alexander Biewald, Patrick Dörflinger, Clément Maheu, Zehua Xu, Hannah Illner, Oleksandr Arsatiants, David Helminger, Vladimir Dyakonov, Edoardo Mosconi, Filippo De Angelis, Thomas Mayer, Achim Hartschuh, Hubert Ebert, and Thomas Bein.

The third e-conversion conference 2023, Tuzting, Germany, October 2023.